The psychiatric risk gene *Cacna1c* regulates mitochondrial function in cellular stress responses

Dissertation
zur
Erlangung des Doktorgrades
der Naturwissenschaften
(Dr. rer. nat.)

dem
Fachbereich Pharmazie der
Philipps-Universität Marburg

vorgelegt von

Susanne Michels

aus Koblenz

Marburg/Lahn 2018

Erstgutachter: Prof. Dr. Carsten Culmsee
Zweitgutachter: Prof. Dr. Holger Garn

Eingereicht am 06.11.2018
Tag der mündlichen Prüfung am 18.12.2018

Hochschulkennziffer: 1180

Eidesstattliche Erklärung

Ich versichere, dass ich meine Dissertation

„The psychiatric risk gene *Cacna1c* regulates mitochondrial function in cellular stress responses“

selbständig ohne unerlaubte Hilfe angefertigt und mich dabei keiner anderen als der von mir ausdrücklich bezeichneten Quellen bedient habe. Alle vollständig oder sinngemäß übernommenen Zitate sind als solche gekennzeichnet.

Die Dissertation wurde in der jetzigen oder einer ähnlichen Form noch bei keiner anderen Hochschule eingereicht und hat noch keinen sonstigen Prüfungszwecken gedient.

Marburg, den 06.11.2018

.....

(Susanne Michels)

Table of contents

1 Introduction

"At the interior of our cells, driving them, providing the oxidative energy that sends us out for the improvement of each shining day, are the mitochondria, and … without them, we would not move a muscle, drum a finger, think a thought." Lewis Thomas, 1974 (1)

1.1 Affective disorders

Affective disorders such as major depression (MDD) and bipolar disorder (BD) are among the most prevalent forms of mental illness and affect more than 350 million people worldwide (2). These major neuropsychiatric disorders are chronic, multifaceted, and heterogeneous diseases with shared symptomatic features, also including schizophrenia and autism (3). BD has a lifetime prevalence of 3.9% and is characterized by episodes of mania or hypomania and depression, which typically occur in a cyclical course (4). The manic phase involves symptoms of elevated mood and over-activity (2). Mood stabilizers, such as lithium, antipsychotics, and anticonvulsants, form the basis of BD pharmacotherapy (5). With a lifetime risk of 16.6%, MDD is the more frequent affective disorder and its characteristic symptoms comprise loss of interest, sadness, feelings of guilt, sleep disturbances, and poor concentration (2, 4). Currently available pharmacological treatments are targeted against monoaminergic neurotransmitter imbalances and their main classes include tricyclic antidepressants as well as selective serotonin reuptake inhibitors (6). However, it is estimated that over one-third of MDD patients are resistant to antidepressant therapy (7). In fact, despite being among the leading causes of disability worldwide, their underlying pathophysiology still remains poorly understood (8). Therefore, a better understanding of the neurobiology underlying MDD and BD is highly warranted to improve treatment outcome and to provide greater and sustained rates of remission in the future. Established current neurobiological theories attempting to elucidate the pathophysiology of these complex psychiatric disorders mainly focus on genetic and environmental risk factors, and ,in particular, their interactions (9). The pronounced heritability of affective disorders suggests that genetic influences play a key role in disease pathogenesis (10). Indeed, the heritability ranges from 40-50% in MDD to 80-85% in BD, and family studies indicate for MDD a two- to threefold and for BD a nearly tenfold increase in lifetime risk among first-degree relatives (11, 12).

1.1.1 Psychiatric risk gene *CACNA1C*

During the past decade, several genome wide association studies (GWAS) have identified *CACNA1C* as one of the strongest and most replicable genetic risk factors for the development of affective disorders (13–15). *CACNA1C* codes for the pore-forming α_{1C} subunit of $Ca_V1.2$, the

major L-type voltage-gated calcium channel in the brain. L-type calcium channels (LTCC) are heteromultimeric protein complexes consisting of a pore-forming α_1 as well as auxiliary β and $\alpha_2\delta$ subunits, which are required for functional expression and cell surface trafficking (16). However, the major channel characteristics including voltage sensor, ion selectivity, and pharmacological drug binding domains reside in the transmembrane α_1 subunit (17). LTCCs exhibit long-lasting calcium currents upon strong membrane depolarization and are sensitive to blockade by dihydropyridines (DHP) such as nimodipine (18). There exist four different LTCC isoforms, two of them are expressed in the mammalian brain: Cav1.3, its α_1 subunit is encoded by *CACNA1D*, accounts for ~20% of the brain LTCCs and the more abundant Cav1.2 for approximately 80% (19–21). In the central nervous system (CNS), Cav1.2 is mainly localized in neuronal cell bodies, dendrites, and postsynaptic regions (22, 23). Brain Cav1.2 channels couple Ca^{2+} influx to neuronal gene transcription and play a pivotal role in regulating neuronal excitability, synaptic plasticity, dendritic development, and cell survival (17, 24).

To date, several psychiatric risk-associated single nucleotide polymorphisms (SNP) in *CACNA1C* have been found in its intronic regions, thereby likely affecting Cav1.2 channel expression rather than function. Such genetic changes increase the disease probability, but are not deterministic. So far, both decreased and increased Cav1.2 levels have been associated with the main non-coding risk SNP rs1006737, suggesting that alternations in *CACNA1C* expression may be developmental-stage-, brain-region-, as well as cell-type-specific (25–28). In this context, it has been shown that *Cacna1c* depletion in forebrain glutamatergic neurons, either during development or adulthood, differentially modulates synaptic plasticity, stress susceptibility, and cognition in mice (29). These findings indicate an essential role for Cav1.2 in memory formation during development, whereas Cav1.2 activation during adulthood is even detrimental for synaptic plasticity. Additionally, a number of studies provide convincing evidence that the common risk haplotype rs1006737 is related to impaired calcium signaling as well as compromised structure and function of brain regions relevant for characteristic behavioral changes observed in psychiatric patients (17, 30, 31). Particularly affected brain regions include the prefrontal cortex (PFC) and the hippocampus (HC), which are essential for stress regulation, emotion, cognition, learning, and memory (32). Supportive findings from transgenic animal models confirm the impact of the cross-disorder risk gene *Cacna1c* on PFC- and HC-dependent behaviors. For instance, constitutive *Cacna1c* haploinsufficiency leads to increased anxiety, antidepressant-like effects, and resilience to chronic stress in adult mice (33–36) and causes deficits in social behavior and affective communication in juvenile rats (37). Furthermore, embryonic deletion of *Cacna1c* in mouse forebrain glutamatergic neurons results in diminished synaptic plasticity, cognitive decline, and reduced sociability (29). However, the underlying cellular and molecular mechanisms explaining how genetic *CACNA1C* risk variants contribute to the pathophysiology of neuropsychiatric disorders remain largely unknown (38, 39).

1.1.2 Environmental risk factors

Vulnerability to affective disorders is not only based on genetic predisposition, but also involves diverse environmental risk factors such as intrauterine infections of the embryo, perinatal brain injuries attributed to birth complications, childhood maltreatment, migration, chronic stress and other adverse pathophysiological and psychosocial life events (40–42). There is accumulating evidence that such psychosocial stressors activate oxidative stress pathways, thereby disrupting the oxidant-antioxidant balance within the brain and causing oxidative damage to DNA, mitochondria, lipids, and proteins. Mitochondrial impairment, in turn, can accelerate the production of reactive oxygen species (ROS), which further modifies biological macromolecules and alters cellular functions (43). The brain is especially vulnerable to oxidative stress due to its high metabolic rate coupled with high oxygen consumption and limited levels of antioxidants (44). Additionally, the brain is particularly susceptible to lipid peroxidation because of the large amounts of polyunsaturated fatty acids present in neuronal membranes (45, 46). In the CNS, the accumulation of oxidative damage may result in loss of neuronal plasticity and function, and ultimately in apoptotic cell death, processes that have also been implicated as underlying mechanisms in the neuropathology of affective disorders (47, 48).

Stress is also associated with the activation of the innate immune system and stressful experiences such as adverse childhood events induce long-term alterations of the immune response, lead to elevated levels of pro-inflammatory cytokines in blood and brain, and increase the susceptibility to develop psychiatric disorders later in life (7, 49–51). The early years of life constitute an important and sensitive developmental period in which physiological and behavioral responses to the environment are shaped (52). In line with the effects of psychiatric risk gene variants, early-life adverse experiences are also closely linked to detrimental morphological brain alterations, in this case PFC and HC volume loss (53, 54). Physical and emotional neglect during childhood can be simulated in rodents by post-weaning social isolation, which induces behavioral phenotypes related to various neuropsychiatric disorders including social withdrawal and cognitive inflexibility (55). Moreover, these prominent impairments due to juvenile social deprivation are accompanied by reduced PFC volume and decreased hippocampal synaptic plasticity (56). On the contrary, social and physical environmental enrichment, mimicking positive and protective life experiences, promotes HC neurogenesis, improves learning and memory, reduces depression-related behavior, and has beneficial effects on affective communication through ultrasonic vocalizations in rats (57, 58).

1.1.3 Mitochondrial dysfunction

Various epidemiologic studies indicate that a single risk factor is not sufficient for the development of a certain psychiatric disorder. These complex diseases rather result from multiple interdependent processes involving the interaction of different genetic and environmental factors (9). At the cellular level, the substantial impact of genetic and environmental risks as well as their interplay on neuroplasticity and behavior might be mediated by mitochondrial dysfunction, which has been frequently associated with psychiatric disorders (59). Intra- and intercellular mechanisms of stress adaptation in the brain such as in the course of MDD and BD lead to a significant increase in energy demand (60). Mitochondria are the key organelles of cellular energy metabolism and play a crucial role in regulating calcium homeostasis, redox balance, synaptic plasticity, and cell viability, thereby influencing neural circuits that control high-order functions of the brain such as mood, cognition, and social behavior (61). In this context, emerging evidence strongly suggests impaired mitochondrial bioenergetics as possible underlying mechanism of regional brain abnormalities in mood disorders by compromising energy-dependent processes such as neuronal plasticity and the brain's ability to resist or adapt to genetic and environmental stressors (62).

While affective disorders are not considered as classic mitochondrial diseases, numerous studies propose a substantial link between mitochondrial dysfunction and these disorders in genetic and behavioral animal models, as well as in patients (63, 64). For example, patients suffering from mitochondrial diseases caused by genetic alterations affecting mitochondrial metabolism frequently develop symptoms of MDD, BD, psychosis, and personality changes (65, 66). Further, psychiatric symptoms are often prevalent years before the onset of cognitive and motor impairments in patients later diagnosed with neurodegenerative diseases, such as Alzheimer's, Parkinson's or Huntington's disease (67), which all feature mitochondrial dysfunction in neurons as a major hallmark of their underlying pathology (68–70). Concurrent findings from neuro-imaging, post-mortem brain analyses, GWAS, and studies on peripheral biomarkers suggest that psychiatric disorders are accompanied by mitochondrial dysfunction (59, 71). These investigations revealed reduced complex I activity, increased ROS levels, decreased ATP production, downregulated expression of anti-apoptotic proteins, and upregulated expression of pro-apoptotic proteins in patients suffering from affective disorders or schizophrenia, all indicating impaired mitochondrial function.

Mitochondria are highly dynamic and undergo permanent fission and fusion processes allowing for the transport, reorganization, and regeneration of these organelles within the cell. Intact mitochondrial fission and fusion dynamics are important for proper cristae formation, respiratory functions, and quality control through mitophagy. Perturbations in the structural dynamics lead to reduced energy supply, accumulation of dysfunctional mitochondria, and

increased ROS production. These phenomena are closely associated with both, enhanced inflammatory responses and the risk of psychiatric disorders including MDD and BD (72, 73). Overall, accumulating evidence suggests that mitochondrial dysfunction contributes to disease neuropathology and may therefore represent a converging point of alterations in complex interdependent processes involved in energy metabolism, cellular stress and calcium homeostasis (74). Furthermore, mitochondrial dysfunction is currently being discussed as a potential biomarker for affective disorders supporting early diagnosis, control of disease progression, and evaluation of treatment response (75).

1.1.4 Neuroinflammation

A growing body of evidence suggests the involvement of neuroinflammation and its primary mediators, the brain-resident microglia, in the neurobiology of psychiatric disorders including MDD, BD, schizophrenia, and autism (76–79). Several postmortem brain analyses have shown increased activation of microglia in depressed patients (80) as well as in subjects who committed suicide (81). Concordantly, recent in vivo positron emission tomography (PET) imaging studies, using microglial 18 kDa translocator protein (TSPO) radio ligands, identified elevated microglial activation in cortical areas of MDD and BD patients, which directly correlates with disease severity and duration (82–85).

Microglia represent 10-15% of the total cell population within the CNS (86) and originate from hematopoietic stem cells in the yolk sac (87). They invade the brain early in development, differentiate into a highly ramified phenotype, and continuously survey their micro-environment for signs of damage or pathogens (84). As the resident macrophages of the CNS, microglia regulate innate immunity in the brain and initiate inflammatory responses, which are essential for neuronal survival and maintenance during infection and sterile injury (88). However, excessive or prolonged neuroinflammation is associated with detrimental neuronal degeneration, synaptic deficits, and impaired cognition, thus eventually contributing to the development of psychiatric disorders (89). In response to changes in brain homeostasis microglial cells transform, morphologically and functionally, from a resting into an activated state. ROS production, metabolic reprogramming, and related glycolytic activity play a major role in coordinating these adaptive processes (90). Upon classical M1-like activation, microglia initiate signal transduction cascades resulting in the release of pro-inflammatory cytokines, chemokines and nitric oxide (NO) (87). Alternative M2-like polarization induces an anti-inflammatory microglial phenotype, which promotes debris clearance and wound repair (88, 91). Importantly, this classification system oversimplifies the existing diversity of microglial phenotypes and does not reflect the complexity of activation patterns (87). Microglia share phenotypic characteristics and immunological functions with circulating peripheral blood monocytes and, indeed, also their number is increased in patients with affective disorders

accompanied by a rise in plasma cytokines including pro-inflammatory interleukin 1β (IL-1β), IL-6, and tumor necrosis factor α (TNF-α) (92–94).

A wide variety of studies indicate that exposure to chronic psychological stress causes microglial activation resulting in elevated pro-inflammatory cytokine release (77, 95). These can, in turn, reduce mitochondrial density and impair oxidative phosphorylation, which leads to increased ROS production and oxidative stress, thereby highlighting the close interconnection between different pathogenic processes (96–98). In addition, pro-inflammatory cytokines modulate the tryptophan-kynurenine pathway and enhance microglial synthesis of the neurotoxic N-methyl-D-aspartate (NMDA) receptor agonist quinolinic acid contributing to hippocampal atrophy observed in depression as well as linking inflammation and excitotoxicity, which is also implicated in the pathogenesis of psychiatric disorders (92, 99, 100).

1.1.5 Peripheral blood mononuclear cells as potential biomarker

Human peripheral blood mononuclear cells (PBMCs) are a heterogeneous population of circulating immune cells including lymphocytes (T, B, and natural killer cells), monocytes, and dendritic cells. The frequencies of these populations vary across individuals, but are typically in the range of 70-90% for lymphocytes and 10-30% for monocytes, while the rarer dendritic cells only account for 1-2% (101). About 70% of circulating lymphocytes are T cells, 15% B cells and the remaining 15% consist of natural killer (NK) cells (102). The cytokine-producing, cytotoxic T and the antibody-producing B cells constitute the major cellular components of the adaptive immune response. NK cells are part of the innate immune system and destroy virally infected and tumor cells. Monocytes are phagocytic cells which screen the body for sites of inflammation and play an important role in innate immunity (103). Once migrated into tissues, they differentiate into macrophages. Dendritic cells are antigen-presenting cells, which interact with T and B cells to initiate adaptive immune responses (104).

Besides comprising the main mediators of cellular immunity, PBMCs also provide an accessible source of mitochondria. Furthermore, it has been shown recently in nonhuman primates that the mitochondrial bioenergetics profile of blood monocytes and platelets is positively related to frontal cortex mitochondrial function and metabolism (105). Brain mitochondrial dysfunction, in turn, is significantly involved in the pathophysiology of psychiatric disorders as supported by substantial and growing literature (63, 106). In addition, a few studies already assessed mitochondrial function in circulating blood cells of psychiatric patients (107–109). Mitochondria isolated from PBMCs of patients with chronic schizophrenia showed decreased complex I activity, but no changes in complex II and III compared to healthy individuals (107). Basal and maximal mitochondrial respiration was significantly lower in

platelets (108) as well as PBMCs (109) of depressed patients versus healthy controls. Collectively, these findings indicate that PBMCs may be a valuable surrogate of brain function and establish mitochondrial perturbations in PBMCs as biomarker for neuropsychiatric illnesses.

Previous research has investigated mitochondrial alterations mostly in patients, however, whether mitochondrial dysfunction precedes the onset of psychiatric disorders has not been investigated in detail so far. Therefore, it remains to be elucidated, if changes in mitochondrial bioenergetics are already present in healthy individuals with psychiatric disease-relevant genetic or environmental risk factors and can, thus, serve as prognostic marker before clinical symptoms manifest.

1.2 In vitro stress models

Defined cell model systems are optimally suited to investigate signaling pathways likely involved in the pathophysiology of neuropsychiatric disorders and associated mitochondrial perturbations as well as metabolic impairments. Further, these in vitro models allow for controlled manipulations facilitating systematic studies of gene-environment interactions and their impact on mitochondrial morphology, integrity and function.

1.2.1 Glutamate-induced oxytosis in HT22 cells

Oxidative stress has been frequently linked to the pathophysiology of affective disorders. In MDD patients and in animal models, decreased levels of antioxidants and antioxidant enzymes were detected, suggesting an impaired antioxidant defense associated with depressive behavior (44, 110). The immortalized mouse hippocampal HT22 cell line serves as a well-established model system to investigate oxidative stress, which reflects a common cellular response to environmental stress, and allows for the targeted, e.g. siRNA-mediated, manipulation of gene expression (111, 112).

Since neuronal HT22 cells do not express functional ionotropic glutamate receptors, glutamate-induced cell death is mediated by a caspase-independent, oxidative stress-dependent pathway called oxytosis, a term first introduced by Tan et al. in 2001 (113). As summarized in Figure 1, millimolar extracellular concentrations of glutamate inhibit cystine uptake via the plasma membrane-localized cystine/glutamate antiporter (X_c^-), which is, after reduction to cysteine, essential for the synthesis of the main brain antioxidant glutathione (GSH) (114). Cellular GSH depletion, in turn, involves reduced glutathione peroxidase 4 (GPX4) and enhanced 12/15 lipoxygenase (12/15-LOX) activities (112, 115). In HT22 cells, this consecutively leads to an increase in ROS formation and lipid peroxidation initiating the

activation and mitochondrial translocation of pro-apoptotic BH3-interacting domain death agonist (BID) and the fission-inducing guanosine triphosphatase dynamin-related protein 1 (Drp1) (111, 116, 117). Upon mitochondrial transactivation, these proteins then mediate, at the level of mitochondria, fission, Ca^{2+} overload, ROS production, loss of membrane potential ($\Delta\Psi_m$), ATP depletion, and respiratory dysfunction (118). Finally, these fatal mitochondrial perturbations result in disruption of the mitochondrial membrane and release of apoptosis inducing factor (AIF) causing nuclear DNA fragmentation and ultimately neuronal cell death (119, 120).

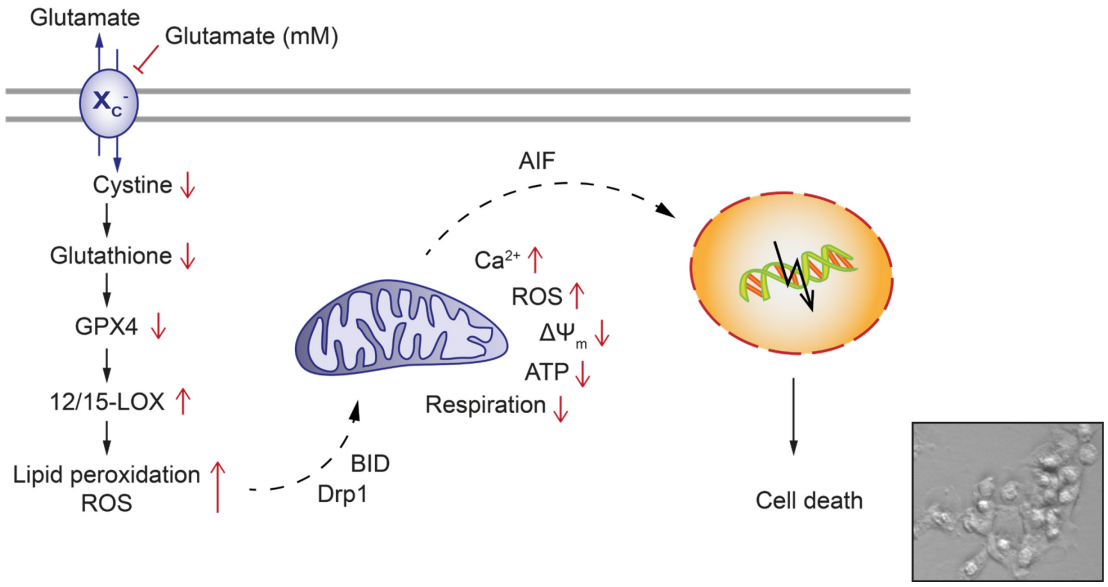

Figure 1. Molecular mechanisms of glutamate-induced oxidative stress in HT22 cells

The scheme illustrates the major hallmarks of oxytosis in immortalized hippocampal HT22 cells. X_C^-, cystine/glutamate antiporter; GPX4, glutathione peroxidase 4; 12/15-LOX, 12/15 lipoxygenase; ROS, reactive oxygen species; BID, BH3-interacting domain death agonist; Drp1, dynamin-related protein 1; $\Delta\Psi_m$, mitochondrial membrane potential; ATP, adenosine triphosphate; AIF, apoptosis inducing factor.

1.2.2 Glutamate-induced excitotoxicity in primary cortical neurons

First described by Olney in 1986 (121), excitotoxicity refers to the toxic effect of prolonged neuronal over-activation by excitatory amino acids and plays a central role in a wide variety of neurological diseases including ischemic stroke, epilepsy as well as psychiatric disorders (99). Glutamate is the primary excitatory neurotransmitter in the CNS and binds, amongst others, to ionotropic glutamate receptors. These ligated-gated ion channels are classified into three subtypes: N-methyl-D-aspartate (NMDA), α-amino-3-hydroxy-5-methyl-4-isoxazolepropionate (AMPA), and kainate receptors (122). Under pathological conditions, excessive extracellular glutamate concentrations are primarily associated with a massive influx of calcium in particular via the over-stimulation of highly Ca^{2+}-permeable NMDA

receptors as well as voltage-gated Ca^{2+} channels, which are indirectly activated by glutamate-induced depolarization (123) (Figure 2). In neurons, intracellular calcium overload subsequently triggers mitochondrial Ca^{2+} accumulation, a critical step in glutamate excitotoxicity. Mitochondrial Ca^{2+} loading, in turn, promotes mitochondrial membrane depolarization ($\Delta\Psi_m$), superoxide generation, respiratory inhibition, and ATP depletion (124). The resulting mitochondrial dysfunction ultimately induces the opening of the mitochondrial permeability transition pore (mPTP), thus causing the disruption of metabolic gradients between mitochondria and cytosol and the release of pro-apoptotic cytochrome c (CytC), which mediates caspase activation and DNA damage (99).

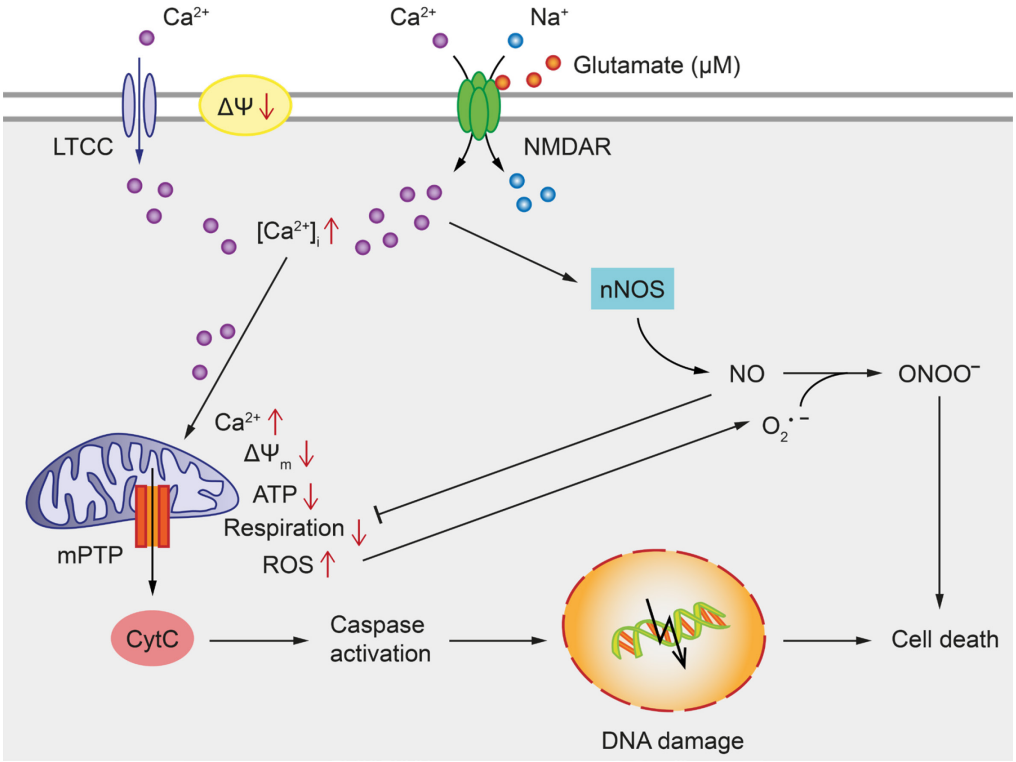

Figure 2. Molecular mechanisms of glutamate-induced neuronal excitotoxicity

The schematic shows the main molecular mechanisms involved in excitotoxic cell death in neurons. NMDAR, N-methyl-D-aspartate receptor; LTCC, L-type calcium channel; ΔΨ, membrane potential; $[Ca^{2+}]_i$, intracellular calcium concentration; $\Delta\Psi_m$, mitochondrial membrane potential; ATP, adenosine triphosphate; ROS, reactive oxygen species; nNOS, neuronal nitric oxide synthase; NO, nitric oxide; $O_2^{\bullet-}$, superoxide anion; $ONOO^-$, peroxynitrite; mPTP, mitochondrial permeability transition pore; CytC, cytochrome c; DNA, deoxyribonucleic acid.

Additionally, Ca^{2+} entry through NMDA receptors stimulates neuronal nitric oxide synthase (nNOS). Activation of nNOS leads to NO production, which inhibits the mitochondrial electron transport chain (ETC) and reacts with superoxide anions ($O_2^{\bullet-}$) to form toxic peroxynitrites, thereby further contributing to excitotoxic neuronal cell death (122, 125). It is

generally agreed that glutamate-induced cell death is not a uniform event, but rather a mixed form of necrosis and apoptosis with the severity of the excitotoxic insult determining the prevalent of both pathways (122, 126). Characterized by loss of plasma membrane integrity, vacuolization and cell swelling, necrosis predominates after intense glutamate insults, whereas mild glutamate exposure results in apoptotic cell death featuring chromatin condensation, nuclear shrinkage, and DNA oligonucleosomal degradation (127, 128).

1.2.3 LPS-induced inflammation in primary microglia

Microglial activation plays a prominent role in the pathogenesis of affective disorders (76, 129) and its underlying molecular pathways can be systematically studied in an in vitro model of lipopolysaccharide-stimulated primary cultures (Figure 3). As integral part of gram-negative bacterial cell walls, lipopolysaccharide (LPS) represents a highly immunogenic antigen and polarizes microglia towards a M1-like phenotype. Microglial cells express intracellular or membrane-bound pattern recognition receptors (PRR), including nucleotide-binding oligomerization domain (NOD)-like receptors (NLR) or Toll-like receptors (TLR), and thus recognize pathogen-associated molecular patterns (PAMPs) such as the TLR4 ligand LPS. Upon PRR activation, microglia acquire an amoeboid-like phenotype, migrate to inflammatory sites and promote innate immune responses (130, 131). Even in the absence of overt pathogenic infection, cell damage or stress responses may activate microglia via endogenous damage-associated molecular patterns (DAMPs) such as ATP or mitochondrial DNA (mtDNA), which also bind to PRRs (132, 133). This triggers the assembly of NOD-, LRR- and pyrin domain-containing 3 (NLRP3) and caspase-1 to form the inflammasome, a multi-protein signaling complex, leading to the processing of pro-IL-1β as well as pro-IL-18 to active IL-1β and IL-18 respectively (134). In addition, a particular role has been described for oxidized mtDNA and mitochondria-derived ROS in pathways that activate the inflammasome (135–138).

The binding of LPS to TLR4 further leads to the activation of redox-sensitive transcription factors, such as nuclear factor κB (NF-κB), and subsequently to an increased expression of pro-inflammatory TNF-α, IL-6, inducible nitric oxide synthase (iNOS) as well as inflammasome components (139). The oxidation of L-arginine (L-Arg) by iNOS produces neurotoxic NO, which, in turn, inhibits oxidative phosphorylation (OXPHOS), thereby shifting the energy metabolism of the cell towards glycolysis (140). Recent studies demonstrated that ATP-mediated Ca^{2+} influx through the purinoceptor P2X7 is required for sustained reduction of the mitochondrial membrane potential ($\Delta\Psi_m$) and generation of mitochondrial ROS upstream of NLRP3 inflammasome formation (141, 142). The elevation in intracellular Ca^{2+} levels constitutes a central element in microglial activation (143) and emerging evidence suggests LTCCs to be involved in $[Ca^{2+}]_i$ increase after LPS stimulation (144).

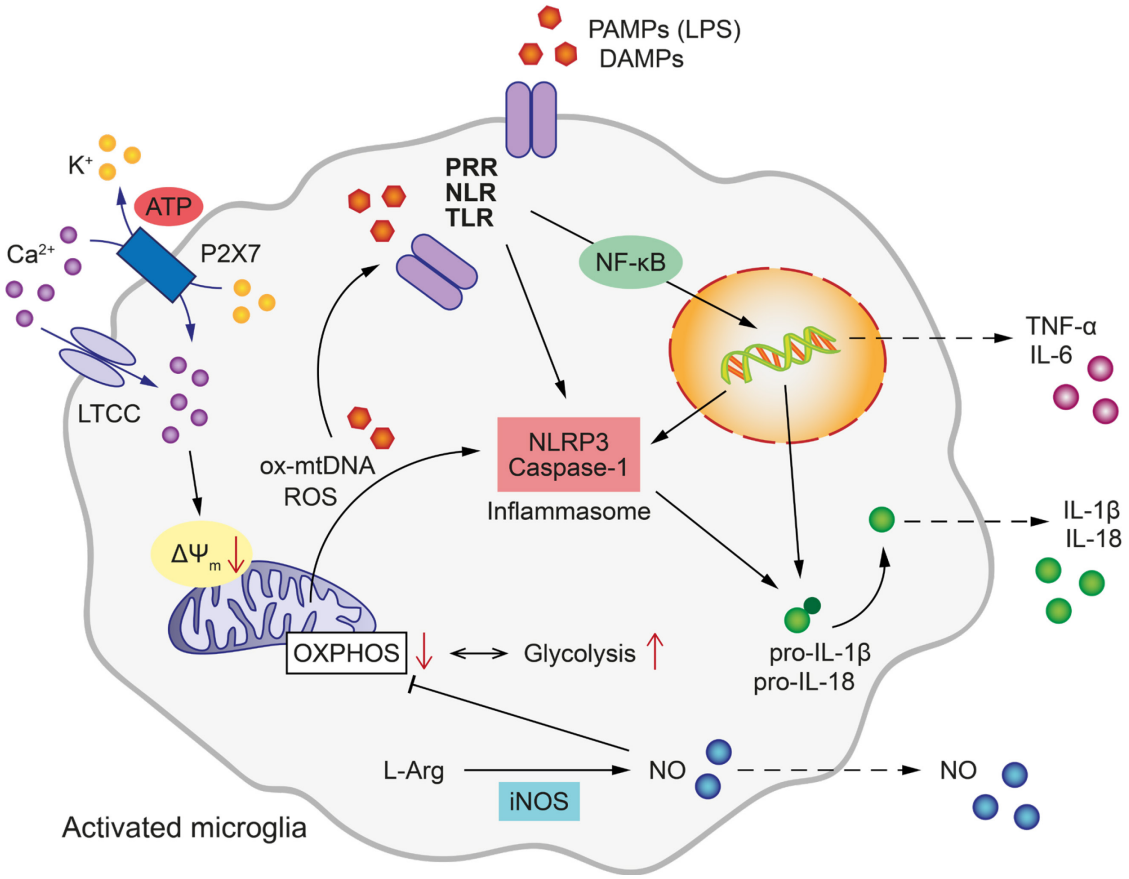

Figure 3. Molecular mechanisms of LPS-induced microglial activation

The scheme provides an overview of the major intracellular mechanisms contributing to the inflammatory activation of microglia. PAMPs, pathogen-associated molecular patterns; LPS, lipopolysaccharide; DAMPs, damage-associated molecular patterns; PRR, pattern recognition receptor; NLR, nucleotide-binding oligomerization domain (NOD)-like receptor; TLR, Toll-like receptor; ox-mtDNA, oxidized mitochondrial DNA; ROS, reactive oxygen species; NLRP3, NOD-, leucine-rich repeat (LRR)- and pyrin domain-containing 3; NF-κB, nuclear factor κB; IL, interleukin; TNF-α, tumor necrosis factor α; $\Delta\Psi_m$, mitochondrial membrane potential; OXPHOS, oxidative phosphorylation; L-Arg, L-arginine; iNOS, inducible nitric oxide synthase; NO, nitric oxide; LTCC, L-type calcium channels; P2X7, ATP-binding purinoceptor; ATP, adenosine triphosphate.

2 Aim and objectives

As part of the DFG Research Group FOR 2107 "Neurobiology of affective disorders: A translational perspective on brain structure and function" (145) this project focused, in a translational setting, on the effects of defined gene-environment interactions on brain mitochondrial integrity and function in order to provide new insights into pathophysiological mechanisms of affective disorders and to identify novel therapeutic targets with potential relevance for future treatment strategies.

The specific research objectives of the present work were as follows:

(1) To study the impact of reduced *Cacna1c* gene expression in combination with glutamate-induced oxidative stress on GSH levels, lipid peroxidation, mitochondrial morphology and function, Ca^{2+} homeostasis, and cell viability in mouse hippocampal HT22 cells.

(2) To evaluate the effect of *Cacna1c* haploinsufficiency on $[Ca^{2+}]_i$, mitochondrial bioenergetics, ATP levels, and cell viability following glutamate-mediated excitotoxicity in primary neuronal cultures of rat cortex.

(3) To examine the impact of *Cacna1c*$^{+/-}$ deficiency and LPS stimulation on cell morphology, metabolism as well as inflammatory cytokine, chemokine, and NO release in primary rat microglial cultures.

(4) To assess the effects of gene-environment interactions on mitochondrial bioenergetics, membrane potential, ROS production, and respiratory chain complex levels in isolated mitochondria from PFC and HC, both representing particularly susceptible brain regions in neuropsychiatric disorders, using a constitutive heterozygous *Cacna1c* rat model in combination with a four-week exposure to either social isolation, standard housing, or social and physical environmental enrichment during the juvenile developmental period.

(5) To investigate the impact of psychiatric disease-relevant genetic and environmental risk factors on mitochondrial function in human PBMCs of healthy subjects by analyzing mitochondrial ROS levels and respiration profiles.

3 Materials and methods

Cell culture sterile plastic ware was obtained from Sarstedt (Nümbrecht, Germany) and Greiner (Frickenhausen, Germany). Unless otherwise stated, all reagents were purchased from Sigma-Aldrich (Munich, Germany). All buffers and solutions were prepared with demineralized, ultrapure water using SG Ultra Clear UV Plus Pure Water System (VWR, Darmstadt, Germany). Demineralized water for aseptic preparations was sterilized by a steam autoclave (Systec V-40; Systec GmbH, Wettenberg, Germany) or sterile filtration (0.22 μm pore size; Sarstedt, Nümbrecht, Germany). DNA/RNA oligonucleotide synthesis and DNA sequencing were performed by Eurofins (Hamburg, Germany).

3.1 HT22 cells

HT22 cells were generated by Prof. David Schubert (Salk Institute, San Diego, CA, USA) and obtained from Prof. Gerald Thiel (University of Saarland, Homburg, Germany). HT22 cells were originally immortalized from primary hippocampal neurons using a temperature-sensitive SV-40 T antigen and selected from HT4 cells based on sensitivity to glutamate (146, 147). HT22 cells were cultured at 37°C and 5% CO_2 in Dulbecco's Modified Eagle's Medium (DMEM High Glucose; Sigma-Aldrich, Munich, Germany) supplemented with 10% fetal bovine serum (FBS; Biochrom, Berlin, Germany), 20 mM HEPES, 100 units/ml penicillin, 100 μg/ml streptomycin, and 2 mM glutamine. HT22 cell cultures were split twice a week at a ratio of 1:10-1:20. For cell detachment 0.05% trypsin/0.02% EDTA in isotonic phosphate buffered saline (PBS) was used.

The cells were transfected with an optimized concentration of 40 nM siRNA using Lipofectamine RNAiMAX (Thermo Fisher Scientific, Darmstadt, Germany) in antibiotic-free growth medium. The siRNA sequences were as follows: scrambled *Cacna1c* siRNA (siScr, 5'-AUU GGC GCA CUA UUA GAC U-3'), *Cacna1c* siRNAs (siCacna1c 1, 5'-GGA AAG CUC UAU ACC UGU U-3'; siCacna1c 2, 5'-CUA GUA UCU UUA CAU UAG A-3'; siCacna1c 3, 5'-GUG CCA CCG UAU UGU CAA U-3'). The plated cells were treated with millimolar concentrations of glutamate for 15 to 18 hours unless otherwise stated and assayed 30 to 48 hours after transfection. The LTCC blocker nimodipine (100 mM stock solution in DMSO; Cayman Chemical, Ann Arbor, MI, USA) was used in a final concentration of 100 μM and applied together with 6 to 8 mM glutamate for 16 hours (see Figure 8 for chemical structure).

3.1.1 Reverse transcription PCR

HT22 cells were seeded at a density of 180,000 cells/well in 6-well plates. Total RNA was isolated with the InviTrap Spin Universal RNA Mini Kit (Stratec Biomedical, Birkenfeld,

Germany) 24 h after siRNA transfection. Reverse transcription polymerase chain reaction (RT-PCR) was performed using SuperScript III One-Step RT-PCR system with platinum Taq DNA polymerase (Thermo Fisher Scientific, Darmstadt, Germany) and the following primers: *Cacna1c* (502 bp) forward 5'-CAA CGC AAC CAT CTC TAC CG-3' and reverse 5'-CAG TGC CTT CAC GTC GAA TC-3'; *Gapdh* (399 bp) forward 5'-CGT CTT CAC CAC CAT GGA GAA GGC-3' and reverse 5'-AAG GCC ATG CCA GTG AGC TTC CC-3'. The PCR protocol included: *Cacna1c* 30 min 45°C cDNA synthesis, 2 min 94°C denaturation, 29x [15 sec 94°C denaturation, 45 sec 55°C annealing, 45 sec 68°C extension], 5 min 68°C final extension; *Gapdh* 30 min 60°C, 2 min 95°C, 26x [30 sec 95°C, 1 min 57°C, 2 min 70°C], 10 min 70°C (T-personal thermocycler; Biometra GmbH, Göttingen, Germany). The amplified products were loaded on a 1.5% agarose gel (Biozym Scientific GmbH, Hessisch Oldendorf, Germany) stained with ethidium bromide. Electrophoresis was performed at 70 V for ~30 min in 40 mM Tris-acetate/0.1 mM EDTA buffer. GeneRuler 100 bp Plus DNA Ladder (Thermo Fisher Scientific, Darmstadt, Germany) served as size standard. The resulting DNA bands were visualized under UV light using a ChemiDoc XRS system (Bio-Rad Laboratories, Hercules, CA, USA).

3.1.2 Protein analysis

Protein extraction and Western blot were performed according to established protocols (119). Briefly, cells were seeded at a density of 180,000 cells/well in 6-well plates and lysed 48 h after siRNA transfection in 0.25 M D-mannitol, 0.05 M Tris base, 1 mM EDTA, 1 mM EGTA, 1 mM DTT, and 1% Triton X-100 supplemented with protease and phosphatase inhibitor cocktail tablets (Roche Diagnostics, Mannheim, Germany). Total protein amounts were determined using the Pierce bicinchoninic acid (BCA) Protein Assay Kit (Thermo Fisher Scientific, Darmstadt, Germany). Under alkaline conditions, the containing Cu^{2+} is concentration-dependently reduced by protein to Cu^{+}, which forms a water-soluble, purple-colored complex with BCA. The resulting absorbance was detected at 595 nm with a FLUOstar OPTIMA reader (BMG Labtech, Ortenberg, Germany). Protein concentrations were calculated with reference to a standard curve of 0-2 µg/µl bovine serum albumin (BSA).

Subsequently, proteins contained were separated by size using sodium dodecyl sulfate polyacrylamide gel electrophoresis (SDS-PAGE). Therefore, 50 to 60 µg protein in sample buffer (60 mM Tris HCl, 2% SDS, 10% glycerol, 5% β-mercaptoethanol, and 0.01% bromophenol blue) were loaded on 7.5% and 12.5% SDS-polyacrylamide gels respectively. Spectra Multicolor High Range Protein Ladder (Thermo Fisher Scientific, Darmstadt, Germany) was used as molecular weight (MW) marker. Gel electrophoresis was performed at 60 V for ~30 min followed by further separation at 120 V for ~1.5 h in running buffer (0.2 M glycine, 24.8 mM Tris base, 3.5 mM SDS). After electrophoresis, the proteins were transferred from the gel onto a polyvinylidene difluoride (PVDF) membrane (Roche Diagnostics,

Mannheim, Germany) by wet blot at 65 V for ~3.5 h in transfer buffer containing 0.2 M glycine, 24.8 mM Tris base, and 20% (v/v) methanol. Next, the membranes were blocked in blocking buffer (5% (w/v) skim milk powder, 0.5 M NaCl, 12 mM Tris base, 0.05% (v/v) Tween 20) and incubated with the respective antibodies overnight at 4°C (Table 1). Protein detection was realized using peroxidase labeled secondary antibodies (Vector Laboratories, Burlingame, CA, USA) and luminol based HRP-Juice Plus (PJK GmbH, Kleinblittersdorf, Germany). The resulting chemiluminescence was imaged with a ChemiDoc XRS system (Bio-Rad Laboratories, Hercules, California, USA). Densitometric protein quantification was performed using the Bio-Rad Image Lab Software.

Table 1. Antibody specifications

Antibody	Dilution	MW (kDa)	Host	Company
$Ca_V1.2$	1:200	240	Rabbit	Alomone Labs
Vinculin	1:20,000	116	Mouse	Sigma-Aldrich
PGC1α	1:1,000	91	Rabbit	Rockland
Drp1	1:500	80	Mouse	BD Bioscience
Mfn2	1:1,000	80	Rabbit	Cell Signaling
p62	1:1,000	62	Rabbit	Cell Signaling
α-Tubulin	1:10,000	55	Mouse	Sigma-Aldrich
MCU	1:1,000	30	Rabbit	Cell Signaling
Fis1	1:500	17	Rabbit	Enzo Life Science
LC3B	1:500	14-16	Rabbit	Cell Signaling

3.1.3 Mitochondrial isolation

Mitochondria were isolated using a pump-controlled cell homogenizer (Isobiotec, Heidelberg, Germany) with a clearance of 10 µm and a constant pump flow rate of 700 µl/min according to existing protocols (148). In brief, the trypsinized HT22 cell suspension was filled in a 1 ml gas tight glass syringe (Supelco, Munich, Germany) and homogenized with three strokes through the cell homogenizer. Subsequently, the homogenate was centrifuged at 800 xg for 10 min at 4°C. The supernatant, referred to as total lysate, was transferred to a new tube and centrifuged at 9,000 xg, again for 10 min at 4°C (Heraeus fresco 17; Thermo Fisher Scientific, Darmstadt, Germany). The resulting supernatant contains the cytosolic fraction and the emerging pellet represents the crude mitochondrial fraction, which was slowly resuspended in 150 µl mitochondrial isolation buffer (70 mM sucrose, 210 mM mannitol, 5 mM HEPES, 1 mM EGTA, 0.5% (w/v) BSA; pH 7.2). All steps were performed on ice. The total protein concentration was determined using the Pierce BCA Protein Assay Kit (Thermo Scientific, Darmstadt, Germany) with BSA standards based on mitochondrial isolation buffer. Sixty

microgram protein per fraction were separated on a two-phase SDS-polyacrylamide gel (7.5/15%). The following antibodies were used: $Ca_V1.2$ (1:200; Alomone Labs, Jerusalem, Israel), α-tubulin (1:10,000), and Tim23 (1:2,000; BD Biosciences, Franklin Lakes, NJ, USA).

3.1.4 Determination of total glutathione

The amount of total glutathione in HT22 cells was quantified using the luminescence-based GSH/GSSG-Glo Assay (Promega, Mannheim, Germany) in accordance with the manufacturer's instructions. The assay is based on the GSH-dependent conversion of luciferin-NT to luciferin by glutathione S-transferase coupled to a firefly luciferase reaction. The produced light depends on the amount of luciferin formed, which, in turn, is depending on the amount of GSH present. HT22 cells were plated at a density of 6,000 cells/well in white-with-clear-bottom 96-well plates. Twenty-four hours after seeding, the cells were incubated for 2, 4, and 6 hours with 10 mM glutamate. The resulting luminescence, which is proportional to the amount of GSH, was detected with a FLUOstar OPTIMA reader (BMG Labtech, Ortenberg, Germany). Absolute glutathione concentrations were calculated from a GSH standard curve.

3.1.5 Mitochondrial morphology

The evaluation of mitochondrial morphology was carried out as reported and validated previously with minor modifications (111). In brief, 14,000 cells/well were seeded in 8-well ibiTreat plates (Ibidi, Martinsried, Germany). To visualize mitochondria, cells were incubated with 0.2 µM MitoTracker Deep Red (Thermo Fisher Scientific, Darmstadt, Germany) for 30 min before adding glutamate. After the fixation with 4% paraformaldehyde (PFA), images were acquired using a fluorescence microscope (DMI6000 B; Leica Microsystems, Wetzlar, Germany) at 63x magnification. To generate reliable results according to previous validation, 500 cells per condition were counted and classified by their mitochondrial morphology into three different categories. Category 1 is defined by elongated and equally distributed mitochondria. Category 2 is characterized by partially fragmented mitochondria that are still distributed throughout the cytosol. Finally, Category 3 is represented by strongly fragmented mitochondria that are located around the nucleus. Three independent experiments were performed and the investigator was always blinded to the treatment history.

3.1.6 ATP measurement

The determination of ATP levels was performed using the ViaLight Plus Kit (Lonza, Verviers, Belgium) according to the manufacturer's protocol. Briefly, cells were lysed, transferred to a white-walled 96-well plate and the luciferase-containing ATP monitoring reagent was added. Luciferase catalyzes the formation of light from ATP and the substrate luciferin. The emitted luminescence intensity is linearly related to the cellular ATP concentration and was measured using a FLUOstar OPTIMA reader (BMG Labtech, Ortenberg, Germany).

3.1.7 Measurement of the oxygen consumption rate

The oxygen consumption rate (OCR) as an indicator of mitochondrial respiration was identified with a Seahorse XF^{e}96 Analyzer (Agilent Technologies, Waldbronn, Germany).

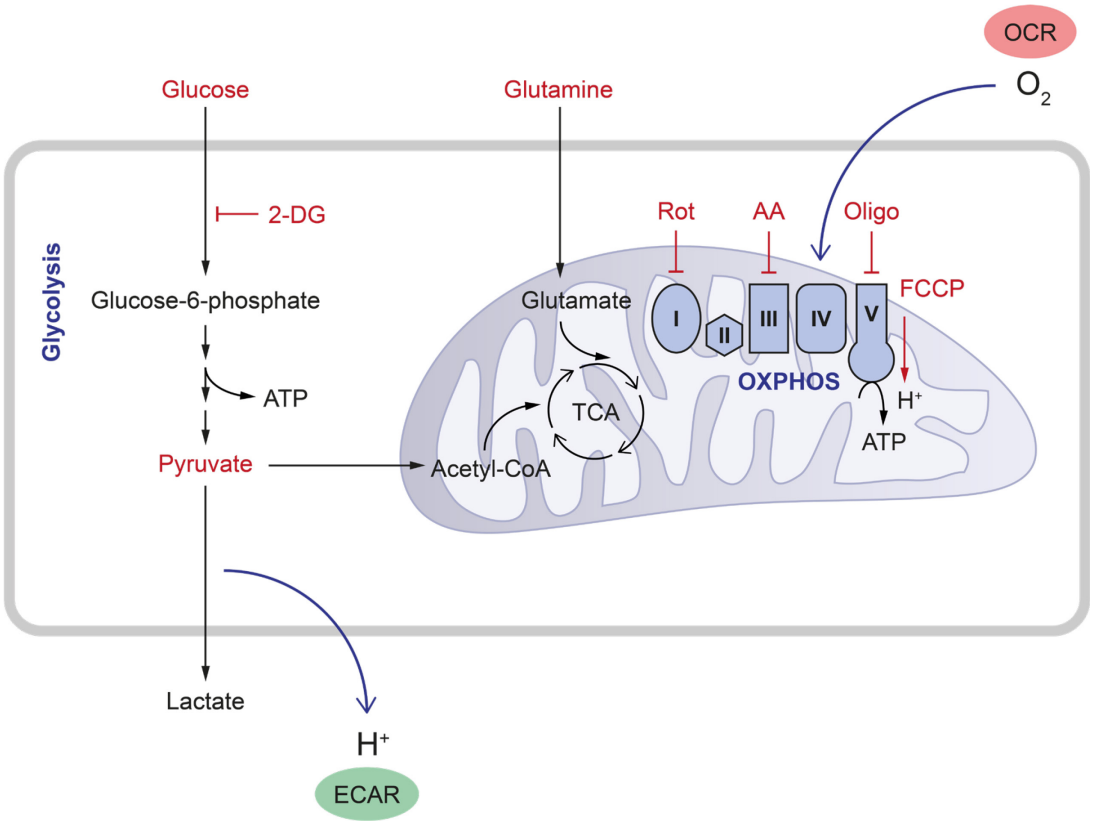

Figure 4. Seahorse assay principle

The scheme illustrates the substrates (media supplements) and compounds used in the Seahorse assays (highlighted in red) and their respective function/effect on cell metabolism. OCR, oxygen consumption rate; ECAR, extracellular acidification rate; 2-DG, 2-deoxy-D-glucose (hexokinase inhibitor); OXPHOS, oxidative phosphorylation; TCA, tricarboxylic acid cycle; Rot, rotenone (complex I inhibitor); AA, antimycin A (complex III inhibitor); Oligo, oligomycin (ATP synthase inhibitor); FCCP, carbonyl cyanide-4-(trifluoromethoxy)phenylhydrazone (protonophore).

The extracellular flux analyzer simultaneously measures the two major energy pathways of the cell, mitochondrial respiration and glycolysis, in real time as oxygen consumption rate (OCR) and extracellular acidification rate (ECAR) respectively (Figure 4). Changes to the concentrations of dissolved oxygen and free protons are assessed in a transient microchamber using inert optical micro sensors. The system allows for the consecutive injection of different modulators of the ETC. The compounds and final concentrations used are as follows: oligomycin 3 μM, FCCP 0.5 μM, rotenone 0.1 μM, and antimycin A 1 μM. Three basal and three measurements after each injection were recorded. HT22 cells were assayed in DMEM containing 143 mM NaCl, 25 mM D-glucose, 2 mM glutamine, and 1 mM sodium pyruvate with an adjusted pH of 7.35.

3.1.8 Flow cytometry

Several parameters associated with glutamate-induced oxidative stress, such as lipid peroxidation, mitochondrial ROS formation, mitochondrial membrane potential, mitochondrial Ca^{2+} levels, and cell death, were analyzed with a Guava easyCyte 6-2L flow cytometer (Merck Millipore, Darmstadt, Germany) using different fluorescent dyes. HT22 cells were plated at 30,000-55,000 cells/well in a 24-well format. Measurements were performed in triplicates, each with a total count of 10,000 cells, and are representative of a least three independent experiments.

Lipid peroxidation

BODIPY 581/591 C11 (4,4-difluoro-5-(4-phenyl-1,3-butadienyl)-4-bora-3a,4a-diaza-s-indacene-3-undecanoic acid; Thermo Fisher Scientific, Darmstadt, Germany) was utilized as a sensor for the oxidation of lipids and membranes. Oxidation of the polyunsaturated butadienyl portion of the dye results in a shift of the fluorescence emission peak from red (690/50 nm) to green (525/30 nm). Here, HT22 cells were treated with 9 mM glutamate 24 h after siRNA transfection. Following 8 h of glutamate treatment, the cells were stained with 2 μM BODIPY dye for 1 h at 37°C.

Mitochondrial superoxide formation

Superoxides are the predominant reactive oxygen species in mitochondria and were detected by incubation of the cells with 1.25 μM MitoSOX Red indicator (Thermo Fisher Scientific, Darmstadt, Germany) for 30 min at 37°C (117). MitoSOX is selectively hydroxylated by superoxides leading to an increase in red fluorescence. Fluorescence signals were excited at 488 nm with emission detection at 690/50 nm.

Mitochondrial membrane potential

Mitochondrial membrane depolarization was determined using the MitoPT TMRE Kit (ImmunoChemistry Technologies, Hamburg, Germany) following the recommendations of

the manufacturer. Tetramethylrhodamine ethyl ester (TMRE) is a cationic, potential-sensitive fluorescent dye and accumulates, under physiological conditions, in negatively charged mitochondria resulting in the emission of red fluorescence. If the mitochondrial membrane potential collapses, e.g. in apoptotic or metabolically stressed cells, TMRE is dispersed throughout the cell cytosol indicated by a loss in 690/50 nm fluorescence. HT22 cells were collected and stained with 0.2 µM TMRE for 30 min at 37°C. The depolarizing reagent CCCP (carbonyl cyanide 3-chlorophenylhydrazone) was used in a final concentration of 50 µM and served as additional positive control.

Mitochondrial calcium concentration

To selectively study mitochondrial calcium levels, the cell-permeant Rhod-2 AM (rhodamine-2 acetoxymethyl ester; Thermo Fisher Scientific, Darmstadt, Germany) was reduced to the colorless, non-fluorescent Dihydrorhod-2 AM with sodium borohydride ($NaBH_4$). Dihydrorhod-2 AM exhibits Ca^{2+}-dependent increase in red fluorescence after re-oxidation and cleavage of the acetoxymethyl ester, processes that occur rapidly in the mitochondrial environment. HT22 cells were harvested and incubated with 2 µM of the reduced dye in DMEM without serum for 30 min.

Cell death

Cell death was evaluated using the Annexin V-FITC Detection Kit (Promokine, Heidelberg, Germany) in accordance with the manufacturer's instructions. The two containing dyes Annexin V and propidium iodide (PI) stain early apoptotic and dead cells respectively. In early apoptotic cells phosphatidyl serine is translocated from the inner to the outer site of the plasma membrane. Once on the cell surface, phosphatidyl serine is detected by the FITC-labeled phospholipid-binding protein Annexin V (green, 525/30 nm). Late apoptotic and necrotic cells are characterized by a loss of membrane integrity and are, thus, permeable to propidium iodide, which intercalates into DNA showing red staining (690/50 nm). Shortly, HT22 cells were trypsinized and the cell suspensions incubated with 5 µl/ml of each dye for 5 min at room temperature.

3.1.9 Cell viability

Metabolic activity as correlate for cell viability was assessed by a colorimetric assay where yellow MTT (3-(4,5-dimethyl-2-thiazolyl)-2,5-diphenyl-2H-tetrazolium bromide) is NADH-dependently reduced to a water-insoluble, purple-colored formazan product. After incubation with 0.5 mg/ml MTT for 1 h at 37°C, the medium was removed and the plates were frozen at -80°C for at least 1 h. The formazan crystals were solved in DMSO and incubated at 37°C for 30 min, followed by quantitative absorbance measurement at 570 nm with a reference filter at 630 nm (FLUOstar OPTIMA reader; BMG Labtech, Ortenberg, Germany).

As described previously, the xCELLigence Real-Time Cell Analysis (RTCA; Roche Diagnostics, Mannheim, Germany) system allows cell viability to be measured continuously in real time via electrical impedance readout (149). Briefly, attached and proliferating cells cause a high and further increasing impedance signal, whereas the detachment of dying cells leads to a decrease in electrical impedance. Changes in the impedance are depicted as normalized cell index. For both assays HT22 cells were seeded in 96-well plates at 6,000-8,000 cells per well.

3.1.10 Statistical analysis

All data are presented as mean values with standard deviation (SD). Multiple comparisons were performed by one-way analysis of variance (one-way ANOVA) followed by Scheffé's post-hoc test. All experiments were performed in 3 to 8 replicates per treatment condition, as indicated, and were independently repeated at least twice for confirmation of the results. The parameters presented were calculated using the WinSTAT statistics Add-In for Microsoft Excel (R. Fitch Software, Bad Krozingen, Germany). A statistical significant difference was assumed at $p < 0.05$ (*), $p < 0.01$ (**), and $p < 0.001$ (***).

3.2 *Cacna1c* rat knockout model

Constitutive heterozygous *Cacna1c*$^{+/-}$ rats were generated by SAGE Labs (now Horizon Discovery Ltd., Cambridge, UK) on a Sprague-Dawley background via zinc-finger nucleases following a previously established protocol (150). *Cacna1c*$^{+/-}$ rats carry a 4 base pair (bp) deletion at 460649-460652 bp in the genomic sequence resulting in an early stop codon in exon 6. Since a homozygous knockout is embryonically lethal (151), wildtype females (Charles River, Sulzfeld, Germany) and heterozygous *Cacna1c*$^{+/-}$ males were paired for breeding to obtain offspring from both genotypes. Breeding was performed by Theresa Kisko and Moria Braun (research group of Prof. Rainer Schwarting, Markus Wöhr) at the Faculty of Psychology, University of Marburg, Germany. All animal procedures were conducted in strict accordance with the National Institutes of Health Guidelines for the Care and Use of Laboratory Animals and the relevant local or national rules and regulations of Germany and were subject to prior authorization by the local government (MR 20/35 Nr. 19/2014; Tierschutzbehörde, Regierungspräsdium Gießen, Germany).

3.3 Primary rat neurons

One or two days prior to dissection, the respective cell culture plates were coated with polyethyleneimine solution (0.005% (w/v) PEI, 50 mM boric acid, 24 mM sodiumtetraborate decahydrate; pH 8.4) for 3 h at 37°C. After 3x washing with aqua bidest and 30 min UV treatment, the plates were filled with Minimum Essential Medium (MEM; Thermo Fisher Scientific, Darmstadt, Germany) supplemented with 0.9 mM HEPES sodium salt, 56 mM glucose, 26 mM sodium bicarbonate, 16 mM potassium chloride, 1 mM sodium pyruvate, 2 mM glutamine, 10 U/ml penicillin, 10 µg/ml streptomycin, and 10% (v/v) FBS (Biochrom, Berlin, Germany), adjusted to pH 7.2 and stored at 37°C, 5% CO_2.

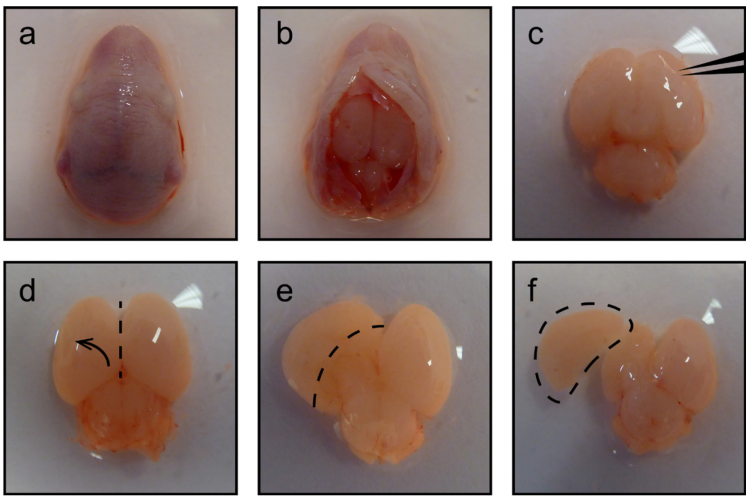

Figure 5. Preparation of cortical tissue from E18 rat embryos
a First, the embryo's head was cut off using scissors. **b** Then, the brain was carefully dissected out of the skull. **c** Subsequently, the isolated brain was placed ventral side up and the meningeal tissue was completely removed from the fore- and midbrain region using forceps. **d** The brain was then turned on its dorsal side to make a sagittal incision (dashed line) between the two hemispheres. Finally, this cut allowed to unfold (arrow) and separate (**e**, dashed line) the cortical tissue (**f**, dashed mark) from the hippocampus, thalamus, and hypothalamus.

Primary cultures of cortical neurons were prepared from embryonic day 18 (E18) Sprague-Dawley rats. To this end, pregnant rats were deeply anesthetized with isoflurane (Baxter, Unterschleißheim, Germany), then decapitated, and the embryos quickly removed. Cortices of both brain hemispheres were dissected as detailed in Figure 5 and transferred to separate tubes for each embryo filled with 1 ml ice-cold Hank's Balanced Salt Solution (HBSS; Thermo Fisher Scientific, Darmstadt, Germany; supplemented with 9 mM HEPES sodium salt, 100 U/ml penicillin, and 100 µg/ml streptomycin; pH 7.2). Additionally, the remaining brain tissue of each embryo was collected for genotyping. After washing once with HBSS, the cortices were incubated with pre-warmed trypsin solution (1 mg/ml in HBSS) for 15 min in the

water bath. Next, deoxyribonuclease I (100 µg/ml) was added for 30 sec, followed by two washing steps with HBSS and a 2 min-incubation with pre-warmed trypsin inhibitor (1 mg/ml in HBSS) at room temperature. After washing twice with HBSS, the cortical cells were mechanically dissociated by slow trituration (15-20x) with a P1000 pipette before adding 1 ml NB^+ (Neurobasal medium plus B-27 Supplement; Thermo Fisher Scientific, Darmstadt, Germany; complemented by 2 mM glutamine, 100 U/ml penicillin, and 100 µg/ml streptomycin). Subsequently, each cell suspension was centrifuged at 1000 rpm for 5 min (Heraeus fresco 17; Thermo Fisher Scientific, Darmstadt, Germany) and the emerging pellet was resuspended in 8 ml NB^+. Cell numbers were determined using a counting chamber (Neubauer Zählkammer; Brand, Wertheim, Germany). Primary cells were seeded on PEI-coated plates at a density of 80-140 $\times 10^3$ cells/cm^2 and cultured in a humidified incubator at 37°C, 5% CO_2. Final volumes per well were as follows: 100 µl for 96-well, 500 µl for 24-well, and 2 ml for 6-well plates. After 3 days in vitro (DIV) one-tenth fresh, warm NB^+ was added to each well. Then, a half media change was performed every three days. As shown by immunostaining, 90-95% of the cells were neurons under these culture conditions (Figure 6).

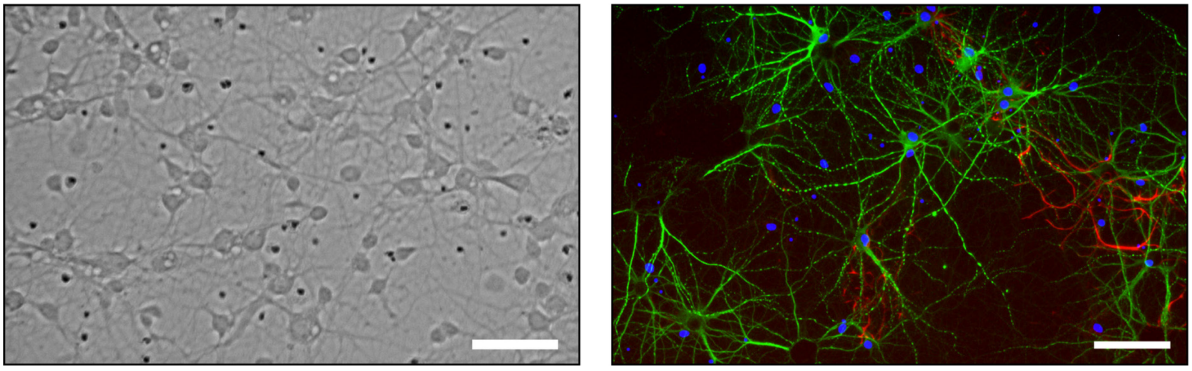

Figure 6. Primary dissociated neuronal cultures from cortex of E18 rat embryos

An exemplary brightfield image (20x; left picture) of a 10-day-old primary culture is shown. Scale bar, 50 µm. Further, PFA-fixated cultures were immunostained for the neuronal marker microtubule-associated protein 2 (MAP2, green, A488), the astrocyte marker glial fibrillary acidic protein (GFAP, red, A650), and the nucleus (DAPI, blue). The composite image section (10x, right picture) was captured at a Leica DMI6000 B microscope. Scale bar, 100 µm.

3.3.1 Genotyping

In order to identify the genotypes of the individual neuronal cultures, DNA was isolated from the remaining embryonal brain tissue and PCR of the deletion site was performed using RED Extract-N-Amp Tissue PCR Kit according to the manufacturer's instructions and the following primers: forward 5'-GCT GCT GAG CCT TTT ATT GG-3', reverse 5'-CCT CCT GGA TAG CTG CTG AC-3'. The PCR protocol included 5 min 95°C, 35x [30 sec 95°C, 30 sec 60°C, 40 sec 68°C], 5 min 68°C (T-personal thermocycler; Biometra GmbH, Göttingen, Germany) resulting

in an expected wildtype product of 369 bp as confirmed by 1.5% agarose gel electrophoresis (Figure 7a). PCR products were treated with ExoSAP-IT (Thermo Fisher Scientific, Darmstadt, Germany) and sent directly to sequencing (Eurofins Genomics, Ebersberg, Germany) for mutation analysis. Exemplary results for wildtype and heterozygous *Cacna1c* rats are illustrated in Figure 7. Genotyping was mainly performed with the help of Katharina Elsässer.

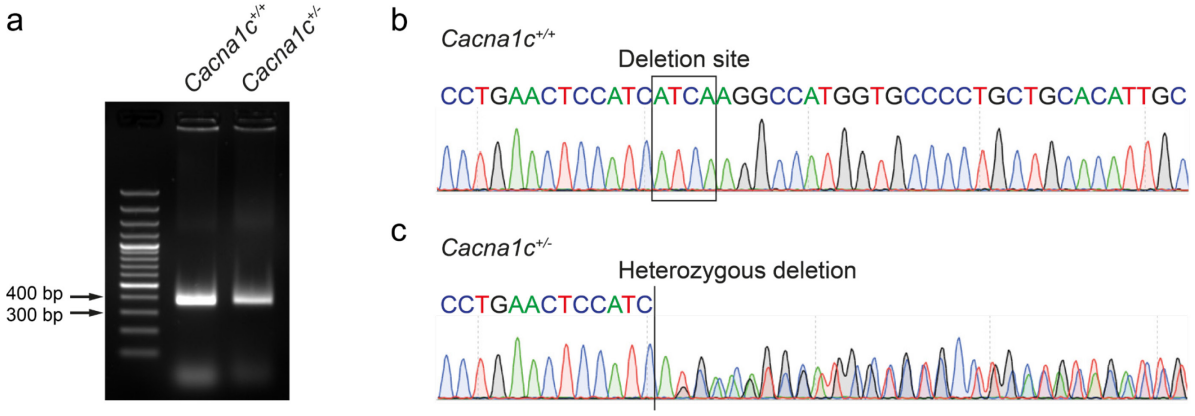

Figure 7. Genotyping to identify wildtype and heterozygous *Cacna1c* animals

a As expected, PCR of both, wildtype and heterozygous *Cacna1c* brain DNA resulted in defined PCR products, which were each visualized as a single band between 300 and 400 base pairs (bp). GeneRuler 100 bp Plus DNA Ladder (Thermo Fisher Scientific, Darmstadt, Germany) was used as marker on a 1.5% agarose gel. Exemplary sequencing results of the amplified PCR products comprising the deletion site: **b** wildtype *Cacna1c*$^{+/+}$ sequence and **c** overlapping pattern of the nucleotide sequence after the deletion site illustrating the presence of two PCR amplification products characteristic for the heterozygous *Cacna1c*$^{+/-}$ genotype.

3.3.2 Treatment with glutamate and different LTCC modulators

Since primary neurons develop functional NMDA receptors after 7 DIV (152), experiments were performed with 10-day-old cultures following a 24 h-treatment with 25 µM glutamate in Earle's Balanced Salt Solution (EBSS). The L-type calcium channel activator (±)-Bay K8644 (10 µM; Biomol, Hamburg, Germany), the dihydropyridine LTCC blockers isradipine (10, 20 µM; Biozol, Eching, Germany) and nimodipine (12.5, 25 µM; Cayman Chemical, Ann Arbor, MI, USA), and the NMDA receptor antagonist MK-801 (10 µM) were all dissolved in dimethyl sulfoxide (DMSO) and applied as co-treatment together with glutamate (for chemical structures see Figure 8).

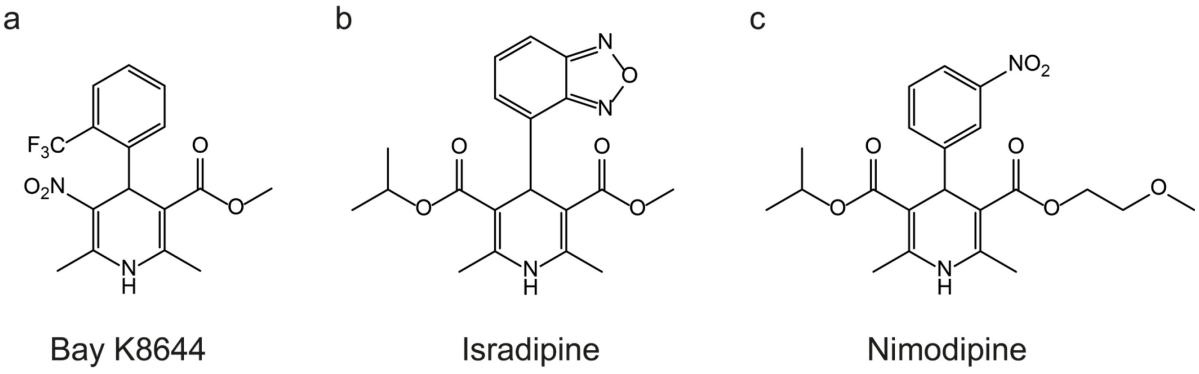

Figure 8. Chemical structures of the L-type calcium channel modulators used
a Bay K8644, **b** isradipine, **c** nimodipine.

3.3.3 Quantitative PCR

Two-step reverse transcription quantitative PCR (qPCR) experiments were conducted with the help of Helena Martins in the lab of Prof. Gerhard Schratt (Institute of Physiological Chemistry, University of Marburg, Germany). In brief, 900,000 cells/well were seeded in 6-well plates. RNA was isolated from 10 DIV neuronal cultures using the InviTrap Spin Universal RNA Mini Kit (Stratec Biomedical, Birkenfeld, Germany) according to the manufacturer's protocol. To remove contaminating genomic DNA from the preparation, 500 ng-1 µg RNA per sample were treated with the DNase containing Turbo DNA-free Kit (Thermo Fisher Scientific, Darmstadt, Germany). After determining the RNA concentration with a NanoPhotometer (Implen, Munich, Germany), reverse transcription of 200 ng DNase-treated RNA was achieved utilizing the iScript cDNA Synthesis Kit (Bio-Rad Laboratories, Hercules, CA, USA) and the following thermocycler program: 5 min 25°C, 30 min 42°C, and 5 min 85°C. The resulting cDNA was diluted 1:5 with aqua bidest before 4 µl were carefully transferred to each appropriate well of a MicroAmp Fast Optical 96-well Reaction Plate (Thermo Fisher Scientific, Darmstadt, Germany). Then, iTaq Universal SYBR Green Supermix (Bio-Rad Laboratories, Hercules, CA, USA) and one of the below-mentioned primer pairs were added: *Cacna1c* forward 5'-AGG CTG AGC GAA GAA GTT GA-3' and reverse 5'-AGA CAG GTC AGT TGT CGG TTT-3'; *Cacna1d* forward 5'-GGG GGA ATC ACC GAA ACC AT-3' and reverse 5'-CGT ACA CAC CGG AAC ACA GA-3'; *U6* forward 5'-CTC GCT TCG GCA GCA CA-3' and reverse 5'-AAC GCT TCA CGA ATT TGC GT-3'. Subsequently, the plate was tightly sealed with MicroAmp Optical Adhesive Film (Thermo Fisher Scientific, Darmstadt, Germany) to reduce sample contamination and evaporation during the qPCR performed with a StepOnePlus Real-Time PCR System (Fisher Scientific GmbH, Schwerte, Germany). The following program was used: 10 min 95°C, 40-50x [15 sec 95°C, 1 min 60°C], 15 sec 95°C, 1 min 60°C, 15 sec 95°C. Data were assessed in triplicates and analysis was realized using the StepOnePlus Software v2.3. For comparative quantitation, ΔC_T values were calculated by

subtracting the C_T values of the gene of interest from the respective C_T of the reference gene U6. Relative mRNA expression levels were presented as 2^ (- average ΔC_T).

3.3.4 Protein analysis

Protein isolation and Western blot were performed in accordance with the standard procedures described in Chapter 3.1.2. To analyze changes in protein expression, 60 µg protein per sample were loaded on 7.5% SDS-polyacrylamide gels. After transfer onto PVDF membranes, these were incubated with anti-Ca_V1.2 (1:1,000; Alomone Labs, Jerusalem, Israel) and anti-Vinculin (1:20,000) antibodies.

3.3.5 MTT and ATP assays

Primary cortical neurons were seeded with a density of 25,000-40,000 cells per well in PEI-coated 96-well plates. Both assays were conducted as described previously (Chapter 3.1.6 and 3.1.9).

3.3.6 Mitochondrial stress test assay

OCR and ECAR of primary cortical neurons were assayed in DMEM supplemented with 143 mM sodium chloride, 15 mM glucose, 10 mM sodium pyruvate, 2 mM glutamine, 0.04% (w/v) BSA and an adjusted pH of 7.35 using a Seahorse XF^e96 Analyzer (Agilent Technologies, Waldbronn, Germany). The following 4 injections were applied: 2 µM oligomycin, 2 µM FCCP, 1 µM rotenone together with 1 µM antimycin A, and 150 mM 2-DG (Figure 4). Three basal and 3 measurements after each injection were recorded and the data was subsequently normalized to total protein amount per well. Thus, after the measurement, the cells were carefully washed once with PBS before adding 50 µl lysis buffer (10 mM Tris base, 0.1% (v/v) Triton X-100) per well and freezing the plate at -80°C. Relative protein absorbance levels were determined using the Pierce BCA Protein Assay Kit (Thermo Fisher Scientific, Darmstadt, Germany) and a FLUOstar OPTIMA reader (Abs 595 nm; BMG Labtech, Ortenberg, Germany).

3.3.7 Calcium imaging

Changes in intracellular free Ca^{2+} concentration in neuronal cell soma were evaluated with the membrane-permeable, high-affinity, dual-excitation ratiometric calcium indicator Fura 2-AM. The peak excitation wavelength for the Ca^{2+}-free form of Fura 2 is 380 nm, whereas the Ca^{2+}-bound Fura 2 has one of 340 nm. By using the ratio of fluorescence intensities produced by

excitation at the two wavelengths 340 and 380 nm, factors such as uneven dye distribution, leakage of dye and photobleaching are minimized allowing accurate measurements of intracellular Ca^{2+} levels (153). Primary cortical neurons were incubated with 3 µM Fura 2-AM for 30 min at 37°C in HEPES-Ringer buffer (136.4 mM NaCl, 5.6 mM KCl, 1 mM $MgCl_2$, 2.2 mM $CaCl_2$, 10 mM HEPES, 5 mM glucose, and 0.1% (w/v) freshly added BSA; pH 7.4) followed by a further 30-min incubation with buffer only to enable complete de-esterification of the intracellular AM esters. Glutamate (25 µM) and potassium chloride (KCl; 50 mM) were diluted in HEPES-Ringer buffer and applied as bolus injection. Images were acquired every 500 ms with a CCD Imaging SensiCam and an Olympus UplanApo 20x/0.80 oil objective at a Ix70 fluorescence microscope (Olympus, Hamburg, Germany) and 37°C. Regions of interest (ROI) selection and data collection were performed using Till Visions 4.50 software (Till Photonics, Martinsried, Germany) and the open-source software application ImageJ (National Institutes of Health, Bethesda, MD, USA). Data are presented as Fura 2 ratio (340/380 nm).

3.3.8 Immunocytochemistry

In 24-well plates, 100,000 cells per well were seeded on glass coverslips (Ø 12 mm). After 10 DIV, the cells were fixed with 4% PFA for 30 min and permeabilized with 0.4% Triton X-100 in PBS for 5 min, blocked with 3% goat serum in PBS for 30 min, and labeled with the respective primary antibodies over night at 4°C. The following antibodies were used: anti-MAP2 (1:200; Cell Signaling Technology, Frankfurt, Germany), anti-GFAP (1:200; Cell Signaling Technology, Frankfurt, Germany). Next, the cells were incubated with secondary antibodies, DyLight 488 and 650 conjugates (1:200; Thermo Fisher Scientific, Darmstadt, Germany) for 2 h in blocking solution, before counterstaining the nucleus with 4',6-diamidino-2-phenylindol (DAPI; 1:1000 in PBS) for 5 min and mounting the coverslips on object slides (Aqua-Poly/Mount; Polysciences Inc., Warrington, PA, USA). Images were acquired using a Leica DMI6000 B microscope at 10x magnification and LAS X software (Leica, Wetzlar, Germany).

3.3.9 Statistical analysis

Pooled data from independent experiments are presented as single values with mean ± SD. For the comparison of two groups, two-tailed unpaired t-tests were used. Multiple comparisons were performed by one-way ANOVA followed by Fisher's LSD post-hoc test. Representative experiments with 3-6 technical replicates are displayed as mean values with SD and were statistically analyzed by one-way ANOVA and Scheffé's-test. Statistical parameters were calculated using the WinSTAT statistics Add-In for Microsoft Excel (R. Fitch Software, Bad Krozingen, Germany). A p-value < 0.05 was considered statistically significant.

3.4 Primary rat microglia

Primary glial cultures were prepared from brain tissue of postnatal day (PND) 1 rat pups. For detailed information concerning the constitutive *Cacna1c* rat model used as well as the genotyping procedure see Chapter 3.2 and 3.3.1. The PND 1 pups were separated from their mother and, using scissors, their heads were quickly decapitated after treating the cutting site shortly with 70% ethanol. The dissection of cortico-hippocampal regions from both brain hemispheres was performed as described previously (Figure 5). In separate tubes for each pup, the dissected brain tissues were instantly placed in cold HBSS (Thermo Fisher Scientific, Darmstadt, Germany; supplemented with 9 mM HEPES sodium salt, 100 U/ml penicillin, and 100 µg/ml streptomycin; pH 7.2), washed once with fresh HBSS, and subsequently incubated with trypsin (1 mg/ml in HBSS) for 15 min at 37°C to allow enzymatic disaggregation. DNase (100 µg/ml) was added for 30 sec at room temperature, followed by another washing step and a 2 min-incubation with trypsin inhibitor (1 mg/ml in HBSS). The brain tissues were washed once again and then carefully triturated 15-20x using a P1000 pipette, before adding 1 ml culture medium (DMEM F-12 Ham complemented with 2 mM glutamine, 10% (v/v) FBS (Biochrom, Berlin, Germany), 100 U/ml penicillin, and 100 µg/ml streptomycin). Next, the cell suspensions were centrifuged at 1000 rpm for 5 min (Heraeus fresco 17; Thermo Fisher Scientific, Darmstadt, Germany). After removing the supernatant, the cell pellets were each resuspended in 12 ml DMEM F-12 Ham, transferred to T-75 cell culture flasks, and incubated at 37°C in a humidified 5% CO_2 atmosphere. Every 3 days, the culture medium was completely replaced by 12 ml fresh, pre-warmed DMEM F-12 Ham.

After 10-14 DIV, the astrocyte layer reached 100% confluence and microglia were growing on top, microscopically visible as bright, small, rounded cells. Then, the microglial cells were separated from the mixed glial cultures by shaking the flasks at 200 rpm, 37°C for 1 h on an orbital shaker (Dual-Action Shaker KL 2; Edmund Bühler GmbH, Bodelshausen, Germany). Subsequently, the supernatant of all flasks was pooled per genotype (*Cacna1c*$^{+/+}$, *Cacna1c*$^{+/-}$) and the containing microglia were pelleted by centrifugation (1000 rpm, 5 min). After resuspension in culture medium (500 µl per flask), cell numbers were quantified (Neubauer Zählkammer; Brand, Wertheim, Germany), and the purified microglia seeded at a density of 80-140 $\times 10^3$ cells/cm^2 in culture plates pre-coated with poly-L-lysine (PLL). The coating was realized on the day of purification by incubation of the respective cell culture plates with PLL hydrobromide (0.1 mg/ml in PBS) for 1 h at room temperature, 3x washing with PBS, and exposure to UV light (30 min) for sterilization. The astrocyte-containing flasks were refilled 1:1 with fresh and conditioned medium respectively, and cultured for another 4-5 days before microglia cells were isolated again. This process was repeated up to three times. The purity of the microglial cultures was ~99% as confirmed by immunostaining using the specific microglia marker CD11b/c and the astrocyte marker GFAP (Figure 9).

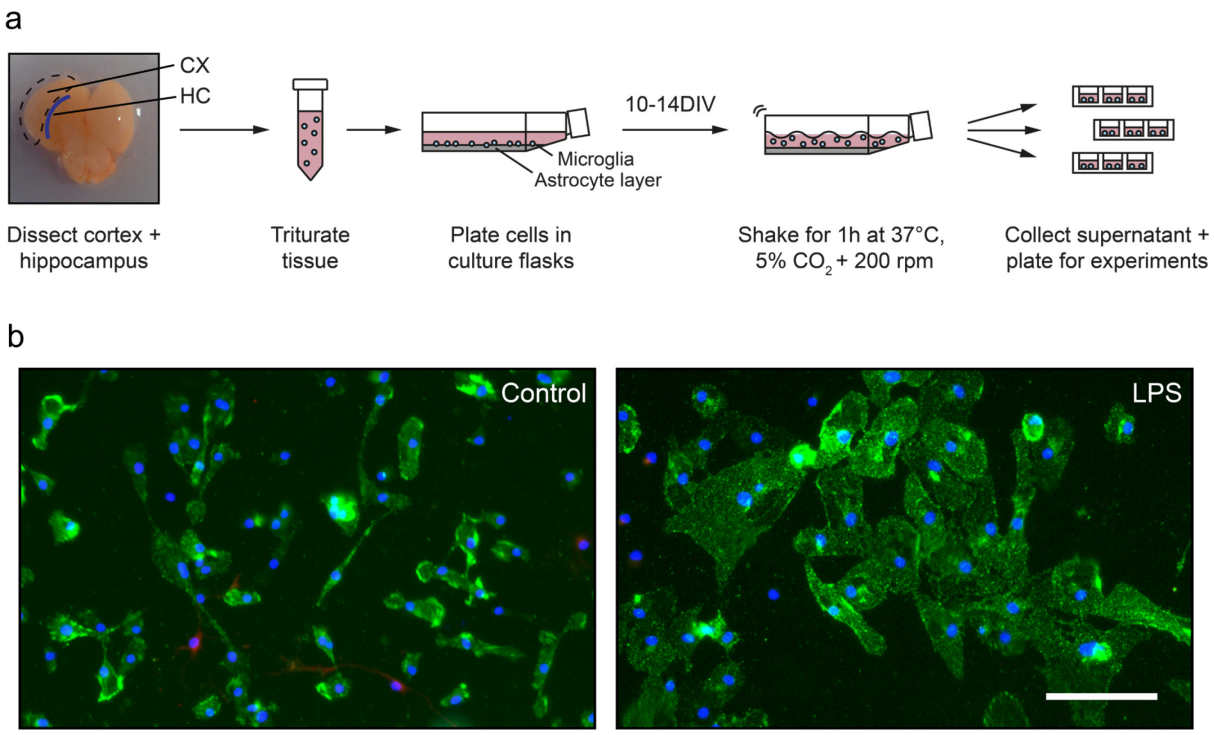

Figure 9. Primary microglia cultures from PND1 rat pups

a Schematic workflow of the culturing procedure. Primary glial cultures were prepared from the cortex and hippocampus of 1-day-old neonatal *Cacna1c*$^{+/-}$ rat pups and their wildtype littermates. After 10-14 DIV, when astrocytes reach 100% confluence, microglia were separated from the underlying astrocyte layer by shaking the flasks for 1 h on an orbital shaker. LPS-treatment was performed 24 h after the seeding of pure microglia in PLL-coated plates. **b** Control and LPS-stimulated (100 ng/ml, 24 h) wildtype cultures were fixated and stained for the microglia marker CD11b/c (Green, A488), the astrocyte marker GFAP (Red, A650), and the nucleus (DAPI; blue). Scale bar, 100 µm.

3.4.1 Treatment with LPS and nimodipine

Pure primary microglia were cultured for 1-2 days before treating them with the inflammatory stimulus LPS (100 ng/ml, 24 h; unless otherwise stated). The DHP LTCC blocker nimodipine (Cayman Chemical, Ann Arbor, MI, USA) was applied as co-treatment in a final concentration of 25 µM (for chemical structure see Figure 8).

3.4.2 Quantitative PCR

RNA isolation and reverse transcription qPCR were performed as specified in Chapter 3.3.3. In addition to *Cacna1c*, *Cacna1d*, and *U6* the following primer pair was employed to evaluate *Nos2* mRNA levels: forward 5′-TGG TGA GGG GAC TGG ACT TTT-3′ and reverse 5′-GCA CCA ACT CTG CTG TTC TC-3′.

3.4.3 Protein analysis

Protein isolation and Western blot were conducted as detailed previously (Chapter 3.1.2). To this end, 7.5% SDS-polyacrylamide gels, 30 µg protein per sample, and anti-iNOS (1:2,000; BD Biosciences, Franklin Lakes, NJ, USA) as well as anti-Vinculin (1:20,000) antibodies were used.

3.4.4 Real-time assessment of changes in cellular morphology

The xCELLigence RTCA instrument (Roche Diagnostics, Mannheim. Germany) monitors and quantifies cell size and shape by measuring electrical impedance in real time, thereby providing a sensitive readout for morphology changes associated with immune cell activation. In this regard, 30,000-40,000 cells per well were seeded in 96-well E-Plates containing gold microelectrodes fused to the bottom surface. Cell size enlargement leads to an increase in electrical impedance reported as normalized cell index.

3.4.5 Cell bioenergetics measurement

OCR and ECAR of primary rat microglia were determined using a Seahorse XF^e96 Analyzer (Agilent Technologies, Waldbronn, Germany). For that purpose, 40,000-50,000 cells per well were assayed in DMEM supplemented with 143 mM sodium chloride, 25 mM glucose, 1 mM sodium pyruvate, 2 mM glutamine, and 0.04% (w/v) bovine serum albumin (pH 7.35). LPS (100 ng/ml) was either injected to each well via the first port or added 24 h prior to the measurement. Further mitochondrial stressor compounds used were as follows: 2 µM oligomycin, 2 µM FCCP, and 0.5 µM rotenone together with 1 µM antimycin A (Figure 4). After assay completion, the data was normalized to total protein amount per well (for details see Chapter 3.3.6) using the Seahorse Wave software 2.6 (Agilent Technologies, Waldbronn, Germany).

3.4.6 Determination of nitrite concentration in cell culture supernatant

To investigate NO formation, nitrite (NO_2^-), a stable breakdown product of NO, was measured in the supernatant of microglial cultures by utilizing the Griess Reagent System (Promega, Mannheim, Germany) in accordance with the manufacturer's instructions. This system is based on a chemical diazotization reaction, which forms a magenta-colored azo compound in the presence of nitrite. A reference curve with nitrite standards ensured the accurate quantitation of NO_2^- levels. Absorbance was determined at 530/10 nm with a FLUOstar OPTIMA reader (BMG Labtech, Ortenberg, Germany).

3.4.7 Rat cytokine and chemokine immunoassay

Cytokine and chemokine concentrations in the cell culture supernatant of primary microglia were assessed by Felix Picard in the lab of Prof. Holger Garn (Institute of Laboratory Medicine and Pathobiochemistry, University of Marburg, Germany) using the Bio-Plex Pro Rat Cytokine Assay (24-Plex panel; BioRad Laboratories, Hercules, CA, USA). This magnetic bead- and antibody-based multiplex immunoassay allows for the simultaneous detection of multiple signaling proteins in a 96-well format. Each individual sample was measured in duplicates. Cytokine levels were calculated from standard curves and are indicated as absolute concentration in ng/ml. Data acquisition and analysis was performed with Bio-Plex Manager software (BioRad Laboratories, Hercules, CA, USA).

3.4.8 Immunocytochemistry

Fixated cells were stained with anti-CD11b/c (1:100; BioLegend, San Diego, CA, USA), anti-GFAP (1:1,000; Dako, Glostrup, Denmark) and DAPI (1:1,000) as described before (Chapter 3.3.8). Images were acquired using an inverted fluorescence microscope (DMI6000 B; Leica Microsystems, Wetzlar, Germany) at 10x magnification. Confocal images were acquiredwith a 40x/1.0 oil objective at a Zeiss LSM700 microscope (Carl Zeiss Microscopy GmbH, Jena, Germany).

3.4.9 Statistical analysis

Data from independent preparations are presented as single values with mean ± SD. For statistical comparisons between two groups, two-tailed unpaired t-tests were used. Multiple comparisons were performed by one-way ANOVA followed by Fisher's LSD post-hoc test. Representative experiments with 3-10 technical replicates are displayed as means with SD and were statistically analyzed by one-way ANOVA and Scheffé's-test. Parameter calculations were realized with the WinSTAT statistics Add-In for Microsoft Excel (R. Fitch Software, Bad Krozingen, Germany). A statistically significant difference was assumed at $p < 0.05$.

3.5 Isolated mitochondria from adult rat brain

This project was realized in collaboration with Prof. Rainer Schwarting and Markus Wöhr as well as with the help of Prof. Amalia Dolga, Moria Braun, Theresa Kisko, Özge Sungur, Ina Eisenbach, Katharina Elsässer, Goutham Ganjam, Lena Hoffmann, Birgit Honrath, Anja Jelinek, Rukhshona Kayumova, Malena Rabenau, Tobias Redecker, and Dominik Seffer.

3.5.1 Animals and breeding

A constitutive heterozygous *Cacna1c*$^{+/-}$ rat model was used as detailed in Chapter 3.2. Genotyping was performed from rat tail snips (PND 5 ± 1) by Prof. Marcella Rietschel and Stephanie Witt (Department of Genetic Epidemiology in Psychiatry, Central Institute for Mental Health, Mannheim, Germany) as reported before (37).

As published previously, a heterozygous breeding protocol was used to obtain offspring from both genotypes (37). To this aim, Sprague-Dawley females (Charles River, Sulzfeld, Germany) and male *Cacna1c*$^{+/-}$ rats were paired for breeding. Sprague-Dawley females were used because breeding efficacy is reduced in female *Cacna1c*$^{+/-}$ rats. In order to avoid litter effects, only litters with both genotypes present were included in the experiments. Breeding was performed at the Faculty of Psychology, University of Marburg, Germany. Approximately two weeks after pairing for breeding, females were individually housed and inspected daily for pregnancy and delivery. The day of birth was considered as postnatal day (PND) 0. Rats were identified by paw tattoo using non-toxic animal tattoo ink (Ketchum permanent tattoo inks green paste; Ketchum Manufacturing Inc., Brockville, Canada). The ink was inserted subcutaneously through a 30-gauge hypodermic needle tip into the center of the paw on PND 5 ± 1. Rats were housed under standard laboratory conditions (22 ± 2°C and 40-70% humidity) with free access to standard rodent chow and water.

3.5.2 Gene-environment study

To study the effects of a gene-environment interaction (GxE) on brain mitochondrial bioenergetics, a 2x3 design was applied and male *Cacna1c*$^{+/-}$ rats and *Cacna1c*$^{+/+}$ littermate controls were exposed to one of three experimental housing conditions for four consecutive weeks after weaning on PND 21, i.e. between PND 22 and 50 ± 1 (Figure 10). From each litter, six rats were included in the experiment whenever possible with a pair of *Cacna1c*$^{+/-}$ and *Cacna1c*$^{+/+}$ siblings each being exposed to (A) post-weaning social isolation (Iso), (B) standard housing (Stand), or (C) social and physical environmental enrichment (Enr).

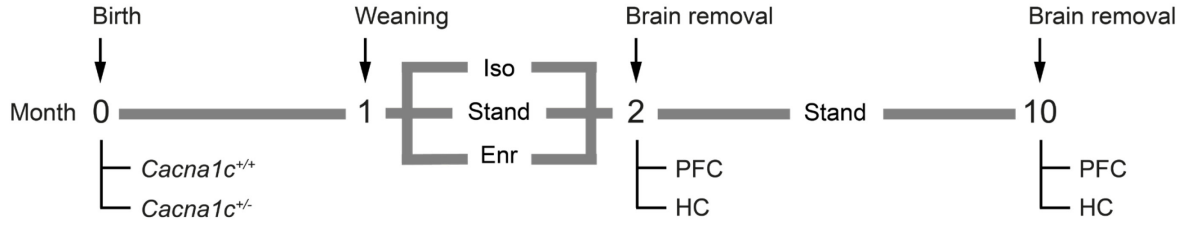

Figure 10. Experimental design

Shortly after birth, the genotypes of the rats (*Cacna1c*$^{+/+}$ vs *Cacna1c*$^{+/-}$) were determined. With three weeks of age (PND 21), the rats were separated from their mothers and allocated to one of three experimental housing conditions, i.e. post-weaning social isolation (Iso), standard housing (Stand), and social and physical environmental enrichment (Enr), where they spend four weeks before their brains were removed (PND 50 ± 1) and the mitochondria were isolated from the prefrontal cortex (PFC) and the hippocampus (HC).

(A) Post-weaning social isolation (Iso) in a Makrolon type III cage (425 x 265 x 150 mm, plus high stainless-steel covers; Tecniplast Deutschland GmbH, Hohenpeißenberg, Germany), housed alone, applying a previously established protocol (55).

(B) Standard housing (Stand) in a polycarbonate Macrolon Type IV cage (580 x 380 x 200 mm, plus high stainless-steel covers; Tecniplast Deutschland GmbH, Hohenpeißenberg, Germany), housed in groups of six rats, consistent with previously applied control conditions (55).

(C) Social and physical environmental enrichment (Enr) in a large commercial rat cage (AniOne Remus, 104 x 59 x 107 cm; MultiFit Tiernahrungs GmbH, Krefeld, Germany) containing three wooden platforms connected by ramps, two metal food dispensers, and an assortment of cage accessories and places to hide, applying a modified protocol previously established (58). The initial cage setup comprised six hiding places (2x Rodent Retreats red, Bio-Serv, Flemington, NJ, USA; 2x AniOne Grasnest Size L, MultiFit Tiernahrungs GmbH, Krefeld, Germany; 1x AniOne Grastunnel, MultiFit Tiernahrungs GmbH, Krefeld, Germany; 1x empty cardboard box, Dallmayr capsa, Munich, Germany), six wooden sticks for the animals to chew on, and two petri dishes with water in addition to the water bottle affixed to the cage wall. Twice a week, various accessories were either added to the cage (e.g. 2x wire feeding balls stuffed with paper tissue, Food-Ball Ø 12 cm, Trixie Heimtierbedarf GmbH, Tarp, Germany; 3x marbles; 2x empty toilet paper rolls) or exchanged, in the case of hiding places (1x wooden rat house, Jesper Eckhaus Size M, Trixie Heimtierbedarf GmbH, Tarp, Germany; 1x JR Farm Heuhaus 85 g, JR FARM GmbH, Holzheim-Pessenburgheim, Germany). During social and physical environmental enrichment, rats further received two servings of six pieces of sweetened puffed wheat cereal (Kellogg's Smacks; Kellogg Deutschland, Hamburg, Germany), which were hidden within the cage.

In standard housing and social and physical environmental enrichment conditions, two siblings were always housed with two further pairs of *Cacna1c*$^{+/-}$ and *Cacna1c*$^{+/+}$ siblings from

different litters. To avoid age differences between litters, all rats included in the experiment were born within a four-day time window. In total, 54 rats were included in the experiment, with n = 9 per genotype and experimental housing condition (*Cacna1c*$^{+/+}$-Iso, *Cacna1c*$^{+/+}$-Stand, *Cacna1c*$^{+/+}$-Enr, *Cacna1c*$^{+/-}$-Iso, *Cacna1c*$^{+/-}$-Stand, *Cacna1c*$^{+/-}$-Enr; short: +/+ Iso, +/+ Stand, +/+ Enr, +/- Iso, +/- Stand, +/- Enr). One *Cacna1c*$^{+/-}$ rat housed under social and physical environmental enrichment conditions died before the end of the experiment and was excluded from data analysis. PFC and HC of the right brain hemispheres were removed on three consecutive days immediately following the four weeks of exposure to the experimental housing conditions at ~2 months of age. All subsequent analyses were conducted blinded to genotype and environmental background.

3.5.3 Supplementary genotype studies

Besides the GxE study, two additional studies were performed. In the first supplementary study, it was tested whether brain mitochondrial bioenergetics differs in *Cacna1c*$^{+/-}$ rats and *Cacna1c*$^{+/+}$ littermate controls depending on brain hemisphere. In this study, six male *Cacna1c*$^{+/-}$ rats and six male *Cacna1c*$^{+/+}$ littermate controls exposed to standard housing conditions were included. Brains were removed at ~2 months of age. The second supplementary study evaluated whether brain mitochondrial bioenergetics differs in *Cacna1c*$^{+/-}$ rats and *Cacna1c*$^{+/+}$ littermate controls depending on age and sex. In this study, eight male *Cacna1c*$^{+/-}$ rats and eight male *Cacna1c*$^{+/+}$ littermate controls as well as eight female *Cacna1c*$^{+/-}$ rats and eight female *Cacna1c*$^{+/+}$ littermate controls exposed to standard housing conditions were included. Brains were removed at ~10 months of age (Figure 10). Rats included in the supplementary studies were used before weaning to study isolation-induced ultrasonic vocalizations, developmental milestones, and somatosensory reflexes ((154); not shown).

3.5.4 Brain extraction

For brain removal, rats were first deeply anesthetized with isoflurane (Baxter, Unterschleißheim, Germany), and then decapitated and their brains were quickly extracted. The HC was identified and removed as described previously (155), following the gross anatomical criteria established before (156). To expose the dorsal part of the HC, the cerebral cortex covering it was incised and pulled up. The HC was then separated from cortex and removed towards the ventral side. Next, using a cold stainless steel adult rat brain matrix (Zivic Instruments, Pittsburgh, PA, USA), the brain was divided into left and right hemispheres and subsequently the prefrontal cortex was isolated via a coronal cut approximately between + 2.5 mm and + 5.0 mm from bregma, using the rat brain atlas as anatomical reference (157).

3.5.5 Mitochondrial isolation

Mitochondria were isolated from both PFC and HC of acutely dissected adult rat brains using a pump-controlled cell homogenizer as detailed in Chapter 3.1.3. Before homogenization, fresh brain tissue (~50 mg), kept in isolation buffer containing 300 mM sucrose, 5 mM TES, 200 µM EGTA, and 1 mM DTT, was coarsely sheared with a 20G Neoject needle (Dispomed, Gelnhausen, Germany) and then strained through a 100-µm nylon cell strainer (Corning Incorporated, Corning, NY, USA). The resulting cell suspension was then homogenized and the emerging crude mitochondrial fraction was slowly resuspended in 500 µl mitochondrial isolation buffer (70 mM sucrose, 210 mM mannitol, 5 mM HEPES, 1 mM EGTA, 0.5% (w/v) BSA; pH 7.2). All steps were performed on ice. The total protein concentration was determined using the Pierce BCA Protein Assay Kit (Thermo Fisher Scientific, Darmstadt, Germany) with BSA standards based on mitochondrial isolation buffer. As isolated mitochondria decline in their functional quality over time, the present study was strictly littermate-controlled and the isolation process was conducted in a randomized order to compensate for potential inter-day and time-dependent variability.

3.5.6 Protein analysis

Protein was extracted from frozen cortical tissue (10 mg) lysed in buffer containing 50 mM Tris-HCl, 150 mM NaCl, 5 mM EDTA, 1.0% (w/v) Triton X-100, and 0.5% (w/v) Na-deoxycholate, freshly supplemented with 2 mM PMSF, 1 mM Na_3VO_4, and 10 mM NaF. Tissue lysis was succeeded by a homogenization step using a T10 basic Ultra-Turrax (IKA-Werke, Staufen, Germany) for 10 sec. The homogenates were then centrifuged for 15 min at 13,000 xg and 4°C resulting in the protein-comprising supernatants (Heraeus Fresco 17; Thermo Fisher Scientific, Darmstadt, Germany). In addition, the collected fractions from the isolation procedure, i.e. total lysate, cytosolic and mitochondrial fraction, were also used for protein quantitation. Protein quantification, SDS-PAGE, and Western blot were performed according to the standard procedures described in Chapter 3.1.2. The following antibodies were used: Cav1.2 (1:1,000; Alomone Labs, Jerusalem, Israel), Vinculin (1:20,000), Lamin A/C (1:1,000; Cell Signaling Technology, Frankfurt, Germany), α-Tubulin (1:10,000), Tim23 (1:2,000; BD Bioscience, Heidelberg, Germany), Mitofusin 2 (Mfn2; 1:1,000; Cell Signaling Technology, Frankfurt, Germany), and MitoProfile Total OXPHOS Rodent WB Antibody Cocktail (1:250; Abcam, Cambridge, UK).

3.5.7 Mitochondrial bioenergetics measurement

The OCR as an indicator of mitochondrial respiration was measured with a Seahorse XF^e96 Analyzer (Agilent Technologies, Waldbronn, Germany). The coupling assay was performed according to existing protocols (158). Briefly, 6 µg of freshly isolated mitochondrial protein per well were assayed in mitochondrial assay solution containing 70 mM sucrose, 220 mM mannitol, 10 mM KH_2PO_4, 5 mM $MgCl_2$, 2 mM HEPES, 1 mM EGTA, and 0.2% (w/v) fatty-acid-free BSA, with an adjusted pH of 7.2 and supplemented with the complex II substrate succinate (10 mM) and the complex I inhibitor rotenone (2 µM). The consistent adherence of the mitochondria to the well ground was ensured by centrifugation of the whole plate at 2,000 xg for 20 min at 4°C (Heraeus Megafuge 40R; Thermo Fisher Scientific, Darmstadt, Germany). The Seahorse system allows for the consecutive injection of different modulators of the electron transport chain. The compounds and final concentrations used are as follows: 4 mM ADP, 2.5 µg/ml oligomycin, 4 µM FCCP, 4 µM antimycin A. Data analysis and parameter calculation were conducted as described previously (159) and in Table 2.

Table 2. Seahorse parameter calculations

Parameter	Rate measurement equation
Anti A	Minimum rate measurement after antimycin A injection
Basal	Last rate measurement before first injection - Anti A
State 3	Maximum rate measurement after ADP injection - Anti A
State 4_o	Minimum rate measurement after oligomycin injection - Anti A
State 3_u	Maximum rate measurement after FCCP injection - Anti A
RCR	Respiratory control ratio = State 3 / State 4_o

3.5.8 Flow cytometry

Freshly isolated mitochondrial protein was suspended in mitochondrial assay solution at a concentration of 50 µg/ml. The probes were stained with fluorescent dye and incubated on ice for 15 min protected from light. Mitochondrial superoxides were detected by incubation with 1.25 µM MitoSOX Red indicator (Thermo Fisher Scientific, Darmstadt, Germany). Changes in mitochondrial membrane depolarization were determined using MitoPT TMRE Kit (0.2 µM; ImmunoChemistry Technologies, Hamburg, Germany) and with 10 mM succinate and 2 µM rotenone added to the buffer. The samples were measured with a total count of 50,000 events utilizing a Guava easyCyte 6-2L flow cytometer (Merck Millipore, Darmstadt, Germany). Analysis and gating were performed with GuavaSoft 3.1.1 software.

3.5.9 Rhodamine 123

Mitochondrial membrane potential ($\Delta\Psi_m$) integrity was assessed over time (40 min) by rhodamine 123 (Thermo Fisher Scientific, Darmstadt, Germany) fluorescence quenching, as previously reported (160). Isolated mitochondrial protein samples (75 µg/well) were resuspended in 200 mM sucrose, 10 mM MOPS-Tris, 5 mM succinate, 1 mM P_i (H_3PO_4), 10 µM EGTA, and 2 µM rotenone (pH 7.3) and dyed with 125 nM rhodamine 123 in a black 96-well plate. Injection of the depolarizing reagent FCCP (500 nM) at the end of the measurement served as internal positive control leading to a complete loss of $\Delta\Psi_m$. The resulting fluorescence signals were detected with a FLUOstar OPTIMA reader (Ex 485/12 nm, Em 530/10 nm; BMG Labtech, Ortenberg, Germany).

3.5.10 Microscopy

To visualize mitochondria, the enriched fractions resulting from the isolation procedure were incubated with 0.2 µM MitoTracker Deep Red (Cell Signaling Technology, Frankfurt, Germany) for 15 min. Thereafter, images were acquired using a fluorescence microscope with a HCX PL Fluotar L 40.0x/0.60 dry objective (DMI6000 B; Leica Microsystems, Wetzlar; Germany).

3.5.11 Statistical analysis

Statistical analyses were performed by Thomas Möbius (research group of Prof. Astrid Dempfle; Institute of Medical Informatics and Statistics, Kiel University, Germany). Data is presented as single values together with their mean and SD. Analysis of PFC and HC were performed separately. The outcome variables studied in the statistical analysis were $Ca_V1.2$ protein levels, body weight, the parameters of the mitochondrial bioenergetics measurements (Basal, State 3, State 4_o, State 3_u, Anti A, and RCR), MitoSOX, and TMRE fluorescence. Besides genotype (*Cacna1c*$^{+/+}$/*Cacna1c*$^{+/-}$), explanatory variables included in the analysis were housing (Iso, Stand, and Enr), brain hemisphere (left/right), age (2/10 months), and sex (male/female). Each of these factors was fully crossed with the genotype, but none of them were crossed with any of the other explanatory variables. Hence, a separate analysis of each of these variables on the respective outcome variables was performed.

In the case of $Ca_V1.2$, body weight, MitoSOX, and TMRE, a preliminary explorative data analysis evaluated the general shapes and locations of the individual distributions in a fully saturated, two-factorial design including interactions. All respective residual distributions were assessed. Standard ordinary least squares techniques were used, where suitable, in order to study the outcome variables in their respective 2x3 factorial designs. In the presence of

variance heteroscedasticity, which was the case for MitoSOX and TMRE, weighted least squares techniques were used instead including Lagrange multiplier tests to assess statistical significance in these cases. Model selection was performed via backwards selection, where the aim of the first test was always to exclude or establish the existence of gene-interaction. Only if gene-interactions could be excluded, the analysis proceeded with the study of the main effects. If interactions were present, the analysis was stratified.

To study the existence of possible gene or gene-interaction effects on either of the bioenergetic parameters, the littermate-controlled design was exploited by first studying the paired differences of the respective measures between *Cacna1c*$^{+/+}$ and *Cacna1c*$^{+/-}$ rat littermate pairs. This analysis strategy was able to counteract potential litter effects or confounding factors that were due to differences in the isolation process when evaluating the existence of gene or gene-interaction effects. Furthermore, variances of these confounding factors were reduced that might have otherwise overlaid gene or gene-interaction effects, thereby increasing statistical power. Analyzing *Cacna1c*$^{+/+}$/*Cacna1c*$^{+/-}$-paired differences resulted in single factor designs, in which the main effect corresponds to gene-interaction and differences from zero correspond to main gene effects on the outcome variable. If gene-interactions were present, the respective analysis was stratified.

All p-values are reported up to four digits of significance and were considered statistically significant at $p < 0.01$. The analysis was carried out using Python (Version 3.5.2; Python Software Foundation, Beaverton, OR, USA) and the Python module Statsmodels (Version 0.9.0). Figures were created with GraphPad Prism (Version 7; GraphPad Software, La Jolla, CA, USA).

Type II error considerations

In a comparable study using a mouse model of chronic mild stress, Gong et al. reported an average reduction of Basal OCR from 95 to 50 nmol/min/mg protein with a maximal standard deviation of 25 nmol/min/mg protein (161). The power to detect such an effect at 1% significance with eight animals per group is 96%. Further, a significant drop of 3.5 in RCR under stress with a SD of 1.2 was reported. The chance to detect this effect with 8 animals per group at 1% significance is 88% implying that the present study was well powered to detect differences in the respective parameters.

3.6 Human PBMCs

Whole blood for the isolation of PBMCs was collected and processed in the psychiatric departments of the university hospitals in Marburg and Münster (Germany) under the direction of Prof. Tilo Kircher, Prof. Udo Dannlowski, and Prof. Petra Pfefferle.

3.6.1 Subjects

Three homogeneous proband subgroups were selected from a larger sample recruited in the Marburg/Münster Affective Disorders Cohort Study (MACS). Study approval was obtained from the local ethics committee and all participants provided informed written consent. Exclusively women, aged between 18 and 50, with no personal history of any psychiatric disorder were included to eliminate possible gender-specific differences in respiratory activity (162). The three extreme groups comprise healthy subjects with genetic risk (GR, n = 20), environmental risk (ER, n = 21), and no risk (NR, n = 20) as age-matched control cohort. The genetic risk group consists of people having at least one first degree relative with a lifetime diagnosis of schizophrenia, major depression, or bipolar disorder. The environmental risk group implies study participants, which experienced at least two forms of childhood maltreatment such as sexual abuse, physical or emotional abuse/neglect. These traumatic early life experiences were retrospectively assessed using the German version of the Childhood Trauma Questionnaire (CTQ) (163, 164). Individuals with no family history of psychiatric disorders and with no CTQ subscale reaching the threshold for maltreatment form the no risk control group.

3.6.2 Isolation and preparation

Human PBMCs were isolated from venous whole blood by Ficoll density gradient centrifugation using BD Vacutainer Cell Preparation Tubes with sodium heparin (Becton, Dickinson and Company, Franklin Lakes, NJ, USA). The structured and quality-controlled PBMC separation, cryopreservation and storage in liquid nitrogen was performed by the Comprehensive Biomaterial Bank Marburg (CBBMR).

On the day of experiments, frozen 2 ml-aliquots were semi-thawed in the water bath and diluted in 5 ml pre-warmed DMEM supplemented with 10% FBS (Biochrom, Berlin, Germany), 20 mM HEPES, 100 units/ml penicillin, 100 µg/ml streptomycin, and 2 mM glutamine. After centrifugation at 2,000 rpm for 5 min (Heraeus Megafuge 11R; Thermo Fisher Scientific, Darmstadt, Germany), the resulting cell pellet was resuspended in 500 µl assay medium containing DMEM, 143 mM sodium chloride, 25 mM D-glucose, 2 mM glutamine, and 1 mM sodium pyruvate with an adjusted pH of 7.35. Subsequently, total cell number and viability were determined using a CASY TT cell counter (OMNI Life Science, Bremen, Germany) and a cut-off diameter of 5.4 µm to exclude cell debris and thrombocytes with the help of Felix Picard in the laboratory of Prof. Holger Garn (Institute of Laboratory Medicine and Pathobiochemistry, University of Marburg, Germany).

3.6.3 Flow cytometry

The isolated PBMCs were examined by flow cytometry with a total count of 10,000 cells per sample utilizing a Guava easyCyte 6-2L flow cytometer (Merck Millipore, Darmstadt, Germany). By plotting the side against the forward scatter, potential differences in cell type composition between samples were assessed. To selectively analyze mitochondrial superoxides, the probes were stained with the fluorescent dye MitoSOX (1.25 µM; Thermo Fisher Scientific, Darmstadt, Germany) and incubated for 30 min at 37°C protected from light. After centrifugation at 10,000 rpm for 5 min (Heraeus fresco 17, Thermo Fisher Scientific, Darmstadt, Germany), the emerging pellet was suspended in PBS to yield a concentration between 1,000 and 4,000 cells/µl. Data analysis and gating were performed with the GuavaSoft 3.1.1 software.

3.6.4 Mitochondrial OCR measurement

To characterize mitochondrial bioenergetic function in human PBMCs, the OCR was quantified with a Seahorse XF^{e}96 Analyzer (Agilent Technologies, Waldbronn, Germany). Therefore, PBMCs were suspended in 180 µl assay medium per well (DMEM supplemented with 143 mM sodium chloride, 25 mM D-glucose, 2 mM glutamine, and 1 mM sodium pyruvate; pH = 7.35). After centrifugation at 50 xg (ACC 5/DEC 5), the plate was turned 180° and centrifuged again at 300 xg (Heraeus Megafuge 40R; Thermo Fisher Scientific, Darmstadt, Germany) to ensure cell adhesion and formation of an evenly distributed monolayer. Three basal and three measurements after each injection were recorded. Prior to experiments, the optimal cell density, FCCP and oligomycin concentration were determined as detailed in Figure 11. An optimal seeding density is reflected in basal OCR values ranging between 60 and 120 pmol/min. Even though 300,000 cells showed an average basal OCR rate of 60 pmol/min compared to 40 pmol/min with 200,000 cells per well, all subsequent measurements were performed using 250,000 viable PBMCs/well due to the limited amount of cells provided per sample. The maximal reaction upon FCCP addition was reached after the third/fourth injection of 0.4 µM each, resulting in an optimal concentration of 1.5 µM. Furthermore, 2 µM oligomcin, which correlates with its second injection (1 µM each), showed maximal OCR reduction. In summary, the following final parameters were employed: 250,000 viable PBMCs/well, 2 µM oligomycin, 1.5 µM FCCP, 1 µM rotenone, and 1 µM antimycin A.

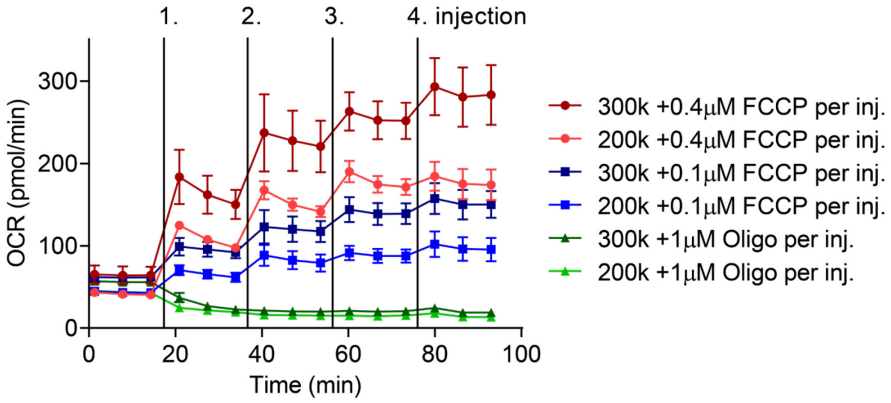

Figure 11. Titration of optimal Seahorse assay conditions for PBMCs

The oxygen consumption rates (OCRs) of PBMCs using two cell densities (200k vs. 300k per well) as well as different FCCP (0.1-1.6 µM) and oligomycin (1-4 µM) concentrations are compared. k, × 10^3; Oligo, oligomycin.

Assay parameter calculations were performed using the Seahorse XF Cell Mito Stress Test and the Bioenergetic Health Index (BHI) Report Generators (Agilent Technologies, Waldbronn, Germany) as outlined in Table 3.

Table 3. Seahorse parameter equations

Parameter	Rate measurement equation
Non-mitochondrial Respiration	Minimum rate measurement after rotenone/antimycin A injection
Basal Respiration	Last rate measurement before first injection - Non-mitochondrial Respiration
ATP Production	Last rate measurement before first injection - Minimum rate measurement after oligomycin injection
Proton Leak	Minimum rate measurement after oligomycin injection - Non-mitochondrial Respiration
Maximal Respiration	Maximum rate measurement after FCCP injection - Non-mitochondrial Respiration
Spare Capacity	Maximal Respiration - Basal Respiration
Spare Capacity (%)	(Maximal Respiration / Basal Respiration) × 100
Coupling Efficiency (%)	(ATP Production / Basal Respiration) × 100
Bioenergetic Health Index	log (Spare Capacity × ATP Production) / (Non-mitochondrial Respiration × Proton Leak)

3.6.5 Statistical analysis

All data are presented as single values with mean ± SD. Comparisons of the three groups NR, GR, and ER were performed by one-way analysis of variance (one-way ANOVA) followed by Fisher's Least Significant Difference (LSD) post-hoc test. Monotonic associations between BHI and mitochondrial ROS levels were assessed by Spearman rank correlation. A statistical significant correlation was assumed at $p < 0.05$ (*). Statistical analyses were realized using the WinSTAT statistics Add-In for Microsoft Excel (R. Fitch Software, Bad Krozingen, Germany).

4 Results

4.1 Effects of *Cacna1c* knockdown on oxidative stress in HT22 cells

In order to study the effects of *Cacna1c* depletion on mitochondrial parameters, the siRNA-mediated knockdown was first validated at the level of mRNA and protein. As shown in Figure 12a, *Cacna1c* siRNA significantly reduced mRNA expression by ~75% compared to control and siScr. In line with this finding, the immunoblot revealed a pronounced downregulation of $Ca_V1.2$ protein levels in siRNA-transfected HT22 cells (Figure 12b). A comparable knockdown was also achieved using another *Cacna1c* siRNA sequence (siCacna1c 3; Figure 13).

Downregulation of *Cacna1c* preserved mitochondrial morphology and function independent of glutathione depletion in glutamate-challenged HT22 cells

To investigate the effects of *Cacna1c* gene silencing on the mechanisms of glutamate-induced oxidative stress, GSH levels and lipid peroxidation were next analyzed in HT22 cells exposed to glutamate. Total glutathione levels were determined 2, 4, and 6 h after the onset of glutamate treatment (Figure 12c). Loss of GSH marks the initial step in oxidative glutamate toxicity and, in fact, a steady decline in GSH concentration over time was observed (117). Notably, there were no significant differences in GSH depletion between *Cacna1c* siRNA-transfected HT22 cells and controls. Glutathione depletion leads to the accumulation of lipid peroxides, which was evaluated here 8 h post-glutamate treatment using the fluorescent dye BODIPY followed by flow cytometric analysis (112). The results revealed that the initial rise in lipid peroxidation upon glutamate exposure was largely prevented in HT22 cells transfected with *Cacna1c* siRNA indicating a partial action upstream of mitochondria in the considered oxidative stress cascade (Figure 12d,e).

Figure 12. siRNA-mediated knockdown of *Cacna1c* prevented lipid peroxidation, but not glutathione depletion following glutamate exposure

a *Cacna1c* mRNA levels were analyzed 24 h after siRNA transfection with 20 and 40 nM. *Gapdh* served as internal control. **b** Protein samples were collected 48 h after transfection with 40 nM siRNA and the $Ca_V1.2$ expression levels were then identified by Western blot. Vinculin was used as loading control. **c** Total glutathione levels were calculated from three replicates per condition after 0, 2, 4, and 6 h of glutamate treatment (10 mM). Data are provided as mean + SD. **d,e** Lipid peroxidation in HT22 cells was determined using BODIPY staining after an 8-hour incubation with 9 mM glutamate. The dot plots show representative replicates and the bar graph summarizes the associated experiment where three replicates per sample are shown as percentage of cells in the upper right quarter (mean + SD; 10,000 cells per replicate). Ctrl, control; siScr, scrambled siRNA; siCacna1c, *Cacna1c* siRNA; Glut, glutamate. ***$p < 0.001$; ns (not significant) compared to glutamate-treated ctrl (ANOVA, Scheffé's-test).

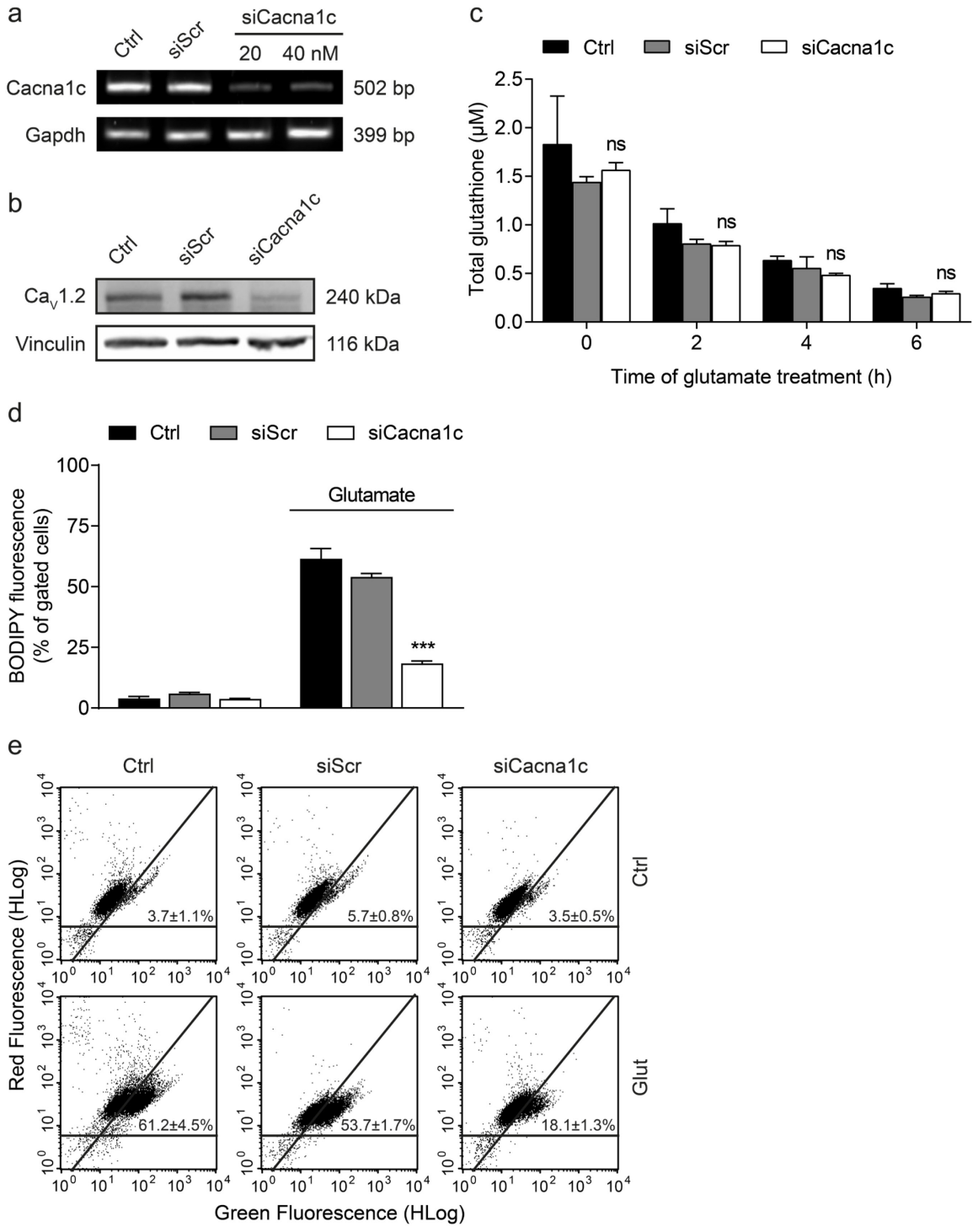
a
Ctrl
siScr
siCacna1c
20 40 nM
Cacna1c
502 bp
Gapdh
399 bp
b
Ctrl
siScr
siCacna1c
$Ca_V1.2$
240 kDa
Vinculin
116 kDa
c
Ctrl
siScr
siCacna1c
Total glutathione (µM)
ns
Time of glutamate treatment (h)
d
Ctrl
siScr
siCacna1c
BODIPY fluorescence (% of gated cells)
Glutamate
***
e
Ctrl
siScr
siCacna1c
Red Fluorescence (HLog)
3.7±1.1%
5.7±0.8%
3.5±0.5%
61.2±4.5%
53.7±1.7%
18.1±1.3%
Glut
Green Fluorescence (HLog)

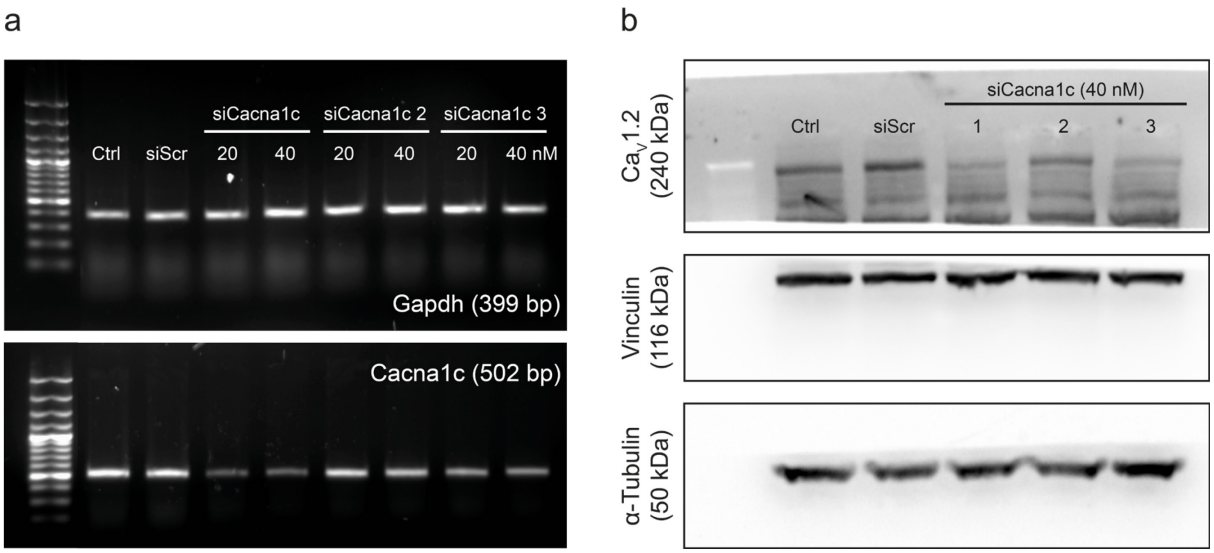

Figure 13. Effects of *Cacna1c* siRNA transfection on *Cacna1c* mRNA and protein levels
a *Cacna1c* mRNA levels from three different *Cacna1c* siRNAs were analyzed 24 h after siRNA transfection using *Gapdh* as internal control. **b** Protein samples were collected 48 h after transfection with 40 nM siRNA and the $Ca_V1.2$ expression levels were then identified by Western blot. Vinculin and Tubulin are used as loading control.

Then, the present work focused on specific parameters of mitochondria, since these organelles play a crucial role in the employed paradigm of oxidative stress (165). As displayed in Figure 14a, a pronounced increase in mitochondrial fragmentation was found in the control and siScr-transfected cells after glutamate treatment. In contrast, *Cacna1c* siRNA-transfected cells mostly maintained their tubular, elongated morphology despite the glutamate challenge. The mitochondrial morphology was quantified by means of a classification into three different categories (111). Briefly, cells containing healthy mitochondria with an elongated, tubule-like structure were defined as Category 1; while dying cells show strongly fragmented mitochondria accumulating around the nucleus and were classified as Category 3. Based on this classification system, the systematic quantification confirmed that *Cacna1c* gene silencing preserved mitochondrial morphology at Category 1 also after glutamate exposure (Figure 14b).

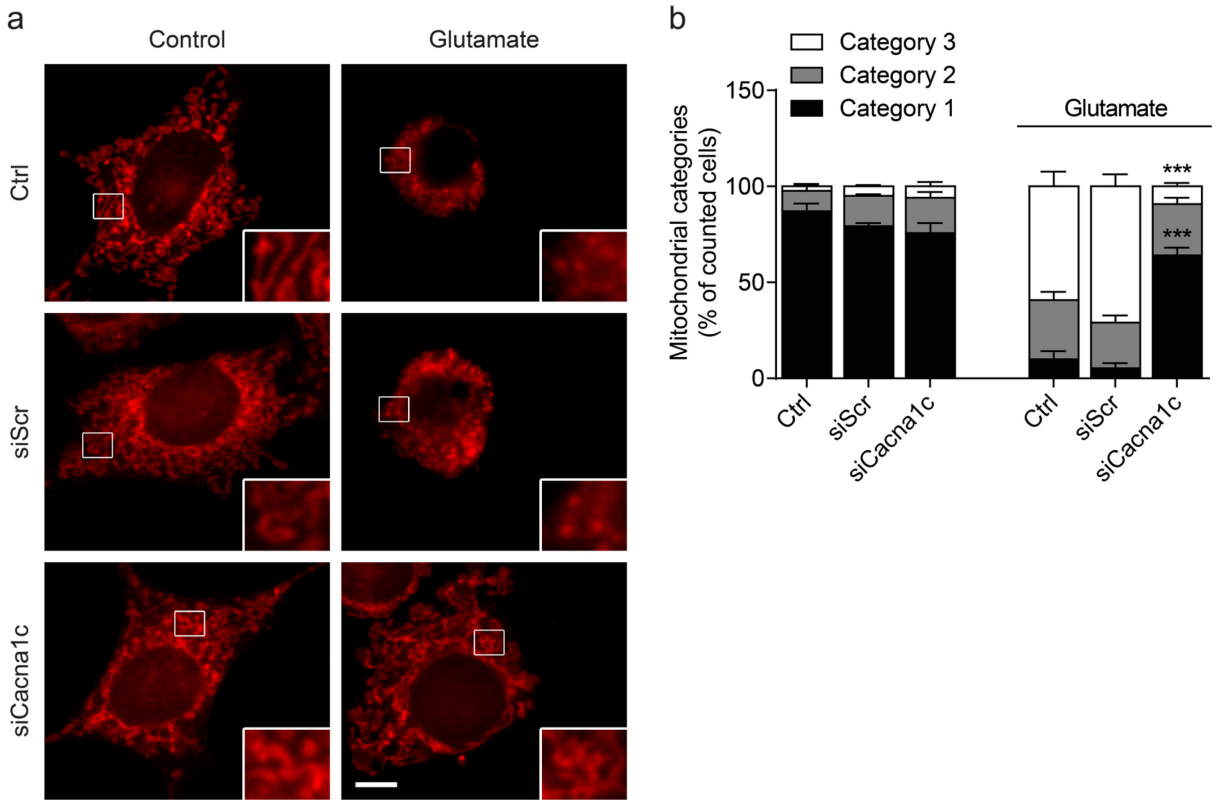

Figure 14. *Cacna1c* gene silencing preserved the morphology of healthy mitochondria in glutamate-challenged HT22 cells

a Changes in mitochondrial morphology were visualized after 15 h of glutamate exposure using MitoTracker Deep Red. Epifluorescence images of representative HT22 cells are shown with details enlarged by 300% at the bottom right. Scale bar, 10 µm. **b** Five hundred cells per condition were classified into three categories of mitochondrial fragmentation (Category 1: elongated; Category 2: intermediate; Category 3: fragmented) and quantified as percentage of counted cells (n = 3, mean + SD). ***p < 0.001 compared to glutamate-treated ctrl (ANOVA, Scheffé's-test).

To substantiate these results, the expression of mitochondrial fission and fusion proteins as well as mitochondrial biogenesis and mitophagy markers were additionally evaluated (Figure 15). While the total levels of mitofusin 2 (Mfn2), a protein that regulates the fusion of the outer mitochondrial membrane, were not significantly altered, changes in the expression of the mitochondrial fission proteins Drp1 and Fis1 were observed. During mitochondrial fission, cytosolic dynamin-related protein 1 (Drp1) is recruited to the mitochondrial outer membrane where it interacts with mitochondrial fission protein 1 (Fis1) leading to constriction and fragmentation of the organelles. Upon glutamate challenge, the levels of both Drp1 and Fis1 were increased in the control conditions, whereas in the siCacna1c-transfected cells their levels remained unchanged. In addition to the rather moderate differences in the actual levels of the related fission and fusion proteins, it is likely that mitochondrial fragmentation is also regulated by modifications in their activity.

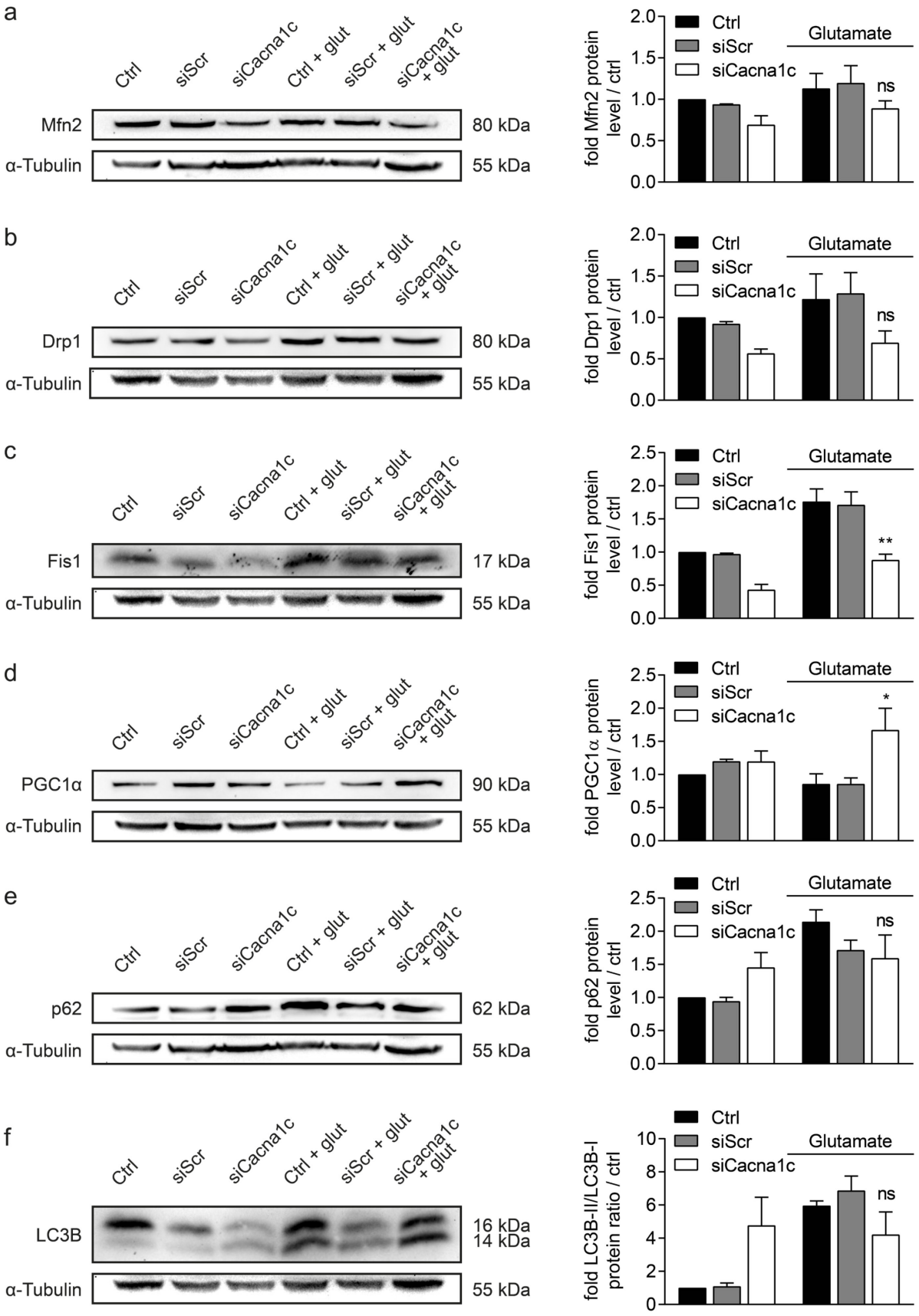
a
Ctrl
siScr
siCacna1c
Ctrl + glut
siScr + glut
siCacna1c + glut
Mfn2
80 kDa
α-Tubulin
55 kDa
fold Mfn2 protein level / ctrl
Ctrl
siScr
siCacna1c
Glutamate
ns
b
Drp1
80 kDa
α-Tubulin
55 kDa
fold Drp1 protein level / ctrl
ns
c
Fis1
17 kDa
α-Tubulin
55 kDa
fold Fis1 protein level / ctrl
**
d
PGC1α
90 kDa
α-Tubulin
55 kDa
fold PGC1α protein level / ctrl
*
e
p62
62 kDa
α-Tubulin
55 kDa
fold p62 protein level / ctrl
ns
f
LC3B
16 kDa
14 kDa
α-Tubulin
55 kDa
fold LC3B-II/LC3B-I protein ratio / ctrl
ns

Figure 15. *Cacna1c* gene silencing led to diminished mitochondrial fission and increased mitochondrial biogenesis following glutamate challenge

After 16 h of glutamate treatment, the expression levels of the mitochondrial fusion protein Mfn2 (**a**), the fission proteins Drp1 and Fis1 (**b,c**), the mitochondrial biogenesis marker PGC1α (**d**) and the mitophagy indicators p62 and LC3B-II (**e,f**) were identified by Western blot. One representative immunoblot per protein is shown (left panel). The bar graphs (right panel) were obtained by densitometric quantification of the Western blot data and normalization to α-Tubulin. Data is presented as mean + SEM (n = 3-4). Ctrl, control; siScr, scrambled siRNA; siCacna1c, *Cacna1c* siRNA; Glut, glutamate. $^{**}p < 0.01$; $^{*}p < 0.05$; ns (not significant) compared to glutamate-treated ctrl (ANOVA, Scheffé's-test).

The peroxisome proliferator-activated receptor gamma coactivator 1 alpha (PGC1α) is a transcription factor that regulates genes involved in mitochondrial biogenesis. In glutamate-treated HT22 cells, *Cacna1c* knockdown led to elevated PGC1α levels, contrary to controls showing slightly decreased levels. Sequestosome 1 (p62) is involved in the recruitment of autophagosomal membranes to the mitochondria and interacts with the microtubule-associated protein light chain 3 isoform B (LC3B). During autophagy LC3B-I (16 kDa) is converted to LC3B-II (14 kDa) through lipidation. The expression of p62 and LC3B-II was increased after 16 h of glutamate treatment in *Cacna1c* siRNA-transfected and control cells alike. However, silencing of *Cacna1c* induced already a considerable increase in basal levels of both p62 and LC3B-II compared to controls. This finding is consistent with earlier studies stating that decreases in cytosolic Ca^{2+} can induce autophagy (166). The present results indicate that *Cacna1c* downregulation stimulates mitochondrial biogenesis under oxidative stress without affecting mitophagic processes, thereby promoting the turnover of mitochondria and preventing the accumulation of dysfunctional mitochondria in HT22 cells.

At the functional level, the concentration of cellular ATP was determined next, which provides the energetic basis for neuronal plasticity, viability, and function. In line with the previous findings on mitochondrial morphology, the downregulation of *Cacna1c* blocked the loss of ATP levels in response to glutamate (Figure 16a). To further confirm the protective effects of *Cacna1c* knockdown in this model of oxytosis, the OCR was analyzed as a measure of mitochondrial respiration. As illustrated by the OCR graphs shown in Figure 16b, the basal respiration, represented by the OCR before injection of oligomycin (Oligo), was considerably higher in *Cacna1c* siRNA-transfected cells compared to controls after glutamate treatment. In line with this observation, the maximal mitochondrial respiration, detected after FCCP injection, was also significantly higher in glutamate-exposed cells with *Cacna1c* depletion versus controls. Here, the mitochondrial uncoupler FCCP mimics an increased energy demand as, for example, present in times of stress and, thereby, allows for the evaluation of the respiratory reserve. The present findings imply that mitochondrial dysfunction attributed to oxidative glutamate toxicity leads to decreased stress adaptation, which is prevented by a knockdown of *Cacna1c*.

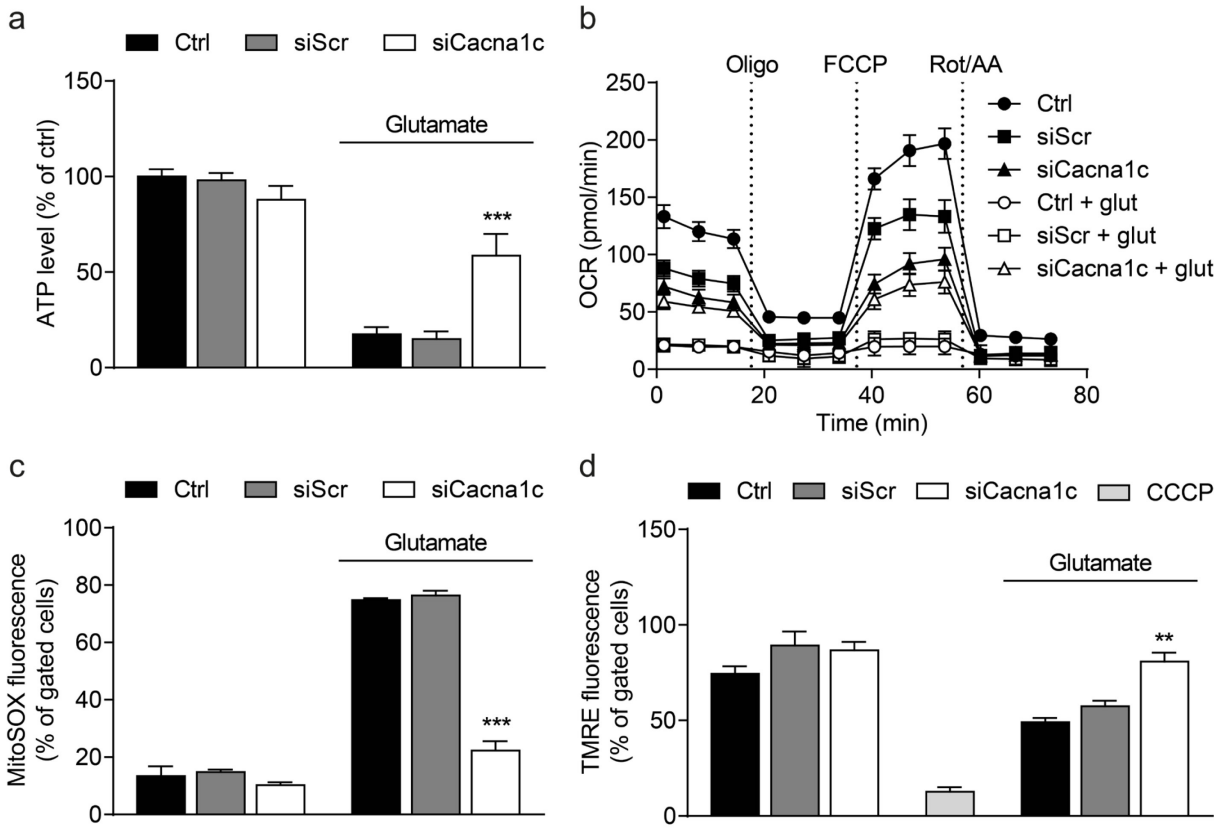

Figure 16. Downregulation of *Cacna1c* gene expression mediated protection of mitochondrial function against glutamate-induced oxidative stress

a A luciferase-based assay was used to determine ATP levels in glutamate-exposed (8 mM) HT22 cells. Values from eight replicate wells per condition are displayed as mean + SD. The luminescence under control conditions is set as 100%. **b** After 16 h of glutamate challenge, the oxygen consumption rate (OCR) was analyzed with a Seahorse XF^{e}96 Analyzer. Data of 3-7 replicate wells per condition are given as mean ± SD. Oligo, oligomycin; FCCP, carbonyl cyanide 4-(trifluoromethoxy)phenylhydrazone; Rot, rotenone; AA, antimycin A. **c** Mitochondrial superoxide formation was investigated by flow cytometry using the fluorescent dye MitoSOX. HT22 cells were treated with 9 mM glutamate for 18 h. **d** Flow cytometric analysis of the mitochondrial membrane potential was realized via TMRE staining after 18 h of glutamate treatment. CCCP (carbonyl cyanide 3-chlorophenylhydrazone, 50 µM) is a mitochondrial membrane depolarizer and serves as positive control. **c,d** Each bar chart depicts one representative experiment with three replicates per sample (mean + SD; 10,000 cells per replicate). ***p < 0.001; **p < 0.01 compared to glutamate-treated ctrl (ANOVA, Scheffé's-test).

Besides the effects of *Cacna1c* downregulation after glutamate challenge, differences in the OCR between untreated conditions and *Cacna1c* siRNA-transfected cells can be observed, which may be functionally relevant. Compared to untreated controls, silencing of *Cacna1c* led to a lower basal and maximal OCR without a compensatory increase in glycolysis, as measured by the ECAR (Figure 17a). Thus, consistent with the slightly decreased basal ATP levels, depletion of *Cacna1c* resulted in a reduced metabolic potential suggesting in particular a constitutively inhibited respiratory chain (Figure 16a and Figure 17b). Reportedly, the activity of the electron transport complex IV is disinhibited by increases in cytosolic calcium concentration ($[Ca^{2+}]_i$) and is thereby presumably dependent on *Cacna1c* function.

Consequently, *Cacna1c* knockdown may act as a form of preconditioning that prevents glutamate toxicity via complex IV inhibition and concurrent decrease in mitochondrial ROS production (167).

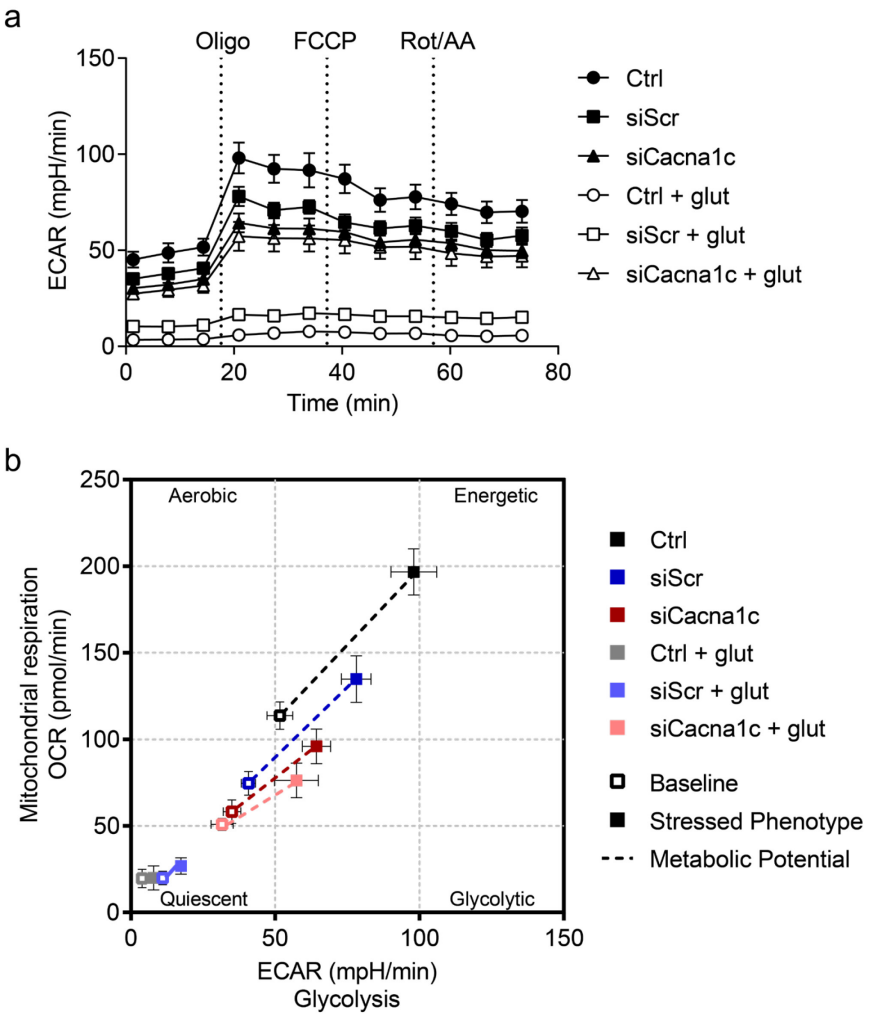

Figure 17. Extracellular acidification rate and cell energy phenotype

a After 16 h of glutamate challenge, the extracellular acidification rate (ECAR) was determined with a Seahorse XF^{e}96 Analyzer. Data of 3-7 replicate wells per condition are given as mean ± SD. Oligo, oligomycin; FCCP, carbonyl cyanide 4-(trifluoromethoxy)phenylhydrazone; Rot, rotenone; AA, antimycin A. **b** In the cell energy phenotype graph the OCR is plotted against the ECAR. The baseline phenotype (open square) represents the OCR and ECAR of HT22 cells at starting assay conditions. The stressed phenotype (filled square) displays the OCR and ECAR under an induced energy demand, i.e. in the presence of the two stressors oligomycin and FCCP. The resulting metabolic potential (dashed line) reflects the ability to meet an induced energy demand.

As described previously, the mitochondrial ETC is the major source of ROS in this paradigm of glutamate-induced stress. Therefore, mitochondrial superoxide levels were detected by MitoSOX Red staining (117). Figure 16c demonstrates that mitochondrial ROS formation was

significantly elevated in glutamate-challenged HT22 cells, but not in the *Cacna1c* siRNA-transfected cells.

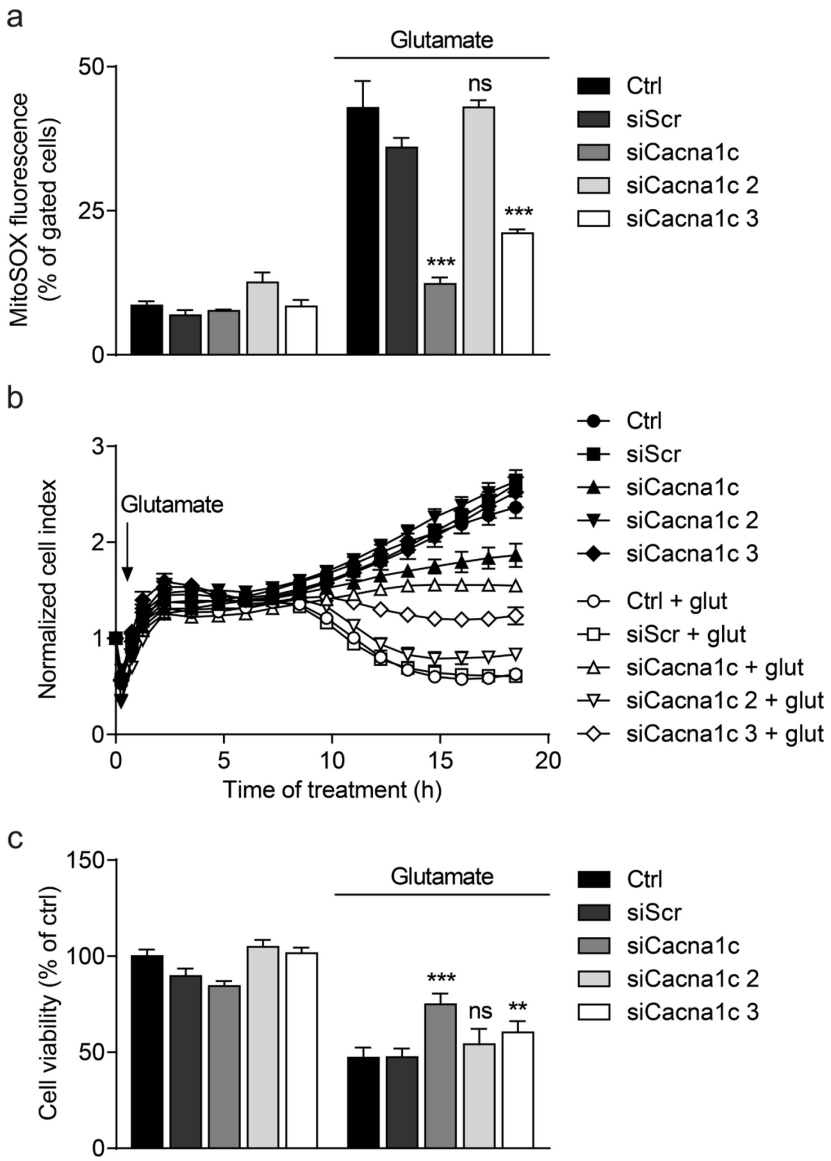

Figure 18. Only a pronounced knockdown of *Cacna1c* mediated protective effects against glutamate toxicity in HT22 cells

a Mitochondrial superoxide formation was assessed by flow cytometry using 1.25 µM MitoSOX. The bar graph shows one representative experiment with three replicates per sample (mean + SD; 10,000 cells per replicate). **b** xCELLigence measurements were conducted after the treatment with 10 mM glutamate. Three to six replicate wells per condition are displayed as mean ± SD. **c** Cell viability was evaluated in glutamate-challenged HT22 cells by measuring MTT formazan absorbance (9 mM, 17 h). Eight replicate wells per condition are displayed as mean + SD. The absorbance under control conditions is set as 100%. ***$p < 0.001$; **$p < 0.01$; ns (not significant) compared to glutamate-treated ctrl (ANOVA, Scheffé's-test).

This protective effect was confirmed by another siRNA sequence (siCacna1c 3; comparable 62% reduction of Cav1.2 protein levels versus control), whereas a further siRNA (siCacna1c 2; only 21% reduction of Cav1.2 protein levels compared to controls) did not provide sufficient knockdown to affect mitochondrial ROS levels in glutamate-treated cells (Figure 18a). These results suggest that the functional effects of *Cacna1c* siRNA transfection strongly correlate with the extent of reduction in mRNA and protein levels (Figure 13). Another common feature of apoptotic and metabolically stressed cells is the collapse of the mitochondrial membrane potential ($\Delta\Psi_m$) (119). According to Figure 16d, the breakdown of $\Delta\Psi_m$ in response to glutamate is indicated by a loss in TMRE fluorescence and this was visibly attenuated in *Cacna1c*-silenced cells.

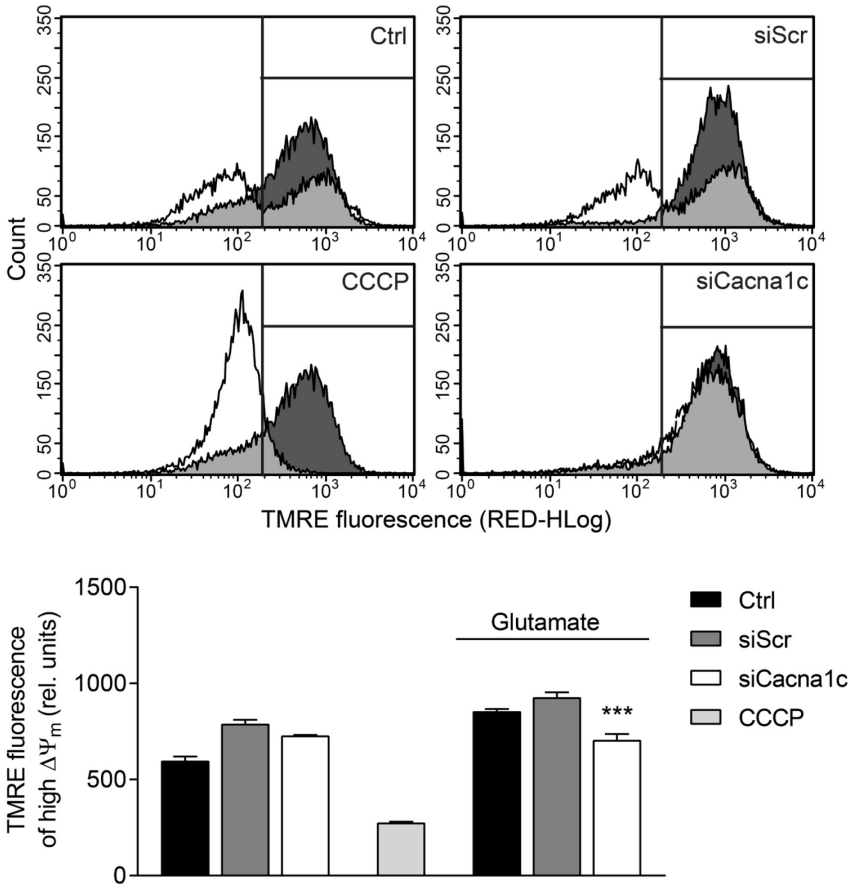

Figure 19. Assessment of $\Delta\Psi_m$ hyperpolarization after glutamate treatment

The mitochondrial membrane potential was analyzed by flow cytometry using the voltage-sensitive fluorescent dye TMRE. In the histograms, the dark grey graphs represent the untreated conditions, the white graphs the glutamate-treated samples, and the light grey areas the overlay of both graphs. CCCP (carbonyl cyanide 3-chlorophenylhydrazone; 50 µM) is a mitochondrial membrane depolarizer and serves as positive control. Mitochondrial membrane depolarization leads to a left shift in TMRE fluorescence, whereas $\Delta\Psi_m$ hyperpolarization results in a right shift. The bar graph shows one representative experiment with three replicates per sample (mean + SD). ***$p < 0.001$ compared to glutamate-treated ctrl (ANOVA, Scheffé's-test).

Furthermore, *Cacna1c* siRNA-transfected HT22 cells exhibited significantly less $\Delta\Psi_m$ hyperpolarization in the surviving cell population after glutamate damage (Figure 19). A lower $\Delta\Psi_m$ results from a decreased $[Ca^{2+}]_i$ and is accompanied by less mitochondrial superoxide formation (Figure 16c) (168). These results further substantiate the findings from the OCR measurements and assist in elucidating the protective mechanisms of *Cacna1c* downregulation.

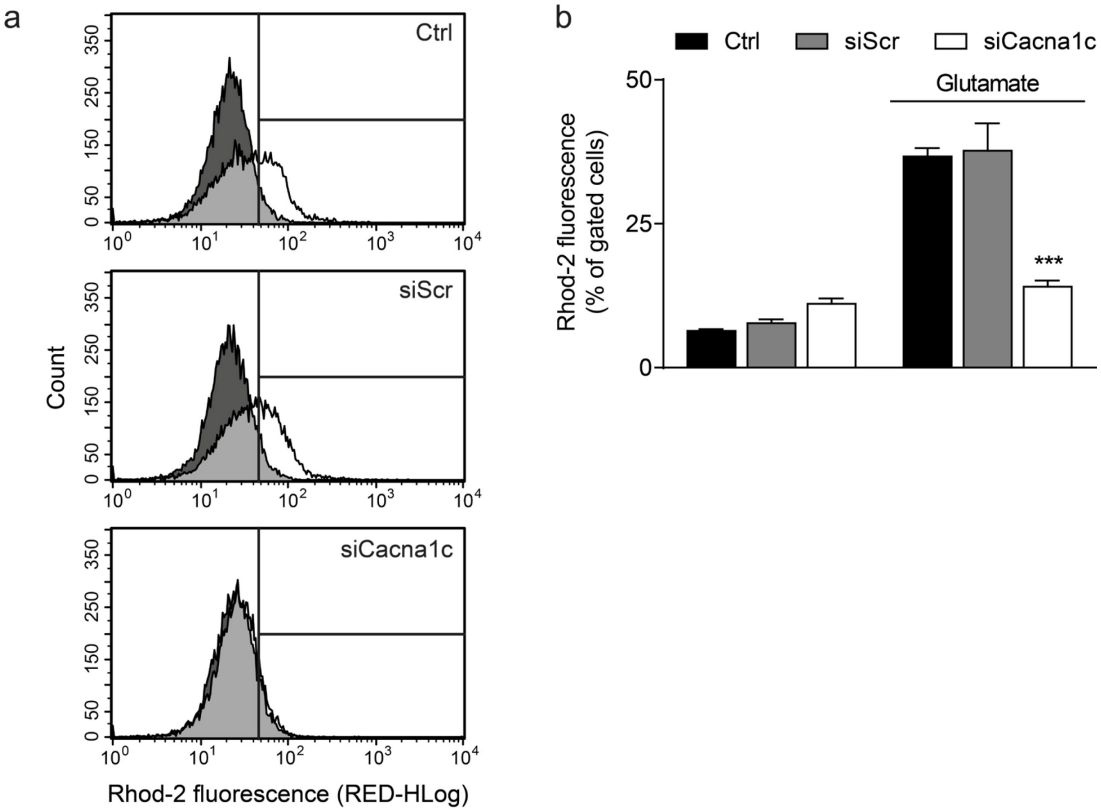

Figure 20. Depletion of *Cacna1c* attenuated the glutamate-induced rise in mitochondrial calcium concentration

a The mitochondria-specific dye dihydrorhod-2 AM was used for the flow cytometric calcium measurements. The dark grey graphs represent the untreated controls, the white graphs the glutamate-treated samples, and the light grey areas the overlay of both graphs. **b** Here, the right shift in Rhod-2 fluorescence in response to 11 mM glutamate was quantified. The bar graph shows one representative experiment with three replicates per sample (mean + SD; 10,000 cells per replicate). ***$p < 0.001$ compared to glutamate-treated ctrl (ANOVA, Scheffé's-test).

Importantly, the detrimental mitochondrial Ca^{2+} overload constitutes a central event during programmed cell death and is tightly coupled to excessive mitochondrial ROS production (124). Here, mitochondrial calcium concentrations were assessed using the fluorescent dye rhodamine-2. The fluorescence intensity of rhodamine-2 increases upon binding calcium and the quantification of gated cells displays that the glutamate-induced rise in mitochondrial

calcium was fully blocked in *Cacna1c* siRNA-transfected cells compared to the controls (Figure 20a,b). This effect of *Cacna1c* siRNA could be attributed to lower levels of Cav1.2 in the cell membrane, which may contribute to a reduced influx of exogenous Ca^{2+}, thereby positively influencing the deregulated calcium homeostasis in this model of oxidative stress (169).

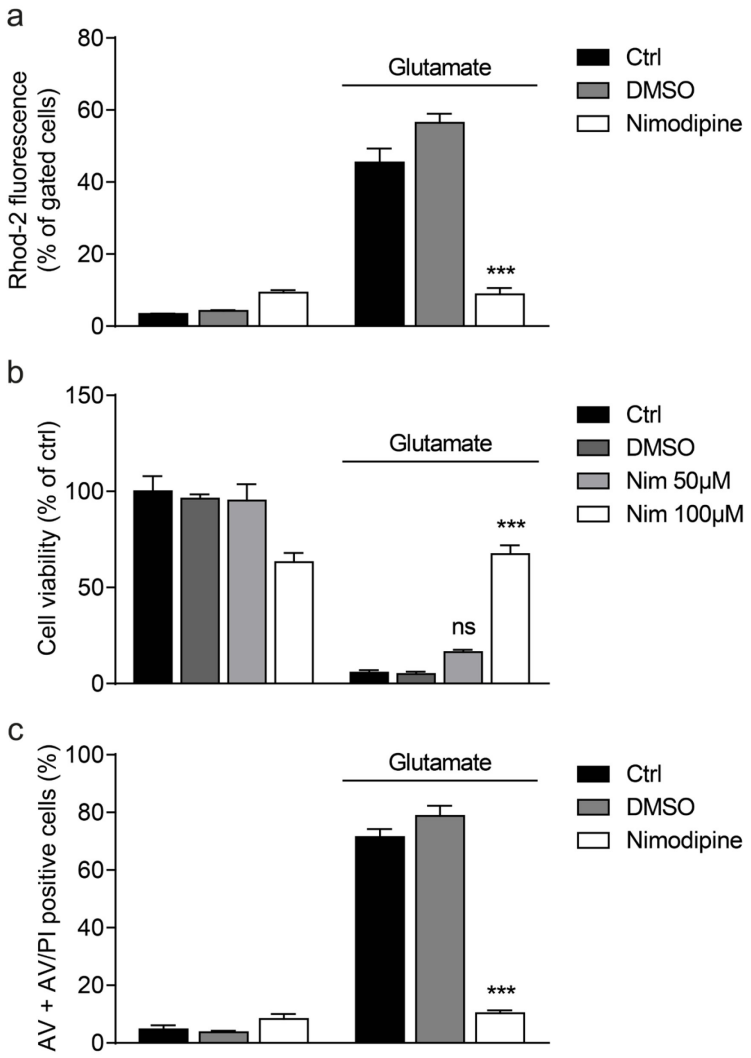

Figure 21. The L-type calcium channel blocker nimodipine ameliorated mitochondrial function and cell survival under glutamate treatment

a Mitochondrial calcium levels were investigated by flow cytometry using Rhod-2. HT22 cells were co-treated with 100 µM nimodipine and 6 mM glutamate for 16 h. The bar graph depicts one representative experiment with three replicates per sample (mean + SD; 10,000 cells per replicate). **b** Cell viability was assessed after 16 h of glutamate and nimodipine exposure by a colorimetric MTT assay. Six replicate wells per condition are displayed as mean + SD. The absorbance under control conditions is set as 100%. **c** The bar graph shows the percentage of annexin V and AV/PI positive cells after 16 h of glutamate (7 mM) and nimodipine (100 µM) co-treatment. One representative experiment with three replicates per sample is depicted (mean + SD; 10,000 cells per replicate). DMSO concentration in all experiments was 0.1%. Nim, nimodipine; AV, annexin V; PI, propidium iodide. ***$p < 0.001$; ns (not significant) compared to glutamate-treated ctrl (ANOVA, Scheffé's-test).

This conclusion was further supported by the effects of the DHP calcium channel blocker nimodipine, which protected HT22 cells against glutamate-induced mitochondrial calcium overload at a concentration of 100 μM similar to the effects achieved by *Cacna1c* knockdown (Figure 21a).

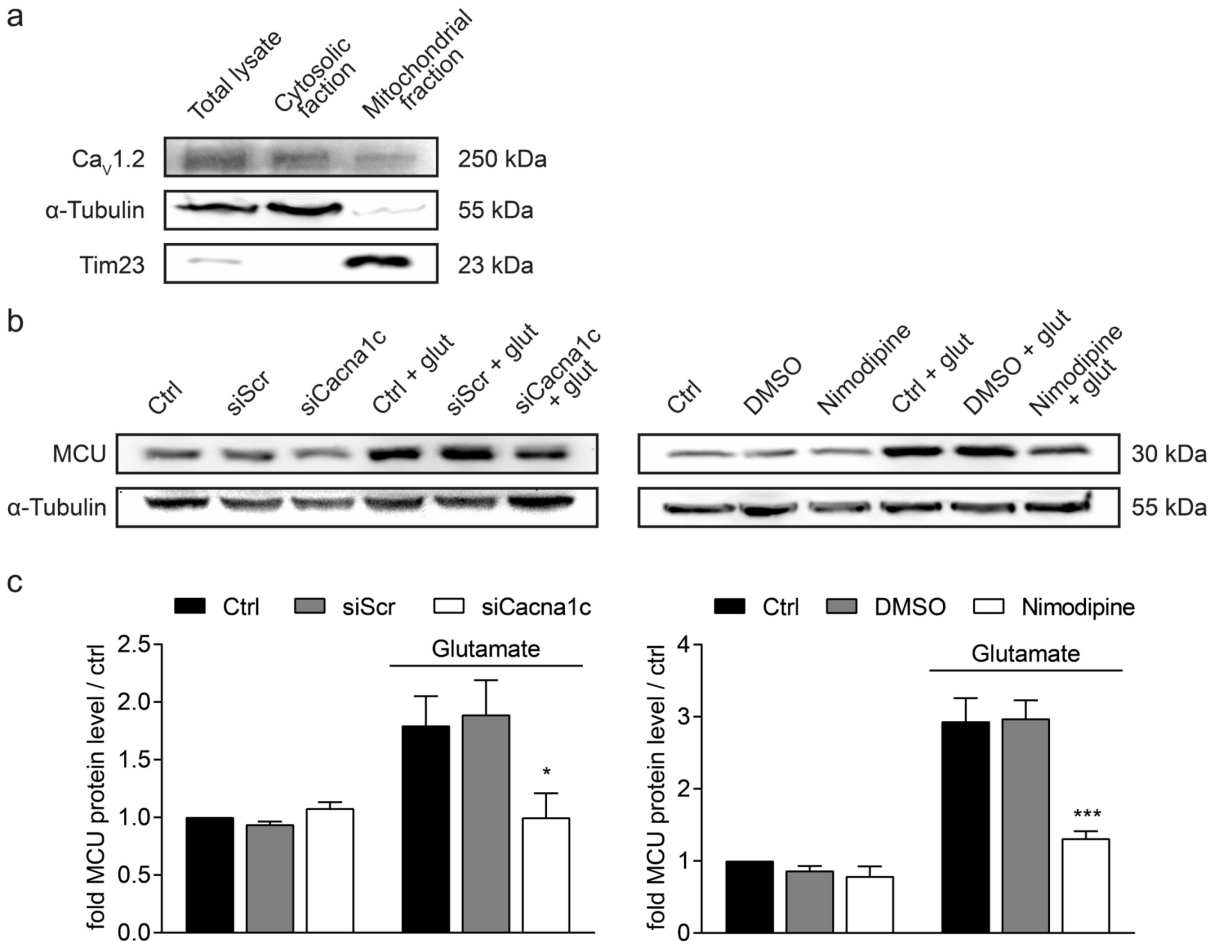

Figure 22. Ca$_V$1.2 localization and MCU expression levels

a Ca$_V$1.2 protein expression levels in the total lysate, the cytosolic and the mitochondrial fraction of HT22 cells were identified by Western blot. α-Tubulin was used as cytosolic marker protein. The inner mitochondrial membrane protein Tim23 served as indicator for mitochondrial enrichment. **b** The MCU expression levels in both *Cacna1c* siRNA-transfected and nimodipine-treated HT22 cells after 16 h of glutamate exposure were assessed by Western blot. One representative immunoblot per treatment condition is shown. **c** The relative MCU protein abundance was densitometrically quantified and α-Tubulin-normalized. Data is presented as mean + SEM (n = 4-5). Ctrl, control; siScr, scrambled siRNA; siCacna1c, *Cacna1c* siRNA; Glut, glutamate. ***p < 0.001; *p < 0.05 compared to glutamate- treated ctrl (ANOVA, Scheffé's-test).

To further investigate the mechanisms linking *Cacna1c* downregulation to mitochondrial calcium load, the cellular localization of Ca$_V$1.2 in HT22 cells was assessed next (Figure 22a). Consistent with existing evidence describing a plasma membrane localization of voltage-gated

calcium channels, the present study confirmed that Cav1.2 was mostly present in the total lysate and to a lesser extent in the cytosolic fraction. As expected, Cav1.2 was not appreciably expressed in the mitochondrial fraction rather excluding a direct effect of *Cacna1c* gene silencing on mitochondrial calcium concentration. Therefore, it was then evaluated if *Cacna1c* knockdown indirectly affects the expression of the mitochondrial calcium uniporter (MCU; Figure 22b,c). The MCU is an inner mitochondrial membrane transport protein and essential for the regulation of calcium uptake. Under control conditions, oxidative glutamate toxicity caused an increase in MCU levels after 16 h. This glutamate-induced rise in MCU expression was significantly abolished in both *Cacna1c* siRNA-transfected and nimodipine-treated cells, thereby correlating well with the findings from the Rhod-2 calcium measurements. Furthermore, these results are in line with a previous study showing that knockdown of MCU in mouse neurons reduces NMDA-induced increases in mitochondrial calcium resulting in resistance to excitotoxicity (170). Overall, these results demonstrate that both *Cacna1c* gene silencing and pharmacological inhibition of LTCCs provided a consistent protection of different mitochondrial parameters in paradigms of oxidative glutamate neurotoxicity.

Knockdown of *Cacna1c* mediated protection against glutamate-induced cell death

The positive effects of *Cacna1c* depletion in the applied model of oxidative stress were also reflected at the level of cell morphology and viability. Representative images of glutamate-treated controls showed characteristic features of dying cells, which were shrinking, rounding up, and detaching from the culture dish. In contrast, healthy and viable cells appeared elongated and well attached to the well bottom, as detected in the untreated control and glutamate-exposed siCacna1c conditions (Figure 23a).

Finally, cell proliferation and viability were investigated in real time via continuous electrical impedance readout and it was found that, compared to controls, *Cacna1c* siRNA-transfected cells showed a significantly lower proliferation rate under basal conditions (Figure 23b). As cell proliferation is tightly coupled to energy metabolism, this effect may be due to the before mentioned siCacna1c-mediated inhibition of the mitochondrial ETC (171). However, *Cacna1c* silencing mediated persistent protection of HT22 cells from glutamate toxicity. On the contrary, in the glutamate-treated controls a fast decrease in the normalized cell index was observed after 12 to 15 h of glutamate administration indicating cell death. In line with this result from real time impedance measurements, the protective effect of the *Cacna1c* siRNA was also detected in the MTT reduction assay after 16 h of glutamate exposure (Figure 23c). Both findings were independently confirmed by an additional siRNA sequence (siCacna1c 3; Figure 18b,c). Accordingly, flow cytometric measurements using annexin V and propidium iodide (PI) provided concurrent results. The two dyes stain early apoptotic and late apoptotic/necrotic cells respectively (Figure 23d,e). The quantification presented in Figure 23d indicates a significantly enhanced resistance against glutamate-induced cell death in *Cacna1c* siRNA-

transfected cells. Supporting these results, nimodipine (100 μM) also protected the cells from glutamate toxicity as shown by the MTT assay and annexin V/PI staining (Figure 21b,c).

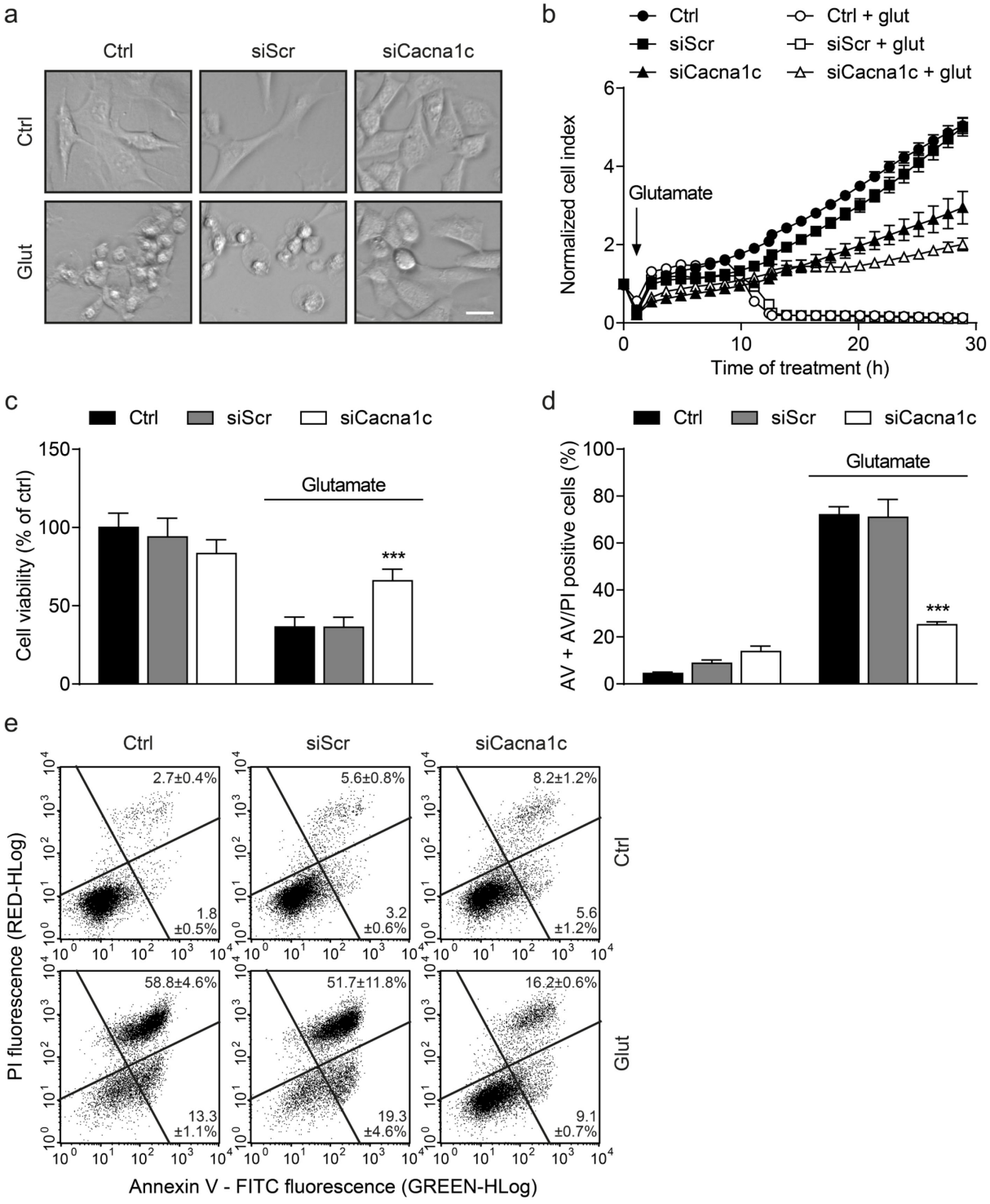

Figure 23. *Cacna1c* silencing protected HT22 cells from glutamate-induced cell death

a Representative phase-contrast images of glutamate-treated HT22 cells illustrate changes in cell morphology. Scale bar, 25 µm. **b** A representative real time cell impedance measurement over 30 h after the treatment with 8 mM glutamate is shown. Eight replicate wells per condition are displayed as mean ± SD. **c** Before cell viability was determined by MTT assay, HT22 cells were challenged with 8 mM glutamate for 16 h. Values from 8 wells per condition are presented as mean + SD. The absorbance under control conditions is set as 100%. **d** The bar graph shows the percentage of annexin V and AV/PI positive cells. One representative experiment with three replicates per sample is depicted (mean + SD; 10,000 cells per replicate). **e** In addition, the dot plots exemplify the subdivision into AV (lower right quarter) and AV/PI positive cells (upper right quarter). AV, annexin V; PI, propidium iodide. ***p < 0.001 compared to glutamate-treated ctrl (ANOVA, Scheffé's-test).

4.2 Effects of *Cacna1c* haploinsufficiency on excitotoxicity in PCNs

Following the promising effects of *Cacna1c* downregulation on glutamate-induced oxidative stress in neuronal HT22 cells, cell viability, mitochondrial bioenergetics, ATP and Ca^{2+} levels were next investigated in a model of glutamate-mediated excitotoxicity using heterozygous *Cacna1c* primary cortical neurons (PCN). First, potential acute impacts of *Cacna1c* haploinsufficiency on neuronal calcium influx directly after glutamate stimulation (25 µM) were assessed by ratiometric Fura 2 calcium imaging. As evident from Figure 24, glutamate addition triggered an immediate increase in $[Ca^{2+}]_i$ irrespective of the neuronal genotype. However, no differences in the intracellular free calcium concentration, both basal and after glutamate injection, were observed between wildtype and heterozygous *Cacna1c* cultures. Even further depolarization with potassium chloride (KCl, 50 mM) led to a similar increase in the 340/380 nm ratio. These findings suggest that either $Ca_V1.2$ is not involved in the initial early Ca^{2+} influx after glutamate stimulation, or $Ca_V1.2$ function is compensated by another calcium channel such as $Ca_V1.3$, or wildtype and heterozygous *Cacna1c* neurons exhibit the same surface expression levels of $Ca_V1.2$.

Next, delayed long-term effects on mitochondrial bioenergetics and cell viability were evaluated 24 h after continuous glutamate exposure (25 µM). Glutamate-challenged wildtype and *Cacna1c* heterozygous neurons both showed a marked decrease in basal (before the first injection) and most notably maximal (after FCCP addition) mitochondrial respiration (OCR) as well as glycolysis (ECAR) compared with untreated controls (Figure 25a,b). This was also reflected in a reduced metabolic potential of the cortical neurons following sustained glutamate treatment (Figure 25c). The metabolic potential is a measure of the cells' ability to meet an induced energy demand via respiration and glycolysis. As illustrated by Figure 25c, untreated control cells clearly featured this energetic ability, whereas prolonged glutamate excitotoxicity resulted in a completely quiescent phenotype. However, the present bioenergetic measurements did not reveal any significant differences in OCR and ECAR between the glutamate-challenged wildtype $Cacna1c^{+/+}$ and heterozygous $Cacna1c^{+/-}$ rat neuronal cultures.

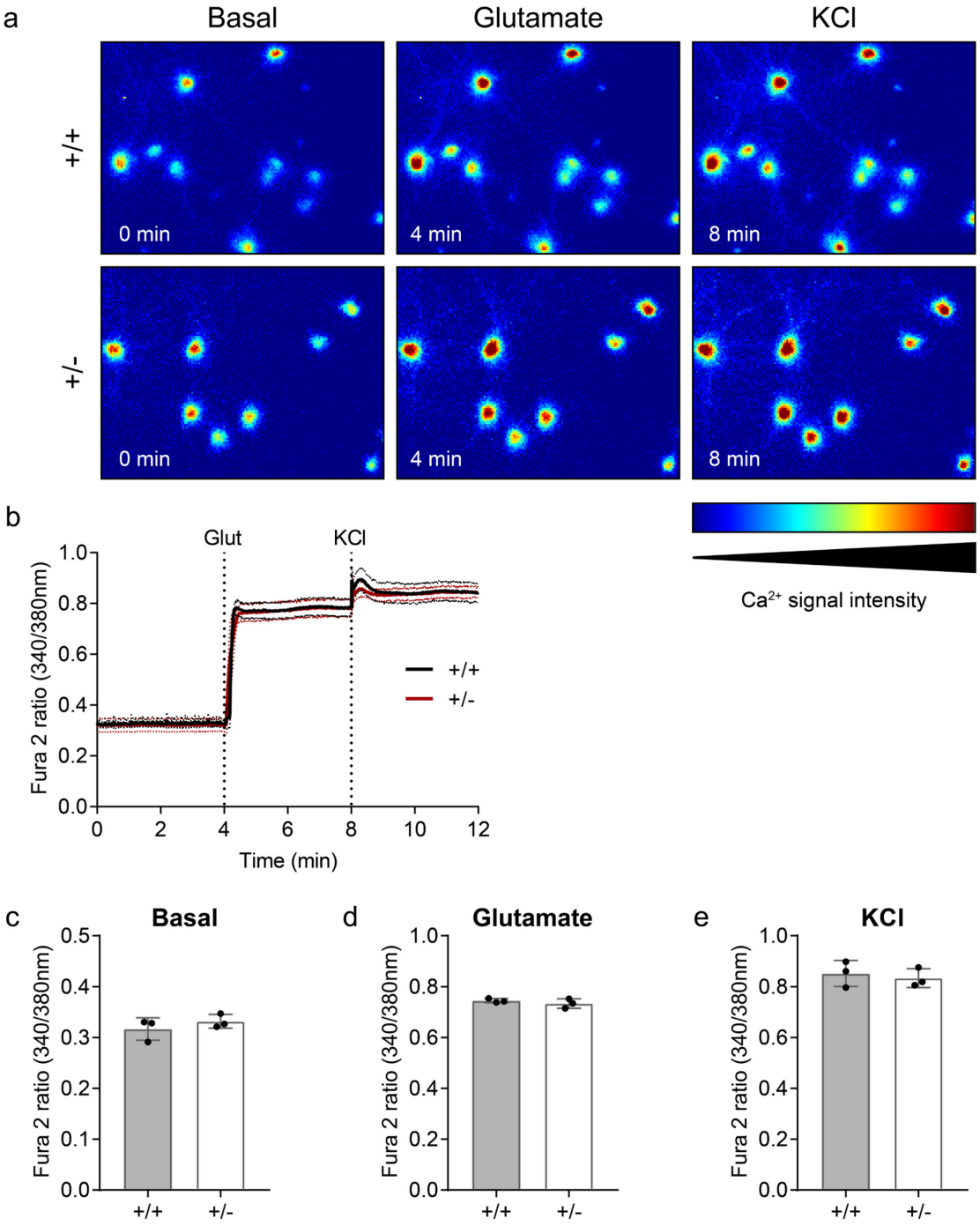

Figure 24. Acute effects of glutamate and depolarization on intracellular calcium concentration in primary neuronal cultures

Intracellular calcium concentrations were assessed using the ratiometric Fura 2 dye. **a** Exemplary images of the calcium signal intensity (Jet LUT) were acquired at 20x magnification, 340 nm excitation and different time points. **b** A representative measurement of the Fura 2 ratio (340/380 nm) in the soma of *Cacna1c*$^{+/+}$ and *Cacna1c*$^{+/-}$ cortical neurons is depicted as mean ± SD (dotted line). The bar graphs summarize the **c** mean basal, **d** mean glutamate-induced (25 µM) and **e** maximal KCl-evoked (50 mM) intracellular calcium levels. Pooled data of n = 3 littermate cultures per genotype, each with 6-10 cells per measurement are shown (ns; two-tailed unpaired t-test). +/+, wildtype *Cacna1c*$^{+/+}$; +/-, heterozygous *Cacna1c*$^{+/-}$; Glut, glutamate.

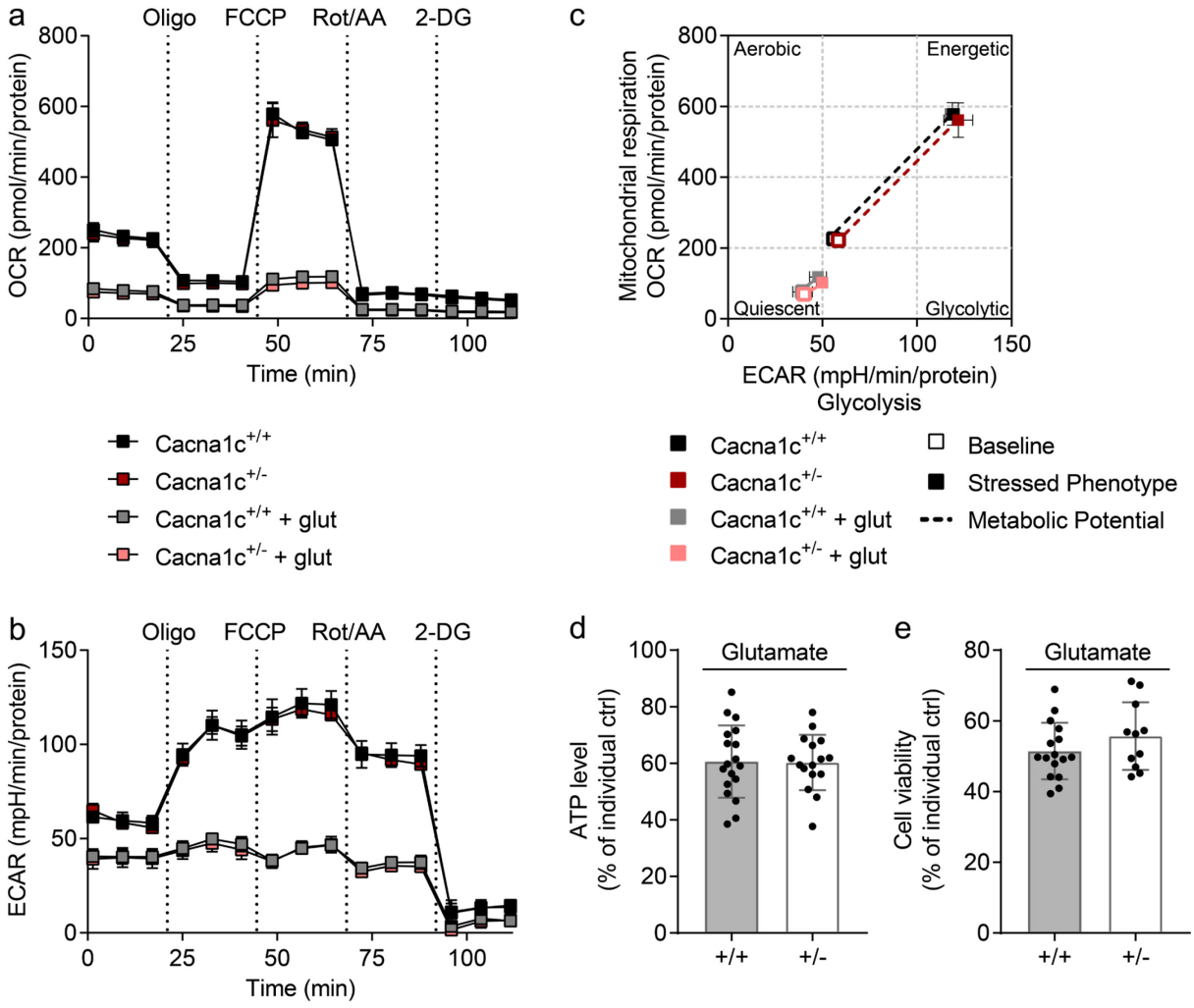

Figure 25. Assessment of mitochondrial bioenergetics, ATP levels and cell viability in *Cacna1c*$^{+/+}$ and *Cacna1c*$^{+/-}$ neuronal cultures following glutamate-induced excitotoxicity

A representative measurement of **a** the oxygen consumption rate (OCR) and **b** the extracellular acidification rate (ECAR) is shown including injections of the ATP synthase inhibitor oligomycin (Oligo), the uncoupling agent FCCP, the complex I inhibitor rotenone (Rot), the complex III inhibitor antimycin A (AA), and the glycolysis inhibitor 2-deoxy-D-glucose (2-DG). **c** To visualize the cells' energy phenotype, the OCR was plotted against the ECAR. The baseline phenotype (open square) represents the OCR and ECAR at starting assay conditions. The stressed phenotype (filled square) displays the OCR and ECAR in the presence of the two stressor compounds oligomycin and FCCP. The resulting metabolic potential (dashed line) reflects the cells' ability to meet an induced energy demand. Three to six replicate wells are presented as mean ± SD. **d** ATP levels were determined using a luminescence-based assay in a 96-well plate format (mean ± SD; +/+, n = 18; +/-, n = 16). **e** Cell viability was assessed by the colorimetric MTT assay (mean ± SD; +/+, n = 16; +/-, n = 11). **d,e** Each value is related to its individual untreated control, which is set as 100%. Differences between glutamate-treated *Cacna1c*$^{+/+}$ and *Cacna1c*$^{+/-}$ cortical neurons were not significant (ns; two-tailed unpaired t-test) **a-e** After 9 DIV, the PCN cultures were treated with 25 µM glutamate in EBSS and assayed 24 h later. +/+, wildtype *Cacna1c*$^{+/+}$; +/-, heterozygous *Cacna1c*$^{+/-}$; Glut, glutamate.

These findings were further confirmed by an unaltered, and thereby genotype-independent, reduction of ATP levels (mean +/+ 60.6%; +/- 60.3%) as well as cell viability (mean +/+ 51.5%; +/- 55.7%) in response to persistent glutamate stimulation for 24 h and compared to untreated

controls (100%; Figure 25d,e). Subsequently, *Cacna1c* expression was analyzed and verified the heterozygous knockout model by substantiating a ~40% reduction on mRNA and protein level in *Cacna1c*$^{+/-}$ versus wildtype neurons (Figure 26). Moreover, the results demonstrated comparably decreased *Cacna1c* mRNA as well as $Ca_V1.2$ protein levels upon 24 h glutamate exposure in both *Cacna1c* heterozygous and wildtype cells. With reductions by ~45% in mRNA and ~75% in protein expression compared to untreated wildtype controls, these were even more pronounced than the genotype effect, which may explain the identical mitochondrial bioenergetics and cell death rates of *Cacna1c*$^{+/+}$ and *Cacna1c*$^{+/-}$ neurons after glutamate treatment. Interestingly, *Cacna1c* downregulation was not accompanied by a compensatory increase in *Cacna1d* mRNA, which encodes the other LTCC in the brain $Ca_V1.3$ (Figure 26b). $Ca_V1.2$ degradation after activation of glutamate receptors might therefore constitute a negative feedback mechanism and an attempt to protect the cell from Ca^{2+} overload.

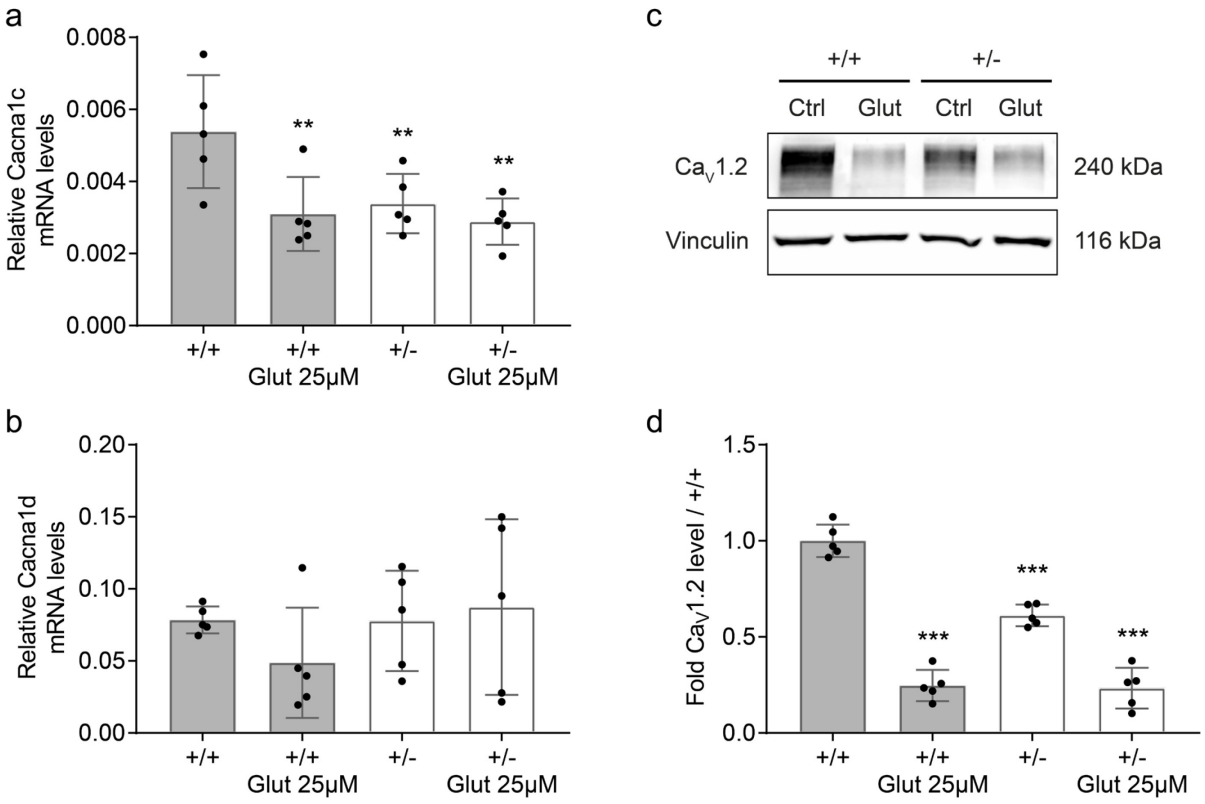

Figure 26. *Cacna1c*, *Cacna1d* mRNA and $Ca_V1.2$ protein levels of rat cortical neurons in response to glutamate excitotoxicity

Relative **a** *Cacna1c* and **b** *Cacna1d* mRNA levels normalized to the reference gene *U6* were determined by quantitative PCR (mean ± SD; n = 5). $Ca_V1.2$ protein expression levels were analyzed by Western blot. **c** One representative immunoblot is shown. **d** The bar graph was obtained by densitometric quantification of the Western blot data. The values were normalized to the loading control vinculin and presented as fold of *Cacna1c*$^{+/+}$ (mean ± SD; n = 5). After 9 DIV, the PCN cultures were treated with 25 µM glutamate in EBSS for 24 h followed by mRNA and protein isolation respectively. +/+, wildtype *Cacna1c*$^{+/+}$; +/-, heterozygous *Cacna1c*$^{+/-}$; Ctrl, untreated control; Glut, glutamate; ***p < 0.001; **p < 0.01 compared to untreated +/+ (ANOVA, Fisher's LSD-test).

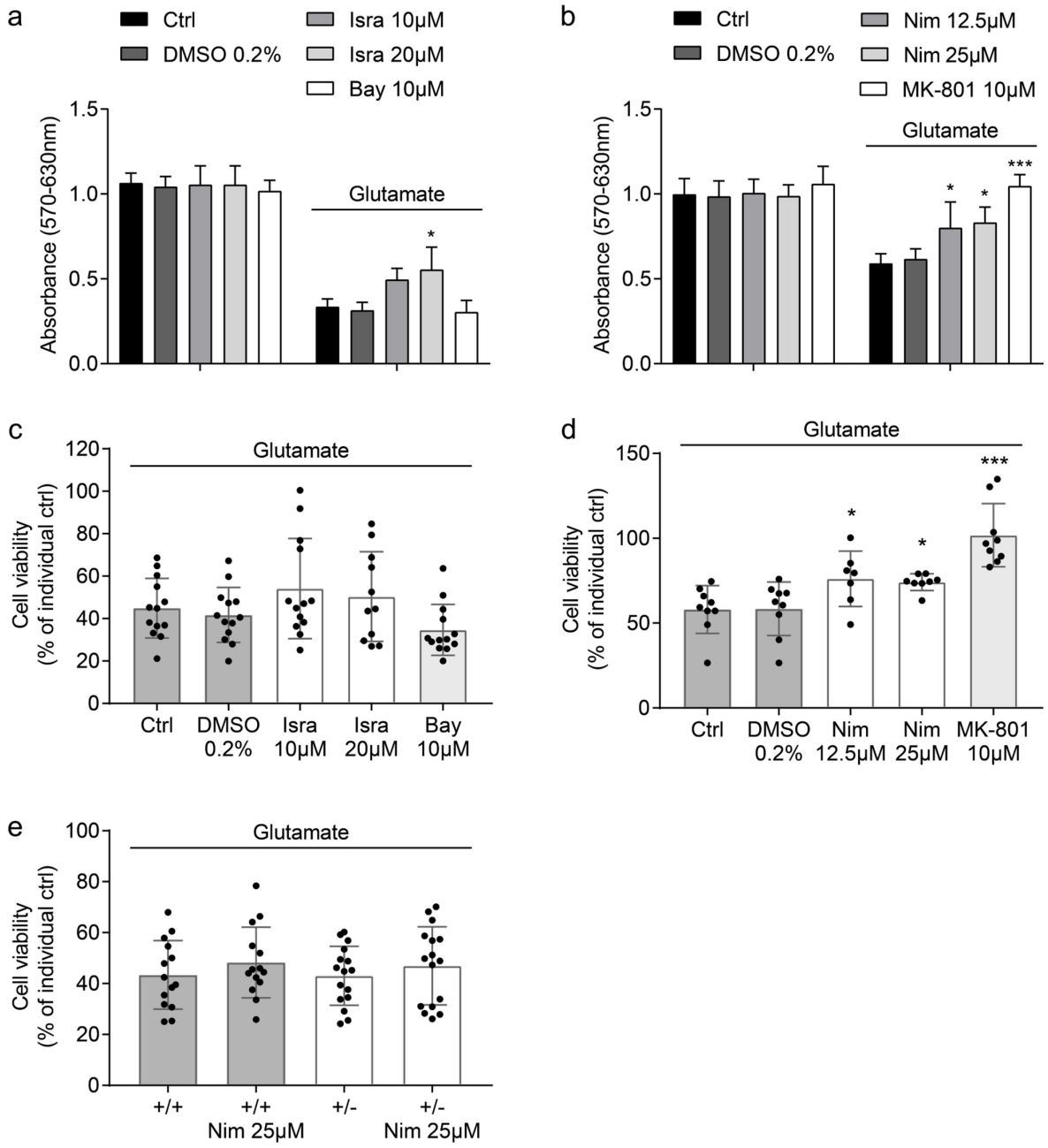

Figure 27. Effects of different L-type calcium channel modulators on excitotoxic cell death in PCN cultures

a,b Absolute absorbance values (570-630 nm) of two representative cell viability experiments resulting from the NADH-dependent reduction of MTT to a purple-colored formazan product are depicted. The bar graphs present 5-6 technical replicates as mean + SD. Statistical significance was tested by ANOVA and Scheffé's post-hoc test. The results of **c** n = 13 and **d** n = 9 MTT assays using wildtype cultures treated either with the LTCC activator Bay K8644 (10 µM), the DHP LTCC blockers isradipine (10, 20 µM) and nimodipine (12.5, 25 µM), or, as positive control, the NMDA receptor antagonist MK-801 are summarized. **e** The bar graph displays the combined effects of nimodipine treatment (25 µM) and *Cacna1c*$^{+/-}$ deficiency on cell viability in glutamate-exposed cortical rat neurons (mean ± SD; +/+, n = 14; +/-, n = 16). **c-e** Each value is related to its individual untreated control, which is set as 100% (mean ± SD; ANOVA, Fisher's LSD-test). The PCN cultures were co-treated with 25 µM glutamate and the respective modulating substance for 24 h in EBSS and assayed after 10 DIV. ***p < 0.001; *p < 0.05; ns (not significant) compared to glutamate-treated controls (Ctrl, DMSO 0.2%, +/+); Ctrl, wildtype control; Isra, isradipine; Nim, nimodipine; +/+, wildtype *Cacna1c*$^{+/+}$; +/-, heterozygous *Cacna1c*$^{+/-}$.

Besides studying the effects of *Cacna1c* haploinsufficiency in a model of glutamate excitotoxicity, the impact of different pharmacological LTCC modulators on cell viability was tested in wildtype rat cortical neurons treated with glutamate. Initially, as displayed in Figure 27a,b, the substance concentrations used showed no basal effect on neuronal metabolic activity. Co-treatment of 25 μM glutamate with the LTCC activator Bay K8644 for 24 h had a slightly negative effect on cell viability compared to glutamate-treated controls, whereas the DHP LTCC blockers isradipine and nimodipine led to a trend towards and to a significant protection from glutamate-induced cell death respectively (Figure 27a-d). These results are in contrast to the non-protective findings from the heterozygous *Cacna1c* neuronal cultures indicating a dose-dependent effect on $Ca_V1.2$ activity and function, which was also observed in the HT22 cells (Figure 13 and Figure 18). In this regard, the combination of *Cacna1c* haploinsufficiency and nimodipine treatment had no synergistic protective effect on cell viability in glutamate-exposed cortical rat neurons though (Figure 27e). By validating a full protection of the non-competitive NMDA receptor antagonist MK-801 (Figure 27b,d), the present measurements further confirmed that NMDA receptors are the primary triggers of exicitotoxic cell death, but, by identifying a moderate protective effect of nimodipine (~20%), they also strengthen the, at least, partial role of LTCCs in this process.

In summary, heterozygous *Cacna1c* knockout in primary cortical neurons had no impact on either initial increase in $[Ca^{2+}]_i$, or delayed perturbations in mitochondrial bioenergetics and cell viability after glutamate treatment. Furthermore, *Cacna1c* mRNA and protein expression levels were strongly regulated in this paradigm of glutamate-induced neuronal excitotoxicity. Finally, partial neuroprotection against long-term glutamate toxicity by pharmacological blockade of LTCCs may highlight a potential dose-effect-dependency and the involvement of LTCCs in the present cell death pathway.

4.3 Effects of *Cacna1c* haploinsufficiency on inflammation in microglia

Using primary rat microglia cultures, the potential impact of *Cacna1c* haploinsufficiency on cell morphology and bioenergetics as well as on secretion of inflammatory mediators was examined in a model of LPS-mediated neuroinflammation. First, as evident from Figure 28a, the expression of *Cacna1c* in rat microglial cells was validated by qPCR and, furthermore, a significant ~50% reduction at the level of mRNA was confirmed in heterozygous *Cacna1c* microglia compared to wildtype. *Cacna1d* mRNA levels, on the other hand, were unchanged highlighting the specificity of the *Cacna1c* knockout model (Figure 28b).

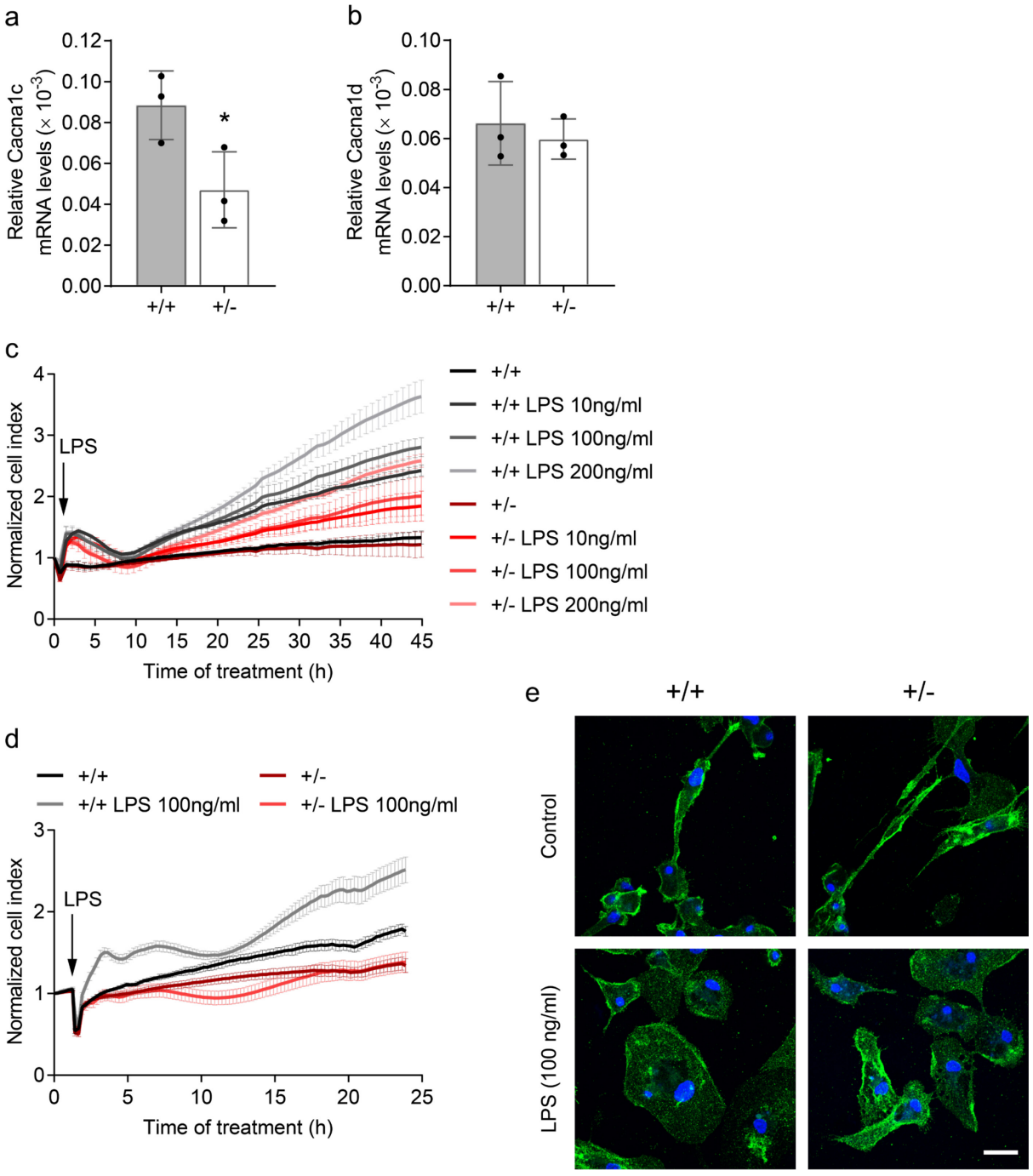

Figure 28. LPS-induced morphological alterations were diminished in *Cacna1c*$^{+/-}$ microglia

Relative **a** *Cacna1c* and **b** *Cacna1d* mRNA levels normalized to the reference gene *U6* were evaluated in heterozygous *Cacna1c*$^{+/-}$ and wildtype microglia by qPCR (mean ± SD; n = 3). *p < 0.05 (two-tailed unpaired t-test). **c,d** Morphological alterations after LPS treatment were monitored in real time via electrical impedance measurements (45/25 h). Two representative experiments using different LPS concentrations (10, 100, 200 ng/ml) are shown. Three to 10 replicate wells per condition are displayed as mean ± SD. **e** Confocal images of representative PFA-fixated microglial cells, which were immunostained for the microglia marker protein CD11b/c (Green, A488) and the nucleus (DAPI, blue), additionally illustrate the LPS-induced morphology changes. Scale bar, 25 µm. +/+, wildtype *Cacna1c*$^{+/+}$; +/-, heterozygous *Cacna1c*$^{+/-}$.

LPS-induced morphological alterations were diminished in *Cacna1c*$^{+/-}$ microglia

In vitro, primary microglial cells changed their morphology from spindle-shaped to ameboid-like structures in response to bacteria-derived LPS as illustrated by Figure 28e. These LPS-induced morphological alterations were monitored and quantified in real time via electrical impedance readout resulting in characteristic kinetic profiles of microglial activation (Figure 28c,d). In detail, LPS addition led to an initial increase in the normalized cell index, which correlates with morphological cell expansion, followed by a decline ~10 h after LPS stimulation. This decrease to basal cell indices was succeeded by a steady rise over time, whose extent was LPS concentration- and *Cacna1c* genotype-dependent. While cellular impedance increased with rising LPS concentrations (10, 100, 200 ng/ml), this trend was consistently less pronounced in *Cacna1c*$^{+/-}$ microglial cultures compared to wildtype (Figure 28c,d). *Cacna1c* haploinsufficiency had no effect on basal, unstimulated cellular impedance levels. Based on these findings, the majority of further experiments were conducted after a 24 h-treatment with 100 ng/ml LPS (Figure 28d,e); a concentration also relating to clinical conditions (172).

Cacna1c$^{+/-}$ as well as nimodipine-treated microglia displayed reduced bioenergetic capacities in response to LPS

LPS-mediated microglial activation also involved changes in cellular energy metabolism, which were next studied by assessing the OCR, a measure of mitochondrial respiration, and the ECAR, an indicator of glycolysis. After acute injection of LPS, the OCR remained stable over the measurement period of 7 h, whereas LPS provoked a rapid glycolytic burst shortly after its application (Figure 29a,b). This continuous increase in ECAR was significantly lower in LPS-treated *Cacna1c*$^{+/-}$ versus *Cacna1c*$^{+/+}$ microglia (Figure 29b). From Figure 29a it can be observed that basal respiration (before oligomycin addition) and mitochondrial reserve capacity (OCR increase in response to FCCP) were at the same level as untreated controls after LPS stimulation for 7 h. After a 24 h-treatment with LPS, however, the microglial cells showed a decrease in basal respiration and were unresponsive to the different mitochondrial stressors oligomycin, FCCP, rotenone, and antimycin A indicating an impaired mitochondrial function (Figure 29c). The observed inhibition of mitochondrial metabolism was accompanied by a compensatory increase in glycolysis ensuring the rapid and sufficient generation of ATP to meet the energy demands of LPS-induced microglial activation (Figure 29d). This glycolytic shift was less prominent in LPS-challenged heterozygous *Cacna1c* microglia compared to wildtype, which was also reflected in a reduced metabolic potential in response to an induced energy demand, i.e. in the presence of the two stressor compounds oligomycin and FCCP (Figure 29e). Furthermore, the present measurements confirm a two-stage activation process upon LPS stimulation (90). Initially, primary rat microglia were capable of utilizing both oxidative and glycolytic metabolism (Figure 29a,b), followed by a second phase in which microglial energy metabolism switched to almost exclusively rely on glycolysis for cell survival (Figure 29c-e).

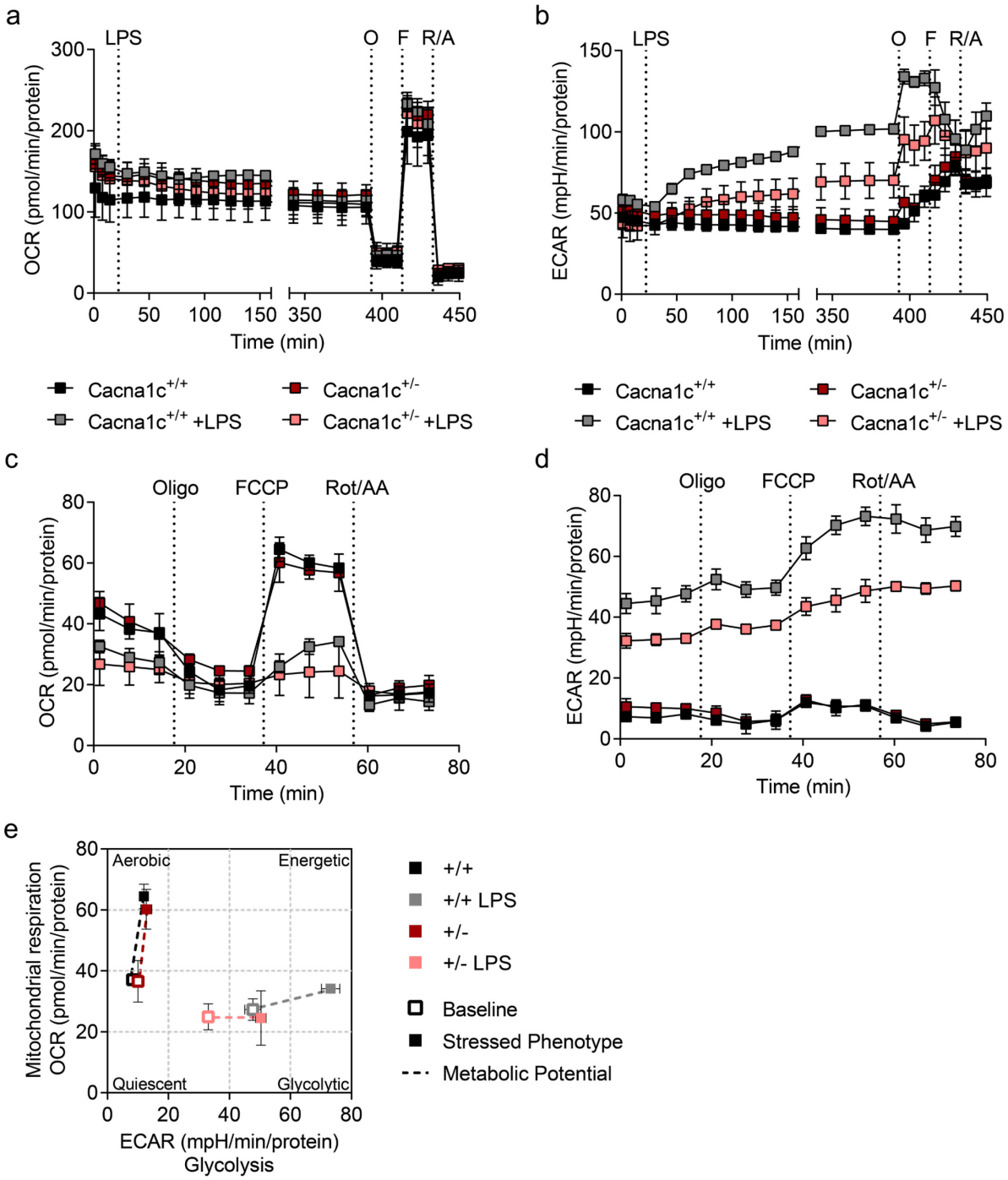

Figure 29. *Cacna1c*$^{+/-}$ microglia displayed reduced bioenergetic capacities in response to LPS

An exemplary measurement of **a** OCR and **b** ECAR following the acute injection of LPS (100 ng/ml) is presented. **c** OCR, **d** ECAR, and **e** the cells' energy phenotype were determined in heterozygous *Cacna1c* versus wildtype microglia 24 h after the treatment with 100 ng/ml LPS. The energy phenotype profile summarizes the relative utilization of the two energy pathways oxidative phosphorylation and glycolysis and was determined under baseline and stressed conditions. The baseline phenotype (open square) represents the OCR and ECAR at starting assay conditions. The stressed phenotype (filled square) demonstrates the OCR and ECAR in the presence of oligomycin and FCCP. The increases in stressed over baseline rates reflect the cells' metabolic potential. **a-e** Three to 8 replicate wells per condition are given as mean ± SD. +/+, wildtype *Cacna1c*$^{+/+}$; +/-, heterozygous *Cacna1c*$^{+/-}$; O/Oligo, oligomycin; F, FCCP; R/Rot, rotenone; A/AA, antimycin A.

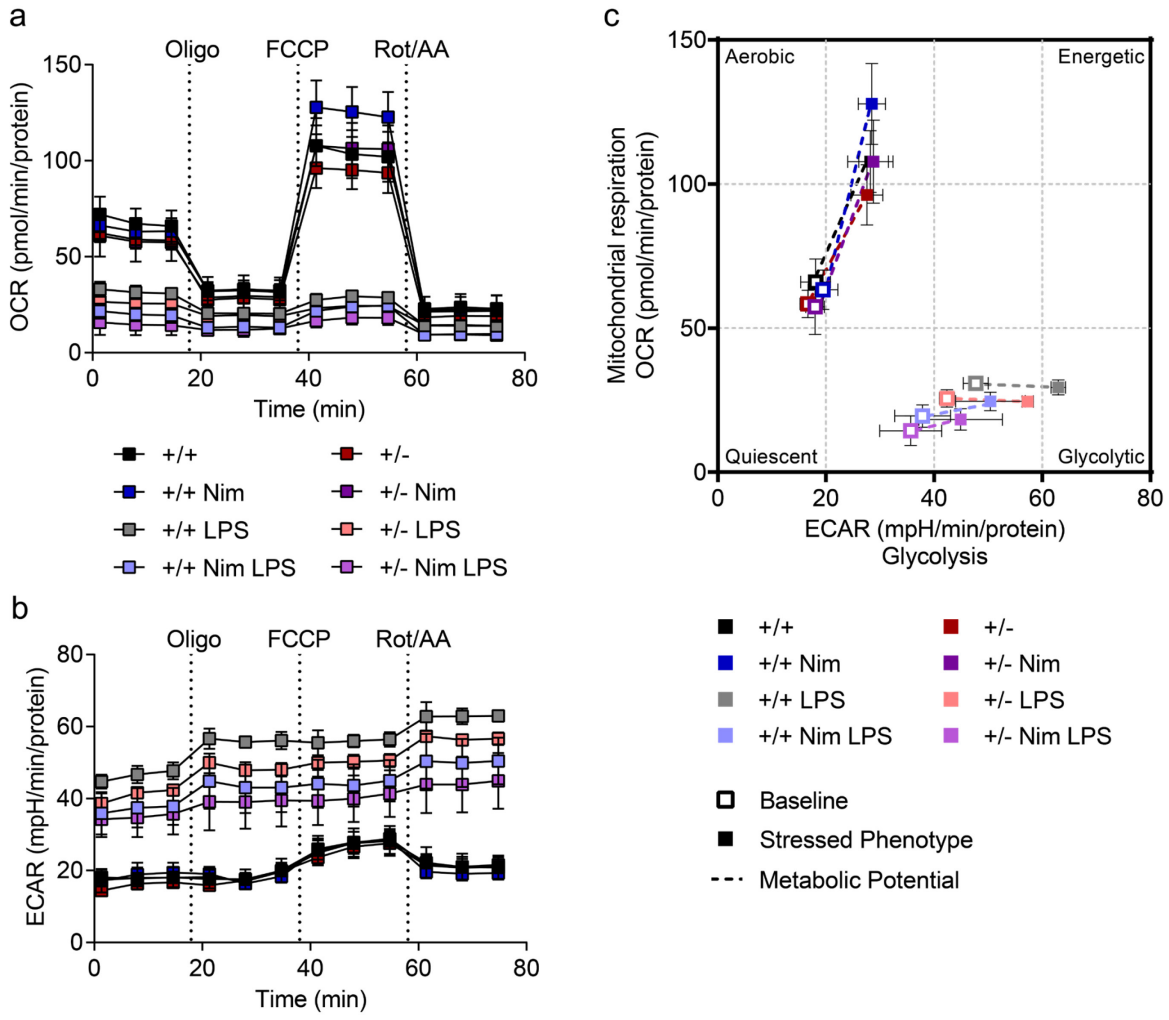

Figure 30. Combined effects of *Cacna1c* haploinsufficiency and pharmacological LTCC blockade on cellular bioenergetics in LPS-treated microglial cells

After a 24-h-treatment with 100 ng/ml LPS, **a** OCR, **b** ECAR, and **c** energy phenotype profile were assessed using a Seahorse XF^{e}96 Analyzer. The DHP LTCC blocker nimodipine (25 µM) was applied as co-treatment together with LPS. Data of 4-8 technical replicates are presented as mean ± SD. +/+, wildtype *Cacna1c*$^{+/+}$; +/-, heterozygous *Cacna1c*$^{+/-}$; Oligo, oligomycin; Rot, rotenone; AA, antimycin A; Nim, nimodipine.

Figure 31. *Cacna1c* haploinsufficiency was associated with reduced NO and cytokine release in LPS-stimulated primary microglia

a Relative *Nos2* mRNA levels normalized to the reference gene *U6* were examined by qPCR (mean ± SD; n = 3). **b** Inducible nitric oxide synthase (iNOS) protein expression levels were evaluated by Western blot. One exemplary Western blot as well as the densitometric quantification of 4 independent blots are depicted (mean ± SD). The values were normalized to the loading control vinculin and presented as fold of *Cacna1c*$^{+/+}$. **c** LPS-mediated NO production was assessed in the supernatant of microglial cells using a colorimetric assay based on the Griess reaction. Three to 7 technical replicates are shown as mean + SD (ANOVA, Scheffé's-test). **a-c** The primary microglia cultures were challenged with 200 ng/ml LPS for 24 h. Concentrations of the following pro- and anti-inflammatory cyto- and chemokines were quantified in the culture supernatant by a magnetic bead-based multiplex immunoassay: **d** IL-1α, **e** IL-1β, **f** IL-6, **g** TNF-α, **h** IL-10, **i** IL-18, **j** MCP-1, and **k** MIP-3α. **d-k** 100 ng/ml LPS for 24 h; n = 3-4; mean ± SD; ANOVA, Fisher's LSD-test. ***p < 0.001, not significant (ns) compared to LPS-treated *Cacna1c*$^{+/+}$; +/+, wildtype *Cacna1c*$^{+/+}$; +/-, heterozygous *Cacna1c*$^{+/-}$.

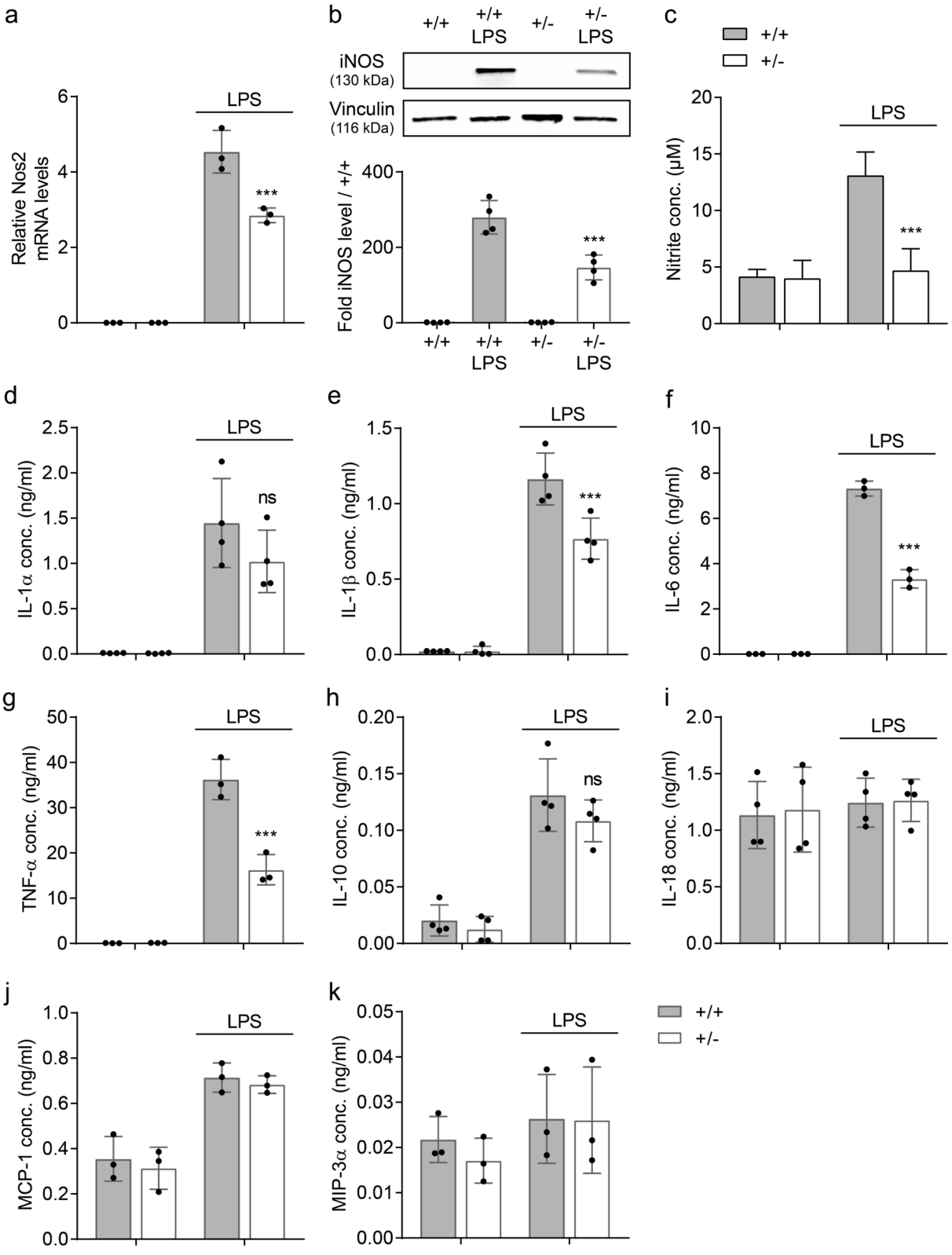

Additionally, the present findings regarding the influence of *Cacna1c* haploinsufficiency on glycolytic energy flux in LPS-stimulated microglia were further supported by pharmacological LTCC blockade with the DHP nimodipine (25 µM). As detailed in Figure 30, treatment of

wildtype cells with nimodipine already led to a stronger reduction in ECAR compared to *Cacna1c*$^{+/-}$ after 24 h of LPS exposure. Moreover, nimodipine-treated heterozygous *Cacna1c* primary microglia even showed an additive reducing effect on LPS-induced glycolysis. Unstimulated OCR and ECAR remained unaffected by both *Cacna1c* haploinsufficiency and nimodipine treatment.

Cacna1c haploinsufficiency and pharmacological LTCC blockade was associated with reduced NO and cytokine release in LPS-stimulated primary microglia

Reportedly, microglial activation is also associated with a massive secretion of NO as well as inflammatory cytokines (79). Nonexistent under resting conditions, microglial expression of *Nos2* (mRNA) and iNOS (protein) was substantially induced in response to LPS (Figure 31a,b). This marked, LPS-mediated increase of *Nos2*/iNOS expression levels was considerably prevented in heterozygous *Cacna1c* microglial cultures. Inducible nitric oxide synthase (iNOS) catalyzes the synthesis of NO, which was assessed via detecting nitrite, a stable reaction product of NO, in the culture supernatant by Griess reaction. Consistently, *Cacna1c* haploinsufficiency significantly inhibited the LPS-induced nitrite release into the microglia culture medium (Figure 31c). These results were further substantiated by the treatment of LPS-stimulated primary microglia with nimodipine, which also resulted in a reduced NO production compared to control (Figure 32a). In addition, NO inhibits oxidative phosphorylation at ETC complex IV, thereby contributing to the glycolytic switch observed in activated microglia (140).

Besides the release of NO, stimulation of microglial cells with the TLR agonist LPS for 24 h involves the production and secretion of inflammatory mediators such as cytokines and chemokines. In the present study, the concentrations of eight different cyto-/chemokines were determined in the culture supernatant of activated rat microglia using a multiplex immunoassay. Among these, the levels of key pro-inflammatory cytokines including IL-1α, IL-1β, IL-6, and TNF-α were analyzed. LPS-mediated extracellular accumulation of all four cytokines was significantly reduced in both heterozygous *Cacna1c* (Figure 31d-g) and nimodipine-treated (Figure 32b-e) microglia compared to wildtype.

Figure 32. Additive effects of *Cacna1c* haploinsufficiency and nimodipine treatment on NO and cytokine release in LPS-challenged rat microglia

a NO release was determined in the culture supernatant using the Griess reagent. A representative measurement with 4-9 technical replicates is presented (mean ± SD; ANOVA, Scheffé's-test). The levels of **b** IL-1α, **c** IL-1β, **d** IL-6, **e** TNF-α, **f** IL-10, **g** IL-18, **h** MCP-1, and **i** MIP-3α from 3-4 independent experiments were pooled and are displayed as mean ± SD. Data was statistically analysed by one-way ANOVA followed by Fisher's LSD post-hoc test. **a-i** The microglia cultures were co-treated with 100 ng/ml LPS and 25 µM nimodipine for 24 h prior to experiments. ***p < 0.001 compared to LPS-treated *Cacna1c*$^{+/+}$; ###p < 0.001, ##p < 0.01 compared to LPS-treated *Cacna1c*$^{+/-}$; +/+, wildtype *Cacna1c*$^{+/+}$; +/-, heterozygous *Cacna1c*$^{+/-}$; Nim, nimodipine.

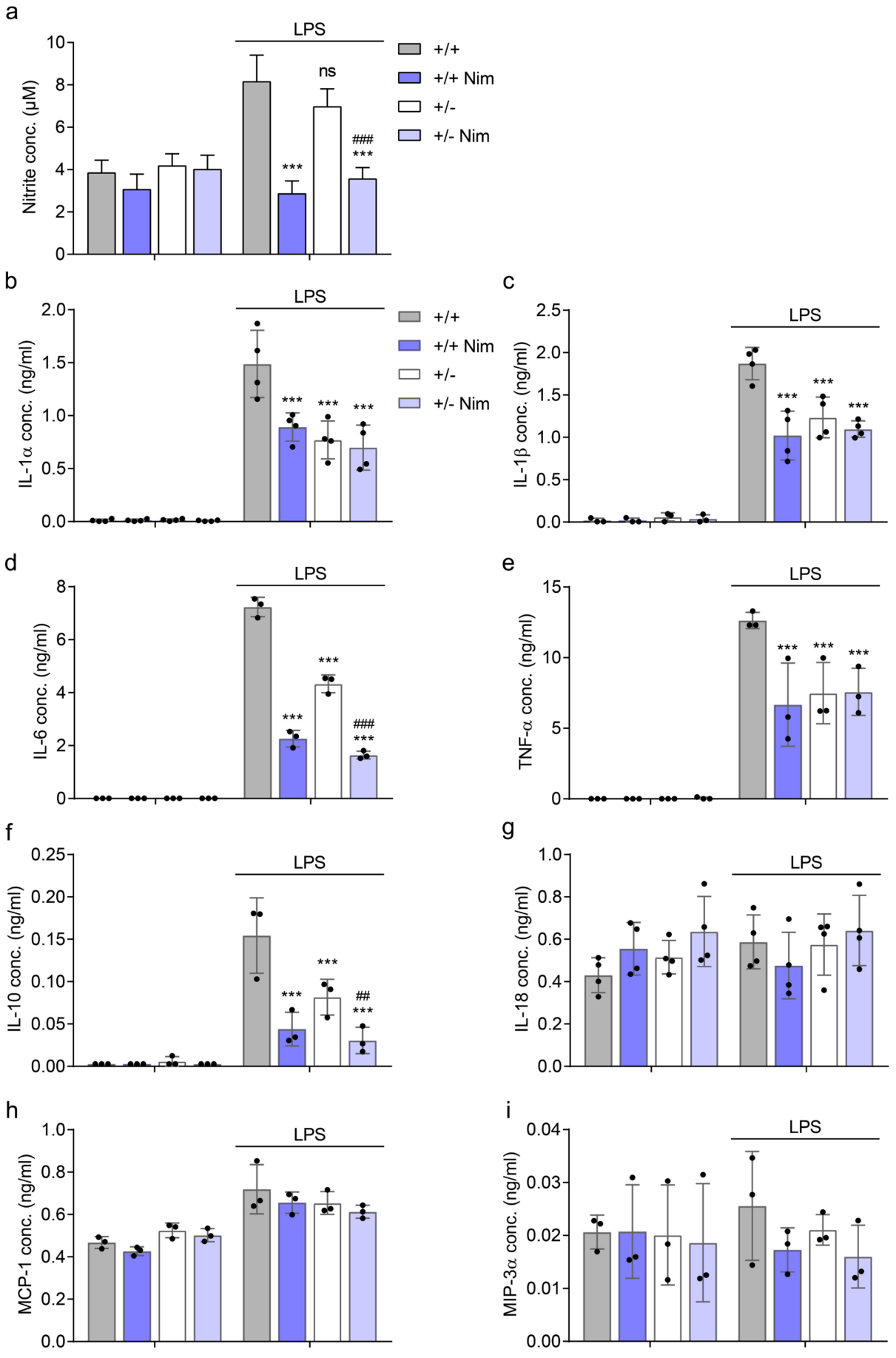
a
LPS
+/+
+/+ Nim
+/-
+/- Nim
Nitrite conc. (µM)
ns
***
###
***
b
IL-1α conc. (ng/ml)
c
IL-1β conc. (ng/ml)
d
IL-6 conc. (ng/ml)
e
TNF-α conc. (ng/ml)
f
IL-10 conc. (ng/ml)
##
g
IL-18 conc. (ng/ml)
h
MCP-1 conc. (ng/ml)
i
MIP-3α conc. (ng/ml)

The same applies to the LPS-induced generation of the anti-inflammatory cytokine IL-10, which was also diminished by *Cacna1c* haploinsufficiency (Figure 31h) as well as pharmacological LTCC blockade (Figure 32f). In the collected culture supernatants of activated rat microglia, IL-10, whose LPS-evoked expression has been reported before (173), was present in a much lower absolute concentration than IL-1α, IL-1β, IL-6, and TNF-α. Moreover, nimodipine treatment had a significantly stronger inhibitory impact on IL-6 and IL-10 release than *Cacna1c* haploinsufficiency in LPS-challenged microglia underlining a certain dose-dependency of the effects (Figure 32d,f). Pro-inflammatory IL-18 as well as the chemokines monocyte chemoattractant protein 1 (MCP-1, CCL2) and macrophage inflammatory protein 3α (MIP-3α, CCL20) were constitutively, in the case of MIP-3α hardly, expressed in primary rat microglia and remained unchanged irrespective of genotype (Figure 31i-k) and treatment condition (Figure 32g-i).

Collectively, the present findings with regard to morphological appearance, metabolic status, and secretion of inflammatory mediators revealed a reduced activation pattern, bioenergetic capacity as well as inflammatory immune response upon LPS stimulation in both heterozygous *Cacna1c* and nimodipine-treated primary rat microglia compared to wildtype. These results suggest that *Cacna1c* might play an important role in the activation of microglia, the resident immune cells of the CNS.

4.4 Effects of gene-environment interactions in isolated mitochondria

In order to study the combined effects of heterozygous *Cacna1c* knockout and different environmental influences on brain mitochondria, first the reduction of Cav1.2 levels in *Cacna1c*$^{+/-}$ rats was validated, the mean body weight per group compared, and the functional integrity of the isolated mitochondria verified. As evident from Figure 33a,b, the Cav1.2 protein content is decreased by around 50% in the PFC of *Cacna1c*$^{+/-}$ rats compared to their *Cacna1c*$^{+/+}$ littermates, irrespective of the environmental condition. In turn, the housing condition had an impact on the body weight of the two-month-old rats. Compared to social isolation and standard housing, social and physical environmental enrichment led to significantly decreased weight in both *Cacna1c*$^{+/-}$ rats and their *Cacna1c*$^{+/+}$ littermates. Further, a trend towards reduced body weight of heterozygous *Cacna1c* rats versus wildtype can be observed in the social isolation as well as the standard housing group (Figure 33c). The previously established isolation of mitochondria from fresh brain tissue using a speed- and pressure-controlled cell rupture system including a Balch-style homogenizer with a defined clearance constitutes a fast, efficient, and replicable method (148), which ensured the separation of a crude fraction of functional active mitochondria from nuclear and cytosolic parts (Figure 34).

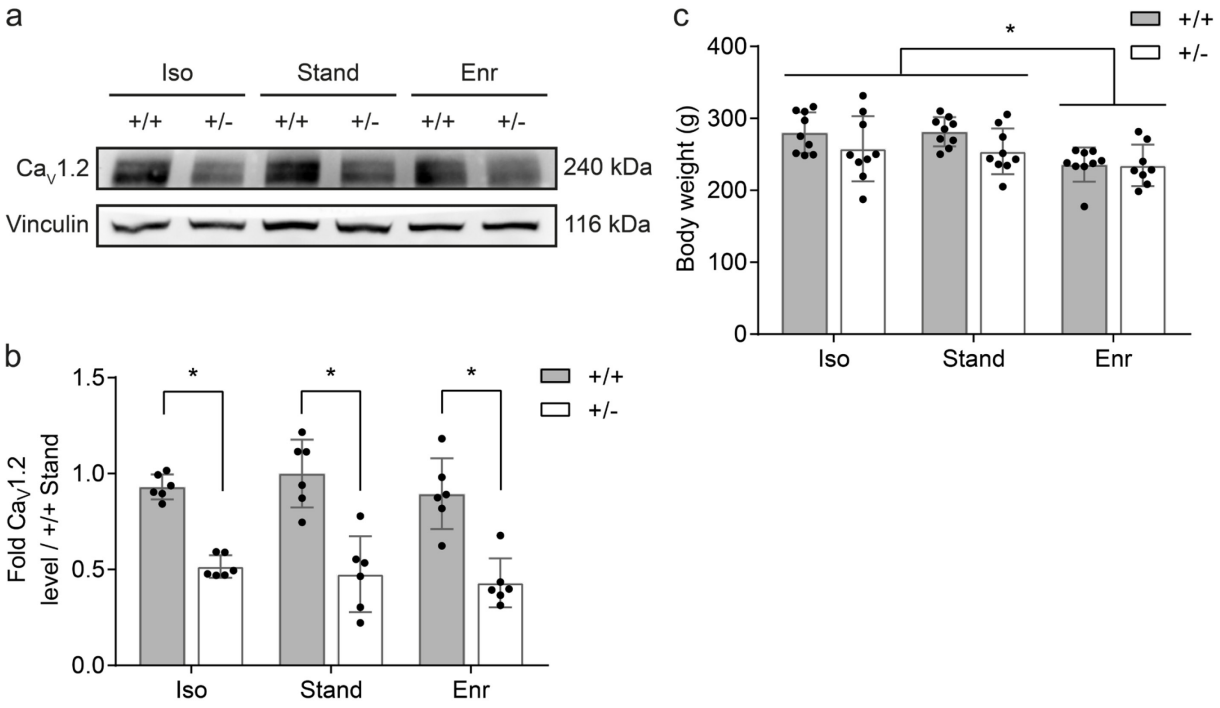

Figure 33. $Ca_V1.2$ protein levels in rat prefrontal cortex and body weight

$Ca_V1.2$ protein expression levels in the right prefrontal cortex of two-month-old male *Cacna1c*$^{+/-}$ rats and *Cacna1c*$^{+/+}$ littermate controls from the different environmental conditions were analyzed by Western blot. **a** One representative immunoblot is shown. **b** The bar graph was obtained by densitometric quantification of the Western blot data. The values are normalized to the loading control vinculin and presented as fold of *Cacna1c*$^{+/+}$-Stand (mean ± SD, n = 6). Statistical analysis found no evidence for a gene-environment interaction (GxE, $p = 0.6632$) or for an environmental effect (E, $p = 0.4050$), but revealed a significant genetic effect (G, $p < 0.0001$). The average relative $Ca_V1.2$ level in *Cacna1c*$^{+/+}$ was 0.94 (95% CI 0.87,1.01) and thereby approximately doubled compared to the mean $Ca_V1.2$ level in *Cacna1c*$^{+/-}$ of 0.47 (95% CI 0.41,0.54). **c** Whole body weight was determined after the four-week exposure to the experimental housing conditions at ~2 months of age (mean ± SD, n = 8-9). There was no evident GxE ($p = 0.4421$; omnibus test) or G effect ($p = 0.0573$). However, animals housed in a social and physically enriched environment weighed on average 33.1 g (95% CI 28.4,37.9) less than animals from the social isolation or standard housing group ($p = 0.0035$). +/+, wildtype *Cacna1c*$^{+/+}$; +/-, heterozygous *Cacna1c*$^{+/-}$; Iso, isolation; Stand, standard housing; Enr, enrichment.

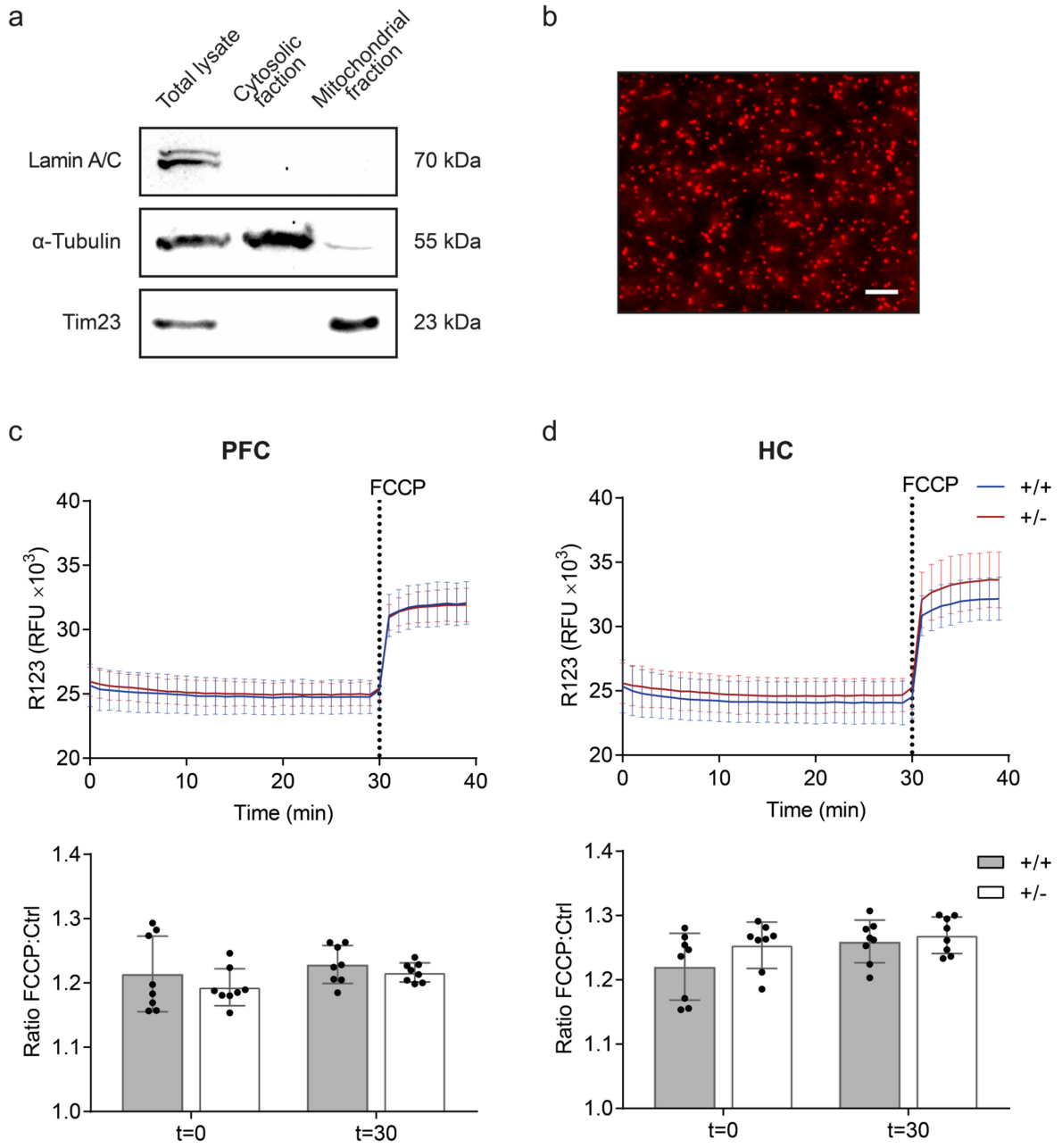

Figure 34. Quality of the isolated mitochondria from rat brain tissue

a The fractionation quality was evaluated by Western blot using the total lysate, the cytosolic and the mitochondrial fraction of hippocampal brain tissue. Lamin A/C was used as nuclear and α-Tubulin as cytosolic marker. The inner mitochondrial membrane protein Tim23 served as indicator for mitochondrial enrichment. **b** To visualize mitochondria, the enriched mitochondrial fraction was stained with MitoTracker Deep Red. One representative image is shown. Scale bar, 10 µm. Mitochondria from **c** the right PFC and **d** the right HC of male *Cacna1c*$^{+/+}$-Stand and *Cacna1c*$^{+/-}$-Stand rats were stained with rhodamine 123 (R123) to test their constant integrity after the isolation procedure. Positively charged R123 accumulates in mitochondria with intact membrane potential ($\Delta\Psi_m$) leading to a time stable fluorescence quenching over 30 min. This is also evident from the constant FCCP to control ratios after zero and 30 min (t = 0, t = 30) (PFC, p = 0.0235; HC, p = 0.0117; two-sided, two-sample t-test with paired observations). The injection of FCCP (0.5 µM) as internal control dissipates the $\Delta\Psi_m$ resulting in an increase in R123 fluorescence. Mean ± SD, n = 8; PFC, prefrontal cortex; HC, hippocampus; RFU, relative fluorescence units; +/+, wildtype *Cacna1c*$^{+/+}$ (grey bars); +/-, heterozygous *Cacna1c*$^{+/-}$ (clear bars).

Mitochondrial bioenergetics and respiratory chain complex levels

To compare brain bioenergetics in the GxE study using extracellular flux analysis, mitochondria were isolated from PFC and HC of *Cacna1c*$^{+/-}$ rats and wildtype littermates, which were each exposed to one of the three experimental housing conditions, i.e. post-weaning social isolation, standard housing, or social and physical environmental enrichment during the critical developmental period of adolescence (Figure 10). As cellular regulation of mitochondrial function was removed during isolation, energy demand and substrate availability can be specifically modulated to identify site-specific changes in mitochondrial activity and to examine the degree of coupling between the ETC and the oxidative phosphorylation machinery. In the performed coupling experiments, respiratory states, indicative of mitochondrial function, were measured as absolute oxygen consumption rate (respiration), normalized to protein content (Figure 35).

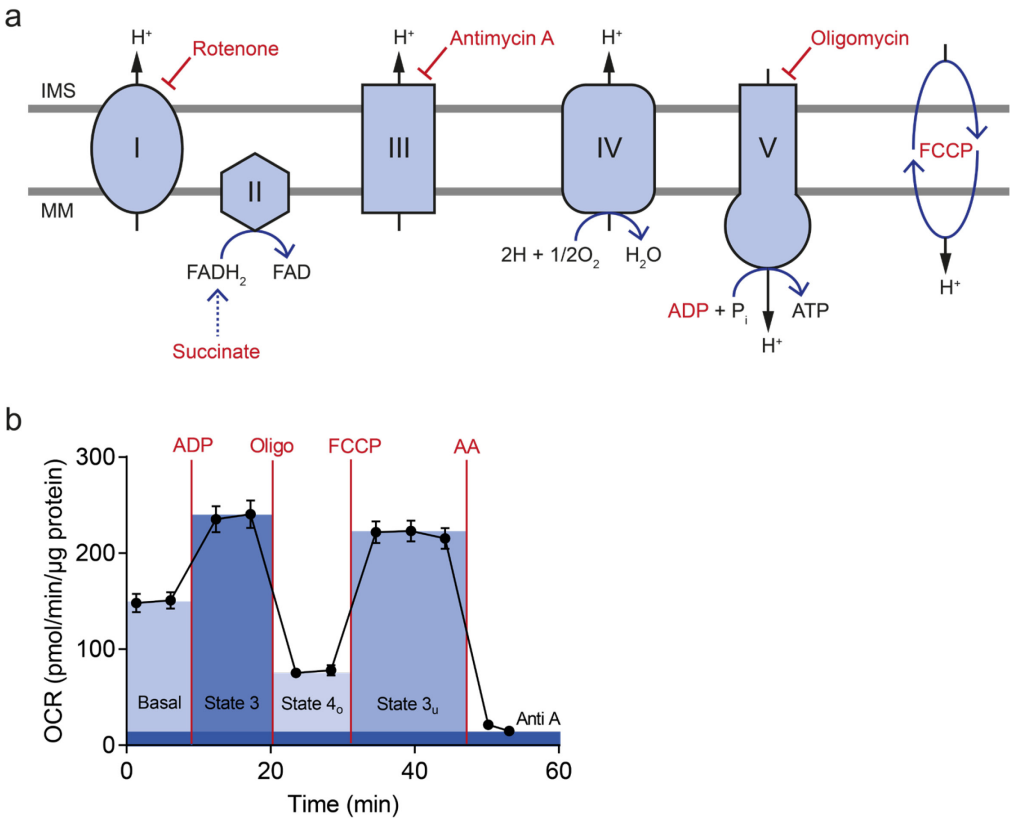

Figure 35. Key steps in oxidative phosphorylation and representative oxygen consumption rate measurement with isolated mitochondria from rat brain

a The scheme illustrates the electron transport chain with its five different complexes. Modulating compounds used in the Seahorse mitochondrial coupling assay are highlighted in red. **b** An exemplary measurement of the oxygen consumption rate (OCR) from isolated rat brain mitochondria is shown together with key parameters of mitochondrial respiration, which were calculated from the data. Five technical replicates are displayed as mean ± SD. IMS, intermembrane space; MM, mitochondrial membrane; OCR, oxygen consumption rate; Oligo, oligomycin; AA, antimycin A.

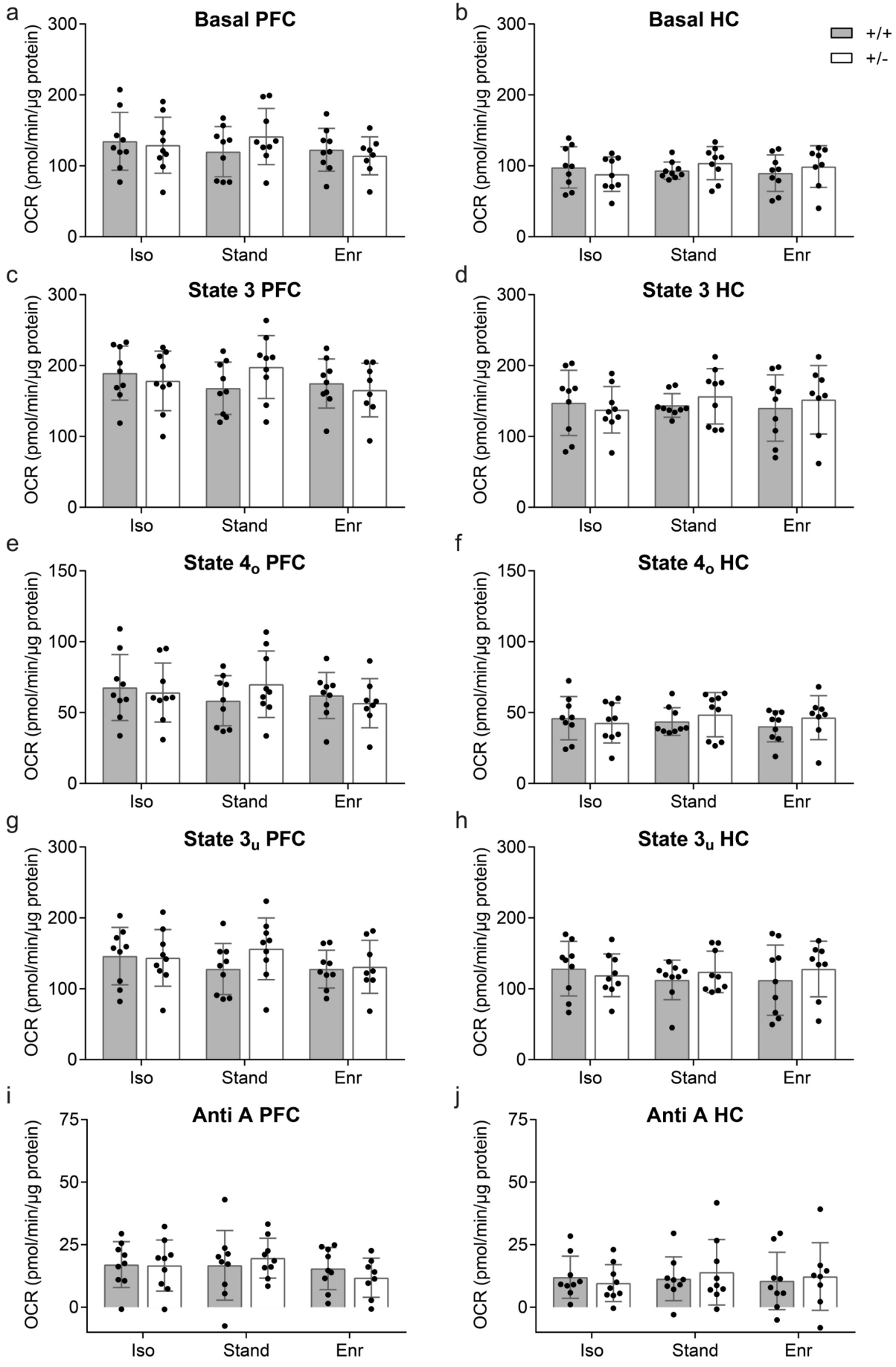
a
Basal PFC
b
Basal HC
+/+
+/-
c
State 3 PFC
d
State 3 HC
e
State 4o PFC
f
State 4o HC
g
State 3u PFC
h
State 3u HC
i
Anti A PFC
j
Anti A HC
OCR (pmol/min/µg protein)
Iso
Stand
Enr

Figure 36. Indices of mitochondrial function calculated from the OCR measurements

Individual parameters of the bioenergetics measurements with isolated mitochondria from rat right prefrontal cortex (PFC; **a,c,e,g,i**) and right hippocampus (HC; **b,d,f,h,j**) are specified. **a,b** With rotenone and succinate present in the assay buffer, the Basal rate implies the ADP-independent, complex II-mediated respiration (E; PFC, p = 0.5066; HC, p = 0.7683). **c,d** The State 3 OCR is initiated with the injection of ADP and accounts for the phosphorylating respiration (E; PFC, p = 0.5777; HC, p = 0.8343). **e,f** State 4_o is induced by the addition of the ATP synthase inhibitor oligomycin and stands for the non-phosphorylating respiration (E; PFC, p = 0.1364; HC, p = 0.8159). **g,h** FCCP uncouples the oxygen consumption from ATP production and is used to assess State 3_u, which represents the maximal respiratory activity (E; PFC, p = 0.4133; HC, p = 0.8917). **i,j** The Anti A rate constitutes the OCR response to antimycin A which inhibits the mitochondrial respiration (E; PFC, p = 0.3915; HC, p = 0.8581). The parameter values are calculated as absolute oxygen consumption rate in $pmolO_2$/min/6 µg mitochondrial protein. The data of n = 8-9 two-month-old male rats per group are presented as mean ± SD and showed no effect of the heterozygous *Cacna1c* genotype in any of the three different environmental conditions (G; PFC, p = 0.9890; HC, p = 0.8567). OCR, oxygen consumption rate; +/+, wildtype *Cacna1c*$^{+/+}$ (grey bars); +/-, heterozygous *Cacna1c*$^{+/-}$ (clear bars); Iso, isolation; Stand, standard housing; Enr, enrichment.

To assess the Basal respiration state, mitochondria were initially incubated with the complex II substrate succinate and, to prevent reverse electron flow, with the complex I inhibitor rotenone (Figure 36a,b). Then, ADP was added to induce phosphorylation and ATP synthesis (State 3; Figure 36c,d). Both parameters did not differ significantly among the six groups, neither in the PFC nor in the HC, thereby excluding an effect on ATP turnover. Next, State 4_o was initiated by the injection of oligomycin to inhibit the ATP synthase (complex V). This state allows to assess proton leak and was not affected by either the genotype or the environment in both brain regions studied (Figure 36e,f). After oligomycin addition the protonophore FCCP was injected to dissipate the proton gradient leading to enhanced oxygen consumption, which is not coupled to phosphorylation. Thus, the achieved State 3_u is exclusively controlled by substrate oxidation. Here, the genotype, the environment, and their interaction also showed no effect on State 3_u respiration of mitochondria isolated from PFC or HC (Figure 36g,h). The final injection of the complex III inhibitor antimycin A was used to correct all parameters for non-mitochondrial respiration, which was consistently low in all conditions as cytosolic oxidases were eliminated during the isolation process (Figure 36i,j).

In line with previous studies investigating brain region-specific differences in mitochondrial bioenergetics (174), all respiration rates in the HC were lower compared to the PFC with no effect on the respiratory control ratio (Figure 36 and Figure 37). The respiratory control ratio (RCR) is defined as the oxygen consumption in State 3 divided by that in State 4_o. This internally normalized parameter provides combined information on substrate oxidation capacity, ATP turnover, and proton leakage making it a potent overall marker of energetic dysfunction (175). In mitochondria from the right PFC (mean RCR 2.97; 95% confidence interval (CI) 2.80,3.13) as well as from the right HC (mean RCR 3.42; 95% CI 3.19,3.64) of two-

month-old male rats constant RCR values were obtained for all the six groups compared (Figure 37).

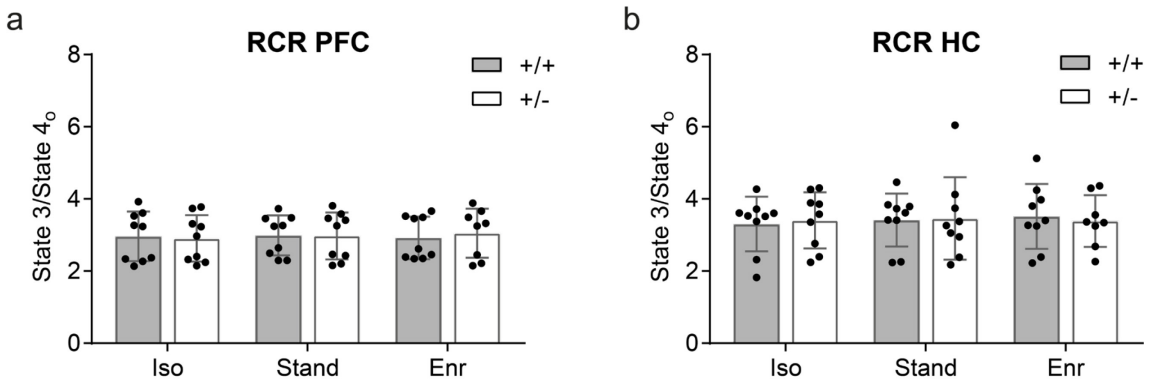

Figure 37. Respiratory control ratio (RCR) as indicator for mitochondrial integrity

The RCR was determined from isolated mitochondria of **a** the right prefrontal cortex and **b** the right hippocampus of two-month-old male *Cacna1c*$^{+/-}$ rats and *Cacna1c*$^{+/+}$ littermate controls which were each kept in one of the three different environmental conditions. The State 3 to State 4$_o$ ratio (RCR) is a measure of the coupling quality between respiration and phosphorylation (mean ± SD, n = 8-9). There was no GxE interaction (PFC, p = 0.3852; HC, p = 0.4914), no genetic (PFC, p = 0.2614; HC, p = 0.7892), and no environmental effect (PFC, p = 0.9640; HC, p = 0.9275) on RCR in both PFC and HC. PFC, prefrontal cortex; HC, hippocampus; +/+, wildtype *Cacna1c*$^{+/+}$ (grey bars); +/-, heterozygous *Cacna1c*$^{+/-}$ (clear bars); Iso, isolation; Stand, standard housing; Enr, enrichment.

To control for potential brain hemisphere-, age-, or sex-related effects, mitochondrial RCRs were also evaluated in right versus left hemisphere, in two- versus ten-month-old animals, and in female versus male, using *Cacna1c*$^{+/-}$ rats and *Cacna1c*$^{+/+}$ littermate controls exposed to standard housing conditions in two supplementary studies (Figure 38). The present measurements did not reveal any significant differences in male PFC RCR between both brain hemispheres and/or genotypes (Figure 38a). Interestingly, in the PFC of ten-month-old normally housed male *Cacna1c*$^{+/-}$ rats, the RCR was moderately, but significantly elevated by 0.45 (95% CI 0.28,0.62) compared to the 3.90 average RCR (95% CI 3.67,4.13) of *Cacna1c*$^{+/+}$ littermate controls (Figure 38b). However, no genotype effect on RCR of ten-month-old animals was observed in male HC (mean 4.50; 95% CI 4.12,4.89), female PFC (mean 4.32; 95% CI 3.94,4.69), and female HC (mean 4.35; 95% CI 4.21,4.49) respectively (Figure 38c-e). Further, male HC RCRs were significantly higher ($p < 0.0001$) in the ten- compared with the two-month-old animals (Figure 38c).

In addition to the functional assessment, the expression levels of the five ETC complexes were quantified by Western blot. Consistently, these showed no changes in relation to genotype and/or environment (Figure 39).

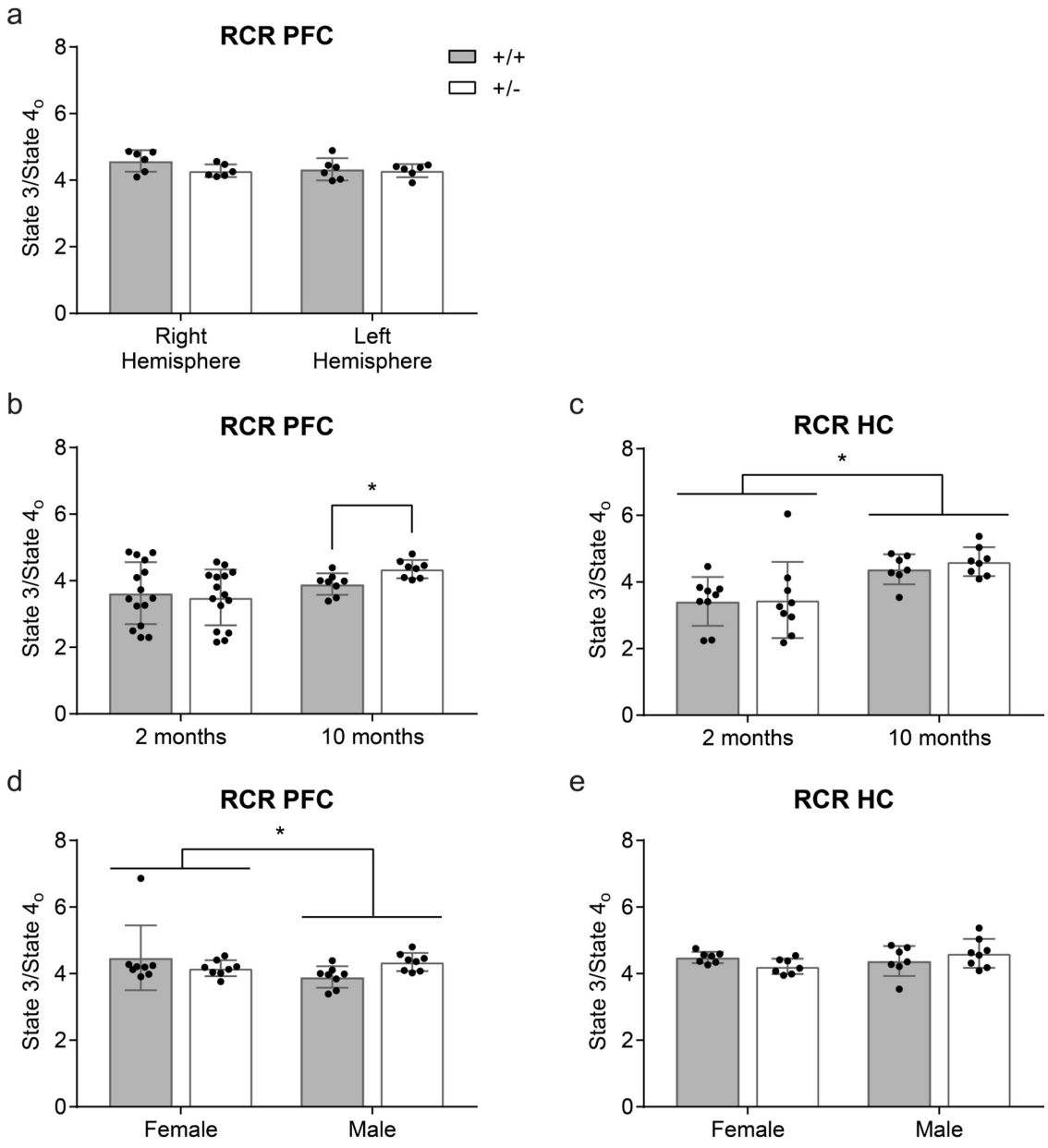

Figure 38. Respiratory control ratio of mitochondria isolated from rats with differing age, sex and from both brain hemispheres

Respiratory control ratios (RCR) calculated from the OCR measurements using isolated mitochondria from: **a** right and left PFC of two-month-old male *Cacna1c*$^{+/+}$-Stand and *Cacna1c*$^{+/-}$-Stand rats, **b** the right PFC and **c** the right HC of two- versus ten-month-old male *Cacna1c*$^{+/-}$ rats and *Cacna1c*$^{+/+}$ littermate controls, which were kept under standard housing conditions, **d** the right PFC and **e** the right HC of ten-month-old male and female *Cacna1c*$^{+/+}$-Stand and *Cacna1c*$^{+/-}$-Stand rats (mean ± SD, pooled data). **a** There was neither a gene-hemisphere interaction ($p = 0.5210$), nor an effect of the genotype ($p = 0.0934$) or the hemisphere ($p = 0.2874$) on RCR alone. **b** Statistical analysis revealed a strong effect of the genotype on RCR in the PFC of ten-month-old male animals ($p < 0.0001$) indicating a gene-age interaction. **c** No gene-age interaction ($p = 0.3524$) as well as no genetic effect ($p = 0.8602$) exists for the RCR of hippocampal mitochondria, but there was a main age effect ($p < 0.0001$). **d** Differences in PFC RCR between sexes were statistically significant ($p < 0.0001$) implying a gene-sex (GxS) interaction. Compared to males, no genotype effect was found for PFC RCR in females ($p = 0.4259$). **e** On the contrary, no GxS interaction ($p = 0.0748$), no genetic effect (female; $p = 0.8742$) and no sex effect ($p = 0.2708$) on HC RCR were observed. +/+, wildtype *Cacna1c*$^{+/+}$ (grey bars); +/-, heterozygous *Cacna1c*$^{+/-}$ (clear bars).

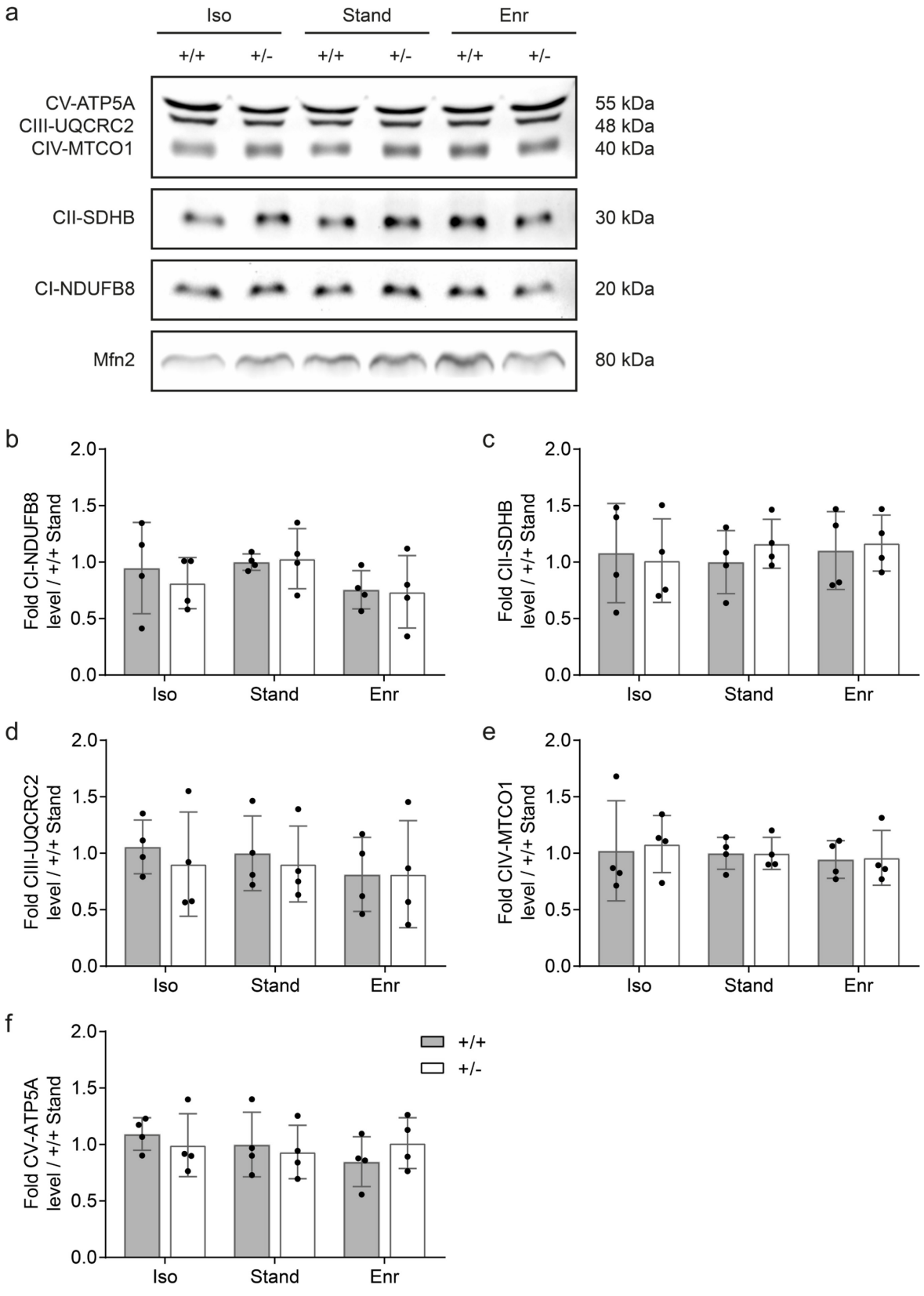
a
Iso
Stand
Enr
+/+
+/-
+/+
+/-
+/+
+/-
CV-ATP5A
CIII-UQCRC2
CIV-MTCO1
55 kDa
48 kDa
40 kDa
CII-SDHB
30 kDa
CI-NDUFB8
20 kDa
Mfn2
80 kDa
b
Fold CI-NDUFB8 level / +/+ Stand
c
Fold CII-SDHB level / +/+ Stand
d
Fold CIII-UQCRC2 level / +/+ Stand
e
Fold CIV-MTCO1 level / +/+ Stand
f
Fold CV-ATP5A level / +/+ Stand
2.0
1.5
1.0
0.5
0.0
Iso
Stand
Enr
+/+
+/-

Figure 39. Protein levels of the five electron transport chain complexes in right prefrontal cortex

Relative protein levels of the five electron transport chain complexes (CI-CV) were assessed in isolated PFC mitochondria from two-month-old male rats. **a** One representative immunoblot and **b-f** the densitometric quantification of the individual complexes (CI-CV) are depicted. The values are normalized to the mitochondrial outer membrane protein Mfn2 and presented as fold of *Cacna1c*$^{+/+}$-Stand (mean ± SD, n = 4). There was no gene-environment interaction in any of the complexes (p = 0.5143). Moreover, neither genotype (p = 0.7529), nor environment (p = 0.3509) had an effect on complex expression levels. +/+, wildtype *Cacna1c*$^{+/+}$ (grey bars); +/-, heterozygous *Cacna1c*$^{+/-}$ (clear bars); Iso, isolation; Stand, standard housing; Enr, enrichment.

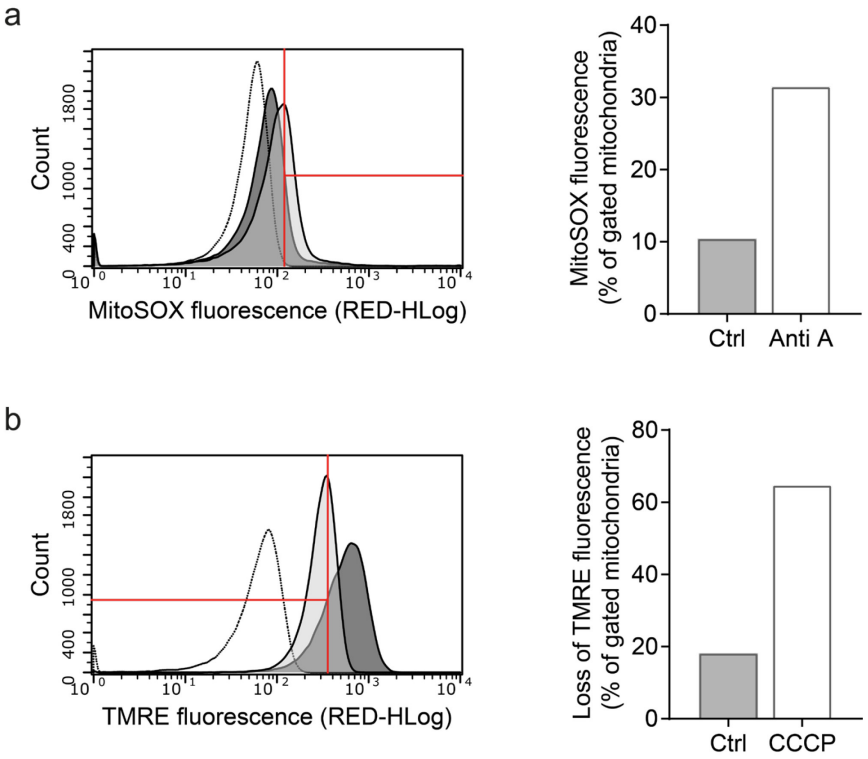

Figure 40. Exemplary histograms and quantifications of flow cytometric measurements with isolated mitochondria from rat prefrontal cortex

Freshly isolated mitochondria were stained with **a** MitoSOX (1.25 µM) and **b** TMRE (0.2 µM). Antimycin A (Anti A, 10 µM) and CCCP (50 µM) respectively were used as validating positive control. The complex III inhibitor antimycin A increased the formation of superoxide leading to a rightward shift in MitoSOX fluorescence. Incubation of mitochondria with CCCP resulted in a decrease in membrane potential, which is visible as a left shift of the peak, indicating a loss of TMRE fluorescence. The histograms (left panel) illustrate that the gate (red) was set at the inflection point of the reference graph (*Cacna1c*$^{+/+}$-Stand, dark grey). The clear graphs with the dotted line represent the unstained controls. The dark grey graphs constitute the control samples, the light grey graphs the Anti A/CCCP-treated samples, and the grey areas the overlay of both graphs. The bar graphs (right panel) display the percentage of mitochondria within the gate (n = 1).

Mitochondrial superoxide levels and membrane potential

To further substantiate the results from the bioenergetics analyses, associated mitochondrial parameters were measured including ROS levels and membrane potential ($\Delta\Psi_m$) by using

flow cytometry (176). The fluorescent dye MitoSOX is rapidly targeted to mitochondria where it is selectively oxidized by superoxide ($O_2^{\bullet-}$) producing red fluorescence (Figure 40a). $O_2^{\bullet-}$ is increasingly formed upon perturbations in the electron flow across the respiratory chain. Moreover, superoxide generation is strongly dependent on the mitochondrial membrane potential, which, in turn, is particularly important for the regulation of ATP synthesis, indicating that all these processes are closely interconnected. The slow-responding cationic dye TMRE accumulates within the mitochondria in a membrane potential-dependent manner and is thereby well suited for measuring pre-existing $\Delta\Psi_m$ (Figure 40b).

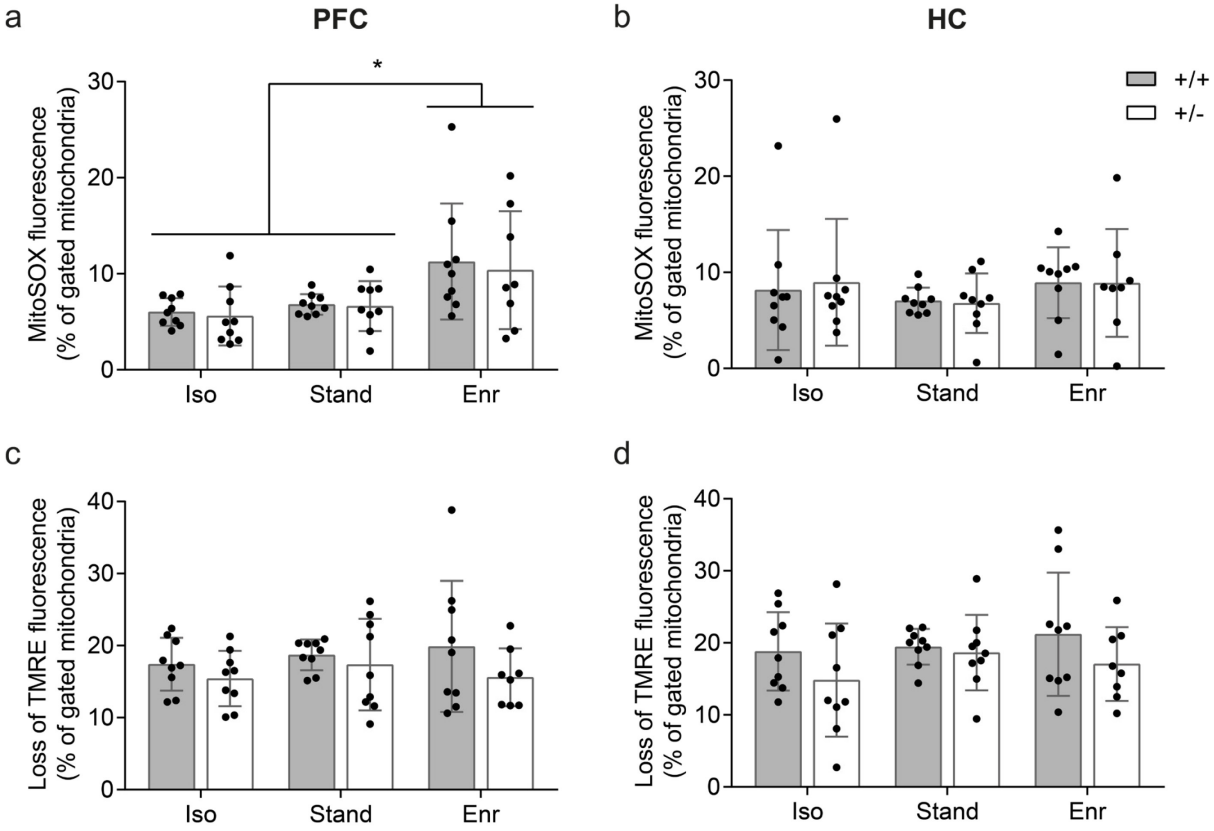

Figure 41. Assessment of mitochondrial superoxide levels and membrane potential

Flow cytometric measurements were conducted with isolated mitochondria from right PFC (**a,c**) and right HC (**b,d**) of two-month-old male rats using (**a,b**) the mitochondrial superoxide indicator dye MitoSOX and (**c,d**) the mitochondrial membrane potential sensitive dye TMRE. The data was gated to the reference condition *Cacna1c*$^{+/+}$-Stand in each group of six and is displayed as mean ± SD (n = 8-9). While showing no gene-environment interaction (p = 0.9608) and no genetic effect (p = 0.6410), mitochondrial ROS levels were significantly higher in the PFC of enriched animals (E, p = 0.0050). No statistical significant differences were observed in hippocampal mitochondrial superoxide levels (mean 8.12; 95% CI 6.83,9.40; GxE, p = 0.9349; G, p = 0.9309; E, p = 0.1700) as well as in the membrane potential of mitochondria isolated from PFC (mean 17.57; 95% CI 16.55,18.59; GxE, p = 0.7319; G, p = 0.0127; E, p = 0.5439) and HC (mean 18.90; 95% CI 17.71,20.09; GxE, p = 0.5196; G, p = 0.1260; E, p = 0.6433). +/+, wildtype *Cacna1c*$^{+/+}$ (grey bars); +/-, heterozygous *Cacna1c*$^{+/-}$ (clear bars); Iso, isolation; Stand, standard housing; Enr, enrichment.

As detailed in Figure 41 and consistent with the previous findings, both superoxide levels and $\Delta\Psi_m$ of mitochondria isolated from PFC and HC remained unaltered in response to *Cacna1c* haploinsufficiency and different environmental situations with the exception of physical and social enrichment. Here, significantly higher mitochondrial ROS levels (mean 10.85; 95% CI 9.02,12.68) were found versus isolation and standard housing (mean 6.27; 95% CI 5.01,7.53), but only in mitochondria isolated from PFC and not from HC.

In summary, genotype and environment alone or in interaction did not have a substantial effect on overall mitochondrial bioenergetics in brain regions that are affected in psychiatric disorders (PFC, HC). Furthermore, the functional profile of the isolated brain mitochondria was completed by the evaluation of respiratory chain complex levels, superoxide formation, and membrane potential also not providing evidence for mitochondrial impairment associated with the investigated conditions.

4.5 Effects of genetic and environmental risk on mitochondria in PBMCs

Before studying the possible effects of psychiatric disease-relevant genetic or environmental risk factors on mitochondrial function in human PBMCs, the quality of the frozen PBMC samples after thawing was evaluated with regard to viability, purity, and total number of cells. Without considering cell debris, dead cells, and platelets, the absolute cell count of viable PBMCs per 2 ml-aliquot ranged from 30,000 to 6.7 million and was not significantly different among the three groups NR, GR, and ER (Figure 42a). The same applies to the percentage of viable PBMCs, which ranged between 8 and 71% (Figure 42b) and is exemplary depicted in Figure 42c. The, in part, limiting amount of viable PBMCs (< 500,000/sample) led to the exclusion of 3-5 samples per group from the subsequent mitochondrial respiration measurements.

Furthermore, based on the characteristic light-scattering properties of the different blood cells, these can be distinguished by flow cytometry (Figure 43). This allows to include (green) and exclude (red) particular cell populations for further flow cytometric analyses. Besides a contamination with cell debris and thrombocytes, most of the present samples (~85%) contained low-granular mononuclear cells, i.e. lymphocytes and monocytes. The remaining ~15% additionally manifested a certain contamination with larger and more complex granulocytes.

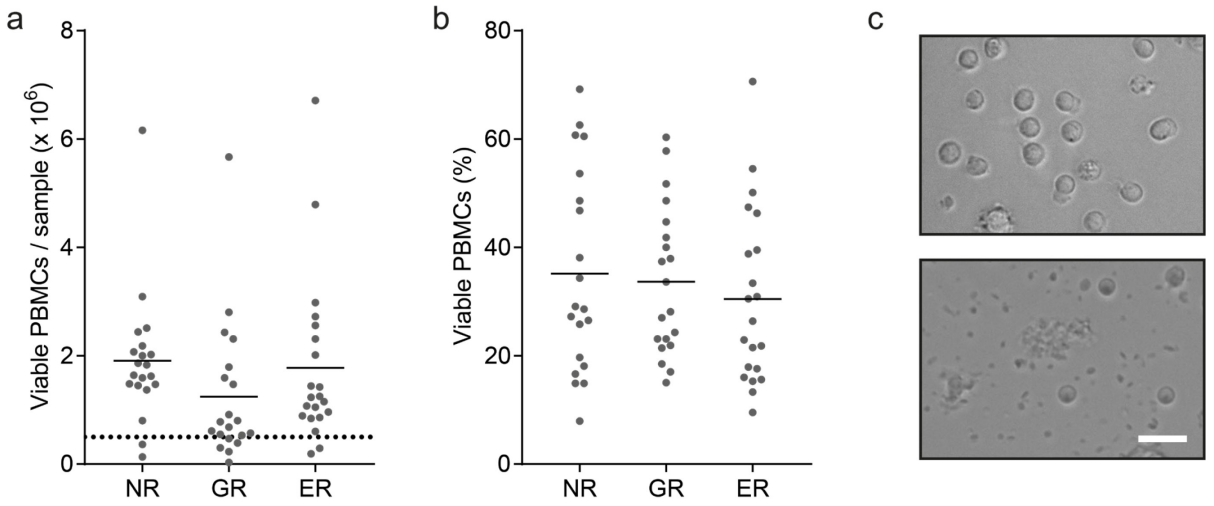

Figure 42. Cell count and viability of the frozen PBMC samples after thawing

a The graph depicts the total number of viable PBMCs per sample excluding cell debris, dead cells, and thrombocytes with a diameter < 5.4 µm. The dotted line marks the minimal cell count for respiration measurements (500,000 viable cells). **b** Viable PBMCs are displayed as percentage of total counts ranging from 8 to 70%. **a,b** Data is shown as mean with single values (NR, n = 20; GR, n = 20; ER, n = 21). Differences between the three groups are not significant (ns; ANOVA, Fisher's LSD-test). NR, no risk; GR, genetic risk; ER, environmental risk. **c** Exemplary images of two PBMC samples with good and poor quality respectively (upper vs lower picture) were captured in differential interference contrast. Scale bar, 20 µm.

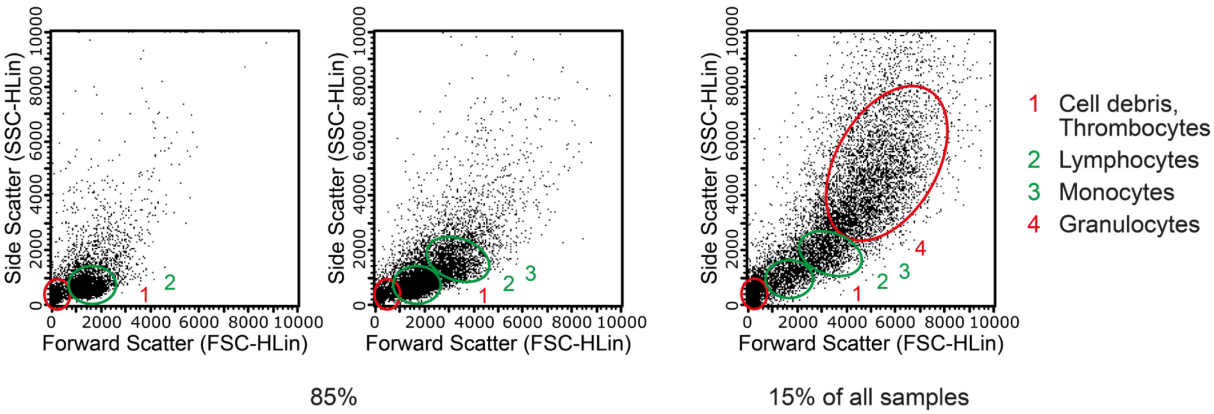

Figure 43. Representative flow cytometric dot plots

The dot blots illustrate the three different identified distributions of cells based upon size (FSC) and granularity (SSC). The first scatter plot displays two distinct populations, cell debris and thrombocytes (1) as well as lymphocytes (2). In addition, the second exemplary distribution also includes monocytes (3). Together these two compositions account for ~85% of all samples. The remaining ~15% contain lymphocytes (2), monocytes (3), and, besides cell debris and thrombocytes (1), a pronounced granulocytes (4) contamination. In all samples, these contaminations (1,4) were excluded from further flow cytometric analyses.

Assessment of mitochondrial ROS levels in human PBMCs

Mitochondria are the major site of superoxide generation in cells. Particularly at complex I and III of the respiratory chain, the leakage of single electrons to O_2 results in the formation of superoxide. If their levels exceed the capacity of the antioxidant defense system, reactive oxygen species cause molecular and functional damage to DNA, lipids, and proteins. Thus, an increased superoxide production can be indicative of mitochondrial dysfunction. However, mitochondrial perturbations may also be associated with decreased ROS levels, depending on the site and cause of the dysfunction (177).

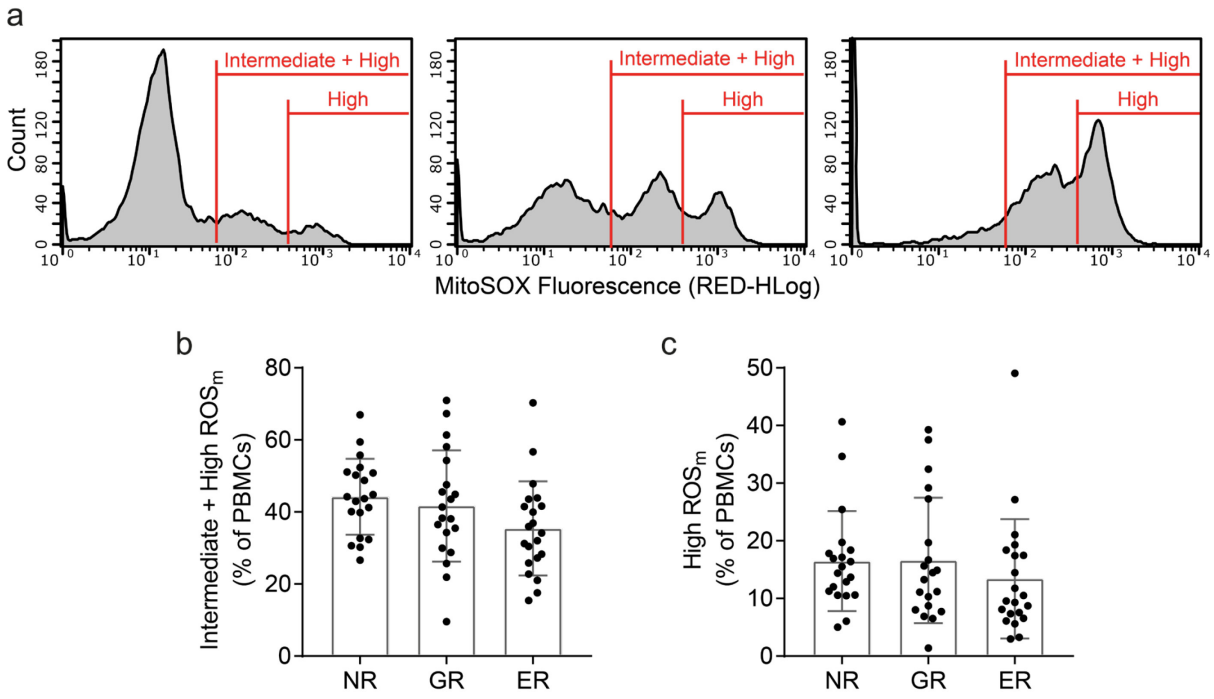

Figure 44. Assessment of mitochondrial ROS levels by flow cytometry

a PBMC samples were stained with the fluorescent dye MitoSOX. A right shift in MitoSOX Red fluorescence indicates an increase in superoxide levels. As demonstrated by three exemplary histograms two fixed gates at 60 and 400 separate the three occurring peaks representing PBMC populations with low, intermediate, and high mitochondrial ROS levels. **b** The bar graph quantifies the amount of PBMCs with intermediate and high ROS_m (gate at 60) as percentage of all PBMCs in each sample. **c** Here, the percentages of PBMCs with high ROS_m (gate at 400) in each sample are summarized. **b,c** Data is displayed as mean ± SD with single values (NR, n = 20; GR, n = 20; ER, n = 21). One-way ANOVA and Fisher's LSD post-hoc test revealed no significant (ns) differences between the three groups. ROS_m, mitochondrial reactive oxygen species; NR, no risk; GR, genetic risk; ER, environmental risk.

In the present study, mitochondrial superoxide levels in human PBMCs were investigated by flow cytometry using the fluorescent dye MitoSOX. MitoSOX is rapidly and selectively targeted to mitochondria, where it is oxidized by superoxide producing red fluorescence. As evident from the exemplary histograms in Figure 44a, all investigated PBMC samples were

subdivided by two fixed gates at 60 and 400 into three populations termed PBMCs with low, intermediate and high mitochondrial ROS levels. Figure 44b,c summarizes the percentages of PBMCs with intermediate and high ROS (gate at 60) as well as high ROS only (gate at 400) of each individual probe. Both quantifications showed a tendency to slightly lower mitochondrial ROS levels in the ER samples, but did not reveal any statistically significant differences between the three groups NR, GR, and ER.

Measurement of cellular bioenergetics in human PBMCs

To investigate different aspects of mitochondrial function in more detail, extracellular flux analyses were performed including all samples with sufficient amount of viable PBMCs (NR, n = 17; GR, n = 15; ER, n = 16). The successive injection of different inhibitors of oxidative phosphorylation allows a bioenergetic profile to be measured in cells. As illustrated in Figure 45a, specific respiratory parameters were analyzed as absolute oxygen consumption rate (respiration) normalized to cell number (175). First, the basal respiration was assessed, which is mainly controlled by cellular ATP demand and partly by mitochondrial proton leak and substrate oxidation (Figure 45b). Then, the rate of mitochondrial ATP production was estimated from the decrease in respiration upon inhibition of the ATP synthase with oligomycin (Figure 45c). The remaining OCR in the presence of oligomycin is a direct measure of the proton leak rate across the inner mitochondrial membrane and is therefore sensitive to uncoupling (Figure 45d) (178). None of these three parameters differed significantly among the three groups studied. However, a trend towards higher mean values and variation in the GR as well as the ER group compared to the NR control can be observed indicating increased proton leak accompanied by elevated ATP demand to maintain organelle integrity. Next, maximal respiration was stimulated by addition of the uncoupler FCCP, which simulates an artificial energy demand and is dependent on the maximum activity of electron transport, substrate oxidation and supply to meet this metabolic challenge (Figure 45e).

Figure 45. Exemplary OCR measurement and subsequently calculated key parameters of mitochondrial respiration

a A representative OCR measurement including injections of the ATP synthase inhibitor oligomycin, the uncoupler FCCP, the complex I inhibitor rotenone, and the complex III inhibitor antimycin A is shown together with key parameters of mitochondrial bioenergetics derived from the measured data. Four replicate wells are displayed as mean ± SD. The specific parameters are depicted as follows: **b** basal respiration, **c** ATP production, **d** proton leak, **e** maximal respiration, **f** non-mitochondrial respiration, **g** spare capacity, and **h** coupling efficiency. **b-h** Data is shown as mean ± SD with single values (NR, n = 17; GR, n = 15; ER, n = 16). Differences between the three groups were not significant (ns; ANOVA, Fisher's LSD-test). Oligo, oligomycin; Rot, rotenone; AA, antimycin A; NR, no risk; GR, genetic risk; ER, environmental risk.

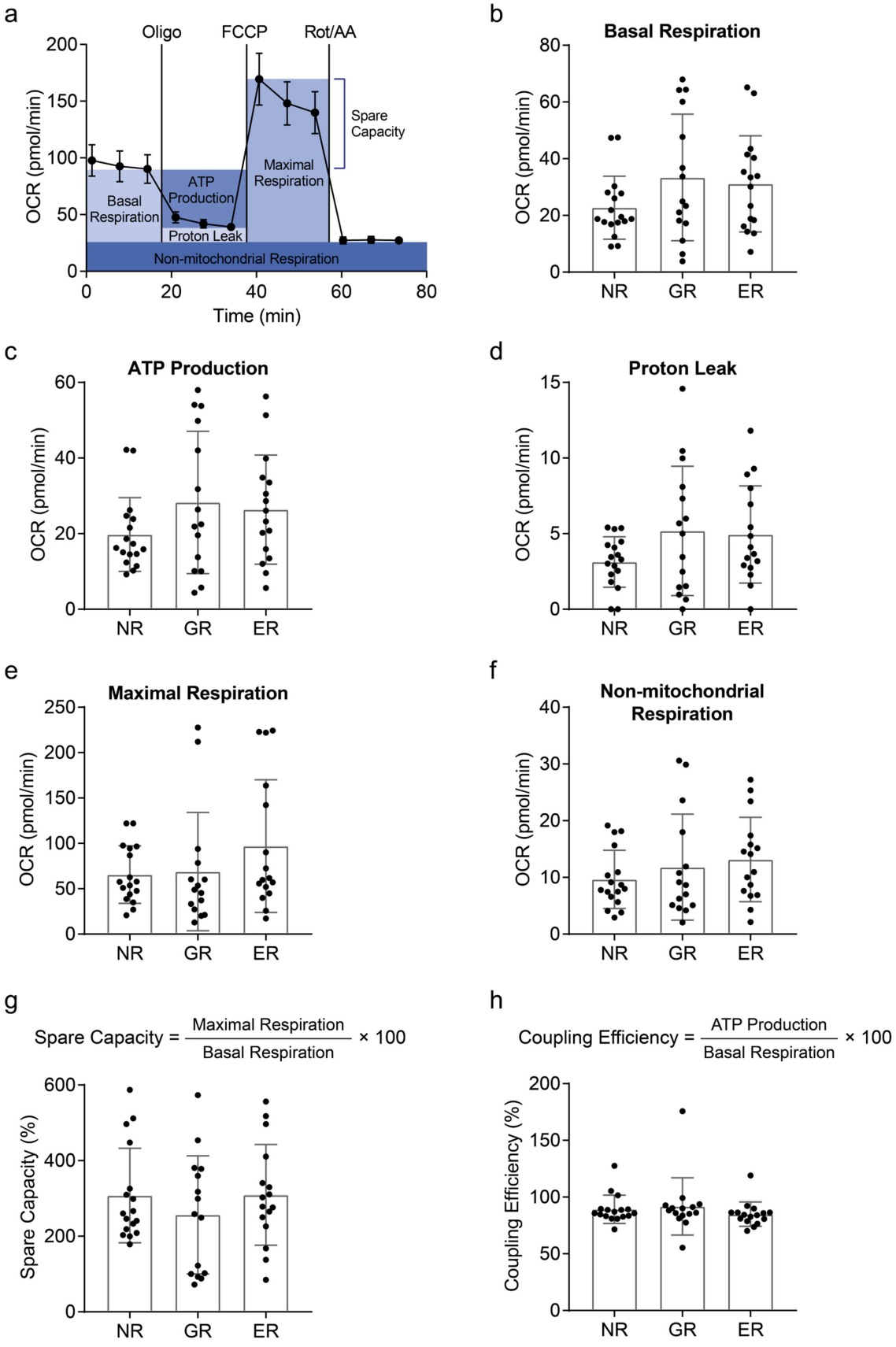
a
Oligo
FCCP
Rot/AA
Spare Capacity
Maximal Respiration
ATP Production
Basal Respiration
Proton Leak
Non-mitochondrial Respiration
OCR (pmol/min)
Time (min)
b
Basal Respiration
c
ATP Production
d
Proton Leak
e
Maximal Respiration
f
Non-mitochondrial Respiration
NR
GR
ER
g
Spare Capacity = Maximal Respiration / Basal Respiration × 100
Spare Capacity (%)
h
Coupling Efficiency = ATP Production / Basal Respiration × 100
Coupling Efficiency (%)

Finally, the combined injection of the complex I inhibitor rotenone and the complex III inhibitor antimycin A leads to a complete inhibition of the mitochondrial respiratory chain. The persisting OCR was subtracted from all other rates to correct these for non-mitochondrial respiration (Figure 45f). In leukocytes, non-mitochondrial respiration is typically attributed to oxygen-consuming pro-inflammatory enzymes such as cyclo-oxygenases, lipoxygenases, or NADPH oxidases (179). Neither maximal nor non-mitochondrial respiration were significantly affected in isolated PBMCs from individuals with genetic or environmental risk respectively.

In addition, two ratios were calculated, which have the advantage of combining the information of two parameters as well as being internally normalized and thereby independent of cell number, size and mitochondrial content. The spare capacity is a measure of the cell's ability to respond to an increased energy demand and indicates how closely a cell is operating to its bioenergetic limit (see Figure 45g for equation) (175). There were no statistical significant differences between the NR, GR, and ER groups. As evident from Figure 45g, however, the genetic risk group tended to have a lower average spare capacity comprising a subpopulation of six samples that exhibited a lack of spare respiratory capacity (72-122%) revealing a mitochondrial dysfunction that was not apparent under basal conditions. The coupling efficiency constitutes the fraction of basal respiration that is used for ATP production and is susceptible to changes in proton permeability (see Figure 45h for equation) (175). With mean values ranging between 85 and 92%, the coupling efficiency was consistently high in all three groups (Figure 45h).

Furthermore, the Bioenergetic Health Index (BHI) was evaluated, which condenses the mitochondrial respiration profile into a single value making it a strong overall indicator of cellular metabolic function. The BHI was introduced in 2014 by Chacko et al. as dynamic prognostic biomarker measured in circulating PBMCs, which are particularly sensitive and responsive to early systemic metabolic and inflammatory changes associated with neurodegeneration, diabetes, and cardiovascular disease (179). As shown in Figure 46a, the BHI equation captures positive aspects of bioenergetic function such as spare capacity and ATP production and contrasts these with potentially detrimental parameters including non-mitochondrial respiration and proton leak. In conformity with its individual components, the BHI showed no significant alterations between the three groups. On average, PBMCs from the genetic risk group had lower Bioenergetic Health Indices and higher data variability compared to the NR and ER samples. Additionally, both mean and SD in each group remained practically unchanged when excluding samples with granulocytes contamination and high platelets content/poor amount of viable PBMCs (< 20%; Figure 46b).

a

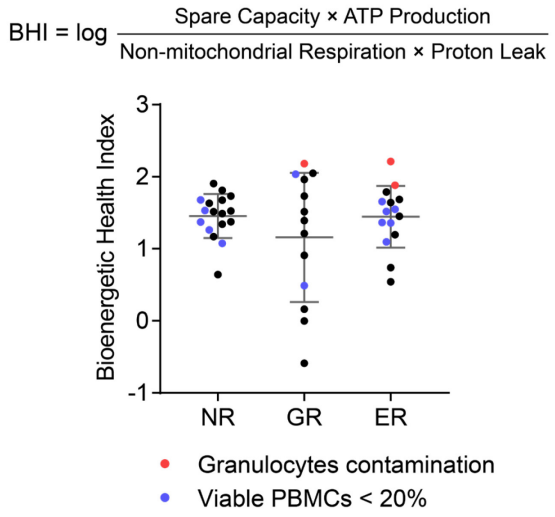

b

	BHI	All samples	Samples - G, - V < 20%
NR	Mean	1.45	1.48
	SD	0.31	0.34
	n	17	12
GR	Mean	1.16	1.03
	SD	0.90	0.90
	n	13	10
ER	Mean	1.44	1.29
	SD	0.43	0.49
	n	15	7

Figure 46. Bioenergetic Health Index (BHI) as indicator of mitochondrial function in PBMCs

a The BHI combines positive aspects of bioenergetic function including spare capacity and ATP production and contrasts these with potentially deleterious parts such as non-mitochondrial respiration and proton leak. The bar graph summarizes the individual BHI values highlighting samples with granulocytes contamination in red and samples with less than 20% viable PBMCs in blue. Data is shown as mean ± SD with single values. Using one-way ANOVA and Fisher's LSD post-hoc test, no significant (ns) differences between the three groups were detected. **b** The table lists the mean BHI, SD, and n of all samples in each group compared to an adjusted cohort excluding samples with granulocytes contamination (- G) and less than 20% viable PBMCs (- V < 20%). NR, no risk; GR, genetic risk; ER, environmental risk.

Correlation of mitochondrial ROS levels and BHI

To determine a potential relationship between mitochondrial ROS levels and BHI, data of all samples (n = 45) were merged. Figure 47a reveals a significant, moderate, negative monotonic correlation between the BHI and intermediate and high mitochondrial ROS levels ($r = -0.35$, $p = 0.01$) indicating that an increase in ROS levels is partly related to a decreased BHI and vice versa. This suggests that mitochondrial superoxide generation amplifies mitochondrial damage, thereby having a negative impact on the cell's bioenergetic health. The association between the BHI and the high risk portion was smaller and not significant ($r = -0.23$, $p = 0.06$; Figure 47b). The total correlation tendency was always reflected in the individual correlations of the NR and ER group, but not the GR group, which showed correlation coefficients near zero.

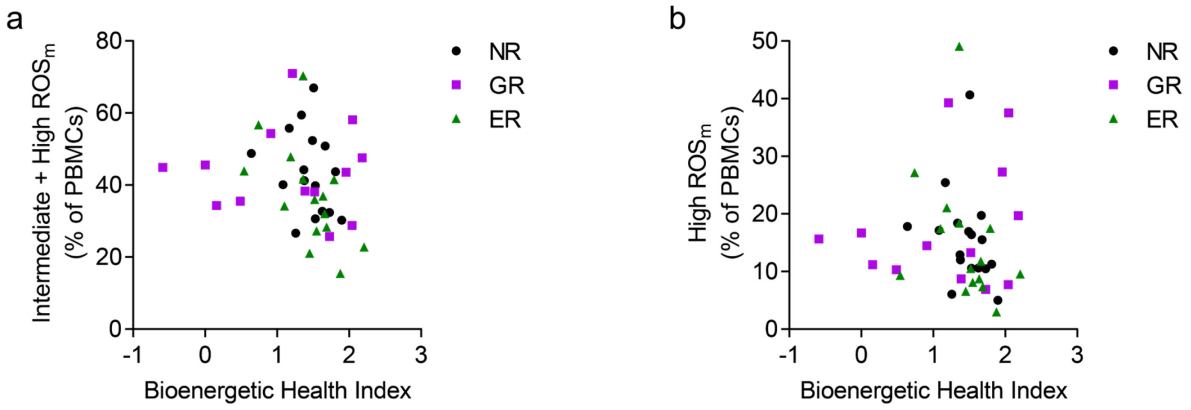

	All	NR	GR	ER
r	-0.35	-0.27	0.02	-0.66
p	*0.01	0.14	0.47	**0.004

	All	NR	GR	ER
r	-0.23	-0.47	0.09	-0.48
p	0.06	*0.03	0.38	*0.03

Figure 47. Correlation of mitochondrial ROS and BHI

Overall and individual group correlations (All, n = 45; NR, n = 17; GR, n = 13; ER, n = 15) of the BHI with intermediate and high ROS (**a**) as well as high ROS only (**b**) are shown together with the resulting Spearman correlation coefficients (r) and correlating p-values. **p < 0.01; *p < 0.05; p > 0.05 ns (not significant); NR, no risk; GR, genetic risk; ER, environmental risk.

Overall, neither psychiatric disease-relevant genetic nor environmental risk factors had a significant effect on superoxide levels and mitochondrial bioenergetics in PBMCs from healthy subjects. However, there seems to be a tendency towards reduced spare respiratory capacity as well as BHI in the GR group. Moreover, the correlation analysis confirmed a significant inverse relation between mitochondrial ROS levels and BHI in human PBMCs.

5 Discussion

5.1 Effects of *Cacna1c* knockdown on oxidative stress in HT22 cells

As summarized in Figure 48, the present study found that both siRNA-mediated downregulation and pharmacological inhibition of *Cacna1c* in neuronal HT22 cells mediated substantial protective effects on lipid peroxidation, mitochondrial integrity and function, and cell viability in a model of glutamate-induced cell death. These results suggest that, in paradigms of oxidative stress, *Cacna1c* is significantly involved in mechanisms of neuronal damage.

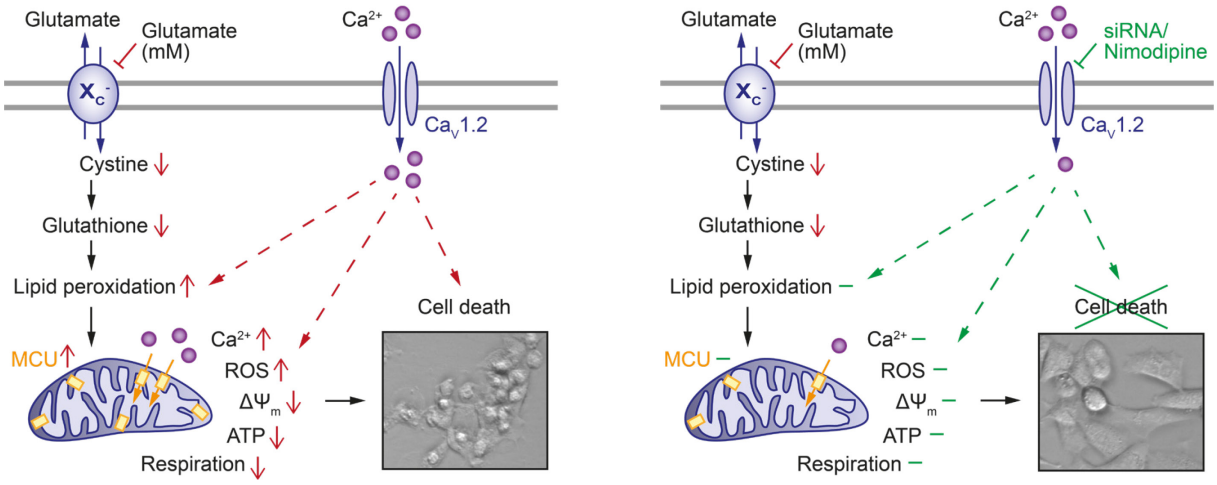

Figure 48. *Cacna1c* downregulation preserved mitochondrial function in glutamate-challenged neuronal HT22 cells

As mouse hippocampal HT22 cells do not express functional ionotropic glutamate receptors, glutamate toxicity is mediated via an oxidative stress-dependent pathway including inhibition of the glutamate/cystine antiporter, a subsequent depletion of glutathione and a consecutive impairment of mitochondrial function, which ultimately leads to neuronal cell death (left panel). This glutamate-induced cascade is positively affected by *Cacna1c* knockdown (siRNA) and pharmacological LTCC inhibition (nimodipine), which both mediate substantial protective effects on lipid peroxidation, mitochondrial integrity and function, and cell viability (right panel). X_C^-, glutamate/cystine antiporter; $Ca_V1.2$, voltage-gated L-type calcium channel; MCU, mitochondrial calcium uniporter; ROS, reactive oxygen species; $\Delta\Psi_m$, mitochondrial membrane potential; ATP, adenosine triphosphate.

These findings may also be of potential relevance in human diseases, since hippocampal and cortical atrophy, which are closely associated with abnormalities in neuronal plasticity and reduced resilience to cellular stress, have been frequently reported in patients with psychiatric disorders and early-life adverse experiences (53, 180). Furthermore, recent studies revealed that healthy subjects carrying the *CACNA1C* risk variant rs1006737 also show decreased prefrontal cortex activation and hippocampal dysfunction (30, 31). Even though it is not consistently observed (25, 181), the majority of evidence suggests that the non-coding risk SNP

rs1006737 is associated with enhanced *CACNA1C* expression and a gain of Cav1.2 function (26, 28, 182) suggesting deregulated Ca^{2+} signaling in the affected population and a significantly increased probability of psychiatric diseases (17). These findings are further confirmed by several animal studies demonstrating that, besides an increase in anxiety-associated behavior (183), *Cacna1c* heterozygous and forebrain-specific knockout mice exhibit an antidepressant-like phenotype, resilience to chronic stress, and a protective phenotype against mania-related behavior (33–35, 184). In addition to the data based on genetic modifications, the pharmacological inhibition of L-type calcium channels has repeatedly been linked to anti-stress and antidepressant-like effects, and reduced despair-like behavior in rodents (185–187). Moreover, dihydropyridine compounds with good CNS penetration, such as nimodipine showed promising mood stabilizing effects in humans with affective disorders, suggesting that LTCC antagonists represent an additional option in the pharmacotherapy of psychiatric diseases, and especially patients carrying the *CACNA1C* risk SNP could benefit from this alternative treatment strategy (17, 182, 188). Elevated cytosolic calcium levels, which may be associated with the *CACNA1C* risk SNP rs 1006737, represent a major upstream pathway that impairs mitochondrial function in BD (74). In this regard, it has been reviewed recently that systemic administration of the DHP isradipine suppresses cytosolic calcium transients, increases mitochondrial mass and lowers mitophagy in dopaminergic neurons (189). These findings in vivo are in line with the present results in vitro, revealing an enhanced resistance against oxidative stress and beneficial effects on mitochondrial function in conditions of reduced *Cacna1c* expression and LTCC blockade with nimodipine.

As reported previously, impaired cellular adaptation to environmental stress constitutes another major trigger in the pathophysiology of psychiatric disorders (9). In particular, it has been demonstrated in animal models that psychosocial stress results in depression-like behavior through the activation of oxidative and apoptotic mechanisms, including increased ROS levels, lipid peroxidation, reduced Bcl-2 expression, and increased caspase-3 (48). Additionally, in human post-mortem studies a downregulation of several antioxidant genes and an increase in protein oxidation have been observed in the hippocampus and prefrontal cortex of patients with BD (190, 191). Hence, the applied model of glutamate-induced oxidative stress in hippocampal HT22 cells constitutes a suitable system reflecting a common cellular response to environmental stress in the development and course of psychiatric illnesses.

It has been repeatedly proposed that interactions between genetic and environmental risk factors significantly contribute to the complex and heterogeneous clinical manifestations of affective disorders (9). The present study provides valuable insights into a gene-stress interaction by showing that reduced *Cacna1c* expression, which represents a beneficial genetic factor, mediated neuroprotective effects against oxidative stress, particularly at the level of mitochondria. Mitochondrial function is essential for cellular resilience and adaptation to oxidative stress. Here, siRNA-mediated knockdown of *Cacna1c* preserved mitochondrial

morphology, ATP values, respiration, membrane potential, and calcium homeostasis, and, furthermore, diminished excessive ROS formation in the employed model of oxidative glutamate toxicity. These findings are highly relevant as increasing evidence suggests a crucial role for mitochondrial dysfunction and related key determinants of cellular stress, such as intracellular Ca^{2+} deregulation and ROS formation in the development of mood disorders (71).

Furthermore, the present findings indicate a possible link between *Cacna1c* expression and mitochondrial function in oxytosis. In this paradigm of oxidative cell death, both *Cacna1c* gene silencing and pharmacological inhibition of LTCC using nimodipine were found to significantly diminish the glutamate-induced rise in mitochondrial calcium levels. It is concluded that this effect was attributed to a reduced cellular calcium influx, thereby leading to a mild inhibition of complex IV and also affecting the downstream mitochondrial Ca^{2+} influx. It has been shown previously, however, that Ca^{2+} influx through the plasma membrane only partially contributes to mitochondrial damage and cell death in the applied model of glutamate-induced oxidative stress (192). Based on the pronounced protective effects of *Cacna1c* knockdown and LTCC blockade, it has to be taken into consideration that, beyond its influence on calcium homeostasis at the plasma membrane, *Cacna1c* is possibly involved in further regulatory pathways at the level of mitochondria. For example, the calcium-dependent cytosolic phosphatase calcineurin dephosphorylates Drp1, thereby promoting its translocation to mitochondria and triggering detrimental mitochondrial fission; a process that is likely inhibited by *Cacna1c* gene silencing (193). Moreover, both *Cacna1c* knockdown and LTCC blockade probably lead to altered $Ca_V1.2$-dependent gene transcription regulation and may suppress toxic mitochondrial Ca^{2+} uptake via transcriptional repression of enhanced MCU expression following glutamate treatment in HT22 cells (170). Conversely, it has been described in arterial myocytes that mitochondria stimulate NF-κB-dependent $Ca_V1.2$ expression via elevated mitochondrial calcium concentration and subsequently induced mitochondrial ROS generation (194). In this regard, it is suggested that silencing of *Cacna1c* possibly counteracts the respective feed-forward signaling cascade. In mast cells, however, *Cacna1c* knockdown augmented apoptosis after IgE stimulation by disrupting mitochondrial integrity emphasizing that the maintenance of an appropriate mitochondrial calcium concentration is also essential for cell survival (195). The present study also revealed that *Cacna1c* downregulation led to a reduced formation of lipid peroxides in HT22 cells upon glutamate exposure indicating a partial action upstream of mitochondria. But since mitochondrial damage acts as an amplification factor of lipid peroxidation, mitochondria might still represent the main point of action of *Cacna1c* silencing in this model of oxidative glutamate toxicity (112).

Overall, the present findings suggest that the GWAS-confirmed psychiatric risk gene *CACNA1C* plays a major role in oxidative stress pathways with particular impact on mitochondrial integrity and function. However, the precise molecular mechanisms underlying

the effects of *CACNA1C* regulation on mitochondrial performance in neurons and the emerging link to neuronal plasticity, maintenance and function in the context of affective disorders remain to be elucidated.

5.2 Effects of *Cacna1c* haploinsufficiency on excitotoxicity in PCNs

In an in vitro model of neuronal excitotoxicity, heterozygous *Cacna1c* primary rat cortical cultures were continuously activated by 25 μM glutamate for 24 h before the cells' energy phenotype and viability were analyzed. As reported previously in cerebellar granule cells (127) and mouse cortical neurons (128), mild insults with low micromolar concentrations of glutamate triggered acute early necrosis in a very small proportion of cells, but predominantly induced delayed-onset apoptotic cell death after 24 h.

In the present study, *Cacna1c* haploinsufficiency in dissociated cortical neurons had no impact on the acute immediate increase in $[Ca^{2+}]_i$ after glutamate stimulation. This result corresponds to prior evidence showing that during the initial phase of excitotoxicity Ca^{2+} influx was primarily mediated by stimulated NMDA receptors and only secondary by other calcium channels such as $Ca_V1.2$ (196, 197). However, further depolarization with 50 mM KCl, thereby fully activating all voltage-sensitive channels including LTCC, also resulted in equal $[Ca^{2+}]_i$ elevations in both wildtype and constitutively heterozygous *Cacna1c* cultures. In this context, it has been identified before that chronic genetic loss of $Ca_V1.2$ channels in the CNS of mice led to a compensatory upregulation of Ca^{2+}-permeable AMPA receptors, but not $Ca_V1.3$ channels, thereby providing an alternative source of ligand-gated calcium signaling to maintain normal neuronal functioning (198).

Consequently, when focusing on the delayed long-term excitotoxic disturbances, the conducted measurements did not reveal any significant differences in respiratory and glycolytic rate, ATP levels as well as cell viability between the glutamate-treated wildtype *Cacna1c*$^{+/+}$ and heterozygous *Cacna1c*$^{+/-}$ neurons. Moreover, the neuronal cultures showed a strong, genotype-independent reduction in both *Cacna1c* mRNA and $Ca_V1.2$ protein levels after 24 h of glutamate exposure. These results, which highlight the tight regulation of $Ca_V1.2$, are in line with previous studies indicating rapid, dynamic calcium- and voltage-dependent inactivation mechanisms for $Ca_V1.2$ (23, 199) and stating that sustained glutamate exposure and excessive activation of NMDA receptors caused adaptive internalization and lysosomal degradation of $Ca_V1.2$ channels in cortical neurons already at subtoxic conditions (200). This protective negative feedback mechanism after the activation of ionotropic glutamate receptors has also been described for $Ca_V1.3$ in salamander retinal neurons, additionally identifying the endocytotic internalization process to be dynamin- and actin-dependent (201). Stronger stimulation, however, overrode this protective mechanism and the neurons underwent excitotoxicity (200) consistent with the current findings.

In accordance with the present study, the neurotoxic impact of pharmacological LTCC activation (202) and the, in turn, excitotoxic cell death reducing effect of LTCC blockade by dihydropyridines in vitro (200, 203, 204) and in vivo (197, 205) have been repeatedly demonstrated earlier. The protective effect of DHPs, which reversibly stabilize and induce inactivated channel states (18), underline the contribution of Ca^{2+} influx through $Ca_V1.2$ to neuronal death during glutamate-induced excitotoxicity. However, the multiplicity of conditions including substance concentrations, treatment combinations, time points, functional assays, culture characteristics, and in vivo models used, makes specific overall comparisons difficult. As mentioned before, differences between genetically and pharmacologically achieved effects may result from an adaptive compensation for the genetic loss of $Ca_V1.2$, thereby sustaining neuronal excitability (198, 206, 207).

In conclusion, the present findings from the heterozygous *Cacna1c* cortical rat cultures did not replicate the effects of the siRNA-mediated *Cacna1c* knockdown in hippocampal HT22 cells suggesting the need for a stronger, CNS-specific homozygous *Cacna1c* knockout to reach significance, the involvement of different glutamate-induced signaling cascades, and/or the complex regulation of $Ca_V1.2$ expression in primary neurons to be potential reasons. Future research may additionally focus on psychiatric disease-relevant model systems for example patient-derived (26) or CRISPR-edited (208) induced neurons carrying the intronic risk SNP rs 1006737 with special emphasis on changes in mitochondrial respiratome, proteome, and function in combination with cellular stress. Besides glutamate, other primarily ROS generating stressors such as RSL3, H_2O_2, tert-butyl hydroperoxide, or menadione (209) might be studied, also evaluating the effect of pharmacological LTCC blockade in these settings. A further promising future task might be the investigation of neuronal network activity in cultures or acute brain slices with genetic or pharmacological $Ca_V1.2$ modifications by using multielectrode array (MEA) recordings (210). In addition, this technique would allow for assessing the effects of neuron-glia interaction and inflammatory stimuli on neuronal circuit function; mechanisms that are also significantly involved in the pathophysiology of psychiatric disorders (76, 77).

5.3 Effects of *Cacna1c* haploinsufficiency on inflammation in microglia

In the present study, primary rat microglial cultures were stimulated in vitro with the bacterial endotoxin LPS mimicking a gram-negative infection and inducing an inflammatory, neurotoxic phenotype (211). Exposure to LPS activates microglial TLRs and initiates signal transduction cascades including NF-κB and NLRP3 leading to the transcription, synthesis, processing, and secretion of inflammatory cytokines, chemokines, and NO (77). Increasing evidence suggests that LPS-induced microglial activation is associated with a sustained increase in basal $[Ca^{2+}]_i$, which is evident as early as 1 h after LPS application (212) and thereby

coincides with the rise in glycolysis observed in the present work. It has been reported previously that the chronic elevation of basal calcium after LPS treatment (100 ng/ml, 24 h) constitutes a central regulatory element in the activation of mouse microglia, since chelation of intracellular Ca^{2+} strongly attenuated LPS-stimulated cytokine release (143). However, a rise in $[Ca^{2+}]_i$ alone failed to trigger any cytokine production on its own suggesting that increased $[Ca^{2+}]_i$ is necessary, but by itself not sufficient to induce the release of NO and cytokines (143). Dolga et al. further showed that the influx of extracellular calcium was a prerequisite for LPS-induced microglial activation in mouse primary cultures (213). Moreover, several studies indicate the involvement of LTCCs in mediating this Ca^{2+} entry (144). Even though controversially discussed (214, 215) with limited data available, mounting evidence, including the findings from the present study, supports the expression of voltage-gated calcium channels in non-excitable cells such as microglia (144, 216, 217). Reportedly, stimulation of human fetal microglia with chemokines (218, 219) or amyloid-β fragments (220) evoked a voltage-insensitive, DHP-sensitive Ca^{2+} influx. While another study detected a small, voltage-dependent, DHP-sensitive inward calcium current in cultured neonatal rat microglia potentiating superoxide production stimulated by phorbol 12-myristate 13-acetate (221). Further complicating the situation, specific immune splice variants of LTCCs have been described, which are voltage-insensitive and truncated, and might, thus, be differently activated compared to excitable cells and function, besides through ion transport, particularly via transcriptional regulation (217).

The present work demonstrated the expression of the LTCC isoform $Ca_V1.2$ at mRNA level. In line with this, a prior study even found an activation-dependent increase in α_{1C} subunit expression in stimulated rat microglia and murine BV2 cells treated with LPS and interferon-γ (IFN-γ) (144). Moreover, this publication showed that pharmacological LTCC blockade with nimodipine diminished the depolarization-induced increase in $[Ca^{2+}]_i$ as well as the release of TNF-α and NO in LPS + IFN-γ activated BV2 microglia. The inhibitory effect of nimodipine on LPS-stimulated microglial secretion of NO, TNF-α, and IL-1β was also observed in mixed cultures with dopaminergic neurons (222). Besides confirming the anti-inflammatory impact of nimodipine in LPS-challenged primary rat microglia, the present study adds specific genetic evidence by showing that *Cacna1c* haploinsufficiency attenuated, but not completely prevented, microglial activation, which resulted in a decreased downstream release of NO, IL-1α, IL-1β, IL-6, IL-10, and TNF-α after 24 h. It seems likely that a reduced elevation in $[Ca^{2+}]_i$ after LPS stimulation mediated the anti-inflammatory effects in both heterozygous *Cacna1c* and nimodipine-treated microglial cells. Rather than being the only control element for microglial activation, these findings furthermore indicate a more modulatory role for $Ca_V1.2$ in calcium-dependent inflammatory immune responses, also suggesting the involvement of other Ca^{2+} influx routes such as P2X7 and store-operated Ca^{2+} entry (223). Since both mediator systems, NO and cytokine production, were affected, it could be assumed that $Ca_V1.2$ is

possibly engaged in more proximal steps of the induction cascades instead of interfering with the later phases of release performance.

Increasing evidence also points to a key role of metabolic reprogramming in the regulation of the innate immune response (90). In accordance with previous studies, it was observed that, upon stimulation with the TLR agonist LPS, microglia switch from oxidative metabolism towards glycolysis. This LPS-induced elevation in glycolytic activity seems essential for the inflammatory response by providing energy and metabolic resources necessary for the associated microglial proliferation and cytokine production (224). Indeed, blockade of glycolysis using 2-DG resulted in a reduced TNF-α and IL-6 production in sevoflurane-stimulated primary mouse microglia (225) and LPS-activated human PBMCs (226) respectively. Additionally, mitochondrial ROS, generated in the course of microglial metabolic reprogramming, further assists in the activation of redox-sensitive signaling pathways including NF-κB and NLRP3 and could thereby represent an important intermediate step in pro-inflammatory gene expression (227). As shown previously, blocking the LPS-induced ROS generation with rotenone inhibited pro-inflammatory IL-1β secretion in mouse macrophages (228). Mitochondrial ROS production can be promoted through the LPS-mediated rise in cytosolic Ca^{2+}, which is dynamically stored in mitochondria, where it enhances electron flow into the ETC via TCA stimulation as well as inhibits complex IV via NO synthase activation (229). In the present study, *Cacna1c* haploinsufficiency led to an early and long-lasting reduction in glycolytic metabolism compared to wildtype upon LPS treatment. This blunted bioenergetic adaptation to an immune stimulus in heterozygous *Cacna1c* microglia is presumably linked to reduced cytosolic Ca^{2+} levels and might, to some extent, account for the observed decrease in the expression of several inflammatory markers including NO, IL-1β, IL-6, and TNF-α. Overall, these results strengthen the emerging role of $Ca_V1.2$ in regulating the TLR-mediated, calcium-dependent activation of microglia. However, in order to further elucidate the underlying molecular mechanisms, the specific effects of *Cacna1c* haploinsufficiency on $[Ca^{2+}]_i$, ROS generation, NADPH oxidase activity, expression of genes involved in the glycolytic switch, e.g. HIF-1α and c-Myc, as well as on critical convergent signaling pathways such as NF-κB activation and NLRP3 inflammasome formation remain to be investigated (90). In addition, co-cultures of activated microglia with neurons or even astrocytes would shed more light on related neuronal stress responses in respect of the *Cacna1c* genotype-dependent microglial susceptibility to LPS.

A wide variety of studies have identified microglial activation in psychiatric disorders including schizophrenia, BD, and MDD (77, 94, 230). Since isolated culture systems cannot reflect the heterogeneity of microglia and the complexity of their responses in the physiological environment, future studies may focus on the impact of *Cacna1c* haploinsufficiency and pharmacological LTCC blockade on microglial activation in an in vivo rat model of neuroinflammation, additionally assessing its effect on anxiety- and depressive-like behaviors.

This would also provide an opportunity to correlate the cytokine profiles of brain microglia and PBMCs in order to establish these as potential peripheral biomarkers reflecting the severity of microglial activation and depressive symptoms/behaviors. Furthermore, it should be considered that the bacterial endotoxin LPS stimulates microglia only on a single receptor, which may lead to findings not transferable to the signaling cascades involved in vivo.

In conclusion, the present findings suggest that the GWAS-confirmed psychiatric risk gene *CACNA1C* plays a significant role in neuroinflammatory processes with particular impact on microglial activation and bioenergetics. Moreover, a dual mode of action might be assumed, since reduced *Cacna1c* expression and DHP treatment had neuroprotective as well as anti-inflammatory effects on glutamate-challenged neuronal HT22 cells and LPS-stimulated microglia, respectively. Thus, modulating L-type calcium signaling may offer an effective therapeutic strategy in psychiatric disorders, where neuronal atrophy and inflammation both contribute to disease onset and progression.

5.4 Effects of gene-environment interactions in isolated mitochondria

In contrast to the initial evidence-based hypothesis, no major differences in brain mitochondrial performance could be detected between constitutive haploinsufficient *Cacna1c*$^{+/-}$ rats and wildtype littermates irrespective of the environmental condition, i.e. post-weaning social isolation, standard housing, and social and physical environmental enrichment. By studying different aspects of mitochondrial function such as respiration, ROS production, $\Delta\Psi_m$, and ETC complex protein levels, it was repeatedly confirmed that there is no genotype effect, no distinct environment effect, and also no GxE interaction, emphasizing the robustness and reliability of the present (negative) results. A potential link between altered expression of the psychiatric risk gene *Cacna1c* and cerebral mitochondrial function has not been investigated in vivo so far. It is well known, however, that the respiratory chain is regulated by the cytosolic calcium concentration (231), which, in turn, is very likely dependent on the level of Cav1.2 at the cell membrane. Despite a ~50% reduction in brain Cav1.2 levels in the present rat model, the heterozygous *Cacna1c* genotype consistently had no effect on PFC and HC bioenergetics compared to wildtype littermates, independent of the hemisphere and environmental condition studied. One possible reason might be that developmental *Cacna1c* heterozygosis either is not sufficient to perceive detectable changes, or induces adaptive mechanisms facilitating alternative calcium influx routes. In this regard, it has been reported previously that chronic genetic loss of Cav1.2 in the CNS of mice leads to a compensatory upregulation of calcium-permeable AMPA receptors, thereby maintaining appropriate intracellular calcium concentrations and normal neuronal plasticity (198).

In the context of GxE interactions, it has been shown in Chapter 4.1 that *Cacna1c* downregulation mediates cellular resilience against oxidative stress in neuronal HT22 cells particularly at the level of mitochondria (232). Furthermore, using different *Cacna1c* siRNAs, these previous findings indicate that a sufficiently strong knockdown of at least 62% in Cav1.2 expression is essential to achieve significant protective effects in mouse hippocampal HT22 cells exposed to oxidative stress including the maintenance of ATP production, respiration, and $\Delta\Psi_m$ as well as the prevention of excessive ROS formation (232, 233). Consistently, several animal studies have confirmed that modified *Cacna1c* expression modulates stress susceptibility in adult male mice (29, 234). However, in these previous studies, mitochondrial parameters were not analyzed. For example, the region-specific deletion of *Cacna1c* in the nucleus accumbens was associated with increased stress sensitivity in mice exposed to chronic social defeat for ten days (234). Accordingly, *Cacna1c* depletion in forebrain glutamatergic neurons during embryonic development promoted susceptibility to chronic stress in mice subjected to social defeat for three weeks (29). Conversely, four weeks of chronic unpredictable stress induced depressive- and anxiety-like behavior in both *Cacna1c* heterozygous mice and their wildtype littermates when assessed 1-2 days following stress (34). Similar to this unchanged performance in PFC-dependent behavioral tasks, *Cacna1c* haploinsufficiency did not interact with four-week early life social isolation stress to affect PFC or HC mitochondrial bioenergetics in the present rat study. Discrepancies in the above-mentioned findings might be related to different species, sites of the genetic modification, age, stress paradigms and duration, or readouts. Environmental enrichment was initially intended for rescuing potential adverse genotype effects on mitochondrial performance and had neither a combined gene-environment impact, nor a beneficial influence on its own in the current experiments. However, physical and social environmental enrichment showed a general effect on the rats' biometric characteristics and ROS generation. In line with prior studies, environmentally enriched animals had significantly lower body weights than their non-enriched controls, possibly attributed to a higher physical activity and most likely influenced by the type and duration of enrichment (235). Moreover, four weeks of environmental enrichment resulted in significantly increased mitochondrial ROS levels in the rats' prefrontal cortex, which constitutes a common response of tissues to physical exercise (236).

Compared to *Cacna1c*-associated effects, the impact of chronic stress alone on brain mitochondrial function has already been examined in a number of rodent studies (for review see (61, 237)). Traditional chronic stress paradigms, including chronic unpredictable stress (CUS) for six weeks and chronic restraint stress (CRS) for two to three weeks, are established animal models of depression. Published findings indicate that CUS in adult male rats is accompanied by inhibited activities of the mitochondrial respiratory chain complexes I, III, and IV in whole tissue homogenates from cerebral cortex and cerebellum, but not from PFC and HC (238). Under the same conditions, another study described decreased complex I and

IV activities in isolated PFC and HC mitochondria (239). Opposing results, however, showed increased complex I, II, and III activities in PFC tissue of adult Wistar rats exposed to CUS (240). In mice, CUS led to a reduced respiratory control ratio in isolated mitochondria from cortex and HC (161). Using the CRS model, further research revealed decreases in enzyme activity of complex I-III without affecting complex IV activity, oxygen consumption, and ATP production in isolated cortical rat mitochondria (110). CRS in mice caused complex IV inhibition in mitochondria isolated from HC (241) and diminished complex I-driven State 3 respiration in isolated forebrain mitochondria (242). Collectively, variations in stress induction paradigms, brain region selection, tissue processing, method application, and parameter evaluation probably contribute to the diverging and in part conflicting results regarding the impact of chronic stress on mitochondrial outcomes. Furthermore, existing studies largely focused on ETC complex activity measurements and observed in most cases decreased activities with effects ranging between 30 and 70% (237). However, it has been demonstrated in isolated non-synaptic rat mitochondria that complex I, III and IV activities could be reduced by more than 60% before respiration and ATP synthesis are considerably affected (243). This suggests that moderate changes in candidate complex activities have little effect on the overall capability of mitochondria to maintain brain energy homeostasis, which is dependent on the integrity of many processes. On the contrary, the oxygen consumption and RCR, which were measured in the present and some previous studies, represent a more comprehensive and revealing option to detect bioenergetic dysfunction in isolated mitochondria (175).

With four weeks of post-weaning social isolation, the present work used a different model of environmental stress and found no changes in mitochondrial respiration, membrane potential, ROS formation, or protein levels of the ETC complexes in rat PFC and HC compared to the socially reared littermate controls. Such chronic social isolation represents a mild and more natural stressor than CUS and CRS, which still evokes a variety of neurobehavioral changes in rodents comparable to those observed in patients with psychiatric disorders, including anxiety and depression (244). As reported previously, four weeks of juvenile social isolation stress led to decreased ATP and elevated ROS levels in the HC of male mice (245). Post-weaning social isolation for eight weeks also resulted in reduced ATP accumulation in the frontal cortex, but not in the striatum of male Sprague-Dawley rats (246). In addition, male Wistar rats showed slightly increased complex IV activity as well as unchanged mitochondrial membrane potential and ROS production in the PFC after one-week social isolation during the pre-pubertal period (247). All these parameters, which were used as measures of mitochondrial function, were assessed from whole frozen tissue, whereas the present experiments were predominantly conducted with isolated fresh mitochondria. Thus, the published measurements are solely normalized to the total protein content in the tissue homogenates, making it impossible to distinguish if the existent findings are based on altered mitochondrial quantity or quality. Whilst the meaningful normalization to mitochondrial protein in the

present study allowed to specifically evaluate the functional status of brain mitochondria. Besides varying stress duration and assays used, this apparent difference in the normalization procedure might be a further explanation for the inconsistent findings and additionally impedes the comparability of the studies.

PFC and HC are among the most frequently studied brain regions in neuropsychiatric disorders based on their documented stress sensitivity, especially during the juvenile developmental period and their particular implication in disease-relevant neuronal circuits (248). Nonetheless, while providing brain-region-specific analyses of PFC and HC mitochondria, the present work did not differentiate between cells or cell subtypes, sharing this limitation also with all relevant prior studies. Mitochondria isolated from brain tissue originate from different cell types including neuronal and glial cells. This heterogeneous composition of cells could mask potential cell type-dependent variations in stress susceptibility and changes in the glia-neuron ratio. Furthermore, the expression of Cav1.2 varies between excitable and non-excitable cells (249), which might, thus, be differently affected by the heterozygous *Cacna1c* knockout. The investigation of cell type-specific mitochondrial bioenergetics therefore constitutes a key challenge for future studies.

Although brain mitochondrial function was not affected or adaptive mechanisms were not yet exhausted in the particular risk GxE setting studied, i.e. *Cacna1c* haploinsufficiency and post-weaning social isolation, mitochondria might still represent an important intersection point between genetic alternations, psychosocial experiences and abnormalities in cerebral energy metabolism, synaptic plasticity in psychiatric disorders (59). The overall inconsistent findings in this research field highlight the complexity and heterogeneity of those illnesses and suggest that study results are strongly dependent on many factors, such as animal species, experimental design, and analysis methods. Hence, additional investigations are required to determine the disease-relevant effects on bioenergetics also including long-term studies of gene-environment interactions in both sexes, since the present study found a significant effect of *Cacna1c* haploinsufficiency on mitochondrial respiration in the PFC of ten-month-old male, but not female rats, which was not evident in the two-month-old animals. The extent of this observed genotype effect under standard housing conditions might further vary in combination with different environmental situations and may overall contribute to our understanding of the pathophysiology of neuropsychiatric disorders.

5.5 Effects of genetic and environmental risk on mitochondria in PBMCs

In the present study mitochondrial ROS levels and respiratory parameters in PBMCs of healthy females with either a family history of psychiatric disorders or an experience of maltreatment during childhood were compared to those of a no risk control group. Both, the

genetic and the environmental component, are strong risk factors for the development of neuropsychiatric illnesses, which, reportedly, are also associated with mitochondrial dysfunction (59). However, significant alterations in mitochondrial ROS formation, ATP production, proton leak, basal, maximal, and non-mitochondrial respiration were not yet evident in the cryopreserved PBMCs of healthy subjects with genetic or environmental risk. Consistent with these results from the GR and ER group, a recent study found unchanged mitochondrial complex I-V function using monocytes of individuals that were at clinical high risk for psychosis and already showed prodromal symptoms (250). Nevertheless, complex III function was inversely associated with the severity of prodromal negative symptoms such as social anhedonia (251). In contrast to these findings, mitochondrial perturbations were detected in PBMCs of patients with an established psychiatric disorder (107–109). Decreased complex I, but not complex II and III activity was found in frozen mitochondria isolated from PBMCs of chronic schizophrenic patients (107). These changes in complex I activity were accompanied by increased levels of lipid peroxidation, but not protein oxidation in blood plasma. PBMCs of euthymic BD patients revealed no differences in the respective parameters though. Fresh intact platelets of depressive patients in partial remission showed decreased basal and maximal respiration, whereas the ratio of both values remained unchanged compared to healthy controls (108). Besides basal and maximal respiration, ATP production, spare capacity, and coupling efficiency were significantly lower in cryopreserved PBMCs of female patients with a current diagnosis of major depression (109). In the present study, a trend towards reduced mitochondrial spare capacity was also observed in PBMCs from the genetic risk group. By focusing on environmental risk factors for psychiatric disorders, it has been shown recently that frozen PBMCs of chronically stressed females caring for a child with an autism spectrum disorder exhibited decreased complex II and IV activity per unit of mitochondria (252). Conversely, increased ratios of basal, ATP-linked, and non-mitochondrial respiration over maximal respiration were identified in cryopreserved PBMCs of females, which experienced severe maltreatment during childhood, also including individuals with psychiatric diagnoses (52). This higher physiological activity was accompanied by increased serum ROS levels, unaltered mitochondrial density as well as enhanced spontaneous secretion of pro-inflammatory cytokines. In comparison, frozen PBMCs of healthy females with environmental risk, i.e. exposed to at least two forms of maltreatment during childhood, showed slightly lower mitochondrial ROS levels and unchanged respiratory ratios in the present study. Differences in study cohort characteristics, potential antipsychotic medication, cell type, cell storage, and measuring method to assess mitochondrial function make overall comparability of the reported findings difficult. In most studies, however, reduced ETC complex activity or respiration was linked to the risk for or already established psychiatric disorders using frozen PBMCs.

Since the Bioenergetic Health Index (BHI) comprises several parameters of a person's respiration profile and thereby provides more information than the individual mitochondrial function measures (179), it was also calculated in this study. Here, though not significant, a trend towards lower BHI in PBMCs of the GR, but not the ER group compared to the no risk control was observed. By considering i.a. the spare respiratory capacity, the BHI even has predictive value because it can already identify alterations in mitochondrial performance before cellular energy failure occurs. Furthermore, it has been demonstrated previously that the BHI is dynamically sensitive to acute oxidative stress in human monocytes (253). This observation is in line with the present results showing a significant correlation of decreased BHI with increasing levels of mitochondrial superoxide. In relation to these findings, compromised mitochondrial metabolism often leads to excess superoxide production, thereby modulating redox-sensitive inflammatory pathways and inducing oxidative stress, which most likely play a role in diverse psychiatric disorders (45, 229).

The outcomes of this study should be interpreted in view of the following limitations. First, a broad range of cell viabilities (8-71%) were encountered after thawing suggesting considerable quality differences between the individual PBMC samples. It is known that mononuclear cell recovery decreases with increased time delay before PBMC isolation. Furthermore, as tested previously, cryogenic storage reduced cell viability of human peripheral blood leucocytes by 20% (254). Beyond that, cryopreservation also had a time-dependent impact on mononuclear cell bioenergetics, including decreased basal respiration, ATP production, and BHI as well as increased non-mitochondrial respiration compared to fresh PBMCs. Spare capacity and proton leak, however, remained unchanged (226). Freezer storage time should therefore be evaluated as potential confounding factor. Second, as supported by the flow cytometric analyses, the PBMC samples were probably contaminated with platelets, red blood cells, and/or granulocytes to varying extents. Prior research revealed that each type of blood cell is characterized by a distinct bioenergetic profile (255). Consequently, the mitochondrial function measurements of these mixed populations were weighted averages of the metabolic activities of the different cell types included. Subsequent studies should aim for cell type-specific investigations or the quantitative assessment of PBMC composition to ensure conformity among the samples. Lastly, data variation was considerably high, particularly in the GR and ER group. In this study, variance of the BHI was not affected by sample quality and composition suggesting an involvement of other covariates or a substantial inter-individual variability. Detecting potential, subtle changes in mitochondrial bioenergetics between the psychiatric risk groups might therefore require more specific risk cohorts or a larger sample size.

Further analyses of the existing data could imply correlations with individual subject characteristics such as age, body mass index, organic diseases, or smoking status. It has been published previously that smoking, for example, leads to a decreased ETC complex IV activity

in PBMCs (256), thereby possibly also influencing mitochondrial respiration and ROS levels. In addition, a detailed evaluation of the underlying subjects from the observed subpopulation in the GR group with particularly low spare capacity might reveal a certain relationship. Moreover, a longitudinal follow-up assessment of all probands to check for a potential switch from healthy to diseased and associated changes in PBMC mitochondrial bioenergetics would enrich the current findings. Beyond that, future studies may include a combined GxE and a specific *CACNA1C*-related risk group as well as MDD, BD, and SZ patients serving as direct reference. To substantiate future conclusions, the obtained results should be normalized to mitochondrial content per cell by measuring citrate synthase activity (52, 252). Since stimulation of the PBMC samples was not feasible due to insufficient amount of cells, studying changes in mitochondrial performance in response to either immune-inflammatory challenges with LPS and polyinosinic:polycytidylic acid (257) or oxidative stress generated by 2,3-dimethoxy-1,4-napthoquinone (258) could also be a focus of subsequent investigations.

In conclusion, mitochondrial bioenergetics and ROS levels in human PBMCs were correlated, but alterations in both parameters were not yet evident in the psychiatric disease-relevant genetic or environmental risk groups. Consequently, further research is required in order to shed more light on the early pathological mechanisms underlying neuropsychiatric disorders.

6 Summary

Affective disorders such as major depression and bipolar disorder are among the most prevalent forms of mental illness, and their pathophysiology involves complex interactions between genetic and environmental risk factors. However, the underlying mechanisms explaining how genetic and environmental alterations affect the risk for psychiatric disorders are still largely unknown. Confirmed by several genome-wide association studies over the past ten years, *CACNA1C* represents one of the strongest and most replicable psychiatric risk genes. Besides genetic predispositions, environmental influences such as childhood maltreatment or chronic stress also contribute to disease vulnerability. In addition, increasing evidence suggests a crucial role for mitochondrial dysfunction, oxidative stress, excitotoxicity, and neuroinflammation in the development of major neuropsychiatric disorders. Furthermore, mitochondrial dysfunction in peripheral blood mononuclear cells (PBMCs) is currently being discussed as a potential biomarker for affective disorders supporting early diagnosis, control of disease progression, and evaluation of treatment response.

In a translational setting, the present project focused on the effects of defined gene-environment interactions on brain mitochondrial integrity and function in order to provide new insights into pathophysiological mechanisms of affective disorders and to identify novel therapeutic targets with potential relevance for future treatment strategies.

Using immortalized mouse hippocampal HT22 cells, a well-established model system to investigate glutamate-mediated oxidative stress, it was demonstrated that both siRNA-mediated *Cacna1c* gene silencing and L-type calcium channel (LTCC) blockade with nimodipine significantly prevented the glutamate-mediated rise in lipid peroxidation, excessive ROS formation, collapse of mitochondrial membrane potential, loss of ATP, reduction in mitochondrial respiration, and ultimately neuronal cell death. Moreover, both *Cacna1c* knockdown and pharmacological LTCC inhibition altered $Ca_V1.2$-dependent gene transcription, thereby suppressing the glutamate-induced expression of the inner mitochondrial membrane calcium uptake protein MCU. Accordingly, downregulation of *Cacna1c* substantially diminished the elevation in mitochondrial calcium levels after glutamate treatment. In the employed paradigm of oxidative glutamate toxicity, *Cacna1c* depletion also protected against detrimental mitochondrial fission and stimulated mitochondrial biogenesis without affecting mitophagy, thus promoting the turnover of mitochondria and preventing the accumulation of dysfunctional mitochondria in neuronal HT22 cells. These data imply that upstream genetic modifications, e.g. reduced *CACNA1C* expression, converge to control mitochondrial function, resulting in cellular resilience against oxidative stress.

In primary cortical rat neurons, heterozygous *Cacna1c* knockout partially reduced *Cacna1c* expression but had no impact on either initial increase in $[Ca^{2+}]_i$ or delayed perturbations in

mitochondrial bioenergetics, ATP levels, and cell viability in response to glutamate-mediated excitotoxicity. Furthermore, *Cacna1c* mRNA and protein expression levels were subject to strong regulation and degradation in this model of neuronal excitotoxicity. Partial neuroprotection against long-term glutamate toxicity by pharmacological LTCC blockade highlighted a potential dose-effect-dependency and the involvement of LTCCs in this cell death pathway.

In primary rat microglia cultures, both *Cacna1c* haploinsufficiency and nimodipine treatment were associated with reduced morphological changes and glycolytic metabolism upon lipopolysaccharide (LPS) stimulation. The LPS-induced shift from oxidative phosphorylation towards glycolysis seems essential for the inflammatory response, since the downstream release of NO, IL-1α, IL-1β, IL-6, IL-10, and TNF-α was also decreased in heterozygous *Cacna1c* as well as nimodipine-treated microglial cells. These results indicate a major functional role for Ca$_V$1.2-dependent signaling in the pro-inflammatory activation of microglia, the innate immune cells of the central nervous system.

By simulating the interaction of psychiatric disease-relevant genetic and environmental factors in vivo, the present study additionally evaluated their potential effect on brain mitochondrial function using a constitutive heterozygous *Cacna1c* rat model in combination with a four-week exposure to either post-weaning social isolation, standard housing, or social and physical environmental enrichment during the juvenile developmental period. In this specific gene-environment setting, isolated mitochondria from prefrontal cortex and hippocampus, both representing particularly susceptible brain regions in neuropsychiatric disorders, did not reveal considerable differences in mitochondrial bioenergetics, respiratory chain complex protein levels, superoxide formation, and membrane potential between the investigated conditions.

Finally, mitochondrial function was investigated in human PBMCs from probands recruited in the Marburg/Münster Affective Disorders Cohort Study (MACS). However, neither a family history of psychiatric disorders nor an experience of maltreatment during childhood had a significant effect on mitochondrial superoxide levels and respiratory parameters in PBMCs from healthy female subjects. Consequently, further research is required in order to shed more light on the early pathological mechanisms underlying neuropsychiatric disorders.

Overall, the present findings suggest that the GWAS-confirmed psychiatric risk gene *CACNA1C* plays a significant role in oxidative stress as well as neuroinflammatory pathways with particular impact on mitochondrial integrity and function, thereby adding to a better understanding of the intracellular processes likely involved in the pathophysiology of *CACNA1C*-associated disorders. Thus, modulating L-type calcium signaling may offer an effective therapeutic strategy in psychiatric disorders, where neuronal atrophy and inflammation contribute to disease pathophysiology.

7 Zusammenfassung

Affektive Störungen wie schwere Depressionen und bipolare Störungen gehören zu den häufigsten Formen psychischer Erkrankungen. Ihre Pathophysiologie beruht auf komplexen Wechselwirkungen zwischen genetischen und umweltbedingten Risikofaktoren. Wie genetische und umweltbedingte Veränderungen das Risiko für psychiatrische Erkrankungen auf molekularer Ebene beeinflussen, ist jedoch noch weitgehend ungeklärt. Mehrere genomweite Assoziationsstudien (GWAS) der letzten zehn Jahre zeigen eindeutig, dass *CACNA1C* zu den bedeutendsten neuropsychiatrischen Risikogenen zählt. Neben genetischen Prädispositionen tragen auch Umwelteinflüsse wie Misshandlung in der Kindheit oder chronischer Stress zu einer erhöhten Krankheitsanfälligkeit bei. Darüber hinaus gibt es in letzter Zeit vermehrt Hinweise darauf, dass mitochondriale Dysfunktion, oxidativer Stress, Exzitotoxizität und Neuroinflammation bei der Entwicklung psychiatrischer Störungen eine entscheidende Rolle spielen. Zudem werden mitochondriale Funktionsstörungen in peripheren mononukleären Blutzellen (PBMCs) derzeit als potentieller Biomarker für affektive Störungen diskutiert, die eine frühe Diagnose, eine Beurteilung des Krankheitsverlaufs und die Bewertung des Ansprechens auf eine Behandlung unterstützen sollen.

Mit Hilfe eines translationalen Ansatzes, beschäftigte sich die vorliegende Arbeit mit den Auswirkungen definierter Gen-Umwelt-Interaktionen auf die Integrität und Funktion von Mitochondrien in Neuronen und Mikrogliazellen, um tiefere Einblicke in pathophysiologische Mechanismen affektiver Störungen zu gewinnen und neue therapeutische Zielstrukturen mit potentieller Relevanz für zukünftige Behandlungsstrategien zu identifizieren.

In immortalisierten hippokampalen HT22 Mauszellen, einem etablierten Modellsystem zur Untersuchung von Glutamat-vermitteltem oxidativem Stress, konnten durch *Cacna1c*-Inhibition auf mitochondrialer wie auch auf zellulärer Ebene protektive Effekte aufgezeigt werden. Sowohl *Cacna1c* Knockdown als auch die Blockade von L-Typ-Calciumkanälen (LTCC) mit Nimodipin hemmten den Glutamat-induzierten Anstieg der Lipidperoxidation, die übermäßige Bildung reaktiver Sauerstoffspezies (ROS), den Abfall des mitochondrialen Membranpotentials, den Verlust an ATP, die Verringerung der mitochondrialen Atmung und letztlich auch den neuronalen Zelltod. Darüber hinaus führten *Cacna1c* „Gen-Silencing“ sowie pharmakologische LTCC-Hemmung zu einer veränderten $Ca_V1.2$-abhängigen Regulation der Gentranskription, wodurch die Expression des mitochondrialen Calcium-Uniporters (MCU) nach Glutamatschädigung signifikant unterdrückt wurde. Dies führte in den *Cacna1c*-defizienten Zellen auch zu einem deutlich verminderten Calciumanstieg in den Mitochondrien nach Glutamatexposition. Im verwendeten Modell der oxidativen Glutamattoxizität schützte die siRNA-vermittelte *Cacna1c* Depletion auch vor mitochondrialer Fragmentierung und stimulierte die mitochondriale Biogenese, ohne sich auf die Mitophagie

auszuwirken, wodurch der mitochondriale Umsatz gefördert und die Akkumulation dysfunktionaler Mitochondrien in neuronalen HT22-Zellen vermindert wurde. Dies deutet darauf hin, dass die Effekte vorgeschalteter genetischer Modifikationen, wie zum Beispiel einer reduzierten *CACNA1C* Expression, konvergieren und sich auf die mitochondrialen Funktionen auswirken, was zu einer erhöhten zellulären Resilienz gegen oxidativen Stress beiträgt.

In primären kortikalen Rattenneuronen reduzierte der heterozygote *Cacna1c* Knockout die Proteinexpression auf etwa die Hälfte der Wildtyp-Level. Nach Glutamat-vermittelter Exzitotoxizität war jedoch weder ein Einfluss auf den initialen Anstieg der intrazellulären Calciumkonzentration noch auf die zeitverzögerten Störungen der mitochondrialen Bioenergetik, der ATP Spiegel oder der Zellviabilität nachzuweisen. Ferner unterlagen die *Cacna1c* mRNA- und Proteinexpressionsspiegel in diesem Modell der neuronalen Exzitotoxizität starken Regulations- und Abbaumechanismen. Dagegen unterstreicht die partielle Neuroprotektion gegen Glutamattoxizität durch pharmakologische LTCC-Blockade mit Dihydropyridinen eine mögliche Dosis-Wirkungs-Abhängigkeit und die Beteiligung von LTCCs im Glutamat-vermittelten exzitotoxischen Zelltod.

In primären Mikroglia-Kulturen der Ratte waren *Cacna1c* Haploinsuffizienz sowie Nimodipin-Behandlung assoziiert mit reduzierten morphologischen Veränderungen und einer abgeschwächten glykolytischen Aktivität nach Lipopolysaccharid (LPS)-Stimulation. Darüber hinaus scheint die LPS-induzierte Verschiebung vom oxidativen Metabolismus hin zur Glykolyse für die weitere Entzündungsreaktion essenziell zu sein, da zusätzlich eine verminderte Freisetzung von NO, IL-1α, IL-1β, IL-6, IL-10 und TNF-α sowohl in heterozygoten *Cacna1c* als auch in Nimodipin-behandelten Mikrogliazellen beobachtet wurde. Diese Ergebnisse weisen auf eine wichtige funktionelle Rolle Cav1.2-abhängiger Signalwege in der pro-inflammatorischen Aktivierung der Mikroglia als zellulärer Bestandteil der angeborenen Immunität im zentralen Nervensystem hin.

Durch die Simulation krankheitsrelevanter Interaktionen genetischer und umweltbedingter Faktoren im Tiermodell wurden in dieser Studie zudem ihre potentiellen Effekte auf die Funktion zerebraler Mitochondrien evaluiert. Dies wurde mithilfe konstitutiv heterozygoter *Cacna1c* Ratten realisiert, welche während der juvenilen Entwicklungsphase für vier Wochen entweder in sozialer Isolation, unter Standardbedingungen oder in sozial und materiell angereicherter Umgebung gehalten wurden. Allerdings zeigten isolierte Mitochondrien sowohl aus dem präfrontalen Cortex als auch aus dem Hippocampus keine wesentlichen Unterschiede zwischen den untersuchten Gen-Umwelt Kohorten im Hinblick auf die mitochondriale Bioenergetik, die Proteinkomplexe der Atmungskette, die Superoxidproduktion und das Membranpotential.

In einem weiteren Teil dieser Studie wurde an humanen PBMCs aus der MACS (Marburg/Münster Affective Disorders Cohort Study) Kohorte gezeigt, dass weder eine familiäre Vorgeschichte psychischer Störungen noch die Erfahrung von Misshandlung in der Kindheit einen signifikanten Effekt auf mitochondriale ROS Level und Parameter der mitochondrialen Respiration in PBMCs gesunder weiblicher Probanden hatte. Hierzu sind weitere Untersuchungen erforderlich, um die frühen pathologischen Mechanismen besser zu verstehen, die neuropsychiatrischen Erkrankungen zugrunde liegen.

Insgesamt deuten die vorliegenden Forschungsergebnisse darauf hin, dass das durch GWAS ermittelte psychiatrische Risikogen *CACNA1C* eine zentrale Rolle in der Regulation mitochondrialer Integrität und Funktion spielt und so auch neuroinflammatorische Signalwege und die Resilienz gegen oxidativen Stress beeinflusst. Diese Arbeit trägt damit zu einem besseren Verständnis der intrazellulären Prozesse bei, die vermutlich an der Pathophysiologie von *CACNA1C*-assoziierten Erkrankungen beteiligt sind. Die Modulation zerebraler LTCC könnte somit eine therapeutische Option bei psychiatrischen Störungen darstellen, die sowohl durch neuronale Atrophie als auch durch Entzündungsprozesse gekennzeichnet sind.

Abbreviations

2-DG	2-Deoxy-D-glucose
ADP	Adenosine diphosphate
AIF	Apoptosis inducing factor
AM	Acetoxymethyl
AMPA	α-Amino-3-hydroxy-5-methyl-4-isoxazolepropionate
ANOVA	Analysis of variance
ATP	Adenosine triphosphate
BCA	Bicinchoninic acid
BD	Bipolar disorder
BHI	Bioenergetic health index
BID	BH3-interacting domain death agonist
bp	Base pair
BSA	Bovine serum albumin
$[Ca^{2+}]_i$	Intracellular calcium concentration
CCCP	Carbonyl cyanide 3-chlorophenylhydrazone
CI	Confidence interval
CNS	Central nervous system
CRS	Chronic restraint stress
CTQ	Childhood trauma questionnaire
CUS	Chronic unpredictable stress
CytC	Cytochrome C
$\Delta\Psi_m$	Mitochondrial membrane potential
DAMPs	Damage-associated molecular patterns
DAPI	4′,6-Diamidine-2′-phenylindole
DHP	Dihydropyridine
DIV	Days in vitro
DMEM	Dulbecco’s modified Eagle’s medium
DMSO	Dimethyl sulfoxide
DNA	Deoxyribonucleic acid
DNase	Deoxyribonuclease
Drp	Dynamin-related protein
EBSS	Earle’s balanced salt solution
ECAR	Extracellular acidification rate
ETC	Electron transport chain
FBS	Fetal bovine serum
FCCP	Carbonyl cyanide-4-(trifluoromethoxy)phenylhydranzone

GFAP	Glial fibrillary acidic protein
GPX	Glutathione peroxidase
GSH	Glutathione
GWAS	Genome wide association study
GxE	Gene-environment interaction
HBSS	Hank's balanced salt solution
HC	Hippocampus
IFN	Interferon
IL	Interleukin
L-Arg	L-Arginine
LC3B	Light chain 3 isoform B
LOX	Lipoxygenase
LPS	Lipopolysaccharide
LTCC	L-type calcium channel
MACS	Marburg/Müster affective disorders cohort study
MAP	Microtubule-associated protein
MCP	Monocyte chemoattractant protein
MCU	Mitochondrial calcium uniporter
MDD	Major depressive disorder
MEA	Multielectrode array
MEM	Minimum essential medium
Mfn	Mitofusin
MIP	Macrophage inflammatory protein
mPTP	Mitochondrial permeability transition pore
MTT	3-(4,5-Dimethyl-2-thiazolyl)-2,5-diphenyl-2H-tetrazolium bromide
MW	Molecular weight
NF	Nuclear factor
NLR	Nucleotide-binding oligomerization domain (NOD)-like receptor
NLRP	NOD-, leucine-rich repeat (LRR)- and pyrin domain-containing
NMDA	N-methyl-D-aspartate
NO	Nitric oxide
NOS	Nitric oxide synthase
OCR	Oxygen consumption rate
OXPHOS	Oxidative phosphorylation
P2X	ATP-binding purinoceptor
PAMPs	Pathogen-associated molecular patterns
PBMCs	Peripheral blood mononuclear cells
PBS	Phosphate buffered saline

PCN	Primary cortical neurons
PCR	Polymerase chain reaction
PEI	Polyethyleneimine
PET	Positron emission tomography
PFA	Paraformaldehyde
PFC	Prefrontal cortex
PGC	Peroxisome proliferator-activated receptor gamma coactivator
PI	Propidium iodide
PLL	Poly-L-lysine
PND	Postnatal day
PRR	Pattern recognition receptor
PVDF	Polyvinylidene difluoride
RCR	Respiratory control ratio
ROI	Region of interest
ROS	Reactive oxygen species
RTCA	Real-time cell analysis
SD	Standard deviation
SDS-PAGE	Sodium dodecyl sulfate polyacrylamide gel electrophoresis
SNP	Single nucleotide polymorphism
TCA	Tricarboxylic acid cycle
TLR	Toll-like receptor
TNF	Tumor necrosis factor
TMRE	Tetramethylrhodamine ethyl ester

References

1. Thomas L. The lives of a cell: Notes of a biology watcher. Seventh printing. New York: The Viking Press; 1975.

2. World Health Organization. Mental disorders: Fact sheet; 2018 [cited 2018 Oct 16]. Available from: URL: http://www.who.int/mediacentre/factsheets/fs396/en/.

3. Adam D. Mental health: On the spectrum. Nature 2013; 496(7446):416–8.

4. Kessler RC, Berglund P, Demler O, Jin R, Merikangas KR, Walters EE. Lifetime prevalence and age-of-onset distributions of DSM-IV disorders in the National Comorbidity Survey Replication. Arch Gen Psychiatry 2005; 62(6):593–602.

5. Bowden CL. A different depression: Clinical distinctions between bipolar and unipolar depression. J Affect Disord 2005; 84(2-3):117–25.

6. Kupfer DJ, Frank E, Phillips ML. Major depressive disorder: new clinical, neurobiological, and treatment perspectives. Lancet 2012; 379(9820):1045–55.

7. Krishnan V, Nestler EJ. The molecular neurobiology of depression. Nature 2008; 455(7215):894–902.

8. Kessler RC, Aguilar-Gaxiola S, Alonso J, Chatterji S, Lee S, Ormel J et al. The global burden of mental disorders: an update from the WHO World Mental Health (WMH) surveys. Epidemiol Psichiatr Soc 2009; 18(1):23–33.

9. Keers R, Uher R. Gene-environment interaction in major depression and antidepressant treatment response. Curr Psychiatry Rep 2012; 14(2):129–37.

10. Merikangas KR, Low NCP. The epidemiology of mood disorders. Curr Psychiatry Rep 2004; 6(6):411–21.

11. Lohoff FW. Overview of the genetics of major depressive disorder. Curr Psychiatry Rep 2010; 12(6):539–46.

12. Barnett JH, Smoller JW. The genetics of bipolar disorder. Neuroscience 2009; 164(1):331–43.

13. Ferreira MAR, O'Donovan MC, Meng YA, Jones IR, Ruderfer DM, Jones L et al. Collaborative genome-wide association analysis supports a role for ANK3 and CACNA1C in bipolar disorder. Nat Genet 2008; 40(9):1056–8.

14. Green EK, Grozeva D, Jones I, Jones L, Kirov G, Caesar S et al. The bipolar disorder risk allele at CACNA1C also confers risk of recurrent major depression and of schizophrenia. Mol Psychiatry 2010; 15(10):1016–22.

15. Cross-Disorder Group of the Psychiatric Genomics Consortium. Identification of risk loci with shared effects on five major psychiatric disorders: a genome-wide analysis. Lancet 2013; 381(9875):1371–9.

16. Catterall WA, Perez-Reyes E, Snutch TP, Striessnig J. International Union of Pharmacology. XLVIII. Nomenclature and structure-function relationships of voltage-gated calcium channels. Pharmacol Rev 2005; 57(4):411–25.

17. Bhat S, Dao DT, Terrillion CE, Arad M, Smith RJ, Soldatov NM et al. CACNA1C (Cav1.2) in the pathophysiology of psychiatric disease. Prog Neurobiol 2012; 99(1):1–14.

18. Zamponi GW, Striessnig J, Koschak A, Dolphin AC. The Physiology, Pathology, and Pharmacology of Voltage-Gated Calcium Channels and Their Future Therapeutic Potential. Pharmacol Rev 2015; 67(4):821–70.

19. Clark NC, Nagano N, Kuenzi FM, Jarolimek W, Huber I, Walter D et al. Neurological phenotype and synaptic function in mice lacking the CaV1.3 alpha subunit of neuronal L-type voltage-dependent Ca2+ channels. Neuroscience 2003; 120(2):435–42.

20. Hell JW, Westenbroek RE, Warner C, Ahlijanian MK, Prystay W, Gilbert MM et al. Identification and differential subcellular localization of the neuronal class C and class D L-type calcium channel alpha 1 subunits. J Cell Biol 1993; 123(4):949–62.

21. Sinnegger-Brauns MJ, Huber IG, Koschak A, Wild C, Obermair GJ, Einzinger U et al. Expression and 1,4-dihydropyridine-binding properties of brain L-type calcium channel isoforms. Mol Pharmacol 2009; 75(2):407–14.

22. Dolphin AC. Calcium channel auxiliary $\alpha 2\delta$ and β subunits: trafficking and one step beyond. Nat Rev Neurosci 2012; 13(8):542–55.

23. Simms BA, Zamponi GW. Neuronal voltage-gated calcium channels: Structure, function, and dysfunction. Neuron 2014; 82(1):24–45.

24. Berridge MJ. Calcium signalling and psychiatric disease: bipolar disorder and schizophrenia. Cell Tissue Res 2014; 357(2):477–92.

25. Gershon ES, Grennan K, Busnello J, Badner JA, Ovsiew F, Memon S et al. A rare mutation of CACNA1C in a patient with bipolar disorder, and decreased gene expression associated with a bipolar-associated common SNP of CACNA1C in brain. Mol Psychiatry 2014; 19(8):890–4.

26. Yoshimizu T, Pan JQ, Mungenast AE, Madison JM, Su S, Ketterman J et al. Functional implications of a psychiatric risk variant within CACNA1C in induced human neurons. Mol Psychiatry 2015; 20(2):162–9.

27. Heyes S, Pratt WS, Rees E, Dahimene S, Ferron L, Owen MJ et al. Genetic disruption of voltage-gated calcium channels in psychiatric and neurological disorders. Prog Neurobiol 2015; 134:36–54.

28. Bigos KL, Mattay VS, Callicott JH, Straub RE, Vakkalanka R, Kolachana B et al. Genetic variation in CACNA1C affects brain circuitries related to mental illness. Arch Gen Psychiatry 2010; 67(9):939–45.

29. Dedic N, Pöhlmann ML, Richter JS, Mehta D, Czamara D, Metzger MW et al. Cross-disorder risk gene CACNA1C differentially modulates susceptibility to psychiatric disorders during development and adulthood. Mol Psychiatry 2018; 23(3):533–43.

30. Erk S, Meyer-Lindenberg A, Linden DEJ, Lancaster T, Mohnke S, Grimm O et al. Replication of brain function effects of a genome-wide supported psychiatric risk variant in the CACNA1C gene and new multi-locus effects. Neuroimage 2014; 94:147–54.

31. Paulus FM, Bedenbender J, Krach S, Pyka M, Krug A, Sommer J et al. Association of rs1006737 in CACNA1C with alterations in prefrontal activation and fronto-hippocampal connectivity. Hum Brain Mapp 2014; 35(4):1190–200.

32. Busatto GF. Structural and functional neuroimaging studies in major depressive disorder with psychotic features: A critical review. Schizophr Bull 2013; 39(4):776–86.

33. Dao DT, Mahon PB, Cai X, Kovacsics CE, Blackwell RA, Arad M et al. Mood disorder susceptibility gene CACNA1C modifies mood-related behaviors in mice and interacts with sex to influence behavior in mice and diagnosis in humans. Biol Psychiatry 2010; 68(9):801–10.

34. Bavley CC, Fischer DK, Rizzo BK, Rajadhyaksha AM. Cav1.2 channels mediate persistent chronic stress-induced behavioral deficits that are associated with prefrontal cortex activation of the p25/Cdk5-glucocorticoid receptor pathway. Neurobiol Stress 2017; 7:27–37.

35. Kabir ZD, Lee AS, Burgdorf CE, Fischer DK, Rajadhyaksha AM, Mok E et al. Cacna1c in the Prefrontal Cortex Regulates Depression-Related Behaviors via REDD1. Neuropsychopharmacology 2017.

36. Kabir ZD, Martínez-Rivera A, Rajadhyaksha AM. From Gene to Behavior: L-Type Calcium Channel Mechanisms Underlying Neuropsychiatric Symptoms. Neurotherapeutics 2017.

37. Kisko TM, Braun MD, Michels S, Witt SH, Rietschel M, Culmsee C et al. Cacna1c haploinsufficiency leads to pro-social 50-kHz ultrasonic communication deficits in rats. Dis Model Mech 2018; 11(6).

38. Harrison PJ. Molecular neurobiological clues to the pathogenesis of bipolar disorder. Curr Opin Neurobiol 2016; 36:1–6.

39. Kabir ZD, Lee AS, Rajadhyaksha AM. L-type Ca2+ channels in mood, cognition and addiction: integrating human and rodent studies with a focus on behavioural endophenotypes. J Physiol 2016; 594(20):5823–37.

40. Hagberg H, Mallard C, Ferriero DM, Vannucci SJ, Levison SW, Vexler ZS et al. The role of inflammation in perinatal brain injury. Nat Rev Neurol 2015; 11(4):192–208.

41. Nanni V, Uher R, Danese A. Childhood maltreatment predicts unfavorable course of illness and treatment outcome in depression: a meta-analysis. Am J Psychiatry 2012; 169(2):141–51.

42. Pignon B, Geoffroy PA, Thomas P, Roelandt J-L, Rolland B, Morgan C et al. Prevalence and clinical severity of mood disorders among first-, second- and third-generation migrants. J Affect Disord 2017; 210:174–80.

43. Salim S. Oxidative Stress and the Central Nervous System. J Pharmacol Exp Ther 2017; 360(1):201–5.

44. Maes M, Galecki P, Chang YS, Berk M. A review on the oxidative and nitrosative stress (O&NS) pathways in major depression and their possible contribution to the (neuro)degenerative processes in that illness. Prog Neuropsychopharmacol Biol Psychiatry 2011; 35(3):676–92.

45. Ng F, Berk M, Dean O, Bush AI. Oxidative stress in psychiatric disorders: Evidence base and therapeutic implications. Int J Neuropsychopharmacol 2008; 11(6):851–76.

46. Valko M, Leibfritz D, Moncol J, Cronin MTD, Mazur M, Telser J. Free radicals and antioxidants in normal physiological functions and human disease. Int J Biochem Cell Biol 2007; 39(1):44–84.

47. Kim H-W, Rapoport SI, Rao JS. Altered expression of apoptotic factors and synaptic markers in postmortem brain from bipolar disorder patients. Neurobiol Dis 2010; 37(3):596–603.

48. Kubera M, Obuchowicz E, Goehler L, Brzeszcz J, Maes M. In animal models, psychosocial stress-induced (neuro)inflammation, apoptosis and reduced neurogenesis are associated to the onset of depression. Prog Neuropsychopharmacol Biol Psychiatry 2011; 35(3):744–59.

49. Hazel NA, Hammen C, Brennan PA, Najman J. Early childhood adversity and adolescent depression: The mediating role of continued stress. Psychol Med 2008; 38(4):581–9.

50. Redlich R, Stacey D, Opel N, Grotegerd D, Dohm K, Kugel H et al. Evidence of an IFN-γ by early life stress interaction in the regulation of amygdala reactivity to emotional stimuli. Psychoneuroendocrinology 2015; 62:166–73.

51. Cattaneo A, Macchi F, Plazzotta G, Veronica B, Bocchio-Chiavetto L, Riva MA et al. Inflammation and neuronal plasticity: A link between childhood trauma and depression pathogenesis. Front Cell Neurosci 2015; 9:40.

52. Boeck C, Koenig AM, Schury K, Geiger ML, Karabatsiakis A, Wilker S et al. Inflammation in adult women with a history of child maltreatment: The involvement of mitochondrial alterations and oxidative stress. Mitochondrion 2016; 30:197–207.

53. Frodl T, Reinhold E, Koutsouleris N, Reiser M, Meisenzahl EM. Interaction of childhood stress with hippocampus and prefrontal cortex volume reduction in major depression. J Psychiatr Res 2010; 44(13):799–807.

54. Opel N, Redlich R, Zwanzger P, Grotegerd D, Arolt V, Heindel W et al. Hippocampal atrophy in major depression: a function of childhood maltreatment rather than diagnosis? Neuropsychopharmacology 2014; 39(12):2723–31.

55. Seffer D, Rippberger H, Schwarting RKW, Wöhr M. Pro-social 50-kHz ultrasonic communication in rats: Post-weaning but not post-adolescent social isolation leads to social impairments-phenotypic rescue by re-socialization. Front Behav Neurosci 2015; 9:102.

56. Fone KCF, Porkess MV. Behavioural and neurochemical effects of post-weaning social isolation in rodents-relevance to developmental neuropsychiatric disorders. Neurosci Biobehav Rev 2008; 32(6):1087–102.

57. Brenes JC, Padilla M, Fornaguera J. A detailed analysis of open-field habituation and behavioral and neurochemical antidepressant-like effects in postweaning enriched rats. Behav Brain Res 2009; 197(1):125–37.

58. Brenes JC, Lackinger M, Höglinger GU, Schratt G, Schwarting RKW, Wöhr M. Differential effects of social and physical environmental enrichment on brain plasticity, cognition, and ultrasonic communication in rats. J Comp Neurol 2016; 524(8):1586–607.

59. Manji H, Kato T, Di Prospero NA, Ness S, Beal MF, Krams M et al. Impaired mitochondrial function in psychiatric disorders. Nat Rev Neurosci 2012; 13(5):293–307.

60. Herculano-Houzel S. Scaling of brain metabolism with a fixed energy budget per neuron: Implications for neuronal activity, plasticity and evolution. PLoS ONE 2011; 6(3):e17514.

61. Klinedinst NJ, Regenold WT. A mitochondrial bioenergetic basis of depression. J Bioenerg Biomembr 2015; 47(1-2):155–71.

62. Sousa RT de, Machado-Vieira R, Zarate CA, Manji HK. Targeting mitochondrially mediated plasticity to develop improved therapeutics for bipolar disorder. Expert Opin Ther Targets 2014; 18(10):1131–47.

63. Allen J, Romay-Tallon R, Brymer KJ, Caruncho HJ, Kalynchuk LE. Mitochondria and Mood: Mitochondrial Dysfunction as a Key Player in the Manifestation of Depression. Front Neurosci 2018; 12:386.

64. Morava E, Kozicz T. Mitochondria and the economy of stress (mal)adaptation. Neurosci Biobehav Rev 2013; 37(4):668–80.

65. Fattal O, Link J, Quinn K, Cohen BH, Franco K. Psychiatric comorbidity in 36 adults with mitochondrial cytopathies. CNS Spectr 2007; 12(6):429–38.

66. Petschner P, Gonda X, Baksa D, Eszlari N, Trivaks M, Juhasz G et al. Genes Linking Mitochondrial Function, Cognitive Impairment and Depression are Associated with Endophenotypes Serving Precision Medicine. Neuroscience 2018; 370:207–17.

67. Woolley JD, Khan BK, Murthy NK, Miller BL, Rankin KP. The diagnostic challenge of psychiatric symptoms in neurodegenerative disease: Rates of and risk factors for prior psychiatric diagnosis in patients with early neurodegenerative disease. J Clin Psychiatry 2011; 72(2):126–33.

68. Galindo MF, Ikuta I, Zhu X, Casadesus G, Jordán J. Mitochondrial biology in Alzheimer's disease pathogenesis. J Neurochem 2010; 114(4):933–45.

69. Henchcliffe C, Beal MF. Mitochondrial biology and oxidative stress in Parkinson disease pathogenesis. Nat Clin Pract Neurol 2008; 4(11):600–9.

70. Turner C, Schapira AHV. Mitochondrial matters of the brain: The role in Huntington's disease. J Bioenerg Biomembr 2010; 42(3):193–8.

71. Scaini G, Rezin GT, Carvalho AF, Streck EL, Berk M, Quevedo J. Mitochondrial dysfunction in bipolar disorder: Evidence, pathophysiology and translational implications. Neurosci Biobehav Rev 2016; 68:694–713.

72. Gardner A, Boles RG. Beyond the serotonin hypothesis: Mitochondria, inflammation and neurodegeneration in major depression and affective spectrum disorders. Prog Neuropsychopharmacol Biol Psychiatry 2011; 35(3):730–43.

73. Urrutia PJ, Mena NP, Núñez MT. The interplay between iron accumulation, mitochondrial dysfunction, and inflammation during the execution step of neurodegenerative disorders. Front Pharmacol 2014; 5:38.

74. Machado AK, Pan AY, da Silva TM, Duong A, Andreazza AC. Upstream Pathways Controlling Mitochondrial Function in Major Psychosis: A Focus on Bipolar Disorder. Can J Psychiatry 2016; 61(8):446–56.

75. Sigitova E, Fišar Z, Hroudová J, Cikánková T, Raboch J. Biological hypotheses and biomarkers of bipolar disorder. Psychiatry Clin Neurosci 2017; 71(2):77–103.

76. Réus GZ, Fries GR, Stertz L, Badawy M, Passos IC, Barichello T et al. The role of inflammation and microglial activation in the pathophysiology of psychiatric disorders. Neuroscience 2015; 300:141–54.

77. Wohleb ES, Franklin T, Iwata M, Duman RS. Integrating neuroimmune systems in the neurobiology of depression. Nat Rev Neurosci 2016; 17(8):497–511.

78. Bhattacharya A, Derecki NC, Lovenberg TW, Drevets WC. Role of neuro-immunological factors in the pathophysiology of mood disorders. Psychopharmacology (Berl) 2016; 233(9):1623–36.

79. Jones KA, Thomsen C. The role of the innate immune system in psychiatric disorders. Mol Cell Neurosci 2013; 53:52–62.

80. Steiner J, Walter M, Gos T, Guillemin GJ, Bernstein H-G, Sarnyai Z et al. Severe depression is associated with increased microglial quinolinic acid in subregions of the anterior cingulate gyrus: Evidence for an immune-modulated glutamatergic neurotransmission? J Neuroinflammation 2011; 8:94.

81. Steiner J, Bielau H, Brisch R, Danos P, Ullrich O, Mawrin C et al. Immunological aspects in the neurobiology of suicide: Elevated microglial density in schizophrenia and depression is associated with suicide. J Psychiatr Res 2008; 42(2):151–7.

82. Setiawan E, Attwells S, Wilson AA, Mizrahi R, Rusjan PM, Miler L et al. Association of translocator protein total distribution volume with duration of untreated major depressive disorder: A cross-sectional study. Lancet Psychiatry 2018; 5(4):339–47.

83. Stertz L, Magalhães PVS, Kapczinski F. Is bipolar disorder an inflammatory condition? The relevance of microglial activation. Curr Opin Psychiatry 2013; 26(1):19–26.

84. Wolf SA, Boddeke HWGM, Kettenmann H. Microglia in Physiology and Disease. Annu Rev Physiol 2017; 79:619–43.

85. Hodes GE, Kana V, Menard C, Merad M, Russo SJ. Neuroimmune mechanisms of depression. Nat Neurosci 2015; 18(10):1386–93.

86. Carson MJ, Doose JM, Melchior B, Schmid CD, Ploix CC. CNS immune privilege: Hiding in plain sight. Immunol Rev 2006; 213:48–65.

87. Prinz M, Priller J. Microglia and brain macrophages in the molecular age: From origin to neuropsychiatric disease. Nat Rev Neurosci 2014; 15(5):300–12.

88. Cherry JD, Olschowka JA, O'Banion MK. Neuroinflammation and M2 microglia: The good, the bad, and the inflamed. J Neuroinflammation 2014; 11:98.

89. Park J, Choi H, Min J-S, Park S-J, Kim J-H, Park H-J et al. Mitochondrial dynamics modulate the expression of pro-inflammatory mediators in microglial cells. J Neurochem 2013; 127(2):221–32.

90. Orihuela R, McPherson CA, Harry GJ. Microglial M1/M2 polarization and metabolic states. Br J Pharmacol 2016; 173(4):649–65.

91. Amici SA, Dong J, Guerau-de-Arellano M. Molecular Mechanisms Modulating the Phenotype of Macrophages and Microglia. Front Immunol 2017; 8:1520.

92. Dantzer R, O'Connor JC, Lawson MA, Kelley KW. Inflammation-associated depression: From serotonin to kynurenine. Psychoneuroendocrinology 2011; 36(3):426–36.

93. Dowlati Y, Herrmann N, Swardfager W, Liu H, Sham L, Reim EK et al. A meta-analysis of cytokines in major depression. Biol Psychiatry 2010; 67(5):446–57.

94. Takahashi Y, Yu Z, Sakai M, Tomita H. Linking Activation of Microglia and Peripheral Monocytic Cells to the Pathophysiology of Psychiatric Disorders. Front Cell Neurosci 2016; 10:144.

95. Nair A, Bonneau RH. Stress-induced elevation of glucocorticoids increases microglia proliferation through NMDA receptor activation. J Neuroimmunol 2006; 171(1-2):72–85.

96. Najjar S, Pearlman DM, Alper K, Najjar A, Devinsky O. Neuroinflammation and psychiatric illness. J Neuroinflammation 2013; 10:43.

97. Ott M, Gogvadze V, Orrenius S, Zhivotovsky B. Mitochondria, oxidative stress and cell death. Apoptosis 2007; 12(5):913–22.

98. Valerio A, Cardile A, Cozzi V, Bracale R, Tedesco L, Pisconti A et al. TNF-alpha downregulates eNOS expression and mitochondrial biogenesis in fat and muscle of obese rodents. J Clin Invest 2006; 116(10):2791–8.

99. Olloquequi J, Cornejo-Córdova E, Verdaguer E, Soriano FX, Binvignat O, Auladell C et al. Excitotoxicity in the pathogenesis of neurological and psychiatric disorders: Therapeutic implications. J Psychopharmacol (Oxford) 2018; 32(3):265–75.

100. Cole J, Costafreda SG, McGuffin P, Fu CHY. Hippocampal atrophy in first episode depression: A meta-analysis of magnetic resonance imaging studies. J Affect Disord 2011; 134(1-3):483–7.

101. Kleiveland CR. The Impact of Food Bioactives on Health: in vitro and ex vivo models: Peripheral Blood Mononuclear Cells. Cham (CH); 2015.

102. Israels LG, Israels ED. Lymphocytes. Oncologist 1999; 4(2):129–37.

103. Kramer PA, Ravi S, Chacko B, Johnson MS, Darley-Usmar VM. A review of the mitochondrial and glycolytic metabolism in human platelets and leukocytes: Implications for their use as bioenergetic biomarkers. Redox Biol 2014; 2:206–10.

104. Banchereau J, Steinman RM. Dendritic cells and the control of immunity. Nature 1998; 392(6673):245–52.

105. Tyrrell DJ, Bharadwaj MS, Jorgensen MJ, Register TC, Shively C, Andrews RN et al. Blood-Based Bioenergetic Profiling Reflects Differences in Brain Bioenergetics and Metabolism. Oxid Med Cell Longev 2017; 2017:7317251.

106. Prabakaran S, Swatton JE, Ryan MM, Huffaker SJ, Huang JT-J, Griffin JL et al. Mitochondrial dysfunction in schizophrenia: Evidence for compromised brain metabolism and oxidative stress. Mol Psychiatry 2004; 9(7):684-97, 643.

107. Gubert C, Stertz L, Pfaffenseller B, Panizzutti BS, Rezin GT, Massuda R et al. Mitochondrial activity and oxidative stress markers in peripheral blood mononuclear cells of patients with bipolar disorder, schizophrenia, and healthy subjects. J Psychiatr Res 2013; 47(10):1396–402.

108. Hroudová J, Fišar Z, Kitzlerová E, Zvěřová M, Raboch J. Mitochondrial respiration in blood platelets of depressive patients. Mitochondrion 2013; 13(6):795–800.

109. Karabatsiakis A, Böck C, Salinas-Manrique J, Kolassa S, Calzia E, Dietrich DE et al. Mitochondrial respiration in peripheral blood mononuclear cells correlates with depressive subsymptoms and severity of major depression. Transl Psychiatry 2014; 4:e397.

110. Madrigal JL, Olivenza R, Moro MA, Lizasoain I, Lorenzo P, Rodrigo J et al. Glutathione depletion, lipid peroxidation and mitochondrial dysfunction are induced by chronic stress in rat brain. Neuropsychopharmacology 2001; 24(4):420–9.

111. Grohm J, Plesnila N, Culmsee C. Bid mediates fission, membrane permeabilization and peri-nuclear accumulation of mitochondria as a prerequisite for oxidative neuronal cell death. Brain Behav Immun 2010; 24(5):831–8.

112. Tobaben S, Grohm J, Seiler A, Conrad M, Plesnila N, Culmsee C. Bid-mediated mitochondrial damage is a key mechanism in glutamate-induced oxidative stress and AIF-dependent cell death in immortalized HT-22 hippocampal neurons. Cell Death Differ 2011; 18(2):282–92.

113. Tan S, Schubert D, Maher P. Oxytosis: A novel form of programmed cell death. Curr Top Med Chem 2001; 1(6):497–506.

114. Murphy TH, Miyamoto M, Sastre A, Schnaar RL, Coyle JT. Glutamate toxicity in a neuronal cell line involves inhibition of cystine transport leading to oxidative stress. Neuron 1989; 2(6):1547–58.

115. Seiler A, Schneider M, Forster H, Roth S, Wirth EK, Culmsee C et al. Glutathione peroxidase 4 senses and translates oxidative stress into 12/15-lipoxygenase dependent- and AIF-mediated cell death. Cell Metab 2008; 8(3):237–48.

116. Grohm J, Kim S-W, Mamrak U, Tobaben S, Cassidy-Stone A, Nunnari J et al. Inhibition of Drp1 provides neuroprotection in vitro and in vivo. Cell Death Differ 2012; 19(9):1446–58.

117. Neitemeier S, Jelinek A, Laino V, Hoffmann L, Eisenbach I, Eying R et al. BID links ferroptosis to mitochondrial cell death pathways. Redox Biol 2017; 12:558–70.

118. Jelinek A, Heyder L, Daude M, Plessner M, Krippner S, Grosse R et al. Mitochondrial rescue prevents glutathione peroxidase-dependent ferroptosis. Free Radic Biol Med 2018; 117:45–57.

119. Landshamer S, Hoehn M, Barth N, Duvezin-Caubet S, Schwake G, Tobaben S et al. Bid-induced release of AIF from mitochondria causes immediate neuronal cell death. Cell Death Differ 2008; 15(10):1553–63.

120. Öxler E-M, Dolga A, Culmsee C. AIF depletion provides neuroprotection through a preconditioning effect. Apoptosis 2012; 17(10):1027–38.

121. Olney JW. Inciting excitotoxic cytocide among central neurons. Adv Exp Med Biol 1986; 203:631–45.

122. Wang Y, Qin Z-H. Molecular and cellular mechanisms of excitotoxic neuronal death. Apoptosis 2010; 15(11):1382–402.

123. Choi DW. Excitotoxic cell death. J Neurobiol 1992; 23(9):1261–76.

124. Brookes PS, Yoon Y, Robotham JL, Anders MW, Sheu S-S. Calcium, ATP, and ROS: a mitochondrial love-hate triangle. Am J Physiol Cell Physiol 2004; 287(4):C817-33.

125. Sattler R, Xiong Z, Lu WY, Hafner M, MacDonald JF, Tymianski M. Specific coupling of NMDA receptor activation to nitric oxide neurotoxicity by PSD-95 protein. Science 1999; 284(5421):1845–8.

126. Choi DW. Ischemia-induced neuronal apoptosis. Curr Opin Neurobiol 1996; 6(5):667–72.

127. Ankarcrona M, Dypbukt JM, Bonfoco E, Zhivotovsky B, Orrenius S, Lipton SA et al. Glutamate-induced neuronal death: A succession of necrosis or apoptosis depending on mitochondrial function. Neuron 1995; 15(4):961–73.

128. Cheung NS, Pascoe CJ, Giardina SF, John CA, Beart PM. Micromolar L-glutamate induces extensive apoptosis in an apoptotic-necrotic continuum of insult-dependent, excitotoxic injury in cultured cortical neurones. Neuropharmacology 1998; 37(10-11):1419–29.

129. Tay TL, Béchade C, D'Andrea I, St-Pierre M-K, Henry MS, Roumier A et al. Microglia Gone Rogue: Impacts on Psychiatric Disorders across the Lifespan. Front Mol Neurosci 2017; 10:421.

130. Singhal G, Baune BT. Microglia: An Interface between the Loss of Neuroplasticity and Depression. Front Cell Neurosci 2017; 11:270.

131. Ransohoff RM, Brown MA. Innate immunity in the central nervous system. J Clin Invest 2012; 122(4):1164–71.

132. Rock KL, Latz E, Ontiveros F, Kono H. The sterile inflammatory response. Annu Rev Immunol 2010; 28:321–42.

133. Krysko DV, Agostinis P, Krysko O, Garg AD, Bachert C, Lambrecht BN et al. Emerging role of damage-associated molecular patterns derived from mitochondria in inflammation. Trends Immunol 2011; 32(4):157–64.

134. Heneka MT, McManus RM, Latz E. Inflammasome signalling in brain function and neurodegenerative disease. Nat Rev Neurosci 2018.

135. Fleshner M, Frank M, Maier SF. Danger Signals and Inflammasomes: Stress-Evoked Sterile Inflammation in Mood Disorders. Neuropsychopharmacology 2017; 42(1):36–45.

136. Tschopp J, Schroder K. NLRP3 inflammasome activation: The convergence of multiple signalling pathways on ROS production? Nat Rev Immunol 2010; 10(3):210–5.

137. Zhong Z, Liang S, Sanchez-Lopez E, He F, Shalapour S, Lin X-J et al. New mitochondrial DNA synthesis enables NLRP3 inflammasome activation. Nature 2018; 560(7717):198–203.

138. Zhou R, Yazdi AS, Menu P, Tschopp J. A role for mitochondria in NLRP3 inflammasome activation. Nature 2011; 469(7329):221–5.

139. Chung HY, Cesari M, Anton S, Marzetti E, Giovannini S, Seo AY et al. Molecular inflammation: Underpinnings of aging and age-related diseases. Ageing Res Rev 2009; 8(1):18–30.

140. Morris G, Berk M. The many roads to mitochondrial dysfunction in neuroimmune and neuropsychiatric disorders. BMC Med 2015; 13:68.

141. Deussing JM, Arzt E. P2X7 Receptor: A Potential Therapeutic Target for Depression? Trends Mol Med 2018; 24(9):736–47.

142. Yaron JR, Gangaraju S, Rao MY, Kong X, Zhang L, Su F et al. K(+) regulates Ca(2+) to drive inflammasome signaling: Dynamic visualization of ion flux in live cells. Cell Death Dis 2015; 6:e1954.

143. Hoffmann A, Kann O, Ohlemeyer C, Hanisch U-K, Kettenmann H. Elevation of basal intracellular calcium as a central element in the activation of brain macrophages (microglia): Suppression of receptor-evoked calcium signaling and control of release function. J Neurosci 2003; 23(11):4410–9.

144. Espinosa-Parrilla JF, Martinez-Moreno M, Gasull X, Mahy N, Rodriguez MJ. The L-type voltage-gated calcium channel modulates microglial pro-inflammatory activity. Mol Cell Neurosci 2015; 64:104–15.

145. Kircher T, Wöhr M, Nenadic I, Schwarting R, Schratt G, Alferink J et al. Neurobiology of the major psychoses: A translational perspective on brain structure and function-the FOR2107 consortium. Eur Arch Psychiatry Clin Neurosci 2018.

146. Morimoto BH, Koshland DE. Excitatory amino acid uptake and N-methyl-D-aspartate-mediated secretion in a neural cell line. Proc Natl Acad Sci U S A 1990; 87(9):3518–21.

147. Davis JB, Maher P. Protein kinase C activation inhibits glutamate-induced cytotoxicity in a neuronal cell line. Brain Res 1994; 652(1):169–73.

148. Schmitt S, Saathoff F, Meissner L, Schropp E-M, Lichtmannegger J, Schulz S et al. A semi-automated method for isolating functionally intact mitochondria from cultured cells and tissue biopsies. Anal Biochem 2013; 443(1):66–74.

149. Diemert S, Dolga AM, Tobaben S, Grohm J, Pfeifer S, Oexler E et al. Impedance measurement for real time detection of neuronal cell death. J Neurosci Methods 2012; 203(1):69–77.

150. Geurts AM, Cost GJ, Freyvert Y, Zeitler B, Miller JC, Choi VM et al. Knockout rats via embryo microinjection of zinc-finger nucleases. Science 2009; 325(5939):433.

151. Seisenberger C, Specht V, Welling A, Platzer J, Pfeifer A, Kühbandner S et al. Functional embryonic cardiomyocytes after disruption of the L-type alpha1C (Cav1.2) calcium channel gene in the mouse. J Biol Chem 2000; 275(50):39193–9.

152. Li JH, Wang YH, Wolfe BB, Krueger KE, Corsi L, Stocca G et al. Developmental changes in localization of NMDA receptor subunits in primary cultures of cortical neurons. Eur J Neurosci 1998; 10(5):1704–15.

153. Bootman MD, Rietdorf K, Collins T, Walker S, Sanderson M. Ca2+-sensitive fluorescent dyes and intracellular Ca2+ imaging. Cold Spring Harb Protoc 2013; 2013(2):83–99.

154. Wöhr M, Silverman JL, Scattoni ML, Turner SM, Harris MJ, Saxena R et al. Developmental delays and reduced pup ultrasonic vocalizations but normal sociability in mice lacking the postsynaptic cell adhesion protein neuroligin2. Behav Brain Res 2013; 251:50–64.

155. Sungur AÖ, Jochner MCE, Harb H, Kılıç A, Garn H, Schwarting RKW et al. Aberrant cognitive phenotypes and altered hippocampal BDNF expression related to epigenetic modifications in mice lacking the post-synaptic scaffolding protein SHANK1: Implications for autism spectrum disorder. Hippocampus 2017; 27(8):906–19.

156. Rosen GD, Williams AG, Capra JA, Connolly MT, Cruz B, Lu L et al. The mouse brain library @ www.mbl.org. Int Mouse Genome Conference 2000; 14:166.

157. Paxinos G, Watson C. The rat brain in stereotaxic coordinates. 6th ed. Amsterdam, Boston: Elsevier; 2007.

158. Rogers GW, Brand MD, Petrosyan S, Ashok D, Elorza AA, Ferrick DA et al. High throughput microplate respiratory measurements using minimal quantities of isolated mitochondria. PLoS ONE 2011; 6(7):e21746.

159. Salabei JK, Gibb AA, Hill BG. Comprehensive measurement of respiratory activity in permeabilized cells using extracellular flux analysis. Nat Protoc 2014; 9(2):421–38.

160. Zamzami N, Métivier D, Kroemer G. Quantitation of mitochondrial transmembrane potential in cells and in isolated mitochondria. Meth Enzymol 2000; 322:208–13.

161. Gong Y, Chai Y, Ding J-H, Sun X-L, Hu G. Chronic mild stress damages mitochondrial ultrastructure and function in mouse brain. Neurosci Lett 2011; 488(1):76–80.

162. Silaidos C, Pilatus U, Grewal R, Matura S, Lienerth B, Pantel J et al. Sex-associated differences in mitochondrial function in human peripheral blood mononuclear cells (PBMCs) and brain. Biol Sex Differ 2018; 9(1):34.

163. Bernstein DP, Stein JA, Newcomb MD, Walker E, Pogge D, Ahluvalia T et al. Development and validation of a brief screening version of the Childhood Trauma Questionnaire. Child Abuse Negl 2003; 27(2):169–90.

164. Wingenfeld K, Spitzer C, Mensebach C, Grabe HJ, Hill A, Gast U et al. Die deutsche Version des Childhood Trauma Questionnaire (CTQ): Erste Befunde zu den psychometrischen Kennwerten. Psychother Psychosom Med Psychol 2010; 60(11):442–50.

165. Culmsee C, Landshamer S. Molecular insights into mechanisms of the cell death program: role in the progression of neurodegenerative disorders. Curr Alzheimer Res 2006; 3(4):269–83.

166. Williams A, Sarkar S, Cuddon P, Ttofi EK, Saiki S, Siddiqi FH et al. Novel targets for Huntington's disease in an mTOR-independent autophagy pathway. Nat Chem Biol 2008; 4(5):295–305.

167. Huber SM, Butz L, Stegen B, Klumpp D, Braun N, Ruth P et al. Ionizing radiation, ion transports, and radioresistance of cancer cells. Front Physiol 2013; 4:212.

168. Braun N, Klumpp D, Hennenlotter J, Bedke J, Duranton C, Bleif M et al. UCP-3 uncoupling protein confers hypoxia resistance to renal epithelial cells and is upregulated in renal cell carcinoma. Sci Rep 2015; 5:13450.

169. Li Y, Maher P, Schubert D. Requirement for cGMP in nerve cell death caused by glutathione depletion. J Cell Biol 1997; 139(5):1317–24.

170. Qiu J, Tan Y-W, Hagenston AM, Martel M-A, Kneisel N, Skehel PA et al. Mitochondrial calcium uniporter Mcu controls excitotoxicity and is transcriptionally repressed by neuroprotective nuclear calcium signals. Nat Commun 2013; 4:2034.

171. Birsoy K, Wang T, Chen WW, Freinkman E, Abu-Remaileh M, Sabatini DM. An Essential Role of the Mitochondrial Electron Transport Chain in Cell Proliferation Is to Enable Aspartate Synthesis. Cell 2015; 162(3):540–51.

172. Hanisch UK, Prinz M, Angstwurm K, Häusler KG, Kann O, Kettenmann H et al. The protein tyrosine kinase inhibitor AG126 prevents the massive microglial cytokine induction by pneumococcal cell walls. Eur J Immunol 2001; 31(7):2104–15.

173. Lively S, Schlichter LC. Microglia Responses to Pro-inflammatory Stimuli (LPS, IFNγ+TNFα) and Reprogramming by Resolving Cytokines (IL-4, IL-10). Front Cell Neurosci 2018; 12:215.

174. Pandya JD, Royland JE, MacPhail RC, Sullivan PG, Kodavanti PRS. Age- and brain region-specific differences in mitochondrial bioenergetics in Brown Norway rats. Neurobiol Aging 2016; 42:25–34.

175. Brand MD, Nicholls DG. Assessing mitochondrial dysfunction in cells. Biochem J 2011; 435(2):297–312.

176. Cottet-Rousselle C, Ronot X, Leverve X, Mayol J-F. Cytometric assessment of mitochondria using fluorescent probes. Cytometry A 2011; 79(6):405–25.

177. Brand MD. Mitochondrial generation of superoxide and hydrogen peroxide as the source of mitochondrial redox signaling. Free Radic Biol Med 2016; 100:14–31.

178. Kadenbach B. Intrinsic and extrinsic uncoupling of oxidative phosphorylation. Biochim Biophys Acta 2003; 1604(2):77–94.

179. Chacko BK, Kramer PA, Ravi S, Benavides GA, Mitchell T, Dranka BP et al. The Bioenergetic Health Index: A new concept in mitochondrial translational research. Clin Sci 2014; 127(6):367–73.

180. Schmaal L, Hibar DP, Sämann PG, Hall GB, Baune BT, Jahanshad N et al. Cortical abnormalities in adults and adolescents with major depression based on brain scans from 20 cohorts worldwide in the ENIGMA Major Depressive Disorder Working Group. Mol Psychiatry 2017; 22(6):900–9.

181. Roussos P, Mitchell AC, Voloudakis G, Fullard JF, Pothula VM, Tsang J et al. A role for noncoding variation in schizophrenia. Cell Rep 2014; 9(4):1417–29.

182. Cipriani A, Saunders K, Attenburrow M-J, Stefaniak J, Panchal P, Stockton S et al. A systematic review of calcium channel antagonists in bipolar disorder and some considerations for their future development. Mol Psychiatry 2016; 21(10):1324–32.

183. Lee AS, Ra S, Rajadhyaksha AM, Britt JK, Jesus-Cortes H de, Gonzales KL et al. Forebrain elimination of cacna1c mediates anxiety-like behavior in mice. Mol Psychiatry 2012; 17(11):1054–5.

184. Terrillion CE, Dao DT, Cachope R, Lobo MK, Puche AC, Cheer JF et al. Reduced levels of Cacna1c attenuate mesolimbic dopamine system function. Genes Brain Behav 2017; 16(5):495–505.

185. Kumar N, Singh N, Jaggi AS. Anti-stress effects of cilnidipine and nimodipine in immobilization subjected mice. Physiol Behav 2012; 105(5):1148–55.

186. Cohen C, Perrault G, Sanger DJ. Assessment of the antidepressant-like effects of L-type voltage-dependent channel modulators. Behav Pharmacol 1997; 8(6-7):629–38.

187. Mogilnicka E, Czyrak A, Maj J. Dihydropyridine calcium channel antagonists reduce immobility in the mouse behavioral despair test; antidepressants facilitate nifedipine action. Eur J Pharmacol 1987; 138(3):413–6.

188. Levy NA, Janicak PG. Calcium channel antagonists for the treatment of bipolar disorder. Bipolar Disord 2000; 2(2):108–19.

189. Surmeier DJ, Halliday GM, Simuni T. Calcium, mitochondrial dysfunction and slowing the progression of Parkinson's disease. Exp Neurol 2017; 298(Pt B):202–9.

190. Benes FM, Matzilevich D, Burke RE, Walsh J. The expression of proapoptosis genes is increased in bipolar disorder, but not in schizophrenia. Mol Psychiatry 2006; 11(3):241–51.

191. Andreazza AC, Wang J-F, Salmasi F, Shao L, Young LT. Specific subcellular changes in oxidative stress in prefrontal cortex from patients with bipolar disorder. J Neurochem 2013; 127(4):552–61.

192. Dolga AM, Netter MF, Perocchi F, Doti N, Meissner L, Tobaben S et al. Mitochondrial small conductance SK2 channels prevent glutamate-induced oxytosis and mitochondrial dysfunction. J Biol Chem 2013; 288(15):10792–804.

193. Cereghetti GM, Stangherlin A, Martins de Brito O, Chang CR, Blackstone C, Bernardi P et al. Dephosphorylation by calcineurin regulates translocation of Drp1 to mitochondria. Proc Natl Acad Sci U S A 2008; 105(41):15803–8.

194. Narayanan D, Xi Q, Pfeffer LM, Jaggar JH. Mitochondria control functional CaV1.2 expression in smooth muscle cells of cerebral arteries. Circ Res 2010; 107(5):631–41.

195. Suzuki Y, Yoshimaru T, Inoue T, Ra C. Ca v 1.2 L-type Ca2+ channel protects mast cells against activation-induced cell death by preventing mitochondrial integrity disruption. Mol Immunol 2009; 46(11-12):2370–80.

196. Lobner D, Lipton P. Intracellular calcium levels and calcium fluxes in the CA1 region of the rat hippocampal slice during in vitro ischemia: Relationship to electrophysiological cell damage. J Neurosci 1993; 13(11):4861–71.

197. Schurr A. Neuroprotection against ischemic/hypoxic brain damage: Blockers of ionotropic glutamate receptor and voltage sensitive calcium channels. Curr Drug Targets 2004; 5(7):603–18.

198. Langwieser N, Christel CJ, Kleppisch T, Hofmann F, Wotjak CT, Moosmang S. Homeostatic switch in hebbian plasticity and fear learning after sustained loss of Cav1.2 calcium channels. J Neurosci 2010; 30(25):8367–75.

199. Green EM, Barrett CF, Bultynck G, Shamah SM, Dolmetsch RE. The tumor suppressor eIF3e mediates calcium-dependent internalization of the L-type calcium channel CaV1.2. Neuron 2007; 55(4):615–32.

200. Tsuruta F, Green EM, Rousset M, Dolmetsch RE. PIKfyve regulates CaV1.2 degradation and prevents excitotoxic cell death. J Cell Biol 2009; 187(2):279–94.

201. Mizuno F, Barabas P, Krizaj D, Akopian A. Glutamate-induced internalization of Ca(v)1.3 L-type Ca(2+) channels protects retinal neurons against excitotoxicity. J Physiol 2010; 588(Pt 6):953–66.

202. Barger SW. Complex influence of the L-type calcium-channel agonist BayK8644(+/-) on N-methyl-D-aspartate responses and neuronal survival. Neuroscience 1999; 89(1):101–8.

203. Krieglstein J, Lippert K, Pöch G. Apparent independent action of nimodipine and glutamate antagonists to protect cultured neurons against glutamate-induced damage. Neuropharmacology 1996; 35(12):1737–42.

204. Sendrowski K, Rusak M, Sobaniec P, Iłendo E, Dąbrowska M, Boćkowski L et al. Study of the protective effect of calcium channel blockers against neuronal damage induced by glutamate in cultured hippocampal neurons. Pharmacol Rep 2013; 65(3):730–6.

205. Stuiver BT, Douma BR, Bakker R, Nyakas C, Luiten PG. In vivo protection against NMDA-induced neurodegeneration by MK-801 and nimodipine: Combined therapy and temporal course of protection. Neurodegeneration 1996; 5(2):153–9.

206. Brickley SG, Revilla V, Cull-Candy SG, Wisden W, Farrant M. Adaptive regulation of neuronal excitability by a voltage-independent potassium conductance. Nature 2001; 409(6816):88–92.

207. Davis GW, Bezprozvanny I. Maintaining the stability of neural function: A homeostatic hypothesis. Annu Rev Physiol 2001; 63:847–69.

208. Paquet D, Kwart D, Chen A, Sproul A, Jacob S, Teo S et al. Efficient introduction of specific homozygous and heterozygous mutations using CRISPR/Cas9. Nature 2016; 533(7601):125–9.

209. Nicholls DG. Mitochondrial dysfunction and glutamate excitotoxicity studied in primary neuronal cultures. Curr Mol Med 2004; 4(2):149–77.

210. Obien MEJ, Deligkaris K, Bullmann T, Bakkum DJ, Frey U. Revealing neuronal function through microelectrode array recordings. Front Neurosci 2014; 8:423.

211. Harry GJ, Kraft AD. Neuroinflammation and microglia: Considerations and approaches for neurotoxicity assessment. Expert Opin Drug Metab Toxicol 2008; 4(10):1265–77.

212. Stebbing MJ, Cottee JM, Rana I. The Role of Ion Channels in Microglial Activation and Proliferation - A Complex Interplay between Ligand-Gated Ion Channels, K(+) Channels, and Intracellular Ca(2.). Front Immunol 2015; 6:497.

213. Dolga AM, Letsche T, Gold M, Doti N, Bacher M, Chiamvimonvat N et al. Activation of KCNN3/SK3/K(Ca)2.3 channels attenuates enhanced calcium influx and inflammatory cytokine production in activated microglia. Glia 2012; 60(12):2050–64.

214. Möller T. Calcium signaling in microglial cells. Glia 2002; 40(2):184–94.

215. McLarnon JG, Zhang L, Goghari V, Lee YB, Walz W, Krieger C et al. Effects of ATP and elevated K+ on K+ currents and intracellular Ca2+ in human microglia. Neuroscience 1999; 91(1):343–52.

216. Eder C. Ion channels in microglia (brain macrophages). Am J Physiol 1998; 275(2 Pt 1):C327-42.

217. Davenport B, Li Y, Heizer JW, Schmitz C, Perraud A-L. Signature Channels of Excitability no More: L-Type Channels in Immune Cells. Front Immunol 2015; 6:375.

218. Hegg CC, Hu S, Peterson PK, Thayer SA. Beta-chemokines and human immunodeficiency virus type-1 proteins evoke intracellular calcium increases in human microglia. Neuroscience 2000; 98(1):191–9.

219. Shideman CR, Hu S, Peterson PK, Thayer SA. CCL5 evokes calcium signals in microglia through a kinase-, phosphoinositide-, and nucleotide-dependent mechanism. J Neurosci Res 2006; 83(8):1471–84.

220. Silei V, Fabrizi C, Venturini G, Salmona M, Bugiani O, Tagliavini F et al. Activation of microglial cells by PrP and beta-amyloid fragments raises intracellular calcium through L-type voltage sensitive calcium channels. Brain Res 1999; 818(1):168–70.

221. Colton CA, Jia M, Li MX, Gilbert DL. K+ modulation of microglial superoxide production: Involvement of voltage-gated Ca2+ channels. Am J Physiol 1994; 266(6 Pt 1):C1650-5.

222. Li Y, Hu X, Liu Y, Bao Y, An L. Nimodipine protects dopaminergic neurons against inflammation-mediated degeneration through inhibition of microglial activation. Neuropharmacology 2009; 56(3):580–9.

223. Kettenmann H, Hanisch U-K, Noda M, Verkhratsky A. Physiology of microglia. Physiol Rev 2011; 91(2):461–553.

224. Peruzzotti-Jametti L, Pluchino S. Targeting Mitochondrial Metabolism in Neuroinflammation: Towards a Therapy for Progressive Multiple Sclerosis. Trends Mol Med 2018; 24(10):838–55.

225. Wang Q, Zhao Y, Sun M, Liu S, Li B, Zhang L et al. 2-Deoxy-d-glucose attenuates sevoflurane-induced neuroinflammation through nuclear factor-kappa B pathway in vitro. Toxicol In Vitro 2014; 28(7):1183–9.

226. Jones N, Piasecka J, Bryant AH, Jones RH, Skibinski DOF, Francis NJ et al. Bioenergetic analysis of human peripheral blood mononuclear cells. Clin Exp Immunol 2015; 182(1):69–80.

227. Vilhardt F, Haslund-Vinding J, Jaquet V, McBean G. Microglia antioxidant systems and redox signalling. Br J Pharmacol 2017; 174(12):1719–32.

228. Mills EL, Kelly B, Logan A, Costa ASH, Varma M, Bryant CE et al. Succinate Dehydrogenase Supports Metabolic Repurposing of Mitochondria to Drive Inflammatory Macrophages. Cell 2016; 167(2):457-470.e13.

229. López-Armada MJ, Riveiro-Naveira RR, Vaamonde-García C, Valcárcel-Ares MN. Mitochondrial dysfunction and the inflammatory response. Mitochondrion 2013; 13(2):106–18.

230. Hong H, Kim BS, Im H-I. Pathophysiological Role of Neuroinflammation in Neurodegenerative Diseases and Psychiatric Disorders. Int Neurourol J 2016; 20(Suppl 1):S2-7.

231. Pizzo P, Drago I, Filadi R, Pozzan T. Mitochondrial Ca^{2+} homeostasis: Mechanism, role, and tissue specificities. Pflugers Arch 2012; 464(1):3–17.

232. Michels S, Wöhr M, Schwarting RK, Culmsee C. Psychiatric risk gene Cacna1c determines mitochondrial resilience against oxidative stress in neurons. Cell Death Dis 2018; 9(6):645.

233. Michels S, Ganjam GK, Martins H, Schratt GM, Wöhr M, Schwarting RKW et al. Downregulation of the psychiatric susceptibility gene Cacna1c promotes mitochondrial resilience to oxidative stress in neuronal cells. Cell death discovery 2018; 4:54.

234. Terrillion CE, Francis TC, Puche AC, Lobo MK, Gould TD. Decreased nucleus accumbens expression of psychiatric disorder risk gene Cacna1c promotes susceptibility to social stress. Int J Neuropsychopharmacol 2017.

235. Sparling JE, Baker SL, Bielajew C. Effects of combined pre- and post-natal enrichment on anxiety-like, social, and cognitive behaviours in juvenile and adult rat offspring. Behav Brain Res 2018; 353:40–50.

236. Radak Z, Suzuki K, Higuchi M, Balogh L, Boldogh I, Koltai E. Physical exercise, reactive oxygen species and neuroprotection. Free Radic Biol Med 2016; 98:187–96.

237. Picard M, McEwen BS. Psychological Stress and Mitochondria: A Systematic Review. Psychosom Med 2018; 80(2):141–53.

238. Rezin GT, Cardoso MR, Gonçalves CL, Scaini G, Fraga DB, Riegel RE et al. Inhibition of mitochondrial respiratory chain in brain of rats subjected to an experimental model of depression. Neurochem Int 2008; 53(6-8):395–400.

239. Liu W, Zhou C. Corticosterone reduces brain mitochondrial function and expression of mitofusin, BDNF in depression-like rodents regardless of exercise preconditioning. Psychoneuroendocrinology 2012; 37(7):1057–70.

240. Ortmann CF, Réus GZ, Ignácio ZM, Abelaira HM, Titus SE, Carvalho P de et al. Enriched Flavonoid Fraction from Cecropia pachystachya Trécul Leaves Exerts Antidepressant-like Behavior and Protects Brain Against Oxidative Stress in Rats Subjected to Chronic Mild Stress. Neurotox Res 2016; 29(4):469–83.

241. Seo J-S, Lee K-W, Kim T-K, Baek I-S, Im J-Y, Han P-L. Behavioral stress causes mitochondrial dysfunction via ABAD up-regulation and aggravates plaque pathology in the brain of a mouse model of Alzheimer disease. Free Radic Biol Med 2011; 50(11):1526–35.

242. Kambe Y, Miyata A. Potential involvement of the mitochondrial unfolded protein response in depressive-like symptoms in mice. Neurosci Lett 2015; 588:166–71.

243. Davey GP, Clark JB. Threshold effects and control of oxidative phosphorylation in nonsynaptic rat brain mitochondria. J Neurochem 1996; 66(4):1617–24.

244. Filipović D, Todorović N, Bernardi RE, Gass P. Oxidative and nitrosative stress pathways in the brain of socially isolated adult male rats demonstrating depressive- and anxiety-like symptoms. Brain Struct Funct 2017; 222(1):1–20.

245. Amiri S, Amini-Khoei H, Haj-Mirzaian A, Rahimi-Balaei M, Naserzadeh P, Dehpour A et al. Tropisetron attenuated the anxiogenic effects of social isolation by modulating nitrergic system and mitochondrial function. Biochim Biophys Acta 2015; 1850(12):2464–75.

246. Möller M, Du Preez JL, Viljoen FP, Berk M, Emsley R, Harvey BH. Social isolation rearing induces mitochondrial, immunological, neurochemical and behavioural deficits in rats, and is reversed by clozapine or N-acetyl cysteine. Brain Behav Immun 2013; 30:156–67.

247. Krolow R, Noschang C, Weis SN, Pettenuzzo LF, Huffell AP, Arcego DM et al. Isolation stress during the prepubertal period in rats induces long-lasting neurochemical changes in the prefrontal cortex. Neurochem Res 2012; 37(5):1063–73.

248. Carlson PJ, Singh JB, Zarate CA, Drevets WC, Manji HK. Neural circuitry and neuroplasticity in mood disorders: Insights for novel therapeutic targets. NeuroRx 2006; 3(1):22–41.

249. Harraz OF, Altier C. STIM1-mediated bidirectional regulation of Ca(2+) entry through voltage-gated calcium channels (VGCC) and calcium-release activated channels (CRAC). Front Cell Neurosci 2014; 8:43.

250. Da Silva T, Wu A, Laksono I, Prce I, Maheandiran M, Kiang M et al. Mitochondrial function in individuals at clinical high risk for psychosis. Sci Rep 2018; 8(1):6216.

251. Miller TJ, McGlashan TH, Rosen JL, Cadenhead K, Cannon T, Ventura J et al. Prodromal assessment with the structured interview for prodromal syndromes and the scale of prodromal symptoms: Predictive validity, interrater reliability, and training to reliability. Schizophr Bull 2003; 29(4):703–15.

252. Picard M, Prather AA, Puterman E, Cuillerier A, Coccia M, Aschbacher K et al. A Mitochondrial Health Index Sensitive to Mood and Caregiving Stress. Biol Psychiatry 2018; 84(1):9–17.

253. Chacko BK, Zhi D, Darley-Usmar VM, Mitchell T. The Bioenergetic Health Index is a sensitive measure of oxidative stress in human monocytes. Redox Biol 2016; 8:43–50.

254. Keane KN, Calton EK, Cruzat VF, Soares MJ, Newsholme P. The impact of cryopreservation on human peripheral blood leucocyte bioenergetics. Clin Sci 2015; 128(10):723–33.

255. Chacko BK, Kramer PA, Ravi S, Johnson MS, Hardy RW, Ballinger SW et al. Methods for defining distinct bioenergetic profiles in platelets, lymphocytes, monocytes, and neutrophils, and the oxidative burst from human blood. Lab Invest 2013; 93(6):690–700.

256. Alonso JR, Cardellach F, Casademont J, Miró O. Reversible inhibition of mitochondrial complex IV activity in PBMC following acute smoking. Eur Respir J 2004; 23(2):214–8.

257. Al-Amin MM, Nasir Uddin MM, Mahmud Reza H. Effects of antipsychotics on the inflammatory response system of patients with schizophrenia in peripheral blood mononuclear cell cultures. Clin Psychopharmacol Neurosci 2013; 11(3):144–51.

258. Rose S, Frye RE, Slattery J, Wynne R, Tippett M, Melnyk S et al. Oxidative stress induces mitochondrial dysfunction in a subset of autistic lymphoblastoid cell lines. Transl Psychiatry 2014; 4:e377.

Publications

Michels S, Dolga AM, Braun MD, Kisko TM, Sungur AÖ, Möbius TWD, Dempfle A, Wöhr M, Schwarting RKW, Culmsee C. Interaction of the psychiatric risk gene *Cacna1c* with post-weaning social isolation or environmental enrichment fails to affect brain mitochondrial bioenergetics in rats. In preparation

Culmsee C, **Michels S**, Scheu S, Arolt V, Dannlowski U, Alferink J. Mitochondria, microglia and the immune system – how are they linked in affective disorders? Submitted

Kisko TM, Braun MD, **Michels S**, Witt SH, Rietschel M, Culmsee C, Schwarting RKW, Wöhr M. Sex-dependent effects of *Cacna1c* haploinsufficiency on juvenile social play behavior and pro-social 50-kHz ultrasonic communication in rats. Submitted

Ramzan R, **Michels S**, Weber P, Riehl A, Rastan AJ, Culmsee C, Vogt S. Protamine sulfate: A commonly used cardiovascular drugs' action on mitochondrial bioenergetics profile and ROS production. Revision submitted

Kisko TM, Braun MD, **Michels S**, Witt SH, Rietschel M, Culmsee C, Schwarting RKW, Wöhr M. *Cacna1c* haploinsufficiency leads to pro-social 50-kHz ultrasonic communication deficits in rats. Disease Models & Mechanisms. June 2018

Michels S, Wöhr M, Schwarting RKW, Culmsee C. Psychiatric risk gene *Cacna1c* determines mitochondrial resilience against oxidative stress in neurons. Cell Death & Disease. May 2018

Michels S, Ganjam GK, Martins H, Schratt GM, Wöhr M, Schwarting RKW, Culmsee C. Downregulation of the psychiatric susceptibility gene *Cacna1c* promotes mitochondrial resilience to oxidative stress in neuronal cells. Cell Death Discovery. May 2018

Meetings and Conferences

World Congress on Targeting Mitochondria. Berlin, Germany. October 2018

Meeting of the GBM Study Group „Molecular Neurobiology": Dynamics of the Nervous System in Health and Disease. Marburg, Germany. September 2018

European Calcium Channel Conference and Joint Neuroscience Meeting. Alpbach, Austria. May 2018

Neuroscience. Washington, USA. November 2017
Financially supported by Marburg International Doctorate and Marburg University Research Academy (MARA)

Neurochemical Conference. Warsaw, Poland. October 2017
Young Investigator Travel Award

2. Retreat FOR 2107. Rauischholzhausen, Germany. November 2016

Robert Sommer Award Conference. Gießen, Germany. November 2016

DPhG Jahrestagung. Munich, Germany. October 2016

BPC Graduate School Student Day. Marburg, Germany. March 2016

1. Retreat FOR 2107. Rauischholzhausen, Germany. February 2016

Acknowledgments

Die Seiten 134-136 enthalten personenbezogene Daten und sind daher in der elektronischen Version nicht enthalten.

Curriculum vitae

Die Seite 137 enthält personenbezogene Daten und ist daher in der elektronischen Version nicht enthalten.